

**EVALUATION OF THE BIOPHYSICAL
CHARACTERISTICS OF UPCONVERSION
NANOPARTICLE-BASED NANO-BIO HYBRIDS FOR
BLOOD-BRAIN BARRIER CROSSING**

By

Libing Fu

Department of Biomedical Sciences

Supervisors:

Prof. Roger Chung, Prof. Dayong Jin, Dr. Bingyang Shi



MACQUARIE
University
SYDNEY • AUSTRALIA

This thesis is presented for the degree of Doctor of Philosophy

October 2017

I certify that the work in this thesis has not previously been submitted for a degree nor has it been submitted as part of requirements for a degree to any other university or institution other than Macquarie University.

I also certify that the thesis is an original piece of research and it has been written by me. Any help and assistance that I have received in my research work and the preparation of the thesis itself have been appropriately acknowledged.

In addition, I certify that all information sources and literature used are indicated in the thesis.

The research presented in this thesis was approved by Macquarie University Ethics Review Committee, reference number: 5201100617 LAB on 11 Aug 2011.

A handwritten signature in black ink on a light yellow rectangular background. The signature appears to read "Libing Fu" in a cursive, flowing script.

Libing Fu 15-Oct-2017

Acknowledgements

I would like to appreciate all the people who contributed in some way to this project mentioned in this thesis. First, I express my sincere gratitude to my principle supervisor prof. Roger Chung for giving me the opportunity to improve my research skills in his group. During my PhD candidate period, he offered me an excellent platform to learn biological techniques, supporting my attendance at various academic conferences and teaching me to manage project smartly. Furthermore, he always encouraged me to come up with new ideas and gave me constructive suggestions for this project. Importantly, the joy and enthusiasm he has for his research and work deeply infected me during tough time in the PhD pursuit. I also want to thank Roger for his patiently guiding me on my PhD program and academic writing to be easily understood.

I am also sincerely grateful to my associate supervisor Dr. Bingyang Shi, who gave me professional advice and helped me formulate my PhD research frame. He provided me a lot of thoughtful comments on my publications and thesis draft. I especially appreciate the opportunity he provided me to work in the Department of Biomedical Sciences, learning more biological techniques and giving me a wonderful foundation to build. He is an excellent mentor and fundamental in training and helping me become a proficient experimentalist. I learned a lot from Bingyang's self-motivated, aspiring, energetic and collaborative research style. I sincerely thank his generous help and deep insight on my PhD project but also concern about my research career development. Specially, I would like to appreciate Prof. Jin, who provided me the opportunity to come to Macquarie University as a PhD student for further study. Although he transferred to the UTS, he always cared about my project and generally provided help when I need.

Other fellows in Roger's group had a significant impact on this work. Dr. Marco Morsch is a research fellow and proficient in zebrafish imaging and microinjection. Marco and I worked together in the first and second phase of this project. He generally provided help in microinjection of surface-modified UCNPs into spinal cord of zebrafish. Moreover, thanks to his kind help, I could observe the zebrafish

microinjected with UCNPs with Zeiss confocal microscope. Next, I would like to thank Rowan Radford, a PhD candidate in Roger's group as well. He taught me how to analyse the confocal microscope images with Imaris software and quantify the UCNPs uptake into the cells and zebrafish. Moreover, I also would like to thank Serene Gwee and Stephanie Rayner for teaching me the cellular experiment. For the UCNPs fabrication, I would like to specially thank Dr. Deming Liu and Mr. Shihui Wen, who trained me the synthesis of UCNPs with various size and shape. Meanwhile, they gave me many useful suggestions to specifically control the UCNPs preparation for this project. For the characterization of as-prepared UCNPs, I would like to acknowledge Dr. Yiqing Lu. He graciously allowed us to utilize the Leica confocal microscope setup that they built by themselves. Furthermore, he wholeheartedly supported me to explain the mechanism of optical properties of UCNPs, and his physical insight was instrumental for the completion of this work. In terms of the single nanoparticle characterization, I would like to thank Chao Mi, Zhiguang Zhou and Dr. Xianlin Zheng. Without their professional help and useful guidance, I could not complete the single UCNPs measurement.

My time at Macquarie University was made enjoyable to large extent due to my friends and members from New South Wales Chinese Student Scholar Association (NSWCSSA) that become an important part of my life. In particularly, I would like to thank my lovely friends, Yinghui Chen, Fei Han, Chenshuo Ma, Sheran Li, Zizhen Ming, Yan Wang, Liuen Liang, Wei Ren, Shihui Wen and Hao He for their friendship, laughs, generous support through my PhD study. I won't forget our memorable trips to Blue Mountains, self-driving from Melbourne to Sydney, self-cooking for Sheran's Birthday, picnic in La Perouse and other joyful memories. I'd also like to thank many friends with whom I began my PhD study in 2014. Though many of them transferred to other universities or institutions, they often offered me kind help strong words of encouragement that I sincerely appreciate.

I am also grateful to the staff from Department of Biomedical Sciences, especially Laura Newey who helped me a lot to solve my official and conference application problems. In addition, I would like to acknowledge Viviana Bong from HDRO of

Macquarie University, who gave me patiently guidance on how to prepare for the PGRF application and procedure of the thesis submission.

I gratefully acknowledge the financial support I acquired from both Macquarie University and China Scholar Council (MQ-CSC) that made my PhD work possible, offering me numerous opportunities to expend my research experiences. My work was also supported by the Faculty of Medicine and Health Sciences Scholarship Top-Up throughout my 3-year PhD period.

Finally, I would like to acknowledge my beloved family, mom, dad, my sisters (Meimei and Xiaomeng), my little brother (Jianzhan), my brother-in-law (Qingwei Fu), sister-in-law (Qiuping Chen), my niece (Zihan Fu, Ziyi Fu and Ziyue Fu) and my nephew (Zihao Fu) for backing me up in past years. My parents always encouraged me to pursue my dreams and provided me a constant source of love and endless support. I sincerely appreciate Fei Han, who introduced Jimmy Leung to me in Macquarie University. With the company of Jimmy in the last year of my PhD study, it is much easier for me to go through this challenging and stressful journey. I specially thank Jimmy for his good-to-excellent care, love and unyielding support during my hard times. I am so lucky to meet him in Australia, I am really thankful for the incomparable love and joy he brings to my life.

List of Publications

Papers

- [1] **Fu, L.**, Morsch, M., Shi, B., Wang, G., Lee, A., Radford, R., Lu, Y., Jin, D. and Chung, R., Versatile Upconversion Surface Evaluation Platform for Bio-nano Surface Selection for Nervous System. *Nanoscale* **2017**, 9, 13683-13692.
- [2] **Fu, L.**, Shi, B., Morsch, M., Wang, G., Lu, Y., Jin, D. and Chung, R., Evaluation of the Effect of Shape upon Endocytosis of Transferrin-coated Upconversion nanoparticles, and their Ability to cross the Blood-brain Barrier. Manuscript prepared for submission to *ACS nano*.
- [3] **Fu, L.**, Shi, B., Wang, G., Liu, D., Jin, D. and Chung, R., The Effect of Modifying the Aspect Ratio of PEGylated Upconversion Nanoparticles upon their Cellular Uptake. Prepared for submission to *Biomaterials*.
- [4] Shi, B., Du, X., Chen, J., **Fu, L.**, Morsch, M., Lee, A., Liu, Y., Cole, N., Chung, R., Multifunctional Hybrid Nanoparticles for Traceable Drug Delivery and Intracellular Microenvironment-Controlled Multistage Drug-Release in Neurons. *Small* **2017**, 13, 1603966.
- [5] Wang, G., **Fu, L.**, Shi, B., A New Endogenous Fluorescent Poly(amidoamine) Dendrimer Achieves Excellent Traceable and Controlled Drug Delivery. Prepared for submission to *J. Control. Release*.

([1] - [3] are closely related to my PhD project)

Conference Papers

- [1] **Fu, L.**, Shi, B., Jin, D. and Chung, R., The Effect of Shape and Surface Functionalization upon the Cellular Uptake Characteristics of Upconversion Nanocrystals, *The 7th International Nano Medicine Conference*, **2016**. (Poster)
- [2] **Fu, L.**, Albert, L., Shi, B., Jin, D. and Chung, R., The Influence of Surface Modified Lanthanide-doped Upconversion Nanocrystals on Cellular Endocytosis. *Macquarie University BioFocus Research Conference*, **2016**. (Poster)

- [3] **Fu, L.**, Shi, B. and Chung, R., Crossing Blood Brain Barrier for Dementia Therapy. *Dementia Meeting*, **2016**. (Oral presentation)
- [4] **Fu, L.**, Shi, B. and Chung, R., Nanoparticles Based Blood Brain Barrier Shuttle for Alzheimer's Disease Therapy. *Blood Brain Barrier Meeting*, **2016**. (Oral presentation)
- [5] **Fu, L.**, Wang, G., Shi, B., Jin, D. and Chung, R., Comparison and Evaluation of Nanoparticles Surfaces with Cultured Neuron Cell for the Potential Applications in Brain. *IEEE NANO*, **2017**. (Oral presentation)
- [6] Shi, B., **Fu, L.** and Chung, R., Nanoparticles Based Theranostics. *International Conference of Nanomedicine*, **2017**. (Oral presentation)

EVALUATION OF THE BIOPHYSICAL CHARACTERISTICS OF UPCONVERSION NANOPARTICLE-BASED NANO-BIO HYBRIDS FOR BLOOD-BRAIN BARRIER CROSSING

Abstract:

Brain diseases including Alzheimer's disease, Huntington's disease and amyotrophic lateral sclerosis (ALS) are fatal diseases without effective treatments. In past decades, some potentially effective therapeutics have been developed and demonstrated promising effects for brain diseases in pre-clinical cell culture and animal model evaluation. However, most of these developed drugs cannot reach the brain for therapy due to their inability to cross the blood-brain barrier (BBB). To overcome the BBB, nanotechnology is emerging as a promising approach to mediate and increase BBB penetration of drugs to the specific site of the brain. However, the efficiency of nanoparticle-based BBB penetration is still very low (<1%), with much to learn about how the biophysical properties of nanoparticles such as which size, surface, shape of nanoparticles facilitate BBB penetration. This project takes advantage of the specific properties of upconversion nanoparticles (UCNPs) including low auto-fluorescence, non-photobleaching, deep tissue penetration and adjustable size and shape, to develop a versatile platform to systematically evaluate the effects of nanoparticle surface, shape on BBB crossing in vitro and in vivo for future construction of multifunctional nano-carrier for theranostic applications in neurodegenerative diseases.

In the first chapter, this thesis introduced the BBB and currently understood mechanisms of BBB penetration, and reviewed recent advances in nanoparticle-based BBB penetration strategies and approaches for brain disease therapy.

In the second chapter, I described the key experimental methods that were developed and optimized for use in this project. Typically, the UCNPs employed in this project were fabricated via modified and optimized standard protocols for specific application as required. Importantly, the approaches of zebrafish imaging and microinjection were developed brand new in this project.

In the third chapter, a UCNPs-based evaluation platform was synthesized for bio-nano surface selection in vitro and in vivo to systemically evaluate the suitability of various surface modifications for theranostic applications in neurodegenerative diseases. First, high lanthanide-doped UCNPs was designed, which provide strong tissue penetrable emission at 800nm. Then, these as-prepared UCNPs were further modified with four popular surfaces (OA-free, DNA-modified, silica coated and PEG-COOH capped) for comparison. The result showed that PEG-COOH performed superior cell internalization and excellent uptake capability into spinal motor neurons in zebrafish. Our work provides a versatile strategy via systemically surface evaluation for future construction of multifunctional nano-systems for therapeutic delivery to the central nervous system.

In the fourth chapter, the effect of nanoparticle shape upon cell uptake and BBB penetration was further studied in vivo and in vitro. Firstly, a series of UCNPs with different shapes (including spherical, rod, disk and dumbbell) which retained similar size with each other were fabricated. Thereafter, these UCNPs were further modified with transferrin to make them specifically target the BBB. The results revealed that rod-shaped Tf-UCNPs displayed excellent brain endothelial cell uptake and brain accumulation in living zebrafish. Importantly, this study provides promising morphology information for design of efficient nano-carriers to cross the BBB for treatment of brain disease.

In the fifth chapter, the optimal aspect ratio (AR, width/length) of upconversion nanorods (UCNRs) for BBB penetration were investigated. A series of high-lanthanide doped UCNRs with various aspect ratios (1, 2, 3 and 4) were developed. Then those UCNRs were further modified with PEG-COOH, since PEG-COOH modification was found to have superior cell internalization and excellent uptake capability for central nervous system from the results of Chapter 3. It was found that the aspect ratio of 2 PEGylated UCNRs provides the best cell uptake efficiency in neuron cells (NSC-34 neuron like cells, primary neuron cells and glial cells) compared to nanoparticles with other aspect ratios. This study demonstrates that aspect ratio has a significant influence upon cell uptake of neuron cells, which provides an alternative opportunity for further design of nanoparticle-based therapies for drug delivery of nanoparticles into the brain.

In the sixth chapter, result of this thesis was summarized and perspective for the future applications for UCNPs-based drug delivery across BBB for CNS diseases was presented. To summarise, a transferrin-coated UCNRs with respect ratio of 2 was investigated as a potential drug carrier for treatment of neurodegenerative disease. These nanoparticles were capable of readily crossing the BBB and accumulating within the brains of living zebrafish, highlighting the therapeutic potential of this specific nanoparticle design. Overall, this study demonstrated a novel method to identify preferable biophysical characteristics of upconversion nanoparticle-based nano-bio hybrids to increase targeted nanoparticle accumulation in the brain.

Key Words: blood-brain barrier, lanthanides-doped upconversion nanoparticles, surface modification, morphology control, endothelial cells, living fli zebrafish

Contents

Acknowledgements	v
List of Publications	viii
Abstract	x
List of Acronyms	xvii
Chapter 1: Introduction	1
1.1 Central Nervous System Diseases and the Challenge in Development of Therapies	4
1.1.1 Nervous System	4
1.1.2 Central Nervous System	5
1.1.3 CNS Diseases, their Treatment Challenges and Prospects	5
1.2 Blood-brain Barrier	6
1.2.1 Blood-brain Barrier Structure	6
1.2.2 Functions of Blood-brain Barrier	7
1.2.3 Mechanisms that Facilitate Transport of Molecules across the BBB	8
1.2.4 Strategies for Delivering Therapeutic Molecules across the BBB	8
1.2.4.1 Invasive Techniques	10
1.2.4.2 Non-invasive Techniques	11
1.3 Biophysical Parameters of Nanoparticles Influence their Cellular Uptake	14
1.3.1 Surface Chemistry	14

1.3.1.1	Negative Surface Charge.....	15
1.3.1.2	Positive Surface Charge.....	17
1.3.1.3	Neutral Surface Charge.....	17
1.3.2	Nanoparticle Size.....	18
1.3.3	Nanoparticle Shape.....	22
1.4	Lanthanide-doped Upconversion Nanoparticles (UCNPs).....	25
1.4.1	Optical Properties of Ln^{3+} -UCNPs.....	27
1.4.2	Efficient Enhancement of Upconversion Emission.....	30
1.4.2.1	Adjusting the Dopant Concentration.....	30
1.4.2.2	Surface Passivation with Core-shell Structure.....	31
1.4.3	Surface Engineering of UCNPs.....	32
1.4.3.1	Ligand Removal.....	33
1.4.3.2	Ligand Exchange.....	33
1.4.3.3	Generation of a Silica Shell on the Surface of UCNPs.....	34
1.4.4	Shape Controlled Fabrication of UCNPs.....	36
1.4.4.1	Thermolysis.....	37
1.4.4.2	Hydro(solvo)thermal.....	38
1.4.4.3	Ostwald-ripening.....	39
1.4.5	Biological Applications of Ln^{3+} -UCNPs.....	39
1.4.5.1	Ln^{3+} -UCNPs for Bioimaging.....	40
1.4.5.2	Ln^{3+} -UCNPs for Drug Delivery.....	42
1.5	Conclusions and Outlook.....	45

1.6	Thesis Aims.....	46
1.7	References.....	47
Chapter 2 Protocol Development and Optimization.....		68
2.1	Highly-controlled Size and Shape of Upconversion Nanoparticles	70
2.1.1	Synthesis of Spherical OA-capped UCNPs.....	70
2.1.2	Synthesis of Upconversion Nanorods.....	72
2.1.3	Synthesis of Upconversion Nanodisk.....	75
2.2	Develop a Standard Protocol for Surface Modification of UCNPs.....	77
2.2.1	Stober Method for Silica Coating of Ln^{3+} -UCNPs.....	77
2.2.2	Reverse Micromulsion for Silica Coating of Ln^{3+} -UCNPs.....	79
2.3	High Resolution Fluorescent Imaging of Ln^{3+} -UCNPs in cells.....	81
2.4	Quantification Analysis of UCNPs Internalized by Cultured Cells.....	84
2.5	High Resolution Real-time Confocal Microscopy of UCNPs in Zebrafish.....	87
2.6	Microinjection of UCNPs into Embryo and Muscle of Zebrafish.....	90
Chapter 3 A Versatile Upconversion Surface Evaluation Platform for Bio-nano Surface Selection for the Nervous System.....		95
3.1	Contributions to Paper 1.....	96
3.2	Paper 1.....	97
3.3	Remarks.....	113
Chapter 4 Evaluation of the Effect of Shape upon Endocytosis of Transferrin-coated UCNPs, and their Ability to cross the Blood-brain Barrier.....		114

4.1	Contributions to Manuscript 2.....	115
4.2	Manuscript 2.....	116
4.3	Remarks.....	141
Chapter 5: The Effect of Modifying the Aspect Ratio of PEGylated UCNPs upon their Cellular Uptake.....		142
5.1	Contributions to Manuscript 3.....	143
5.2	Manuscript 3.....	144
5.3	Remarks.....	167
Chapter 6: Summary and Future Scope.....		168
6.1	Summary.....	168
6.2	Future scope.....	170
6.3	Reference.....	173

List of Acronyms (in alphabetic order)

AD	Alzheimer's disease
ARs	aspect ratio
BBB	blood-brain barrier
CAOV3	ovarian cancer cell
CET	cooperative energy transfer
CNS	central nervous system
CTAB	cetyltrimethylammonium bromide
EDTA	ethylenediaminetetraacetic acid
EPR	enhanced permeability and retention
ESA	excited-state absorption
ETU	energy transfer upconversion
FA	folic acid
FR	folate receptor
GM1	monosialotetrahexosylganglioside
HD	heart disease
Ln^{3+}	lanthanide ions-doped
MSNs	mesoporous silica nanoparticles
NAs	nano-agonists
NIR	near-infrared ray
OA	oleic acid
ODE	1-octadecene
OM	oleylamine
PEI	polyethylenimine

PNS	peripheral nervous system
TEM	transmission electron microscopy
Tf	transferrin
TOPO	trioctylphosphine oxide
UC	upconversion
UCL	upconversion luminescence
UCNPs	upconversion nanoparticles

Chapter 1: Introduction

During the first decade of the 21st century, heart disease (HD) and cancer, as the two leading causes of death in the United States, have declined due to advances and progress in prevention and therapy. [1] The age-adjusted mortality rate for cancer has decreased 15% between 2003 and 2013, while the death rate from HD has dropped dramatically by 28% over that same period.[2] However, chronic diseases of the central nervous system (CNS), such as the most common type named Alzheimer's disease (AD), have not benefited similarly. To the contrary, the proportion of deaths from AD has increased 68% over the past decade [3], moving AD from outside the top ten in 1980 to the sixth highest cause of death in the United States in 2013.[2] This dramatic increase is most likely a combination of many factors, including an ageing population, uncertainty on potential prevention strategies, and absence of effective therapies. With a rapidly ageing population across many parts of the world, there is an urgent need to identify novel therapeutic strategies with efficient treatment efficacy for neurodegenerative disorders.

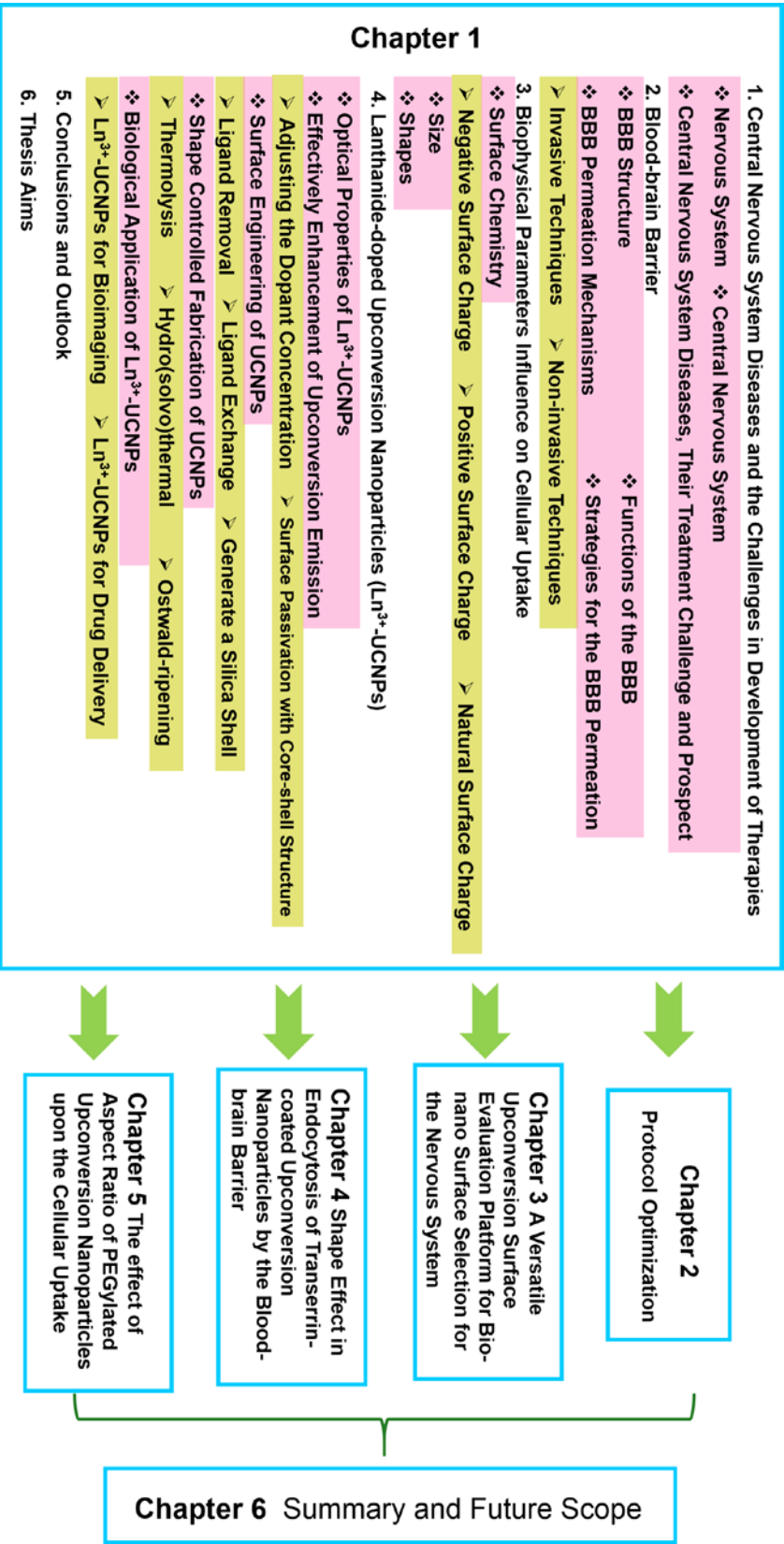
To develop pharmacological treatments for central nervous system (CNS) diseases, a major challenge is the efficient delivery of therapeutic agents across the blood-brain barrier (BBB). The BBB acts to protect the brain from harmful and poisonous agents, however it also significantly hinders most drugs from entering the brain. Recent cellular and molecular biology studies have shed important insight into the structure and function of the BBB. Accordingly, it is now recognized that the BBB is not only an anatomical barrier to diffusion of molecules directly from the blood and into the brain, but also a transport and metabolic barrier. Several approaches have been reported to enhance drug delivery to the CNS, although some of these methods may disrupt the structure and/or function of the BBB by forcibly opening it to increase the penetration of drugs (which may have detrimental effects by altering the movement of other molecules into or out of the brain. Therefore, there is great interest in identifying strategies for controlled drug delivery without causing structural damage to the BBB.

Nanotechnology-based delivery approaches exhibit considerable promise to achieve this goal of delivery drug across BBB without inducing structural damage to the BBB.

Nanoparticles are feasible to be transported across the BBB by vectors, also as carriers without any damage to the BBB.[4] The crucial advantage of nanoparticle-based delivery systems is that they can compensate for the BBB-limited characteristics of drug molecules.[5] In addition, this transport nano-system may prolong and the drug releasing into the brain to alleviate peripheral toxicity. However, there are numerous factors affecting drug transport, including surface modification, size, morphology and the mechanisms involved remain poorly understood. Because there is a lack of platforms to systematically study the interrelationship between these factors (ie. surface chemistry, size and shape) and BBB penetration.

Lanthanide-doped upconversion nanoparticles (UCNPs) are a potential nanoparticle platform for systematic investigation of the influence of nanoparticle surface, size and shape on cellular uptake and BBB penetration. Recently, UCNPs have received considerable attention due to their unique optical properties. They convert near-infrared radiation (NIR) photons to visible or even near-infrared emissions, offering deep tissue imaging within the NIR spectrum (which is biologically safe). These optical properties provide UCNPs with a broad range of biological applications, such as tracking systems, imaging probes and optoelectronic devices.[6–9] In addition, the size, surface and shape of UCNPs are all amenable to modification.

This Introductory Chapter will briefly summarize the current research on nanoparticle and in particularly UCNP-based drug delivery, and give a perspective on the potential applications of nanoparticle-based drug delivery platforms for treatment of neurodegenerative diseases.



Flow graph outlining the structure of this thesis.

1.1 Central Nervous System Diseases and the Challenges in Development of Therapies

1.1.1 Nervous System

In vertebrates, the structure of nervous system contains two key groups, the central nervous system (CNS) and the peripheral nervous system (PNS). (Figure 1) The CNS consists of the brain and spinal cord. The PNS includes numerous nerves which are long fibers, which connect the CNS to other parts of the body. The PNS can be further divided into three separate systems, which are the enteric, autonomic and somatic nervous system. Specifically, the enteric nervous system controls the gastrointestinal system. The autonomic nervous system can be further subdivided into the sympathetic and the parasympathetic nervous systems. The former is activated to mobilize energy in response to emergency or stressful situations (such as the freezing behaviour of scared rabbits), while the latter is active when the animal is in a relaxed state. The somatic nerves mediate voluntary movement.

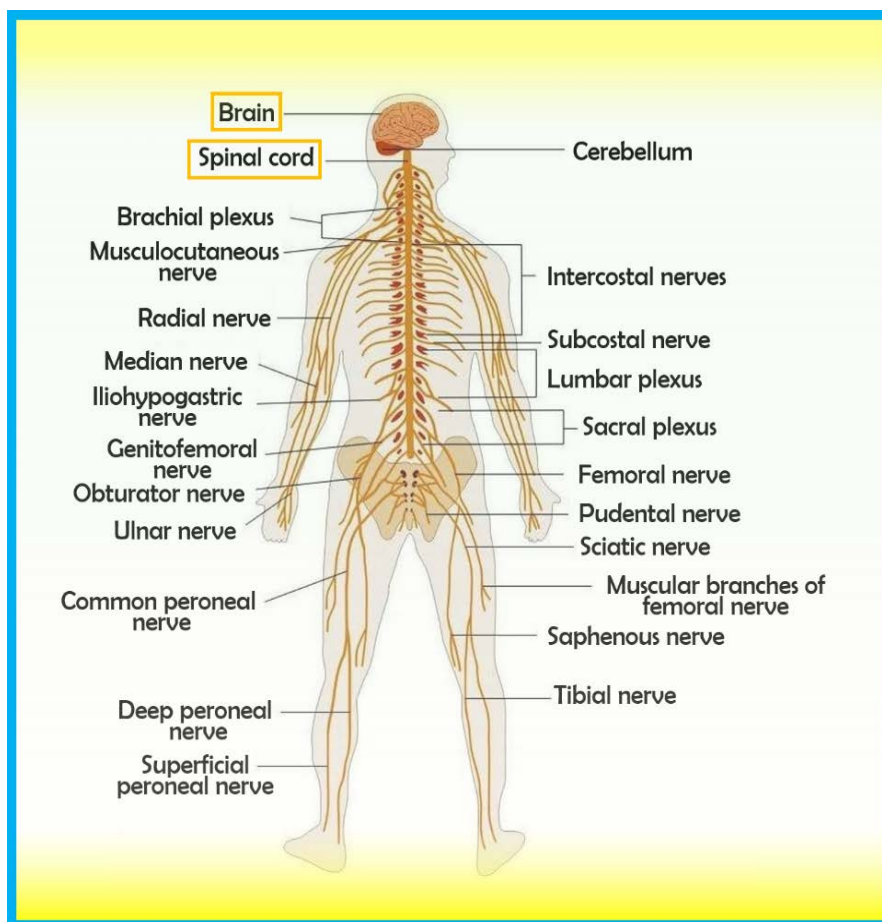


Figure 1. Illustration of the nerve system in a human body.

Collectively, the nerves from the nervous system coordinate and cooperate with each other to control the movement and actions of the animal's body.

1.1.2 Central Nervous System

The CNS integrates signals received from all parts of the bodies of bilaterally symmetric animals (all multicellular animals except sponges and radially symmetric animals). There are two classes of cells in the nervous system, containing neurons (process information) and glia (provide the neurons with mechanical and metabolic support). A single nerve cell is called a neuron. There are approximately a trillion neurons in the human nervous system. In addition, glial cells are also named neuroglia. Although they are not as popular as neurons, they make up about 90% of cells within the CNS. Unlike neurons, glial cells do not conduct nerve electrical signals. They serve to protect and nourish the neurons instead. Neurons depend on glial cells to grow, nourish themselves, and establish effective synapses. The glial cells of the CNS therefore support the neurons both physically and chemically via processes needed for cell survival. There are four major types of glial cells in the CNS, such as astrocytes, oligodendrocytes, microglia and ependymal cells.

1.1.3 Central Nervous System Diseases, their Treatment Challenges and Prospects

CNS diseases include neurodegenerative disorders (such as Alzheimer's disease, Parkinson's disease and Huntington's disease), addiction, bipolar disorder, depression, multiple sclerosis and so on. Among these types of CNS diseases, Alzheimer's disease (AD) is the most common, currently influencing the health of more than five million people from the United States (Figure 2), and is predicted to continually increase up to over thirteen million by 2050. [10]

The predicted total expense of health care in 2015 for people with AD was \$216 billion and is estimated to increase to \$1.2 trillion within the next thirty-five years in the United States (Figure 2).[10] To compare with that, the direct healthcare expenditure in 2010 for heart disease and cancer were predicted to be \$109 billion and \$77 billion, respectively[11]. Therefore, AD is one of the most financially costly diseases in the US. AD also places a high societal burden and there is currently a lack of effective therapies for AD and many other

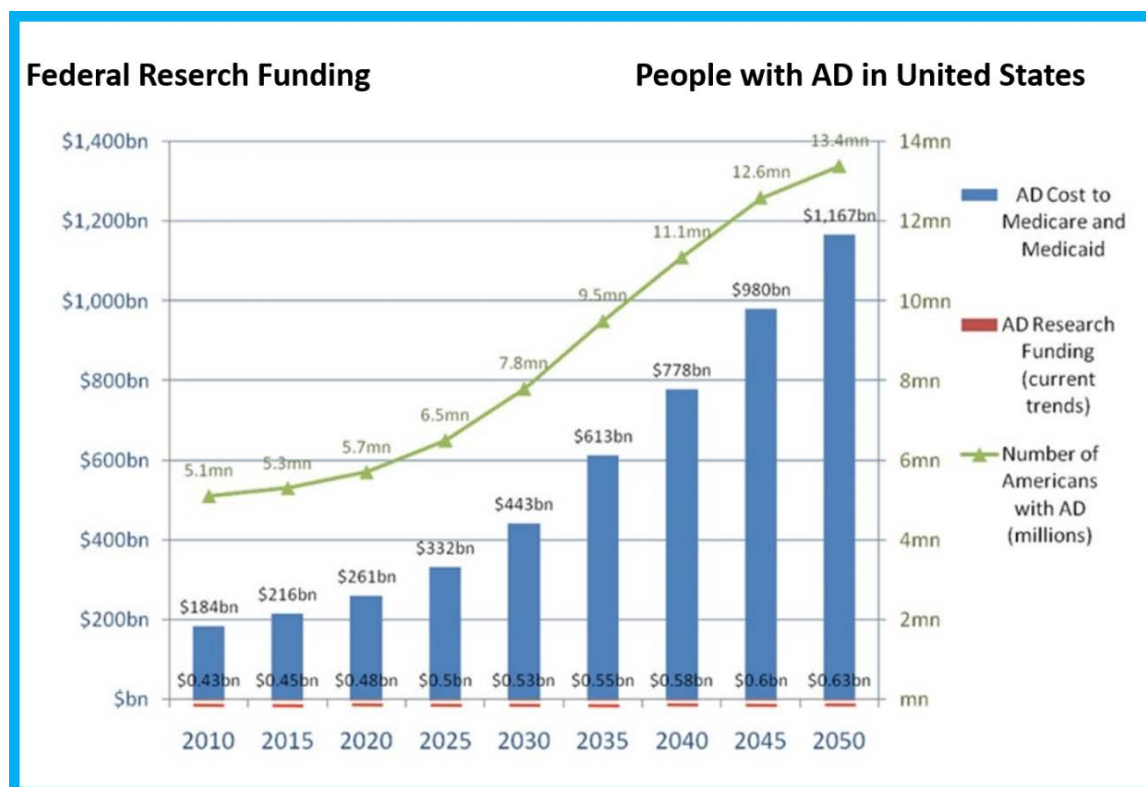


Figure 2 Illustration of the people with Alzheimer's disease in USA and the Federal research funding. (Data is from ref. [10])

neurodegenerative diseases. Therefore, effective treatments for these diseases are urgently required.

While there is enormous expenditure upon research and development towards new therapies for CNS diseases, this has generally not been successful.[12] A major challenge for the development of pharmaceutical treatments is the blood-brain barrier (BBB), which protects the CNS from noxious and harmful agents. However, it also hinders most therapeutic agents from being able to reach the brain. [13] Therefore, it is essential to understand the underlying mechanism of BBB penetration and therefore develop strategies that overcome the BBB to successfully deliver therapeutic molecules into the CNS.

1.2 Blood-brain Barrier

1.2.1 BBB Structure

The BBB is a selectively permeable barrier that separates the brain from the peripheral blood flow. In mammals, the BBB consists of brain capillary endothelial cells and astrocytes

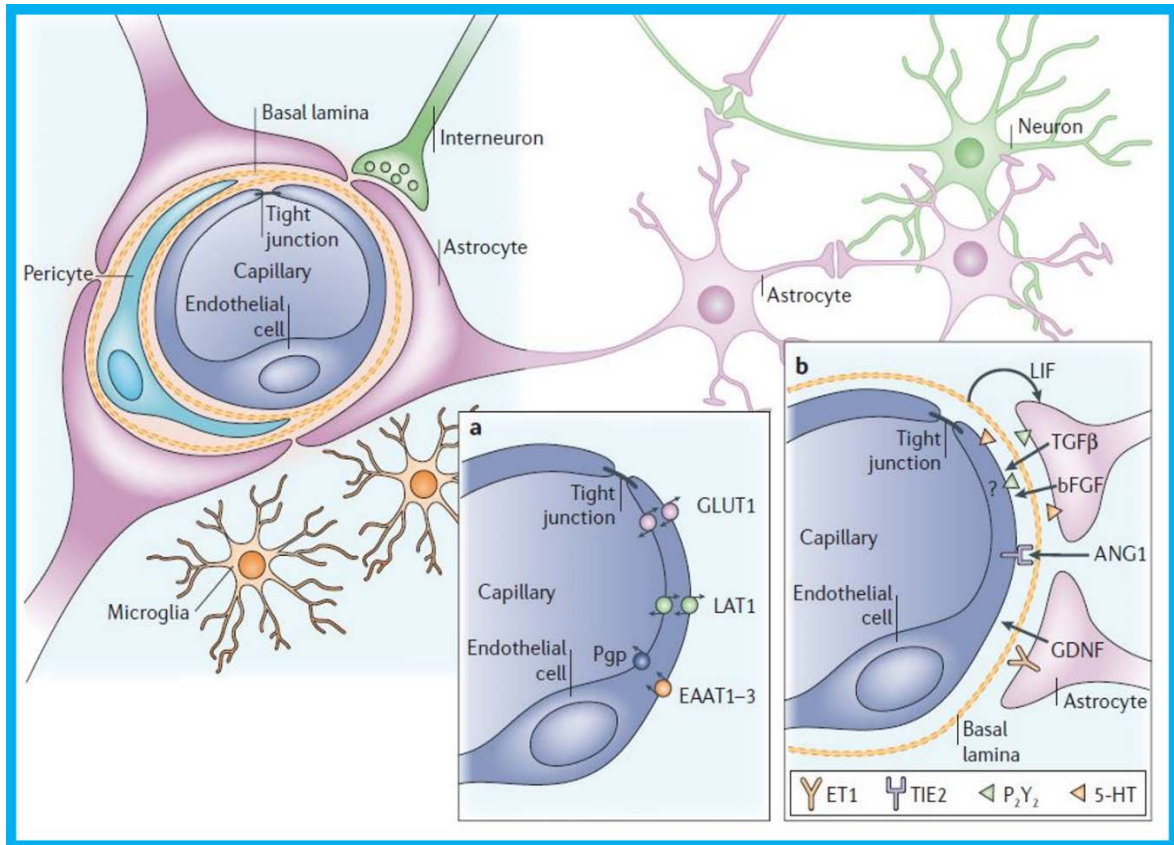


Figure 3. Illustration of structure of the BBB at cellular level. The BBB consists of capillary endothelial cells, surrounded by a basal lamina and astrocytic perivascular end-feet. The astrocytes provide the cellular linkage with the neurons. Pericytes and microglial cells are also shown in this figure. a. Brain endothelial cell express numerous transporters and receptors, such as EAAT1–3 (excitatory amino acid transporters 1–3), GLUT1 (glucose transporter 1), LAT1 (L-system for large neutral amino acids) and Pgp (P-glycoprotein). b. Examples of bidirectional endothelial-astroglial induction necessary to maintain the BBB. Some receptors and transporters are shown, such as 5-HT (5-hydroxytryptamine), ANG1 (angiopoetin 1), bFGF (basic fibroblast growth factor), ET1 (endothelin 1), GDNF (glial cell line-derived neurotrophic factor), LIF (leukaemia inhibitory factor), P₂Y₂ (purinergic receptor), TGFβ (transforming growth factor-β), TIE2 (endothelium-specific receptor tyrosine kinase 2) Data aquired from astroglial–endothelial co-cultures and the use of conditioned medium[15] [22] [23][24][187][188][189][190][191] Copyright with permission from ref. [21].

(Figure 3).[14–16] The function of the BBB is regarded as a “biological barrier” due to the tight junctions between endothelial cells in brain capillaries, forming a water-tight barrier that requires molecules to be transported via transcellular pathways to cross the BBB.[17,18] (Figure 4) Secondly, brain cells (like astrocytes and pericytes) surrounding the endothelial cells form and maintain an enzymatic and physical barrier.

1.2.2 Functions of the BBB

The BBB has several important roles in maintaining brain homeostasis. Firstly, the endothelial cell layer of the BBB regulates the brain microenvironment, as well as the short diffusion distance between capillaries and neurons. Secondly, it provides crucial nutrients for the brain to grow and maintain, meanwhile mediating efflux of plenty of useless agents out of the brain. Importantly, the BBB effectively protects the brain from most pathogens, which is important since infections of the brain are very serious and hard to treat. Thirdly, the BBB restricts fluid and ionic flux between the blood and the brain, which creates an isolated interstitial fluid within the brain that supplies an optimal medium for neuron functions.[19] Fourthly, it separates the neuroactive agents (that act in the CNS, blood and peripheral tissues) and the pools of neurotransmitters, avoiding potential “crosstalk” of two similar agents that are utilized in these two systems. Lastly, continual turnover of cerebrospinal fluid and interstitial fluid via bulk flow helps the drainage of the brain metabolites. Collectively, BBB serve as an essential physical barrier for protecting brain, however also acts as a barrier to effective delivery of drugs to the CNS.

1.2.3 Mechanisms that facilitate transport of molecules across the BBB

Molecules can be transported across the BBB (either into or out of the brain) by means of passive diffusion, active transport, receptor-mediated transport and adsorptive transcytosis (Figure 4).[20, 21] The BBB allows the crossing of water, some water soluble agents, such as O₂, CO₂ and polar drugs by passive diffusion through the junctions. Similarly, lipid-soluble molecules including alcohol, caffeine, nicotine and drugs (like barbiturates) can pass through the BBB by passive diffusion via transcellular lipophilic pathway. Active transport mechanisms regulate the transport of glucose, amino acids, purine bases and choline that are crucial to neural function by special transport proteins. Furthermore, certain proteins (such as transferrin and insulin) attach to specific receptors on the surface of the brain endothelial cells and are internalised through receptor-mediated pathways. Lastly, the endocytosis of some native plasma proteins like albumin can be increased after cationization via interaction with the endothelial membrane (adsorptive transcytosis).

1.2.4 Strategies for delivering therapeutic molecules through the BBB

There are plenty of potentially effective drugs available for some CNS disorders, however few of them successfully enter the pharmaceutical market for clinical application, mainly

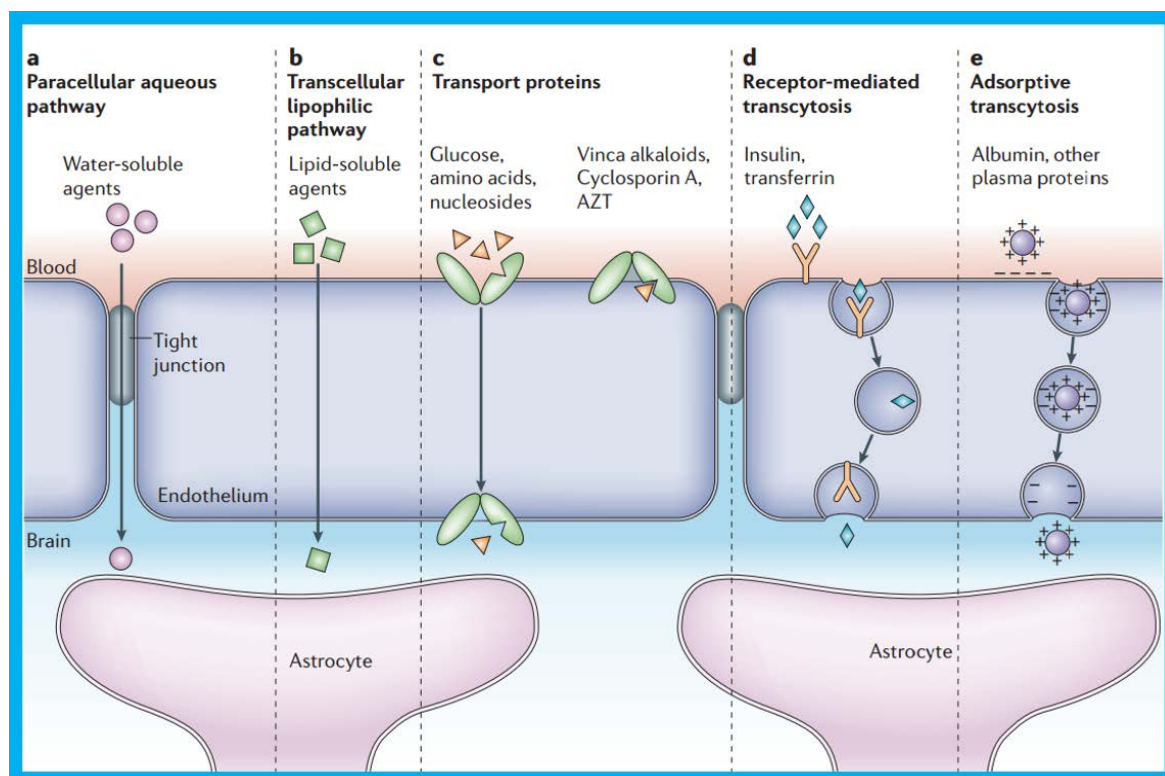


Figure 4. Schematic demonstration of the mechanisms of transport endogenous molecules across the BBB. The key pathways for substance penetrate the BBB are shown. a. the tight junctions strictly restrict penetration of water-soluble agents; b. the lipid membranes of the endothelium provides an effective diffusive route for lipid-soluble substance; c. the endothelium offers transport proteins as carriers for glucose, amino acids, nucleosides and so on. Some transporters are energy-dependent such as P-glycoprotein, vinca alkaloids, cyclosporine A and azidothymidine (AZT); d. certain proteins like insulin and transferrin, are recognised by specific receptors via receptor-mediated endocytosis and transcytosis. e. native plasma proteins such as albumin are poorly transported, but can increase their uptake by adsorptive-mediated endocytosis and transcytosis after cationization. Drug delivery across the BBB via pathways b–e; most CNS drugs enter via route b. Copyright with permission from ref. [21].

due to lack of highly efficient methods to deliver those therapeutic agents across the BBB. For instance, most of the drugs systematically designed for chemotherapy cannot penetrate the BBB at the concentration required for tumor treatment. It has been suggested that small molecules with molecule weight below 400 Da can directly cross the BBB via active efflux transporters (even if they are highly lipophilic). However, more than 98% of small molecules do not meet these requirements for BBB permeation. Furthermore, large molecules are generally unable to penetrate into the brain.

There are approximately 1.5 billion people worldwide suffering from CNS diseases. Thus, there is growing need to develop a feasible strategy to deliver non-permeable drugs into the brain.[22–24] To overcome the BBB, numerous strategies have been applied to improve the penetration of effective therapeutic agents into the brain. Those strategies can be divided to two categories: invasive and non-invasive approaches. (Figure 5) Some special cases aimed at more effective delivery of drugs to the CNS were reviewed and discussed in the subsequent sections.

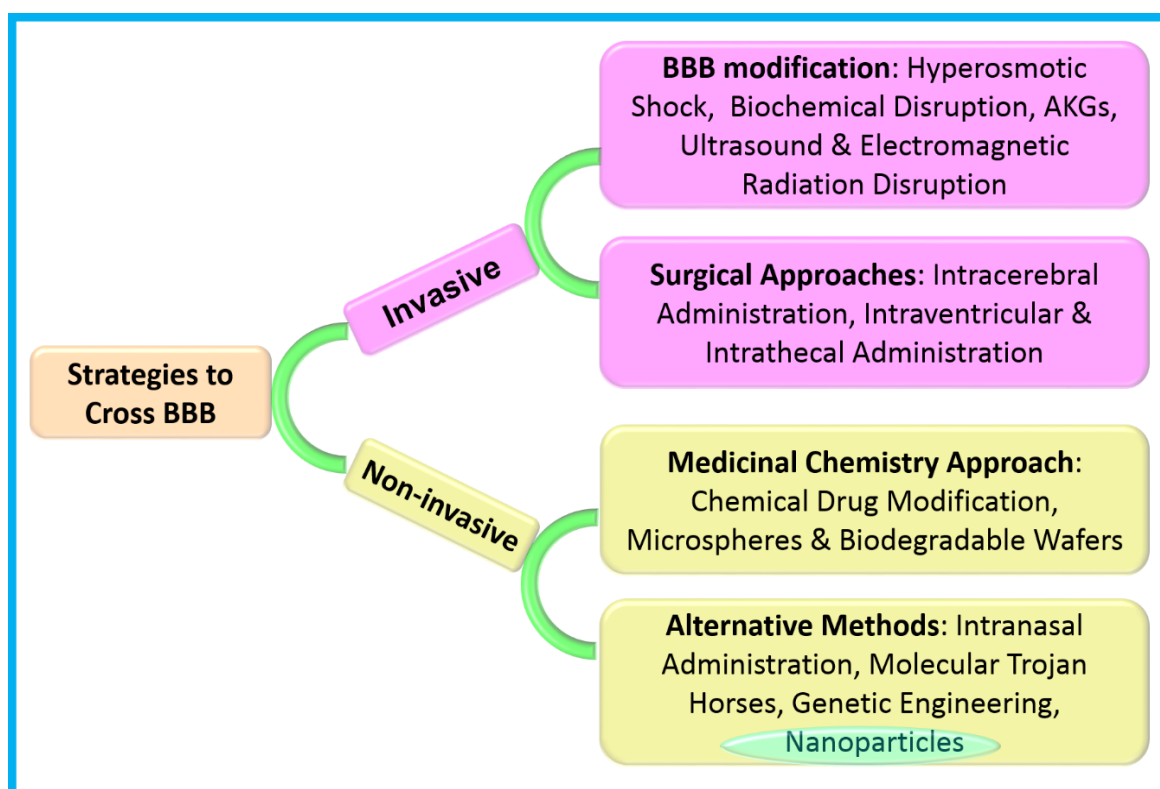


Figure 5. A schematic representation of current strategies to delivery drugs into the brain.

1.2.4.1 Invasive Techniques

BBB modification. The tight junctions of the endothelial cells that form the BBB hinder most drugs from entering the brain. Therefore, strategies have been developed to “open” these tight junctions including: hyperosmoticity,[25] biochemical disruption[17, 26], alkylglycerols (AKG) [17, 27] or ultrasound[28, 29]. These approaches that can transiently open the tight junctions of the BBB have several drawbacks, such as unintended access of potentially toxic agents and decreased control of drug releasing and targeting functions.

Surgical approaches. One of the most direct and simplest ways to deliver drugs into the brain is by local drug infusion. However, this is usually employed only in emergency situations when the therapeutic agents must urgently reach the brain. The diffusion of the drug from the injection site relies upon the site of the drug administration, liposolubility, polarity, tissue affinity and molecular mass of the drug injected. There are various approaches for direct drug injection: including into the cerebrospinal fluid via intraventricular infusion (or intrathecal administration)[30] or to the brain parenchyma by interacerebral implant.(Figure 6)[31, 32]

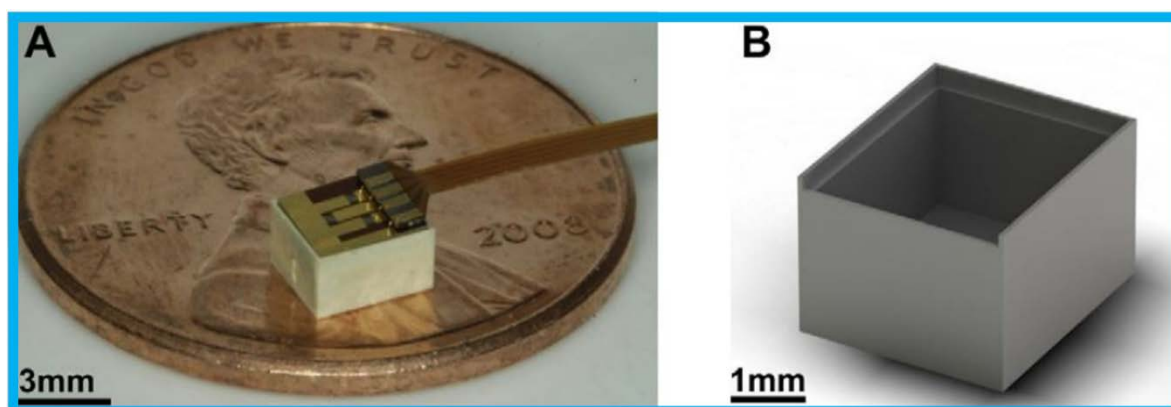


Figure 6. Color photograph of the device (A) and a computer-aided design render of the liquid crystalline polymer LCP reservoir (B). The reservoir size is $3.7 \times 3.2 \times 2.2$ mm. 10 mg of temozolomide is loaded in this device. The 200nm shelf is visible on the interior face of the reservoir walls. This shelf serves as a seat for the chip and as an upper boundary for drug during the loading process. Copyright with permission from ref. [30].

1.2.4.2 Non-invasive Techniques

Medicinal chemistry approach. This includes two directions: chemical drug modification and drug delivery via microspheres and biodegradable wafers. The chemical modification of drugs is a widely used method to change their structure to support their transport via active efflux transporters. [32, 33] It is carried out by increasing the lipophilicity of drugs to enhance their BBB permeability via passive transport. Another method is to mimic a nutrient that is known to cross the BBB, and therefore facilitates transport by one of the specific carriers in the brain. However, modification of a drug may dramatically increase its molecular weight to be over 400 Da. Moreover, improved drug lipophilicity can also increase its uptake by other organs, leading to rapid clearance from the blood before the drug can enter the brain.[34, 35] For drug delivery through microspheres

and wafers, it is carried out by conjugation of water-soluble macromolecular therapeutic agents and tiny spheres or biodegradable wafers before it is inserted into the brain through stereotaxic surgery. However, the drawback of this approach is that some drugs have low diffusion in brain parenchyma, thus need administration close to the target (which can be difficult depending upon the location).

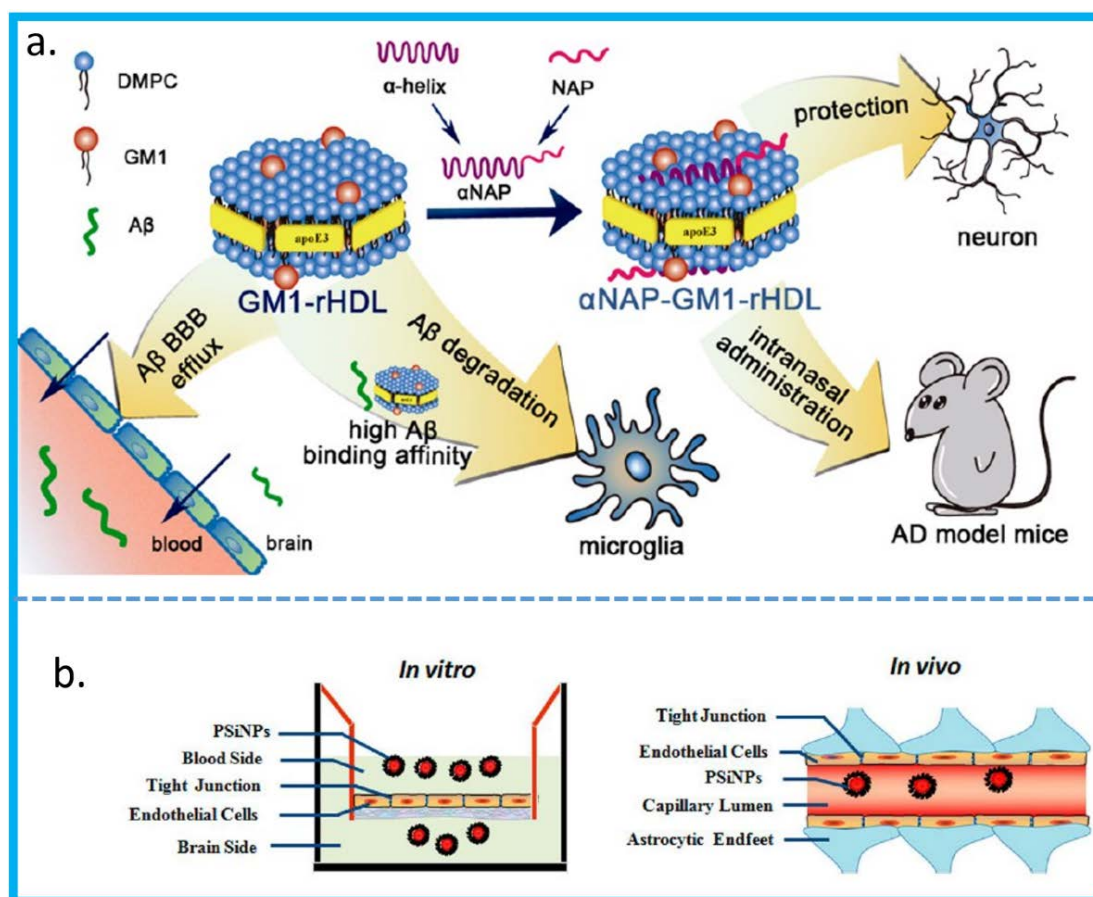


Figure 7 (a). Schematically represents the procedures of fabrication of multi-functional nanostructure (α NAP - GM1 - rHDL) and their BBB penetration. (b) Schematic of PSiNP passing the BBB in vitro (bottom left) and in vivo (bottom right). Copyright permission of ref [40].

Alternative methods. There are several alternative approaches, including intranasal administration, [30, 36] molecular Trojan horses,[35] genetic engineering[37, 38] and nanoparticles. Among these non-invasive methods to transport the drugs to the CNS, nanoparticle-based delivery systems are attracting increasing attention through their capability for versatile modification of the physicochemical properties of their composition. It was reported that a multifunctional nanostructure monosialotetrahexosylganglioside (GM1)-modified reconstituted lipoprotein with high density, loading with a neuroprotective

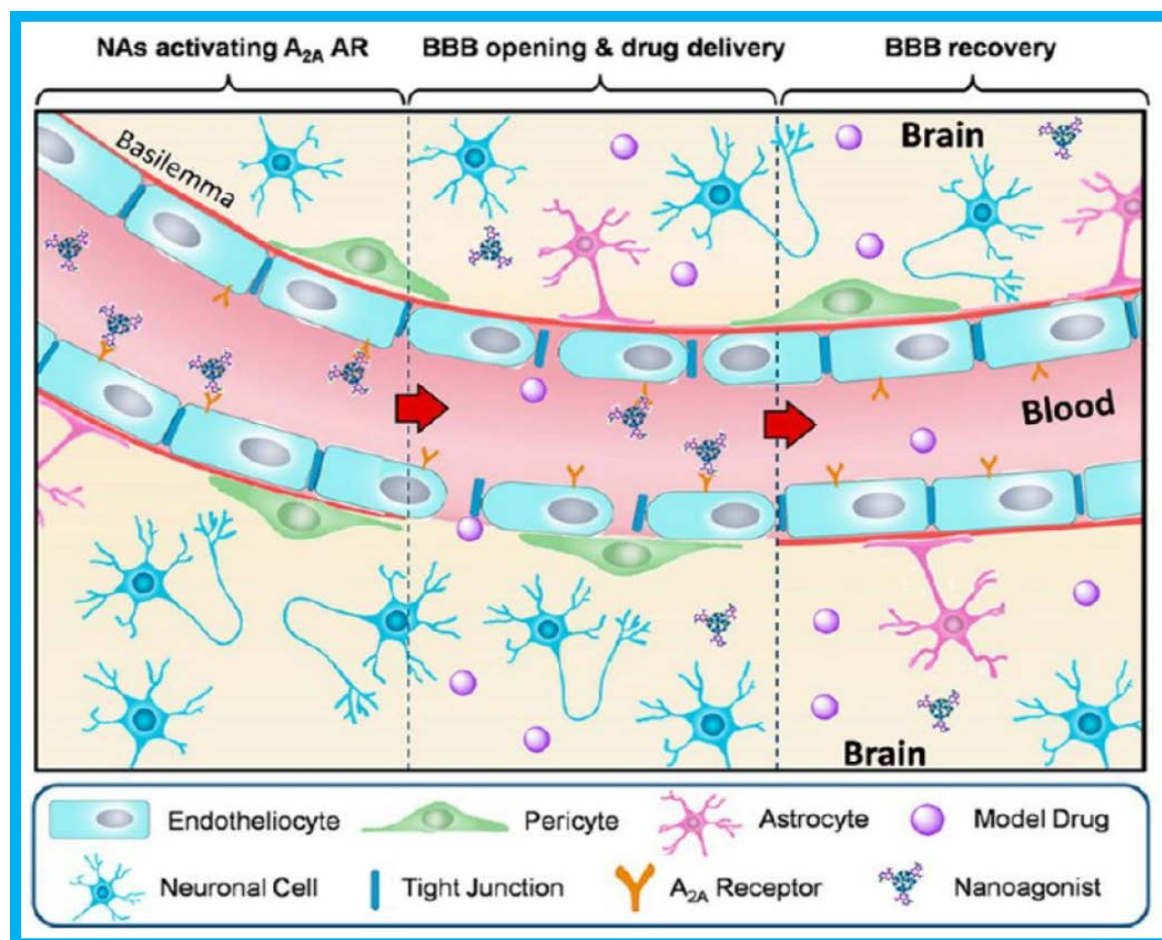


Figure 8 Schematic of brain drug delivery by NA-mediated A_{2A} AR signaling, the permeability of BBB is increased by the signal transduction. Copyright with permission of ref. [41].

peptide (NAP, a neuroprotective peptide for the therapy of AD) possesses better ability to protect neurons via intranasal administration than GM1 *in vitro*. (Figure 7a)[39] Moreover, the size of PEGylated silica nanoparticles (PSiNPs) for BBB penetration *in vitro* and *in vivo* was also further investigated, the result showed that the PSiNPs were capable to pass the BBB, and the smaller size of PSiNPs exhibited better penetration efficiency. (Figure 7b)[40] Importantly, a series of nano-agonists (NAs) were designed by labelling various copies of A_{2A} AR activating ligands on dendrimers, intending to temporarily increase the BBB permeation. The results demonstrated that NAs- A_{2A} AR complex dramatically up-regulated the brain uptake of a macromolecular model drug (45kDa) after intravenous injection of NAs. (Figure 8)[41] Moreover, carmustine (BCNU)-loaded solid lipid nanoparticles (SLNs) were grafted with 83-14 monoclonal antibody (MAb) (83-14 MAb/BCNU-SLNs) and applied to the brain-targeting delivery system.[42] Ruan et al. developed a shrinkable nano-system, G-AuNPs-DOX-PEG. The drug of DOX can be released via a PH- and time-

dependent manner. At Ph 5.0, the release of DOX was more rapid than at a high Ph value, with the release rate of DOX from G-AuNPs-DOX-PEG about 90.9%. [43] Although many studies on efficient targeting and delivery of nanoparticles have been reported, the effect of nanoparticle physicochemical properties (such as surface chemistry, size and shape, etc.) on brain permeation and targeting is still poorly understood.

1.3 Biophysical parameters of nanoparticles influence their cellular uptake

In recent years, numerous nanoparticle-based therapeutics have been evaluated for potential use in neurodegenerative disease therapy. [44–47] Notably, physicochemical characteristics (such as surface chemistry, size and shape etc.) of nanoparticles cause a significant impact on the cellular uptake, biological distribution, permeation across biological barriers such as the BBB, and the resulting treatment effect. [48–50] In this section, the current understanding of the different effects of surface chemistry, nanoparticle size and shape on their cellular uptake, bio-distribution, and clearance by macrophages will be summarised. A deep understanding of the role of physicochemical properties of nanoparticles on treatment efficacy may help to design an optimal nanoparticle-base therapeutic delivery system for the treatment of brain disorders.

1.3.1 Effect of nanoparticle surface chemistry upon cellular uptake

A wide variety of chemical and biological functionalization options are available to modify the surface of nanoparticles, with the goal of altering their bioavailability and cellular uptake properties. This includes surface modifications such as hydrophobicity and surface charge (including negative, positive and neutral) which have all been shown to influence the circulation, bio-distribution, phagocytosis and optimization of nanoparticles. [50, 51] Furthermore, surface chemistry also affects the stability of nanoparticles and their interactions with cell membranes. [52] Understanding the relationship between these nanoparticle surface characteristics and cellular uptake is important in guiding the design of drug delivery systems for therapeutic application. A summary of the physicochemical properties of nanoparticles that are commonly modified and the resultant impact upon cellular uptake is shown in Table 1 and described in further detail in the following sections.

Physicochemical characteristics	Influence	Surface agents	Particles	Refs.
Size	Effect the cellular uptake efficiency and subcellular distribution of nanoparticles	N/A	Gold NPs, polymeric nanoparticles	[53], [83], [84]
Negative surface charge	Increase cellular uptake for gene delivery	Oligonucleotide, lipoplexes	Gold NPs, quantum dots, iron oxide, Gadolinium nanoparticles	[54], [56]
Positive surface charge	Positive charge induces the interaction between particles and membranes	positive amine-polyamidoamine (PAMAM) dendrimers	fluorescein-doped magnetic mesoporous silica nanoparticles (FMNPs)	[54], [55], [60]
Natural surface charge	Higher steric stability and hinders the interaction with cell and phagocytic system	PEG chain, polymer, silica	Silica, polymers, quantum dots or upconversion NPs	[56], [57], [64]
Shape	Rod shaped particles with higher aspect ratio (AR) exhibit more efficient cellular uptake	fluorescein isothiocyanate (FITC) and rhodamine B isothiocyanate (RITC)	Mesoporous silica nanoparticles, radioactive ^{198}Au – doped nanostructures	[58],[59],[98], [99],

Table 1. The summary of physicochemical properties of nanoparticles and their cellular uptake is shown in the Table 1.

1.3.1.1 Negative surface charge

Introduction of a negative surface charge to nanoparticles plays an important role in particle-cell interactions and therefore effects their cellular uptake, although this appears to often be in a non-specific manner that may not be suitable for all therapeutic applications. A challenge with this approach is that the cell membrane is negatively charged, and therefore negatively-charged nanoparticles can't immediately interact with the cell membrane. For instance, it has been reported that carboxymethyl-substituted dextran-coated nanoparticles within size-range from 33-45nm (-50 to 5 mV net surface charge) display increased internalization in CaCo-2 human colon cancer cells in a charge-dependent manner via non-specific uptake.[60] Oligonucleotide-functionalized gold nanoparticles with negative surface charge exhibit greater than 99% cellular uptake (far superior to that of conventional transfection agents such as lipophilic drugs) without toxicity to cells. It is proposed that the oligonucleotide shell introduces a negative charge that binds extracellular proteins and can

therefore facilitate the interaction of nanoparticles directly with the cell membrane. (Figure 9a)[61] Similarly, it is also suggested that the uptake of oligonucleotide-loaded gold nanoparticles (ASNP) is influenced by the density of the oligonucleotide loading on the surface of ASNP. The higher densities of ASNP can absorb a large amount of proteins on the surface, resulting in greater cellular uptake. (Figure 9b)[62] Furthermore, it has been reported that lipid nanoparticles with surface-coating of polyanionic-like aromatic sulfonic acid (negative charged) showed a specific affinity for caveolae of endothelial cells, consequently leading to effective uptake. (Figure 10)[63]

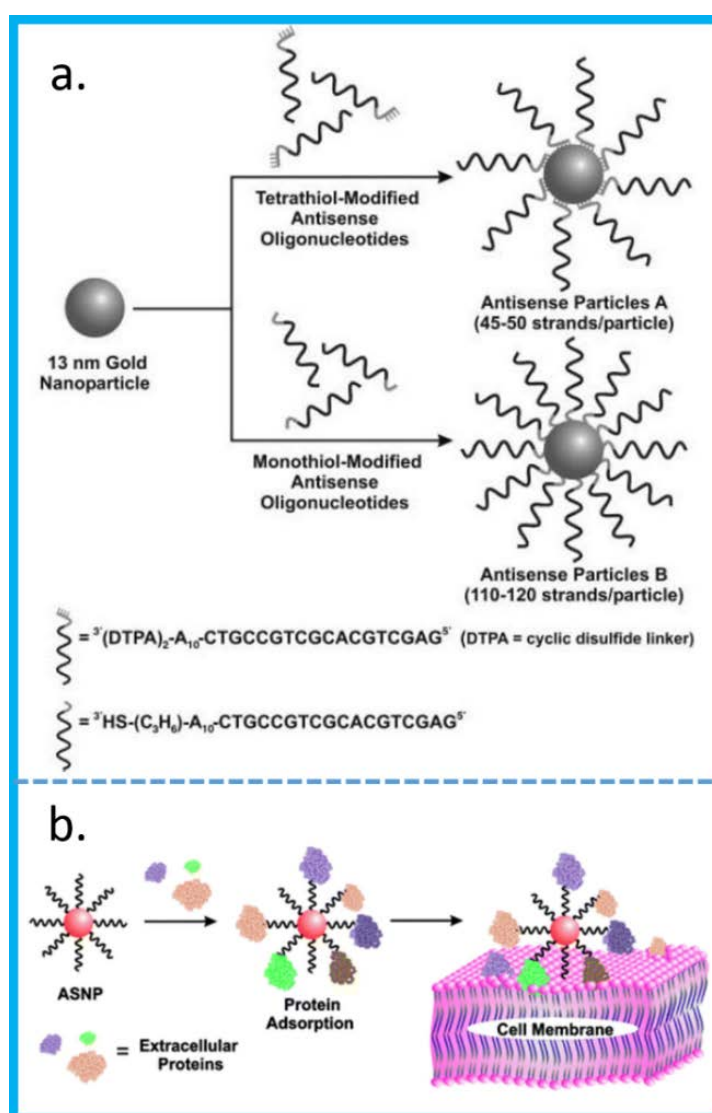


Figure 9 (a). Preparation of antisense gold nanoparticle A and B (13nm). (b). Illustration of the interaction of cell membrane and oligonucleotide-loaded gold nanoparticles (ASNP) with various protein adsorption. Copyright with permission of ref. [61] and ref. [62].

Recently, a wide variety of proteins and peptides, cell penetration peptides or cell-fusogenic peptides have been developed to transport therapeutic agents into their target sites with fewer side effects and have great potential to cure diseases. They are ideal for cellular uptake[64] and they are drug-delivery platforms due to their biocompatibility and biodegradability coupled with low toxicity. A variety of proteins have been used and characterized for drug-delivery systems, including the ferritin/apoferritin protein cage, plant-derived viral capsids, the small Heat shock protein (sHsp) cage, albumin, soy and whey protein, collagen, and gelatin. There are many different types and shapes that have been prepared to deliver drug molecules using protein-based platforms, including various protein cages, microspheres, nanoparticles, hydrogels, films, minirods, and minipellets. The protein cage is the most newly developed biomaterial for drug delivery and therapeutic applications. The uniform size, multifunctionality, and biodegradability push it to the frontier of drug delivery.

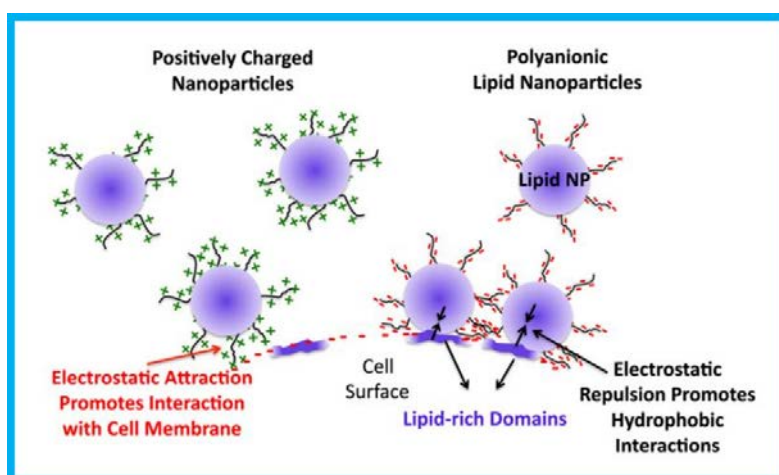


Figure 10. Illustration of the interaction of a positively charged nanoparticles (left) and lipophilic lipid nanoparticles (right) with cell membranes. Copyright with permission of ref. [63].

1.3.1.2 Positive surface charge

The positively charged surface of nanoparticles induces electrostatic interactions with the negatively charged cell membrane.[62, 63] Therefore, nanoparticles with positively charged groups on their surface exhibit higher cellular uptake than negatively charged ones, primarily through endocytosis routes. For instance, the permeability of chitosan-cyclosporine-A (chitosan-Cy-A, $+31.2 \pm 1.6$ mV) coated nanoparticles to the gastrointestinal mucous barrier is higher than negatively (sodium glycocholate) and neutral (Gelatin-A) charged

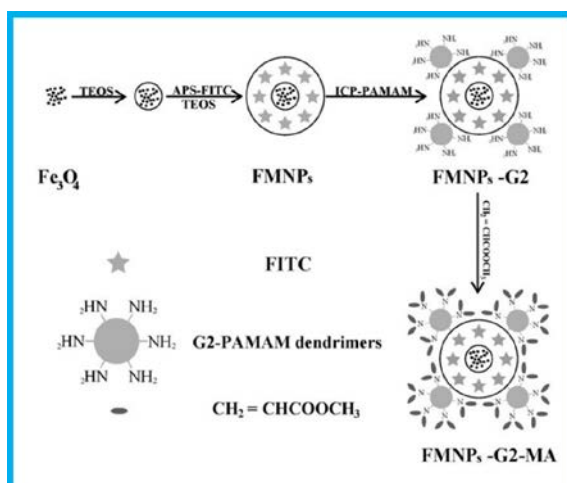


Figure 11. Illustration of the preparation of surface functionalized magnetic silica nanoparticles. Copyright with permission of ref. [66].

nanoparticles because of the presence of the negatively charged protein in the outer surface of gastrointestinal epithelial cells.[65] Furthermore, introduction of positively charged amine-polyamidoamine (PAMAM) dendrimers onto the surface of fluorescein-doped magnetic mesoporous silica nanoparticles (FMNPs) improves their cellular uptake by glioma cells (Figure 11)[66] versus FMNPs that are coated with neutral-charged ester-terminated PAMAM.

1.3.1.3 Neutral surface charge

The modification of nanoparticles with nonionic polymers can improve nanoparticle stability through steric stabilization that reduces phagocytic and immunological clearance pathways.[67] Polyethylene glycol (PEG) is one of the most commonly utilized neutral polymers to modify nanoparticles and prevent them from activating the immune system.(Figure 12)[68] Numerous types of nanoparticles have been coated with PEG and its analogue (such as poloxamer and poloxamine series) to increase the blood circulation and enhance the accumulation of nanoparticles in tumor by exerting the enhanced permeability and retention (EPR) effect, such as single-walled carbon nanotube,[68, 69] gold nanorod,[70] fluorescent silica,[71] quantum dots,[72] poly(hexadecylcyanoacrylate), liposomes.[72, 73] For instance, the cellular uptake capability of polyethylenimine (PEI)-modified gold nanorods by Hela cells have been increased by avoiding the formation of aggregation of nanoparticles.

1.3.2 Nanoparticle size

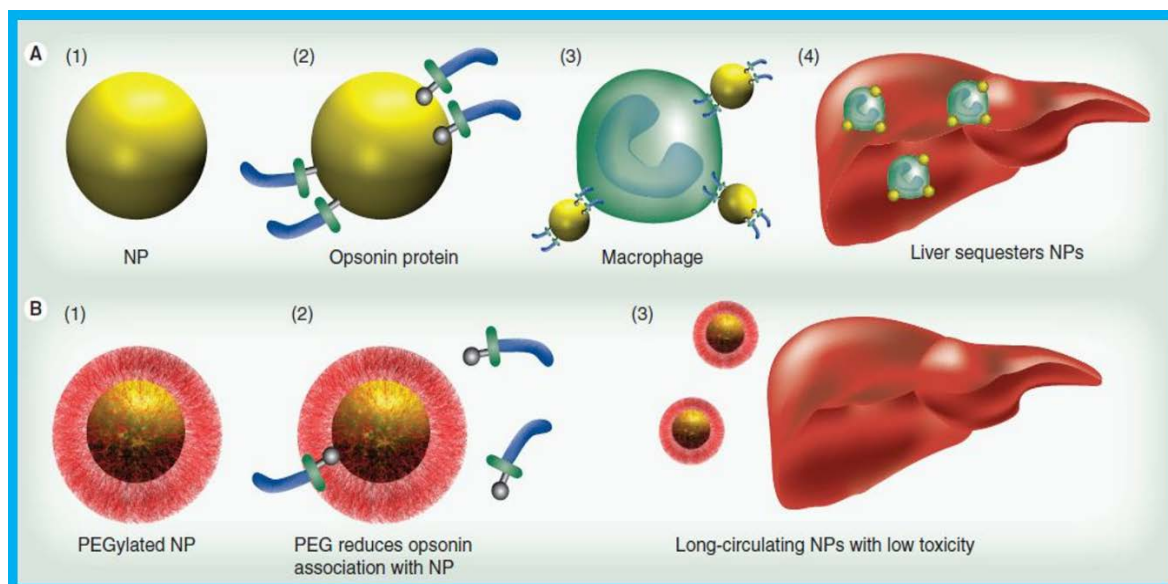


Figure 12. PEG prohibits uptake by the reticuloendothelial system. (A) Nanoparticles, (A1) nanoparticles coated with opsonin protein, (A2) macrophage of opsonin protein-coated nanoparticles, (A4) liver sequesters nanoparticles; (B1) PEGylated nanoparticles, (B2) PEGylated nanoparticles reduces opsonin association with nanoparticles, (B3) PEGylation decreases the liver accumulation of nanoparticles. Copyright with permission from ref. [68].

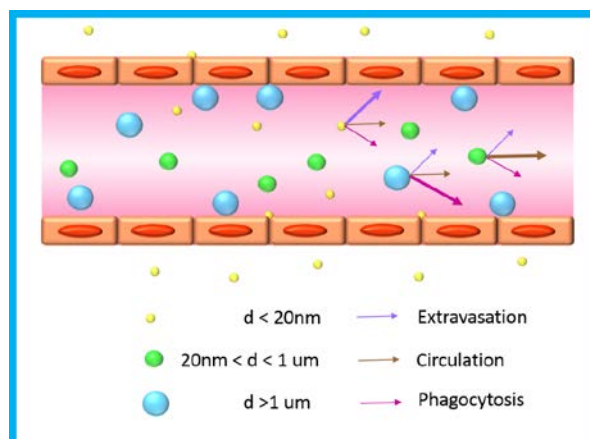


Figure 13. Illustration of the size-dependent mechanism and rate of clearance. The smallest nanoparticles within 20 nm are readily penetration the tight junctions, leading to a quick clearance from the blood circulation. The largest nanoparticles above 1 μm are likely to dominate and wall collisions, inducing fast uptake by the mononuclear phagocytic system. The nanoparticles with size between 20 nm and 1 μm process longer circulation time. Modified with permission of ref. [48].

The size of nanoparticles significantly affects their cellular uptake, bio-distribution and clearance through phagocytic pathways. (Figure 13)[48] There are numerous studies on the effect of nanoparticle size upon the circulation and bio-distribution of a range of different types of nanoparticles, such as silica,[74] silver,[75] quantum dots[76] and titanium

dioxide[77] nanoparticles. Small nanoparticles with 10 - 20 nm exhibit wide diffusion in various organs and are readily excreted by the kidney.[78] Conversely, large nanoparticles (above 1 μm) do not readily distribute to most organs, easily aggregate in the biological environment and can become stuck within smaller capillaries. Finally, most of the large nanoparticles accumulate in the liver, spleen and few spread into the bone marrow.[79] However, when the nanoparticles with a size of 20 nm to 1 μm remain to a greater extent in blood circulation compare to other sized nanoparticles.[64, 76]

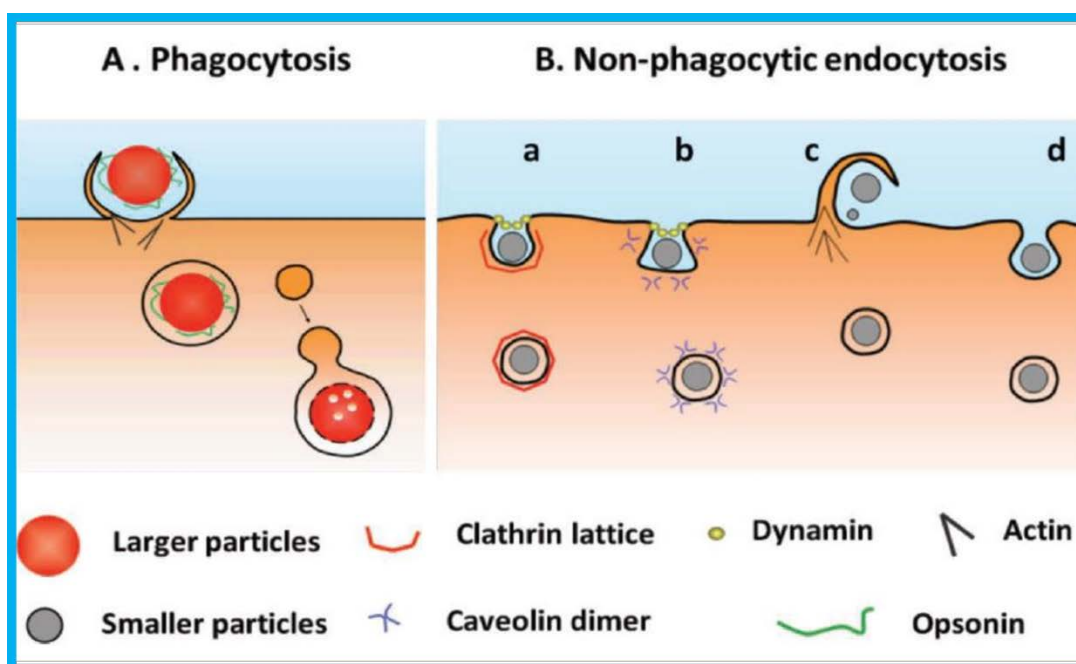


Figure 14. Illustration of the size-dependent pathways for nanoparticles. Large nanoparticles are internalized via phagocytosis (A). Smaller nanoparticles are uptake through non-phagocytic endocytosis, such as clathrin-mediated endocytosis (a), caveolar-mediated endocytosis (b), micropinocytosis (c), and clathrin-independent and caveolin-independent endocytosis. Copyright with permission of ref. [48].

Furthermore, the cellular uptake efficiency and subcellular distribution of nanoparticles is strongly influenced by the size of nanoparticles. (Figure 14) [80–82] For instance, Chithrani's group investigated the size effect of gold nanoparticles (with various sizes, such as 14 nm, 50 nm, and 74 nm) upon cellular uptake by Hela cells.[83, 84] The results showed that the cellular uptake of gold nanoparticles varied with the different sized gold nanoparticles that were tested, with 50 nm nanoparticles exhibiting the maximum cellular uptake efficiency compared to other two sized gold nanoparticles. (14nm and 74 nm). Moreover, the kinetics of cellular uptake of gold nanoparticles was also size dependent, with

uptake half-life of 14, 50 and 74 nm-sized gold nanoparticles being 2.10, 1.90 and 2.24 h, respectively. Further, a wide range of dye-functionalized mesoporous silica nanoparticles (FITC-MSNs) with size ranging from 30 to 280nm have been tested for their size-dependent cellular uptake in HeLa cells. Cellular uptake was found to be strongly influenced by nanoparticle size, with cellular uptake efficiency in the order $50 > 30 > 110 > 280 > 170$ nm. Furthermore, the concentration of 50 nm-sized FITC-MSN that were internalized was almost 2.5 folds greater than that of 30 nm-sized particles.(Figure 15)[74]

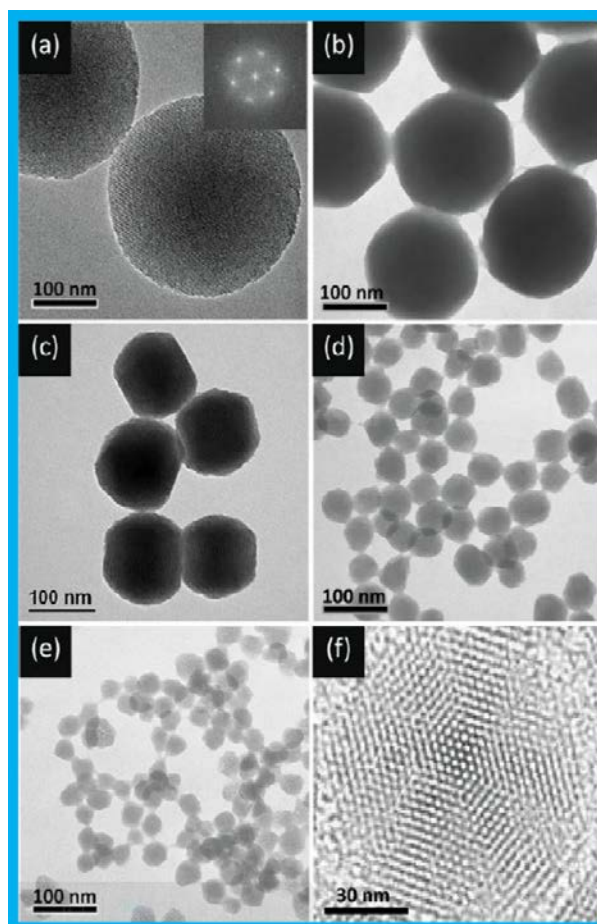


Figure 15. Transmission electron microscope (TEM) images of mesoporous silica particles with a range of average sizes: a) 280nm; inset: FFT analysis of the TEM image; b) 170, c) 110, d) 50, e) 30 nm. f) High-resolution TEM image of a single particle. Copyright with permission of ref.[74].

Finally, it has been suggested that nanoparticle size has a significant impact on the binding and activation of receptors on the cell membrane, and subsequently influences uptake by cells via non-phagocytic endocytosis.[84] For example, a series of fluorescent latex beads with various size (50 - 1000nm) were utilized to investigate the size effect on the cellular uptake pathways in B16 cells. Microspheres with a diameter below 200 nm were found to

enter the cells through clathrin-mediated endocytosis. With increasing size, the uptake mechanism changed to caveolae-mediated internalization, which became the predominant pathway of uptake for 500 nm-sized particles.

In summary, nanoparticle size is one of the most significant physicochemical properties to consider for designing an efficient nanoparticles-based drug delivery system for cell delivery applications.

1.3.3 Nanoparticle shape

Shape is an important physicochemical property of nanoparticles that influences their use as a drug delivery system for biological and medical applications.[58, 84] A wide variety of nanoparticle shapes have been reported, including rod, disk cubic, cylinder and other uncommon shapes such as red cell-like bi-concave discs, filamentous and filovirus-mimicking particles. These different-shaped particles were employed to investigate the steric morphology effect on the cellular endocytosis,[85] circulation half-life,[86] targeting functions[87] and intracellular transport[87, 88].

In the case of circulation half-life in the blood, nanoparticle shape greatly influences their interaction with and clearance by macrophages [89] Specifically, studies suggest that it is the geometry of the nanoparticles at the touch point with macrophages rather than the entire nanoparticle shape that determines whether the nanoparticle is internalized by these phagocytic cells. (Figure 16)[48, 90]Accordingly, Ω is defined as the angle between the

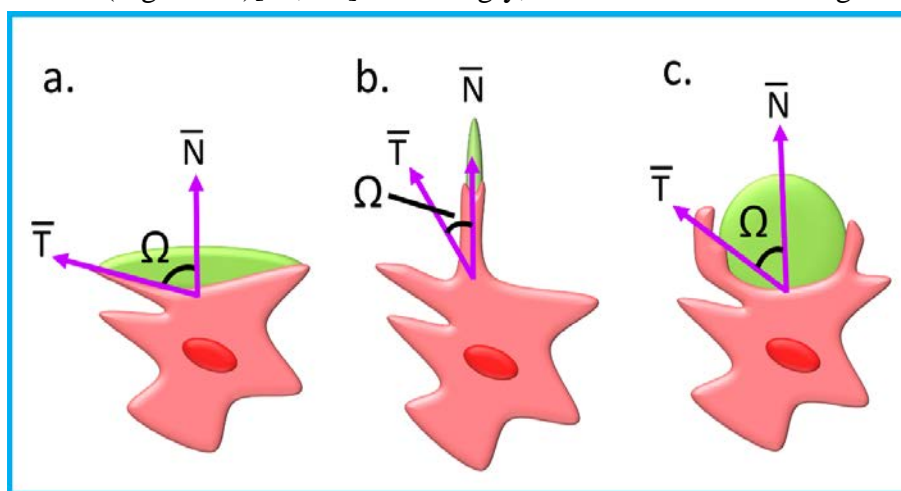


Figure 16. Illustration the relationship of Ω and cell membrane velocity. a). $\Omega > 45^\circ$; b) $\Omega < 45^\circ$ and c) $\Omega = 45^\circ$; when $\Omega > 45^\circ$, there is no internalization, while $\Omega \leq 45^\circ$ means cell can uptake the nanoparticles. Modification with permission of ref. [48].

membrane at the touching point with the cell. When $\Omega \leq 45^\circ$, particles can be uptake by macrophages successfully. However, when $\Omega > 45^\circ$, nanoparticles can temporarily adhere onto the surface of macrophages but fail to be internalised. Therefore, generating nanoparticles with a shape that results in $\Omega > 45^\circ$ can be utilized to “hide” and protect nanoparticles from macrophage phagocytosis. For example, filomicelles (polymer micelles assemblies that resemble thin rod shapes) that have an angle > 45 exhibited long circulation times within the blood of up to a week after intravenous injection, which was about 10 fold-longer than similar sized spherical assemblies.[86] Furthermore, it suggested that increasing aspect ratio even over 20 inhibits internalization by macrophages due to low curvature of

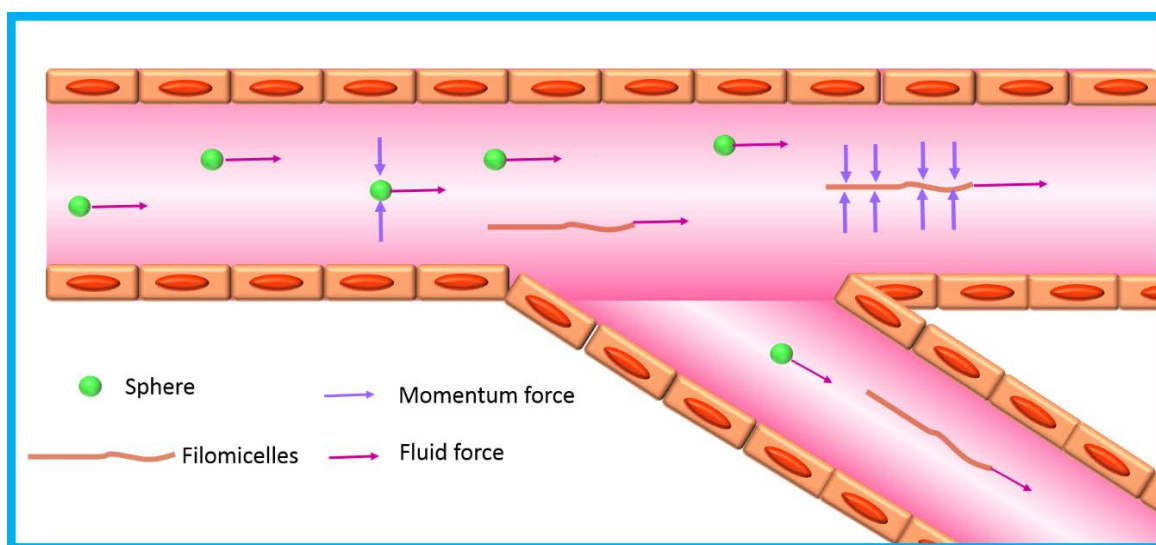


Figure 17. Illustration of the shape effects on circulation. Modification with permission of ref.[48].

long worm-like particles. Moreover, the non-specific particles exhibit a deviating hydrodynamic action compared with spherical nanoparticles, resulting in prolonging circulation time through aligning with blood flow. (Figure 17)[47, 91]

Cellular uptake of nanoparticles is also strongly affected by the shape of a wide variety of nanoparticles (such as gold nanoparticles, silica nanoparticles and polymers). For example, rod-shaped nanoparticles exhibit higher adhering ability and lower non-specific accumulation under flow with the targeted cells than their spherical counterparts, presumably because the curvature of spheres limits their binding efficiency with the target cell. (Figure 18)[92] Similarly, prolate ellipsoid stretched from ellipsoid spheres provide higher cell attachment to the macrophages than an oblate and spherical ellipsoid. However, the internalisation of particles followed another ranking: oblate ellipsoids » spheres > prolate ellipsoids.[89] However, the rod-liked nanoparticles with a higher surface area also induce

multivalent interactions between cell membrane and nanorods. Therefore, the mammalian epithelial and immune cells preferentially uptake disc-shaped hydrophilic nanoparticles compared with the nanorods.[93] Apart from that, mesoporous silica particles with a larger aspect ratio ($AR = 4$) were internalised by A375 human melanoma cells to a great extent and even faster than the particles with lower AR ($AR = 1, 2$). (Figure 19)[94] The process of MSN endocytosis is as following (Figure 22G-I): different shaped MSNs are firstly entered into the A375 cells through nonspecific endocytosis pathways and then merge with

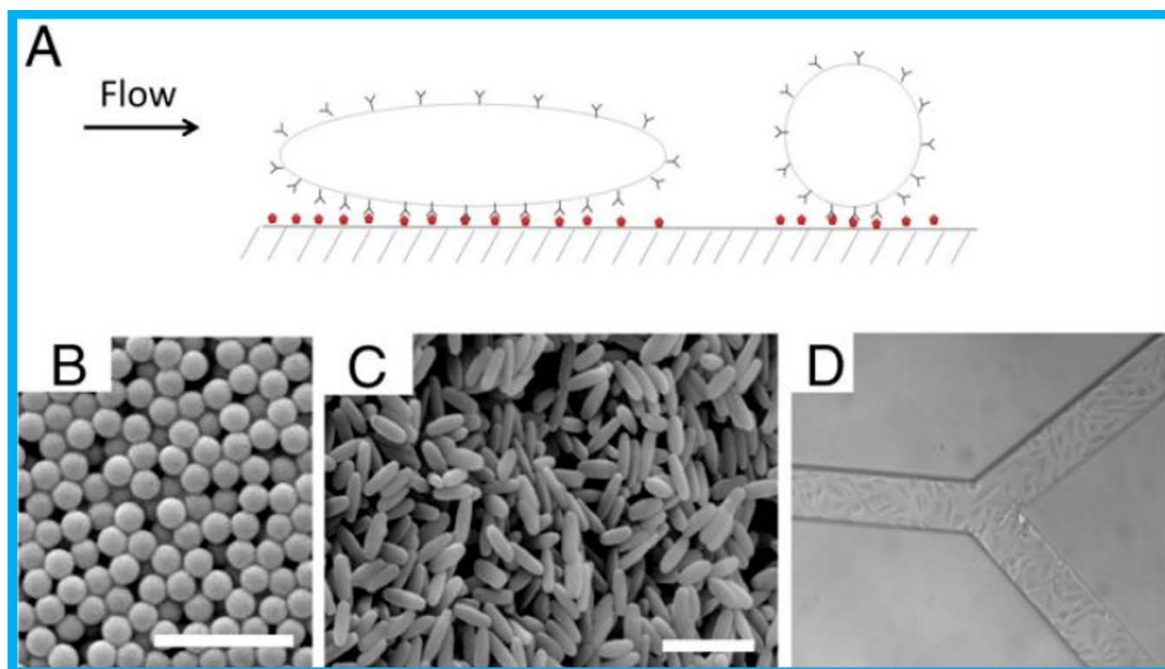


Figure 18. Illustration of the behavior of nanoparticles under flow. (A) Schematic of nanoparticles binding a wall in the blood flow. (B) Scanning electron microscope (SEM) images of polystyrene spheres and (C) worm-shaped particles stretched from 200 nm-sized spheres. Scale bar is 1 μm . (D) Rat brain endothelial cells (RBE4) were plated in the synthetic microvascular networks (SMNs) Copyright with permission of ref. [92].

endosomes. Next, the MSN particles escape from the endosomes and get into the cytoplasm. It indicated that the cell uptake entries depend on the shape of particles. Collectively, the shape-mediated enhancement of endothelial targeting receptors provides a promising application in vascular targeting for medical therapy.

Besides, the cellular uptake of the rod-5 with high-aspect-ratio nanoparticles ($150 \text{ nm} \times 450 \text{ nm}$) provides more rapidly and efficiently than other symmetric low-aspect-ratio particles with similar size by human cervical carcinoma epithelial (Hela) cells. However, $1 \mu\text{m}$ cubic particles showed difficult to enter Hela cells.[95] Moreover, ^{198}Au -incorporated nanospheres provide longest circulation time with negligible clearance by the

reticuloendothelial system and highest tumor uptake compared to nanodisks, nanorods and nanocages. However, nanorods and nanocages could enter the core of tumors, nanospheres and nanodisks only found staying on the surface of the tumors. It indicated that

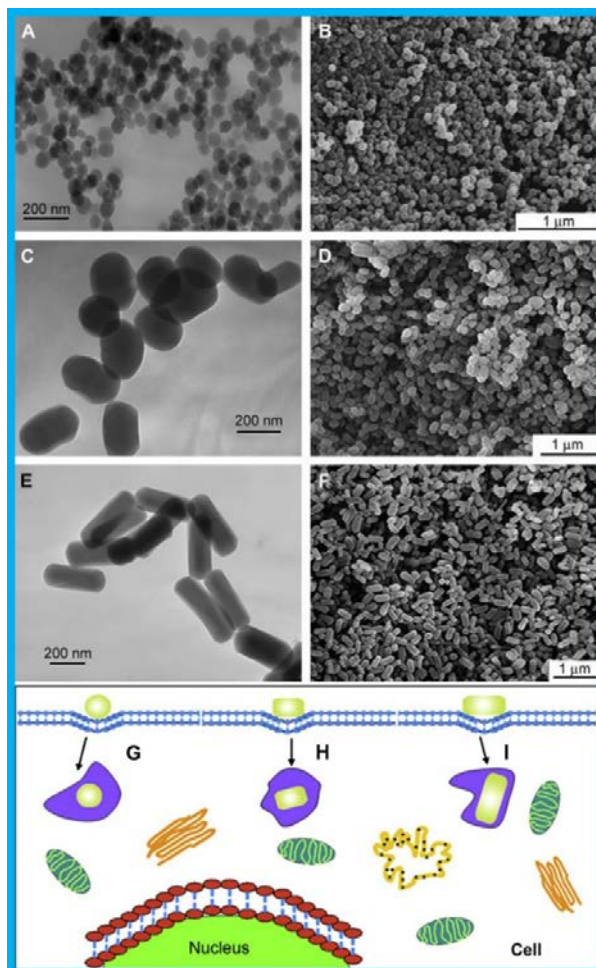


Figure 19. Transmission electron microscopy and scanning electron microscopy images of three different lengths MSNs and the illustration of their endocytosis pathways. (A, C, E) TEM images of sphere-shaped particles (A), short rod-shaped particles (C) and long rod-shaped particles (E). (B, D, F) SEM images of sphere-shaped particles (B), short rod-shaped particles (D) and long rod-shaped particles (F). Illustration of endocytosis pathways for cellular uptake of spherical nanoparticles (G), short nanorods (E) and long nanorods (I). Copyright with permission of ref. [94].

there is an optimal geometry of nano-drug delivery system for efficient treatment of tumors or another disease.[96]

1.4 Lanthanide-doped upconversion nanoparticles (UCNPs)

The lanthanide series of chemical elements consists of fifteen metallic chemical elements with atomic numbers range from 57 (lanthanum) to 71 (lutetium) located at the III^B group

and sixth period in the periodic table (Table 2). These fifteen lanthanide elements and the chemically similar elements (scandium and yttrium both located at the IIIB group labelled

Periodic Table

1	2	3	4	5	6	7	8	9	10	11	12	13	14	15	16	17	18	19	20	21	22	23	24	25	26	27	28	29	30	31	32	33	34	35	36	37	38	39	40	41	42	43	44	45	46	47	48	49	50	51	52	53	54	55	56	57	58	59	60	61	62	63	64	65	66	67	68	69	70	71	72	73	74	75	76	77	78	79	80	81	82	83	84	85	86	87	88	89	90	91	92	93	94	95	96	97	98	99	100	101	102	103	104	105	106	107	108	109	110	111	112	113	114	115	116	117	118	119	120	121	122	123	124	125	126	127	128	129	130	131	132	133	134	135	136	137	138	139	140	141	142	143	144	145	146	147	148	149	150	151	152	153	154	155	156	157	158	159	160	161	162	163	164	165	166	167	168	169	170	171	172	173	174	175	176	177	178	179	180	181	182	183	184	185	186	187	188	189	190	191	192	193	194	195	196	197	198	199	200	201	202	203	204	205	206	207	208	209	210	211	212	213	214	215	216	217	218	219	220	221	222	223	224	225	226	227	228	229	230	231	232	233	234	235	236	237	238	239	240	241	242	243	244	245	246	247	248	249	250	251	252	253	254	255	256	257	258	259	260	261	262	263	264	265	266	267	268	269	270	271	272	273	274	275	276	277	278	279	280	281	282	283	284	285	286	287	288	289	290	291	292	293	294	295	296	297	298	299	300	301	302	303	304	305	306	307	308	309	310	311	312	313	314	315	316	317	318	319	320	321	322	323	324	325	326	327	328	329	330	331	332	333	334	335	336	337	338	339	340	341	342	343	344	345	346	347	348	349	350	351	352	353	354	355	356	357	358	359	360	361	362	363	364	365	366	367	368	369	370	371	372	373	374	375	376	377	378	379	380	381	382	383	384	385	386	387	388	389	390	391	392	393	394	395	396	397	398	399	400	401	402	403	404	405	406	407	408	409	410	411	412	413	414	415	416	417	418	419	420	421	422	423	424	425	426	427	428	429	430	431	432	433	434	435	436	437	438	439	440	441	442	443	444	445	446	447	448	449	450	451	452	453	454	455	456	457	458	459	460	461	462	463	464	465	466	467	468	469	470	471	472	473	474	475	476	477	478	479	480	481	482	483	484	485	486	487	488	489	490	491	492	493	494	495	496	497	498	499	500	501	502	503	504	505	506	507	508	509	510	511	512	513	514	515	516	517	518	519	520	521	522	523	524	525	526	527	528	529	530	531	532	533	534	535	536	537	538	539	540	541	542	543	544	545	546	547	548	549	550	551	552	553	554	555	556	557	558	559	560	561	562	563	564	565	566	567	568	569	570	571	572	573	574	575	576	577	578	579	580	581	582	583	584	585	586	587	588	589	590	591	592	593	594	595	596	597	598	599	600	601	602	603	604	605	606	607	608	609	610	611	612	613	614	615	616	617	618	619	620	621	622	623	624	625	626	627	628	629	630	631	632	633	634	635	636	637	638	639	640	641	642	643	644	645	646	647	648	649	650	651	652	653	654	655	656	657	658	659	660	661	662	663	664	665	666	667	668	669	670	671	672	673	674	675	676	677	678	679	680	681	682	683	684	685	686	687	688	689	690	691	692	693	694	695	696	697	698	699	700	701	702	703	704	705	706	707	708	709	710	711	712	713	714	715	716	717	718	719	720	721	722	723	724	725	726	727	728	729	730	731	732	733	734	735	736	737	738	739	740	741	742	743	744	745	746	747	748	749	750	751	752	753	754	755	756	757	758	759	760	761	762	763	764	765	766	767	768	769	770	771	772	773	774	775	776	777	778	779	780	781	782	783	784	785	786	787	788	789	790	791	792	793	794	795	796	797	798	799	800	801	802	803	804	805	806	807	808	809	810	811	812	813	814	815	816	817	818	819	820	821	822	823	824	825	826	827	828	829	830	831	832	833	834	835	836	837	838	839	840	841	842	843	844	845	846	847	848	849	850	851	852	853	854	855	856	857	858	859	860	861	862	863	864	865	866	867	868	869	870	871	872	873	874	875	876	877	878	879	880	881	882	883	884	885	886	887	888	889	890	891	892	893	894	895	896	897	898	899	900	901	902	903	904	905	906	907	908	909	910	911	912	913	914	915	916	917	918	919	920	921	922	923	924	925	926	927	928	929	930	931	932	933	934	935	936	937	938	939	940	941	942	943	944	945	946	947	948	949	950	951	952	953	954	955	956	957	958	959	960	961	962	963	964	965	966	967	968	969	970	971	972	973	974	975	976	977	978	979	980	981	982	983	984	985	986	987	988	989	990	991	992	993	994	995	996	997	998	999	1000	1001	1002	1003	1004	1005	1006	1007	1008	1009	1010	1011	1012	1013	1014	1015	1016	1017	1018	1019	1020	1021	1022	1023	1024	1025	1026	1027	1028	1029	1030	1031	1032	1033	1034	1035	1036	1037	1038	1039	1040	1041	1042	1043	1044	1045	1046	1047	1048	1049	1050	1051	1052	1053	1054	1055	1056	1057	1058	1059	1060	1061	1062	1063	1064	1065	1066	1067	1068	1069	1070	1071	1072	1073	1074	1075	1076	1077	1078	1079	1080	1081	1082	1083	1084	1085	1086	1087	1088	1089	1090	1091	1092	1093	1094	1095	1096	1097	1098	1099	1100	1101	1102	1103	1104	1105	1106	1107	1108	1109	1110	1111	1112	1113	1114	1115	1116	1117	1118	1119	1120	1121	1122	1123	1124	1125	1126	1127	1128	1129	1130	1131	1132	1133	1134	1135	1136	1137	1138	1139	1140	1141	1142	1143	1144	1145	1146	1147	1148	1149	1150	1151	1152	1153	1154	1155	1156	1157	1158	1159	1160	1161	1162	1163	1164	1165	1166	1167	1168	1169	1170	1171	1172	1173	1174	1175	1176	1177	1178	1179	1180	1181	1182	1183	1184	1185	1186	1187	1188	1189	1190	1191	1192	1193	1194	1195	1196	1197	1198	1199	1200	1201	1202	1203	1204	1205	1206	1207	1208	1209	1210	1211	1212	1213	1214	1215	1216	1217	1218	1219	1220	1221	1222	1223	1224	1225	1226	1227	1228	1229	1230	1231	1232	1233	1234	1235	1236	1237	1238	1239	1240	1241	1242	1243	1244	1245	1246	1247	1248	1249	1250	1251	1252	1253	1254	1255	1256	1257	1258	1259	1260	1261	1262	1263	1264	1265	1266	1267	1268	1269	1270	1271	1272	1273	1274	1275	1276	1277	1278	1279	1280	1281	1282	1283	1284	1285	1286	1287	1288	1289	1290	1291	1292	1293	1294	1295	1296	1297	1298	1299	1300	1301	1302	1303	1304	1305	1306	1307	1308	1309	1310	1311	1312	1313	1314	1315	1316	1317	1318	1319	1320	1321	1322	1323	1324	1325	1326	1327	1328	1329	1330	1331	1332	1333	1334	1335	1336	1337	1338	1339	1340	1341	1342	1343	1344	1345	1346	1347	1348	1349	1350	1351	1352	1353	1354	1355	1356	1357	1358	1359	1360	1361	1362	1363	1364	1365	1366	1367	1368	1369	1370	1371	1372	1373	1374	1375	1376	1377	1378	1379	1380	1381	1382	1383	1384	1385	1386	1387	1388	1389	1390	1391	1392	1393	1394	1395	1396	1397	1398	1399	1400	1401	1402	1403	1404	1405	1406	1407	1408	1409	1410	1411	1412	1413	1414	1415	1416	1417	1418	1419	1420	1421	1422	1423	1424	1425	1426	1427	1428	1429	1430	1431	1432	1433	1434	1435	1436	1437	1438	1439	1440	1441	1442	1443	1444	1445	1446	1447	1448	1449	1450	1451	1452	1453	1454	1455	1456	1457	1458	1459	1460	1461	1462	1463	1464	1465	1466	1467	1468	1469	1470	1471	1472	1473	1474	1475
---	---	---	---	---	---	---	---	---	----	----	----	----	----	----	----	----	----	----	----	----	----	----	----	----	----	----	----	----	----	----	----	----	----	----	----	----	----	----	----	----	----	----	----	----	----	----	----	----	----	----	----	----	----	----	----	----	----	----	----	----	----	----	----	----	----	----	----	----	----	----	----	----	----	----	----	----	----	----	----	----	----	----	----	----	----	----	----	----	----	----	----	----	----	----	----	----	----	----	-----	-----	-----	-----	-----	-----	-----	-----	-----	-----	-----	-----	-----	-----	-----	-----	-----	-----	-----	-----	-----	-----	-----	-----	-----	-----	-----	-----	-----	-----	-----	-----	-----	-----	-----	-----	-----	-----	-----	-----	-----	-----	-----	-----	-----	-----	-----	-----	-----	-----	-----	-----	-----	-----	-----	-----	-----	-----	-----	-----	-----	-----	-----	-----	-----	-----	-----	-----	-----	-----	-----	-----	-----	-----	-----	-----	-----	-----	-----	-----	-----	-----	-----	-----	-----	-----	-----	-----	-----	-----	-----	-----	-----	-----	-----	-----	-----	-----	-----	-----	-----	-----	-----	-----	-----	-----	-----	-----	-----	-----	-----	-----	-----	-----	-----	-----	-----	-----	-----	-----	-----	-----	-----	-----	-----	-----	-----	-----	-----	-----	-----	-----	-----	-----	-----	-----	-----	-----	-----	-----	-----	-----	-----	-----	-----	-----	-----	-----	-----	-----	-----	-----	-----	-----	-----	-----	-----	-----	-----	-----	-----	-----	-----	-----	-----	-----	-----	-----	-----	-----	-----	-----	-----	-----	-----	-----	-----	-----	-----	-----	-----	-----	-----	-----	-----	-----	-----	-----	-----	-----	-----	-----	-----	-----	-----	-----	-----	-----	-----	-----	-----	-----	-----	-----	-----	-----	-----	-----	-----	-----	-----	-----	-----	-----	-----	-----	-----	-----	-----	-----	-----	-----	-----	-----	-----	-----	-----	-----	-----	-----	-----	-----	-----	-----	-----	-----	-----	-----	-----	-----	-----	-----	-----	-----	-----	-----	-----	-----	-----	-----	-----	-----	-----	-----	-----	-----	-----	-----	-----	-----	-----	-----	-----	-----	-----	-----	-----	-----	-----	-----	-----	-----	-----	-----	-----	-----	-----	-----	-----	-----	-----	-----	-----	-----	-----	-----	-----	-----	-----	-----	-----	-----	-----	-----	-----	-----	-----	-----	-----	-----	-----	-----	-----	-----	-----	-----	-----	-----	-----	-----	-----	-----	-----	-----	-----	-----	-----	-----	-----	-----	-----	-----	-----	-----	-----	-----	-----	-----	-----	-----	-----	-----	-----	-----	-----	-----	-----	-----	-----	-----	-----	-----	-----	-----	-----	-----	-----	-----	-----	-----	-----	-----	-----	-----	-----	-----	-----	-----	-----	-----	-----	-----	-----	-----	-----	-----	-----	-----	-----	-----	-----	-----	-----	-----	-----	-----	-----	-----	-----	-----	-----	-----	-----	-----	-----	-----	-----	-----	-----	-----	-----	-----	-----	-----	-----	-----	-----	-----	-----	-----	-----	-----	-----	-----	-----	-----	-----	-----	-----	-----	-----	-----	-----	-----	-----	-----	-----	-----	-----	-----	-----	-----	-----	-----	-----	-----	-----	-----	-----	-----	-----	-----	-----	-----	-----	-----	-----	-----	-----	-----	-----	-----	-----	-----	-----	-----	-----	-----	-----	-----	-----	-----	-----	-----	-----	-----	-----	-----	-----	-----	-----	-----	-----	-----	-----	-----	-----	-----	-----	-----	-----	-----	-----	-----	-----	-----	-----	-----	-----	-----	-----	-----	-----	-----	-----	-----	-----	-----	-----	-----	-----	-----	-----	-----	-----	-----	-----	-----	-----	-----	-----	-----	-----	-----	-----	-----	-----	-----	-----	-----	-----	-----	-----	-----	-----	-----	-----	-----	-----	-----	-----	-----	-----	-----	-----	-----	-----	-----	-----	-----	-----	-----	-----	-----	-----	-----	-----	-----	-----	-----	-----	-----	-----	-----	-----	-----	-----	-----	-----	-----	-----	-----	-----	-----	-----	-----	-----	-----	-----	-----	-----	-----	-----	-----	-----	-----	-----	-----	-----	-----	-----	-----	-----	-----	-----	-----	-----	-----	-----	-----	-----	-----	-----	-----	-----	-----	-----	-----	-----	-----	-----	-----	-----	-----	-----	-----	-----	-----	-----	-----	-----	-----	-----	-----	-----	-----	-----	-----	-----	-----	-----	-----	-----	-----	-----	-----	-----	-----	-----	-----	-----	-----	-----	-----	-----	-----	-----	-----	-----	-----	-----	-----	-----	-----	-----	-----	-----	-----	-----	-----	-----	-----	-----	-----	-----	-----	-----	-----	-----	-----	-----	-----	-----	-----	-----	-----	-----	-----	-----	-----	-----	-----	-----	-----	-----	-----	-----	-----	-----	-----	-----	-----	-----	-----	-----	-----	-----	-----	-----	-----	-----	-----	-----	-----	-----	-----	-----	-----	-----	-----	-----	-----	-----	-----	-----	-----	-----	-----	-----	-----	-----	-----	-----	-----	-----	-----	-----	-----	-----	-----	-----	-----	-----	-----	-----	-----	-----	-----	-----	-----	-----	-----	-----	-----	-----	-----	-----	-----	-----	-----	-----	-----	-----	-----	-----	-----	-----	-----	-----	-----	-----	-----	-----	-----	-----	-----	-----	-----	-----	-----	-----	-----	-----	-----	-----	-----	-----	-----	-----	-----	-----	-----	-----	-----	-----	-----	-----	-----	-----	-----	-----	-----	-----	-----	-----	-----	-----	-----	-----	-----	-----	-----	-----	-----	-----	-----	-----	-----	-----	-----	-----	-----	-----	-----	-----	-----	-----	-----	-----	-----	-----	-----	-----	-----	-----	-----	-----	-----	-----	-----	-----	-----	-----	-----	-----	-----	-----	-----	-----	-----	-----	-----	-----	-----	-----	-----	-----	-----	-----	-----	-----	-----	-----	-----	-----	-----	-----	-----	-----	-----	-----	-----	-----	-----	-----	-----	-----	-----	-----	-----	-----	-----	-----	-----	-----	-----	-----	-----	-----	-----	-----	-----	-----	-----	-----	-----	-----	-----	-----	-----	-----	-----	-----	-----	-----	-----	-----	-----	-----	-----	-----	-----	-----	-----	-----	-----	-----	-----	-----	-----	-----	-----	-----	-----	-----	-----	-----	-----	-----	-----	------	------	------	------	------	------	------	------	------	------	------	------	------	------	------	------	------	------	------	------	------	------	------	------	------	------	------	------	------	------	------	------	------	------	------	------	------	------	------	------	------	------	------	------	------	------	------	------	------	------	------	------	------	------	------	------	------	------	------	------	------	------	------	------	------	------	------	------	------	------	------	------	------	------	------	------	------	------	------	------	------	------	------	------	------	------	------	------	------	------	------	------	------	------	------	------	------	------	------	------	------	------	------	------	------	------	------	------	------	------	------	------	------	------	------	------	------	------	------	------	------	------	------	------	------	------	------	------	------	------	------	------	------	------	------	------	------	------	------	------	------	------	------	------	------	------	------	------	------	------	------	------	------	------	------	------	------	------	------	------	------	------	------	------	------	------	------	------	------	------	------	------	------	------	------	------	------	------	------	------	------	------	------	------	------	------	------	------	------	------	------	------	------	------	------	------	------	------	------	------	------	------	------	------	------	------	------	------	------	------	------	------	------	------	------	------	------	------	------	------	------	------	------	------	------	------	------	------	------	------	------	------	------	------	------	------	------	------	------	------	------	------	------	------	------	------	------	------	------	------	------	------	------	------	------	------	------	------	------	------	------	------	------	------	------	------	------	------	------	------	------	------	------	------	------	------	------	------	------	------	------	------	------	------	------	------	------	------	------	------	------	------	------	------	------	------	------	------	------	------	------	------	------	------	------	------	------	------	------	------	------	------	------	------	------	------	------	------	------	------	------	------	------	------	------	------	------	------	------	------	------	------	------	------	------	------	------	------	------	------	------	------	------	------	------	------	------	------	------	------	------	------	------	------	------	------	------	------	------	------	------	------	------	------	------	------	------	------	------	------	------	------	------	------	------	------	------	------	------	------	------	------	------	------	------	------	------	------	------	------	------	------	------	------	------	------	------	------	------	------	------	------	------	------	------	------	------	------	------	------	------	------	------	------	------	------	------	------	------	------	------	------	------	------	------	------	------	------	------	------	------	------	------	------	------	------	------	------	------	------	------	------	------	------	------	------	------	------	------	------	------	------	------	------	------	------	------	------	------	------	------	------	------	------	------	------	------	------	------	------	------	------	------	------	------	------

terms.[99] This feature provides advantages including excellent photo-stability, large Stokes/anti-long luminescent lifetimes, Stokes shifts and narrow-band emissions for Ln^{3+} activated materials as outstanding optical materials.[100–102] Thus, Ln^{3+} are regarded as potential luminescent supporters for applications such as sensing,[103] bioimaging,[104] therapy[104, 105] and photovoltaic devices.[106] Furthermore, the luminescence of Ln^{3+} can be divided to down-shifting, quantum-cutting (also known as downconversion), and upconversion according to the transition pathways. Both downshifting and downconversion processes requires high-energy photon to excite, whereas upconversion needs lower energy photons to trigger, specifically near-infrared (NIR) light, for frequency upconverting.[107]

In recent years, a novel library of nanomaterials called high-performance lanthanide-doped upconversion nanoparticles (UCNPs) have been extensively investigated for bioimaging and therapeutic applications. With the rapid development of nanotechnology, a variety of nanomaterials, such as silica, gold, quantum dots, magnetic and polymeric nanoparticles have been developed for biological applications based on their various physical or chemical properties. As compared to these conventional nanomaterials, UCNPs exhibit unique properties including negligible photobleaching for long-term tracking, minimum photodamage to living organisms, low auto-fluorescence and high signal-to-noise for sensitive bioimaging, and near infrared (NIR) excitation nature for deeper penetration into biological tissues (while most of traditional bioimaging probes requires visible/ UV excitation). In this section, the properties of UCNPs are described, including surface modification and the recent progress achieved in bioimaging and therapeutic applications using UCNPs. Finally, the challenges and future perspective of Ln^{3+} -based upconversion materials are discussed.

1.4.1 Optical properties of Ln^{3+} -UCNPs

There are abundant energy levels of 4f electron configurations for lanthanides, leading to various electronic transitions.(Figure 21)[108] The mechanism of Ln^{3+} -UCNPs processes can be divided into the following classes: excited-state absorption (ESA), energy transfer upconversion (ETU), cooperative energy transfer (CET) and energy migration-mediated upconversion.

The ESA is an appropriate pumping mechanism for singly-doped upconversion materials, involving successive two-photon absorption in one single Ln^{3+} ion. Under suitable excitation conditions, the excitation energy is resonant with the transition from the ground

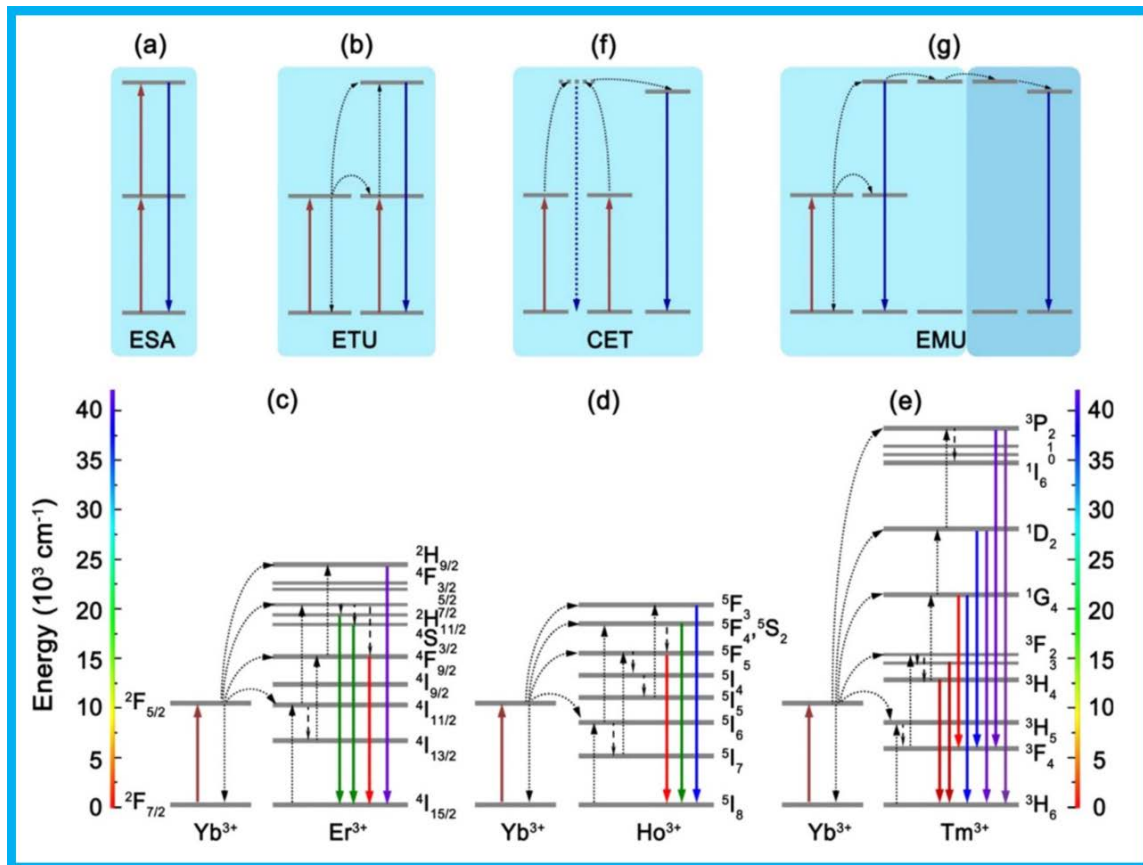


Figure 20. Principal mechanisms of Ln^{3+} related upconversion emissions: excited-state absorption (ESA, a), energy transfer upconversion (ETU, b), ETU-based Yb^{3+} - Er^{3+} pair (c), ETU-based Yb^{3+} - Ho^{3+} pair (d), ETU-based Yb^{3+} - Tm^{3+} pair (e), cooperative energy transfer (CET, f) and energy migration-mediated upconversion (EMU, g). Copyright with permission from ref.[108].

state to the excited metastable level, then the excited state of middle-level successively absorbs another photon with energy that is resonant with the transition from middle level to high-lying excited state. The photon drops from the highly-excited level to the ground level and induces upconversion emission. In this ETU processes, there are two luminescent centres including sensitizer and activator. Energy can be absorbed by sensitizer and transferred to activator from sensitizer to form upconversion emission. A low active ion concentration in the Ln^{3+} -UCNPs (Figure 21) is necessary to avoid transfer losses through cross-relaxation between the luminescent centres (sensitizer and activator) and to increase the gain in the excited-state absorption process.[107] The key difference between ETU and

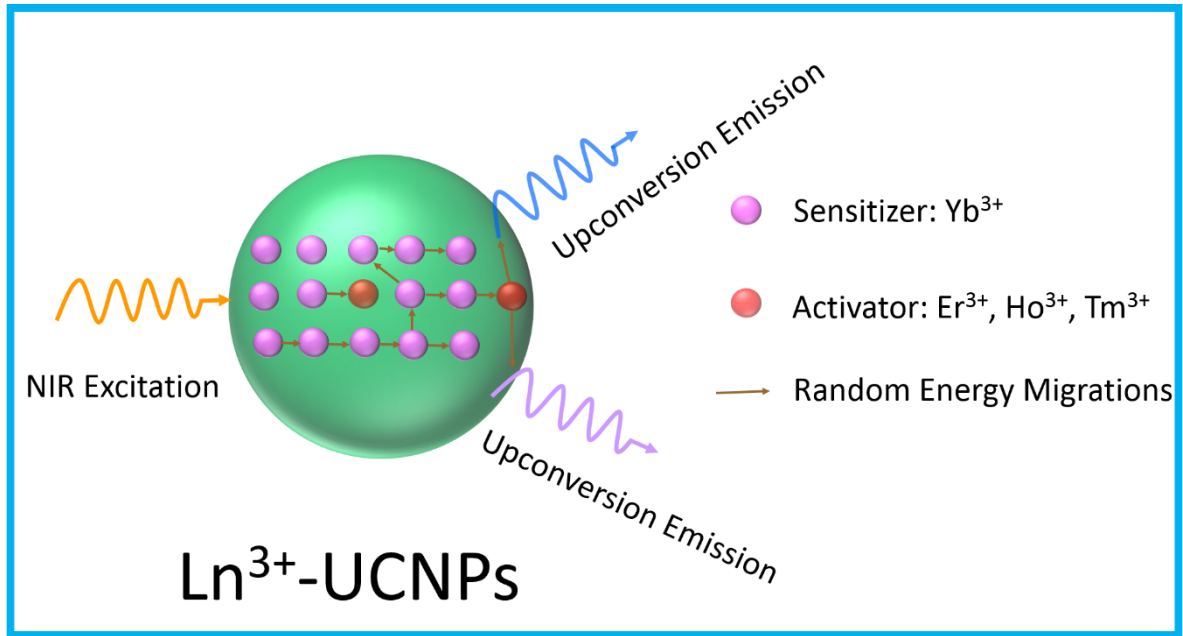


Figure 21. Schematic illustration of the $\text{Ln}^{3+}\text{-UCNPs}$ structure and random energy migration among lanthanide ions in the structure.

CET is the absence of a long-lived middle energy state of the activator, leading to very low efficiency. Furthermore, a broad range of gadolinium-based core/shell nanostructure with the EMU process was developed to tune energy migration. It was found that the efficiency of upconversion emission can be increased through gadolinium sublattice-mediated energy migration for a wide range of lanthanide activators without long-lived intermediary energy states. This demonstrates that this effect enables fine-tuning of upconversion emission through trapping of the migrating energy by the activators. [109] Totally, there are four types of luminescent centres, which are sensitizer, accumulator, migrator, and activator incorporated into various parts with precisely defined concentration. The energy is finally trapped by the activator via sequential energy transfer through the core/shell interface.

The ETU process is the most efficient upconversion process. Most $\text{Ln}^{3+}\text{-UCNPs}$ achieve efficient upconversion emission through an ETU processes. Three most commonly ETU-based Ln^{3+} pairs are shown in Figure 20c-e. Typically, Yb^{3+} firstly absorbs near infrared (NIR) light and then transfers the acquired energy to adjacent Ln^{3+} ($\text{Ln} = \text{Er}$, Ho and Tm). In $\text{Yb}^{3+}\text{-Er}^{3+}$ co-doped UCNPs (Figure 20c), the energy is transferred from the level $^2\text{F}_{5/2}$ Yb^{3+} to the $^2\text{H}_{9/2}$, $^2\text{H}_{11/2}$, $^4\text{S}_{3/2}$, and $^4\text{F}_{9/2}$ states, forming three-photon violet (415 nm, $^2\text{H}_{9/2} \rightarrow ^4\text{I}_{15/2}$), two-photon green (525 nm, $^2\text{H}_{11/2} \rightarrow ^4\text{I}_{15/2}$; 545 nm, $^4\text{S}_{3/2} \rightarrow ^4\text{I}_{15/2}$) and red (655 nm, $^4\text{F}_{9/2} \rightarrow ^4\text{I}_{15/2}$) emissions. Moreover, in $\text{Yb}^{3+}\text{-Ho}^{3+}$ pair, two-photon upconversion can also

occur to generate green (545 nm, $^5F_4, ^5S_2 \rightarrow ^5I_8$) and red (650 nm, $^5F_5 \rightarrow ^5I_8$) emissions, while the three-photon process generates blue (485 nm, $^5F_3 \rightarrow ^5I_8$) emission (Figure 20d). To compare the energy state diagram of Yb^{3+} - Ho^{3+} pairs and Yb^{3+} - Er^{3+} pairs, it is obvious that the energy levels of Yb^{3+} - Ho^{3+} pairs are inferior to that of Yb^{3+} - Er^{3+} pairs, therefore the upconversion efficiency in Yb^{3+} - Er^{3+} is higher than that of Yb^{3+} - Ho^{3+} pairs. On the contrary, multiphoton upconversion emissions can be measured in blue and UV regions from Yb^{3+} - Tm^{3+} co-doped UCNPs (Figure 20e). It is resulted from the simple and discretely arranged energy states of Tm^{3+} , decreasing the non-radiative relaxations and multiphoton cross relaxations within activators. After getting the energy transferred from Yb^{3+} , Tm^{3+} can release two-photon NIR (800 nm, $^3H_4 \rightarrow ^3H_6$) and red (695 nm, $^3F_3 \rightarrow ^3H_6$) emissions, three-photon red (645 nm, $^1G_4 \rightarrow ^3F_4$) and blue (475 nm, $^1G_4 \rightarrow ^3H_6$) emissions, four-photon blue (450 nm, $^1D_2 \rightarrow ^3F_4$) and UV (365 nm, $^1D_2 \rightarrow ^3H_6$) emissions, and five-photon UV (345 nm, $^1I_6 \rightarrow ^3F_4$; 290 nm, $^1I_6 \rightarrow ^3H_6$) emissions.

1.4.2 Efficient Enhancement of Upconversion Emission

The Ln^{3+} -UCNPs can convert near infrared (NIR) radiation to various visible luminescence spectra, and are promising for applications in diagnosis,[110–112] bioimaging[8, 112] and three-dimensional display technologies[106, 113]. The efficacy of bio-applications calls for adequate upconversion emission efficiency. However, it is well known that the intra-configurational transitions of Ln^{3+} are parity-forbidden, leading to low upconversion emission efficiency due to the small absorption cross-section of Ln^{3+} . Moreover, when the size of the particle is down to nanoscale, the upconversion nanoparticles face a profound quenching effect from their surface. During past decades, the design of suitable nanocrystals has improved the performance of upconversion nanocrystals, with several methods being proposed to improve upconversion efficiency. The most common and effective approaches are adjusting the dopant concentration, and surface passivation with core-shell structure.

1.4.2.1 Adjusting the Dopant Concentration

Lanthanide-doped UCNPs are typically doped with ytterbium (Yb^{3+}) as a sensitizer to absorb near infrared light and transfer to an activator such as erbium (Er^{3+}), holmium (Ho^{3+}) and thulium (Tm^{3+}) for upconversion emission. However, there is a main limitation for the

emission efficiency of UCNPs called concentration quenching, which leads to the decreased brightness of UCNPs with increasing dopant density beyond the optimal concentration.[114,115] The optimal concentration of Tm^{3+} in NaYF_4 host lattices is as

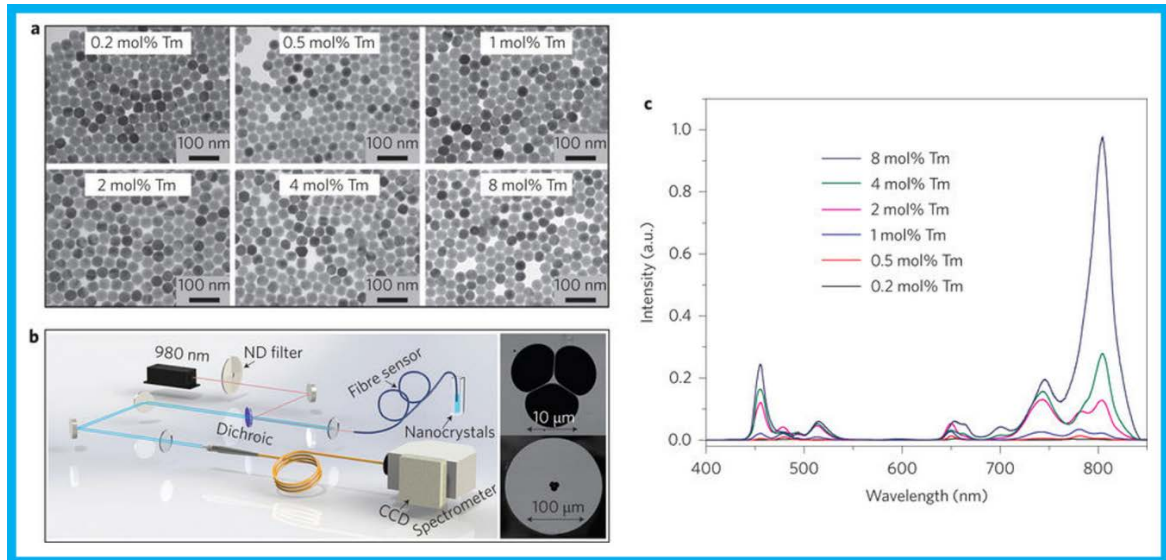


Figure 22. Highly Tm^{3+} -doped NaYF_4 upconversion nanoparticles provide enhanced upconversion emission in a suspended-core fibre. Copyright with permission from ref. [118].

low as ~ 0.2 - 0.5 mol% at excitation power below 100 W cm^{-2} (with ~ 20 - 40 mol% Yb^{3+}). [116] [117] Such nanocrystals have small numbers of activators and therefore produce weak upconversion emission. In 2013, this limitation was solved by increasing activator concentration (Tm^{3+}) up to 8.0 mol% in NaYF_4 to dramatically enhance the upconversion emission efficiency by up to a factor of 70 under the high excitation irradiation. (Figure 22) [118] This represents a significantly improved sensitivity of three orders of magnitude over benchmark nanocrystals such as quantum dots. [119] Apart from this, there are numerous studies using high-radiation excitation to alleviate concentration quenching for orders of magnitude increase in upconversion emission, where the activator concentration of Tm^{3+} and Er^{3+} in NaYF_4 increase from 0.5 mol% to 8 mol%, and from 2 mol% up to more than 10 mol %, respectively. [120–122]

1.4.2.2 Surface Passivation with Core-shell Structure

Surface passivation with core-shell structure is a typical strategy to alleviate the quenching effect caused by surface defects. Furthermore, this strategy also utilizes various lanthanide activators to generate multi-color luminescence via fabrication of an appropriate core-shell structure. This yields a range of high-efficiency tunable emission by removing deleterious

cross relaxations between the lanthanide activators and suppresses surface-related quenching mechanism in the core nanoparticles. It was reported that hexagonal-phase $\text{NaYF}_4:\text{Yb}^{3+}/\text{Tm}^{3+}@\text{NaYF}_4:\text{Yb}^{3+}/\text{Er}^{3+}$ with core-shell structure and $\text{NaYF}_4:\text{Yb}^{3+}/\text{Tm}^{3+}@$

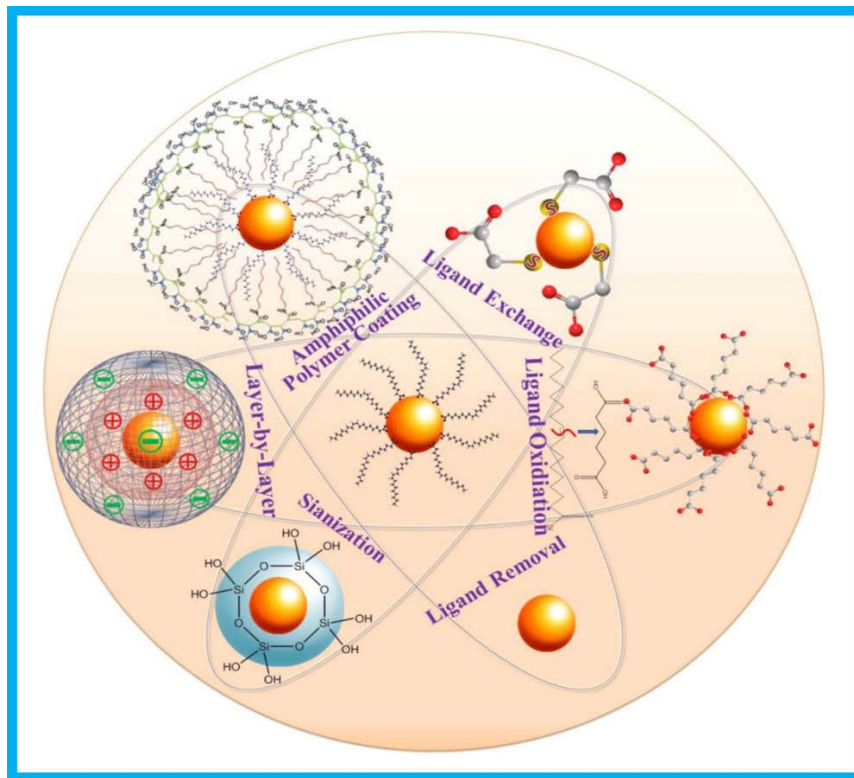


Figure 23. Schematic illustration of general strategies used for surface engineering of UCNPs. Copyright with permission from ref. [130].

$\text{NaYF}_4:\text{Yb}^{3+}/\text{Er}^{3+}@\text{NaYF}_4:\text{Yb}^{3+}/\text{Tm}^{3+}$ nanoparticles with a sandwich structure were fabricated and both of them generate multiple emission peaks.[123] Both Tm^{3+} and Er^{3+} emissions were found from the core-shell structured and sandwich-structured nanoparticles, which is different from the $\text{Tm}^{3+}/\text{Er}^{3+}$ -co-doped NaYF_4 nanoparticles (Tm^{3+} emission was quenched). Furthermore, it was reported on sandwich-structured multicolored core/shell/shell nanoparticles of $\text{NaYF}_4:\text{Yb}^{3+}/\text{Er}^{3+}@\text{NaYbF}_4:\text{Tm}^{3+}@\text{NaYF}_4:\text{Yb}^{3+}/\text{Tm}^{3+}$, $\text{NaYF}_4:\text{Yb}^{3+}/\text{Tm}^{3+}@\text{NaYbF}_4:\text{Er}^{3+}@\text{NaYF}_4:\text{Yb}^{3+}/\text{Er}^{3+}$, and $\text{NaYF}_4:\text{Yb}^{3+}/\text{Tm}^{3+}@\text{NaYbF}_4:\text{Er}^{3+}@\text{NaYF}_4:\text{Yb}^{3+}/\text{Tm}^{3+}$, for multicolour cellular imaging with just a single NIR excitation source. This sandwich structure enables upconversion nanoparticles for multiplex detection of three subcellular targets with minimally toxic NIR light excitation and low background fluorescence.[124]

1.4.3 Surface engineering of UCNPs

The Ln^{3+} -UCNPs are generally fabricated with oleic acid (OA), oleylamine (OM) or trioctylphosphine oxide (TOPO) that are not water-soluble before surface modification and functionalization. However, the biocompatibility of nanomaterials in vitro and in vivo is crucial before they can be further applied for bioimaging and therapeutic application. Therefore, it is essential to modify and functionalize Ln^{3+} -UCNPs to make them water soluble, biocompatible and with functional groups available for further bioconjugation for targeting functions. There are numerous surface modification approaches, including ligand removal, ligand oxidation, ligand exchange, amphiphilic polymer coating, layer-by-layer assembly and silanization for transferring nanoparticles from hydrophobic into hydrophilic surface. (Figure 23)[125] Ligand removal, ligand exchange and silanization are the most commonly utilized for surface modification, and are discussed in the following sections.

1.4.3.1 Ligand Removal

Ligand removal from the surface of nanoparticles is an easy and simple approach to make nanoparticles disperse well into aqueous solutions. This method removes the OA on the surface of UCNPs via treatment with acid. Typically, it was reported that the water-soluble ligand-free upconverting lanthanide-doped $\text{NaYF}_4:\text{Yb}^{3+}, \text{Er}^{3+}$ can be acquired by using a simple acid treatment procedure. (Figure 30) [126] The Ln^{3+} -OA on the surface is replaced by Ln^{3+} -OH whose state of charge can be further adjusted by pH and the efficiency of upconversion luminescence can even be improved by replacing OH with OD. Furthermore, it has been suggested that an easier way to eliminate OA on the surface of $\text{NaYF}_4:\text{Yb}^{3+}, \text{Er}^{3+}$ nanoparticles is by ultrasonic separation. This study demonstrated that the OA-free $\text{NaYF}_4:\text{Yb}^{3+}, \text{Er}^{3+}$ nanoparticles readily disperse in water and ethanol.[127] The purified OA-free nanoparticles can directly conjugate to biocompatible molecules via functional groups (such as $-\text{COOH}$, $-\text{NH}_2$, $-\text{OH}$) in water solution due to their abundant metallic ions on the surface. It has been demonstrated that biomolecules such as heparin can be attached to the surface of ligand-free $\text{NaGdF}_4:\text{Yb}^{3+}/\text{Er}^{3+}$ nanoparticles to allow their use in targeting and delivery of heparin-binding growth factors and imaging of cancer cells.[128]

1.4.3.2 Ligand Exchange

Ligand exchange is the most popular and common approach to modify the surface of UCNPs. In this process, the original ligand on the surface of UCNPs can be exchanged by

other hydrophilic ligands including poly(ethyleneglycol) (PEG) phosphate,[129] poly(acrylic acid) (PAA)[130] and poly(amidoamine) (PAMAM).[131] Typically, it has reported that [129] PEG-phosphated ligand can efficiently replace the OA on the surface of UCNPs and form water-dispersible particles without obvious quenching compared to the original particles. Furthermore, PEG-phosphate-coated upconverting NPs have been used to image a line of ovarian cancer cells (CaOV3) to reveal their potential in biological application.

In additional, the OA can be removed by nitrosonium tetrafluoroborate (NOBF_4) for further use.[132] Specifically, a facile ligand-exchange approach was presented to replace the original organic ligands (like OA) on the surface of inorganic nanocrystals(NCs) with NOBF_4 . Furthermore, the BF_4^- anion attached on the positive charged UCNPs and enabled the UCNPs to disperse in various media such as *N,N*-dimethylformamide (DMF) and dimethyl sulfoxide (DMSO). The BF_4^- -attached NCs can be easily functionalized by hydrophobic ligands such as hexylamine or tetradecylphosphonic acid, or with hydrophilic polymers such as polyvinylpyrrolidone (PVP). (Figure 24)

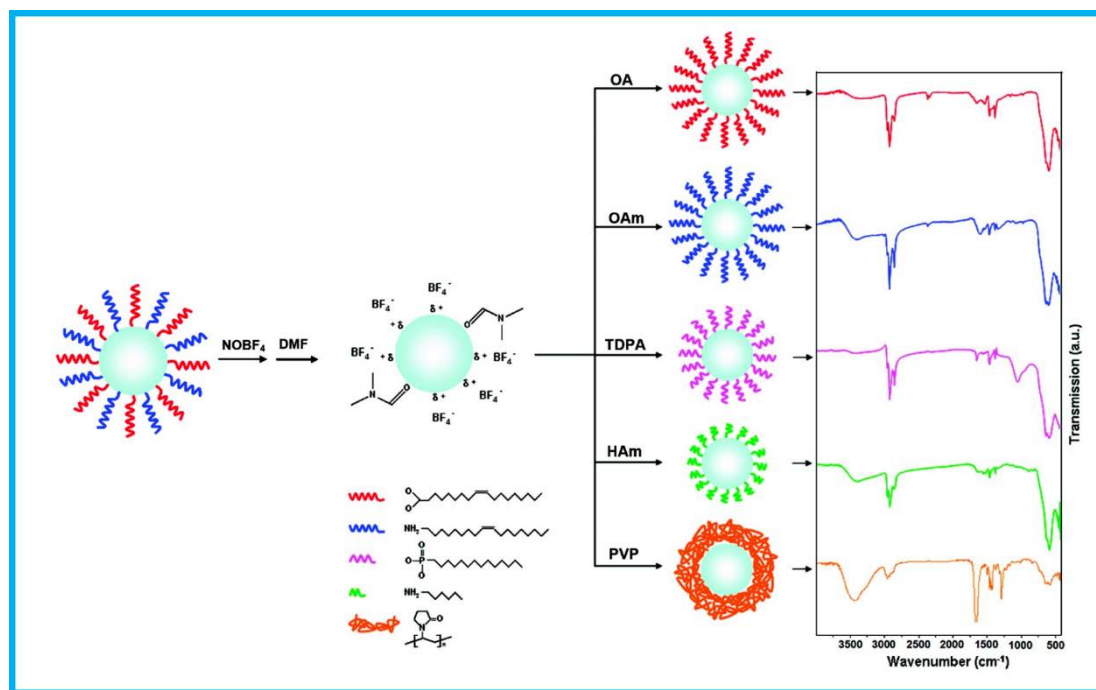


Figure 24. Illustration of the ligand exchange processes of inorganic nanocrystals (NCs). The original oleate ligands capped on the surface of the NCs are firstly exchanged by NOBF_4 , followed by secondly exchanged by various capping molecules. The right column represents the corresponding FTIR spectra. Copyright with permission from ref. [132].

1.4.3.3 Generation of a Silica Shell on the Surface of UCNPs

Silica is also one of the most commonly used materials for growing a bioavailable shell on the surface of UCNPs. However, the silica layer slightly decreases the luminescence of UCNPs due to the scattering of excitation light and emission light by the silica layer.[132,133] Apart from that, the biocompatible and non-toxic properties of silica make them a popular surface choice. Moreover, the chemically active surface of silica is readily available to introduce various functional groups (such as carboxyl, amino and thiol groups) via silanization, presenting a range of functionalization options for nanoparticles and bio-conjugation. Thus, silica is also commonly used to coat the surface of other nanomaterials, including gold, iron oxide and quantum dots.[134–138] Furthermore, silica coating can enable nanoparticles to disperse well in aqueous solutions or biological buffers (such as cell culture media and PBS buffer).[139] Moreover, a mesoporous silica layer provides a large surface area and pore volume for adsorption as well as high loading of various therapeutic agents. Therefore, the combinations of UCNP and mesoporous silica shell will enable the development of multifunctional nanomedical platforms for biosensing, multimodal bioimaging and drug delivery. However, it is found that silica-coated UCNPs modified with amines are susceptible to aggregation due to the electrostatic attraction between positively charged amines and the negatively charged silicate surface in the biological pH. (Figure 34) Further functionalization with methyl-phosphonate is suitable to reduce this electrostatically induced aggregation.(Figure 25) [140]

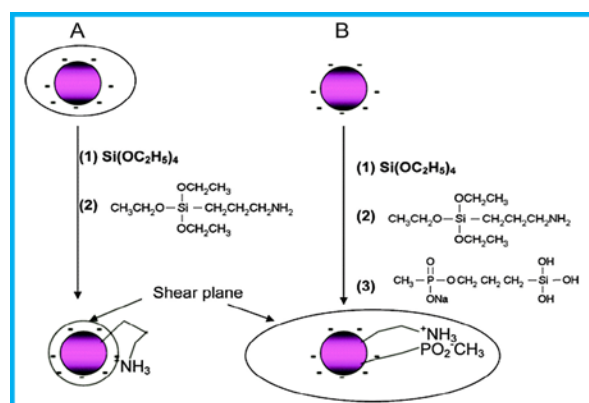


Figure 25. Schematically represents of the mechanism of amine-functionalized silica nanoparticles on the same nanoparticle (A) and the potential avoidance by a silanization with methyl phosphonate (B). Reprinted with permission from ref. [140].

1.4.4 Shape Controlled Fabrication of UCNP

Controlled engineering of Ln^{3+} -UCNP to modify their original physical and chemical properties, and to combine multiple functionalities into one particle with desired size, shape and surface properties, provides a huge potential for enabling new nanotechnologies, including multiplex bioimaging, targeted drug delivery, and ultra-sensitive diagnosis. Although a wide range of drug vectors have been developed, there is still a limited number of them that can be further employed for clinical treatment due to their low targeting efficiency and potential cytotoxicity. To overcome these challenges, it is essential to use nanomaterials as a delivery platform to improve drug transport in the body. Therefore, it is necessary to explore the possibilities to control the engineering of Ln^{3+} -UCNPs in terms of their size, shape and surface properties for further biological application.

In recent years, a variety of synthesis methods for high-quality Ln^{3+} -UCNPs with tunable composition, crystalline phase, size and shape have been explored to adjust their chemical and optical properties for further potential applications in various fields. [141] This section describes three main nanochemistry approaches that have been utilized to produce

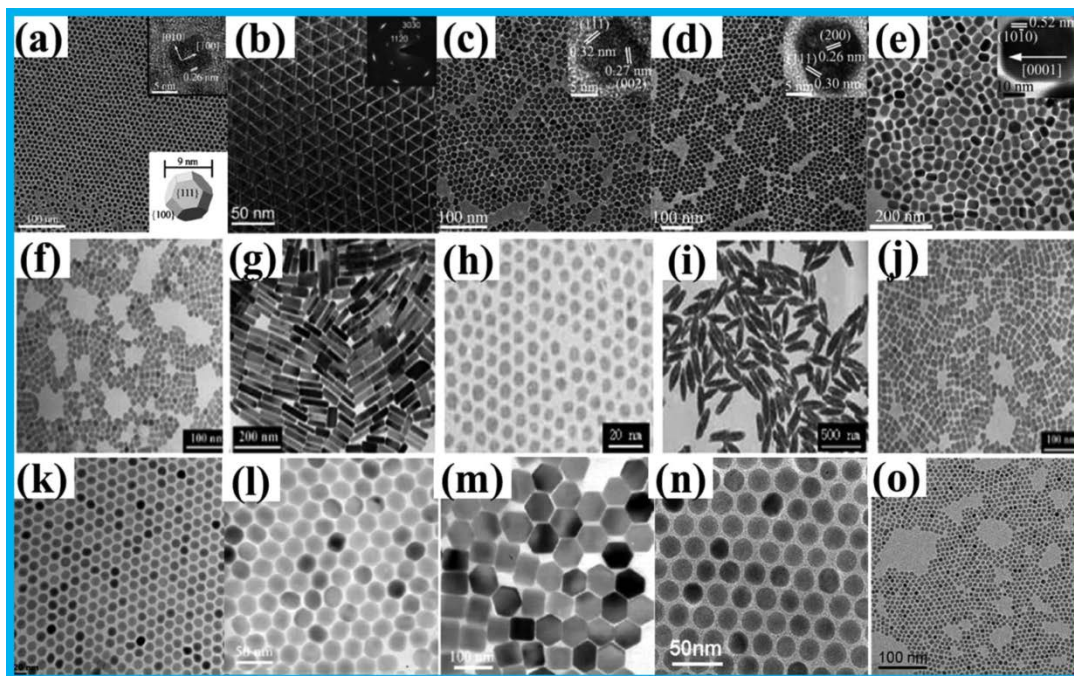


Figure 26. Representative TEM images of Ln-doped (a) LuOF, (b) LaF₃, (c) α -NaYF₄, (d) NaYbF₄, (e) β -NaEuF₄, a-e fabricated by themolysis method; (f) α -NaYF₄:Yb³⁺, Er³⁺, (g) β -NaYF₄:Yb³⁺, Er³⁺, (h) LaF₃, (i) YF₃, (j) α -NaYF₄, f-j synthesized by the hydro(solvo)-thermal method; (k-o) β -NaYF₄ or CaF₂ prepared by the Ostwald-ripening method. Reprinted with permission from ref. [144].

upconversion nanoparticles in a highly controlled manner including thermolysis, hydro(solvo)thermal, and Ostwald-ripening. This section mainly focuses on thermolysis, which is the most widely used method, as it can offer precise control over the phase, shape, size, and stoichiometric composition of the core only and/or the core/shell UCNPs. Figure 26 illustrates some examples of TEM images of UCNPs prepared by these methods.

1.4.4.1 Thermolysis

The thermolysis strategy commonly utilizes organometallic compounds as precursors, which can decompose in an organic solvent (whose boiling point is high) due to their surfactants at an elevated temperature. The precursors commonly utilized include metallic

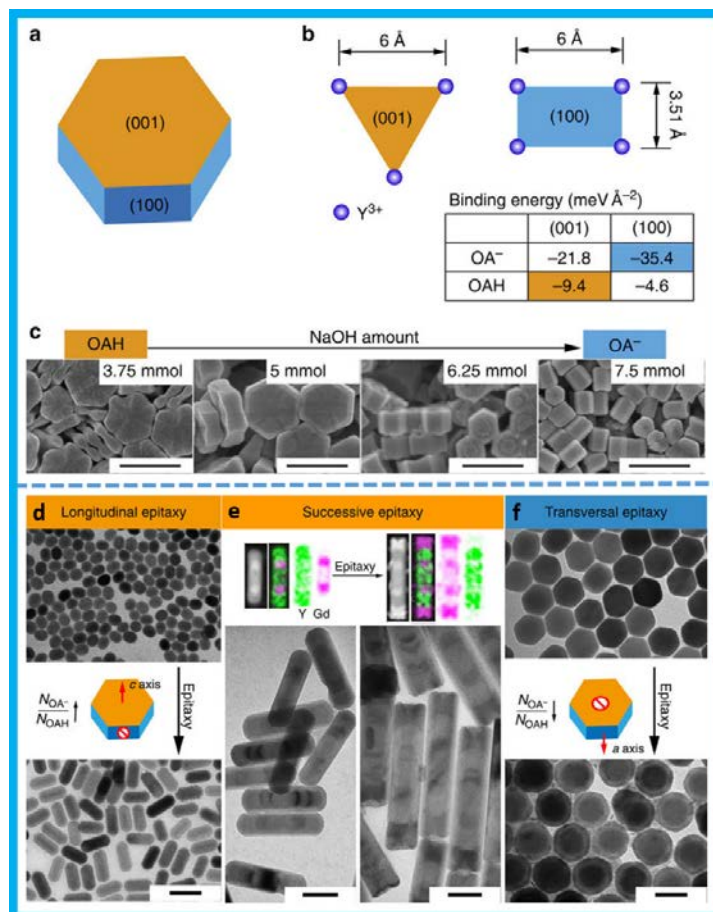


Figure 27. (a) The schematic morphology of a β - NaYF_4 nanocrystal; (b) The Y^{3+} arrangements and binding energies (see insert table) of OAH and OA^- on the most stable (001) and (100) facets; (c) SEM images of submicron-sized nanocrystals (scale bar, 500nm); (d) TEM images of β - NaYF_4 core and homogeneous β - NaYF_4 after epitaxial growth into rod-shaped β - NaYF_4 ; (e) five-section and seven-section "bamboo-shaped" $\text{NaYF}_4/\text{NaGdF}_4$ and $\text{NaGdF}_4\text{-NaYF}_4\text{-NaGdF}_4$ and (f) β - NaYF_4 core and heterogeneous $\text{NaYF}_4/\text{NaGdF}_4$ after epitaxial growth of NaGdF_4 in the transversal directions. Scale bar=50nm. Reprinted with permission from ref. [146].

trifluoroacetate salts; the solvent commonly used is 1-octadecene (ODE); the surfactants used include oleic acid (OA), trioctylphosphine oxide (TOPO) or oleylamine (OM), which typically provide a functional capping group and a long hydrocarbon chain to prohibit nanoparticle aggregation. It is important to note that the rapid decomposition of metallic trifluoroacetate produces a burst of nucleation, which is necessary for forming monodispersed nanophosphors. Murray's group prepared highly uniform hexagonal $\text{NaYF}_4:\text{Yb}^{3+}/\text{Er}^{3+}$ nanoparticles with controlled sizes and morphologies (spheres, nanorods, and hexagonal prisms). The decomposition method has been extended to synthesize other rare earth fluorides, oxides, and oxyfluorides such as LiREF_4 , [142] NaScF_4 , [143] YF_3 , [144] and LnOF ($\text{Ln} = \text{Er}, \text{Tm}, \text{Yb}, \text{Lu}, \text{Tb}, \text{Dy}, \text{Ho}, \text{Y}$). [145] Importantly, our group recently found that OLEATE ANIONS (OA^-) and the dissociated form of oleic acid molecules (OAH) have versatile dynamic roles in mediating the growth of AREF_4 nanocrystals. It showed that the ratio change between OA and OAH could affect the interactions of these ligands with the particle surface and hence the resulting morphology. (Figure 27) [146] Through this thermolysis process, high-quality UCNPs with a narrow size distribution, good crystallization and exceptional optical properties can be prepared by tailoring the nature of the solvents, concentration of metal precursors, reaction temperature, and time. The drawback of the thermolysis strategy is that it involves a fast nucleation or growth process, which can lead to the production of more defects in the synthesized UCNPs, thus resulting in a relatively lower upconversion quantum yield.

1.4.4.2 Hydro(solvo)thermal

The Hydro(solvo)thermal method is a solution-based chemical preparation approach in which the reaction system is in a sealed environment under high pressure and temperature, generally more than the critical point of the solvent to enhance the solubility and reactivity of the inorganic substances. The unique advantages of this approach include forming highly crystalline phases at much lower temperatures and implementing a set of reactions at the same time. However, the disadvantages of this strategy include the need of a special reaction vessel called an autoclave and invisible growing process of nanoparticles. Surfactants such as ethylenediaminetetraacetic acid (EDTA), [147] polyethylenimine (PEI), [114] cetyltrimethylammonium bromide (CTAB) [148] and OA supply chelating ability with cationic ions to tune their reacting concentration, [149] which are crucial for the control of

the crystalline phase, size, and shape as well as the surface modified groups of as-prepared UCNPs.

1.4.4.3 Ostwald-ripening

The Ostwald ripening approach involves a process whereby larger sized particles are favored over less stable smaller particles, resulting in the growth of larger particles at the expense of smaller ones.[150] Zhang's group developed highly uniform hexagonal phase $\text{NaYF}_4:\text{Yb}^{3+}/\text{Er}^{3+}$ (or Tm^{3+}) UCNPs with controllable sizes and shapes via employing OA as the capping ligand and ODE as the high-boiling solvent.[123] This fabrication approach was based on the formation of small amorphous sacrificial NaYF_4 coprecipitates at room temperature (RT) followed by growing nanoparticles with the Ostwald-ripening process at elevated temperatures (300 °C). In comparison with the thermal decomposition method, this approach provides relatively mild reaction conditions, non-toxic byproducts, simple protocols, and short reaction time. A control of the ripening process through control of temperature and reaction time allows one to produce monodispersed nanoparticles, often hexagonal phase, with narrow size distribution. This method has been extensively used to prepare monodispersed Ln^{3+} -doped LiYF_4 , [151] NaYF_4 , [114] NaGdF_4 , [152] and CaF_2 UCNPs.[153] The Ostwald-ripening strategy has also been utilized to produce hierarchical core/shell nanoparticles due to the ability to precisely control the shell thickness in the Ostwald-ripening process. Because it takes a relatively long time to nucleate and grow using the Ostwald-ripening approach, it generally can produce well-crystallized hexagonal UCNPs with decreased defect rate, and thus might have a relatively higher UC efficiency. While it hasn't been undertaken previously, comparison of the absolute quantum yields of the same type of UCNPs that are produced by either thermolysis method, Ostwald-ripening approach, or hydrothermal strategy will be a direct method to evaluate the production embodiment of these synthetic methods.

1.4.5 Biological Applications of Ln^{3+} -UCNPs

The upconversion luminescence (UCL) from Ln^{3+} -UCNPs under 980nm laser excitation is a type a unique optical signal. UCL imaging is a noninvasive diagnostic approach for visualizing various biological processes for the investigation of pathogenesis and progression of many diseases. Furthermore, with the advantages of non-

autofluorescence[154], low photobleaching,[155] nonblinking[155] and deep tissue penetration,[156–158] UCL imaging has been employed to measure the morphological and physiological details in tissues as well as the full range of biological species from cells to animals.[159–162] In this regard, UCNPs utilizing UCL are superior to conventional biomarkers, such as organic dyes and quantum dots, based upon relative differences in signal-to-noise ratio, wide emission bands (leading to cross-talk between emission spectra), poor photostability, low limited penetration depth and prominent biotoxicity prevent their application in bioimaging studies. In the contrary, Ln^{3+} -doped UCNPs exhibit significant promise by overcoming those disadvantages of organic dyes and quantum dots.

1.4.5.1 Ln^{3+} -UCNPs for Bioimaging

In vitro imaging. The in vitro imaging of Ln^{3+} -UCNPs are mostly conducted with cell culture models. The cellular imaging of Ln^{3+} -UCNPs is divided into three types: (1) physiological activity tracking; (2) non-specific endocytosis; (3) targeting cellular labelling or endocytosis. Cellular imaging can directly visualize the physiological processes at the cellular or subcellular level. It is reported that polyethylenimine (PEI) conjugated $\text{NaYbF}_4:\text{Tm}@\text{CaF}_2$ UCNPs was developed to label rat mesenchymal stem cells for tracking cell proliferation and differentiation. The result demonstrated that PEI-UCNPs labelled stem

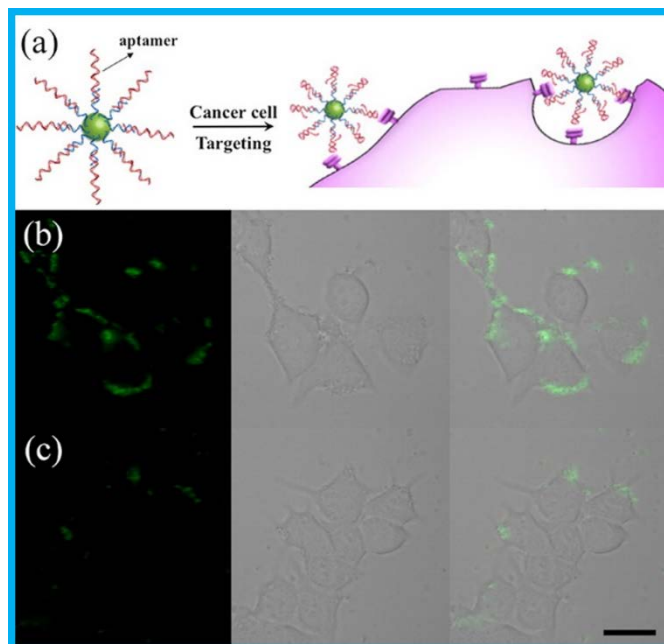


Figure 28. (a) Targeted imaging of cancer cells with aptamer-UCNPs bioconjugates. Confocal microscopy images of MCF-7 cells treated with (b) Apt-UCNPs and (c) Rdm-UCNPs under 980nm laser excitation and emission wavelength range from 510 nm to 560 nm. Scale bar = 20um. Copy with permission of ref. [165].

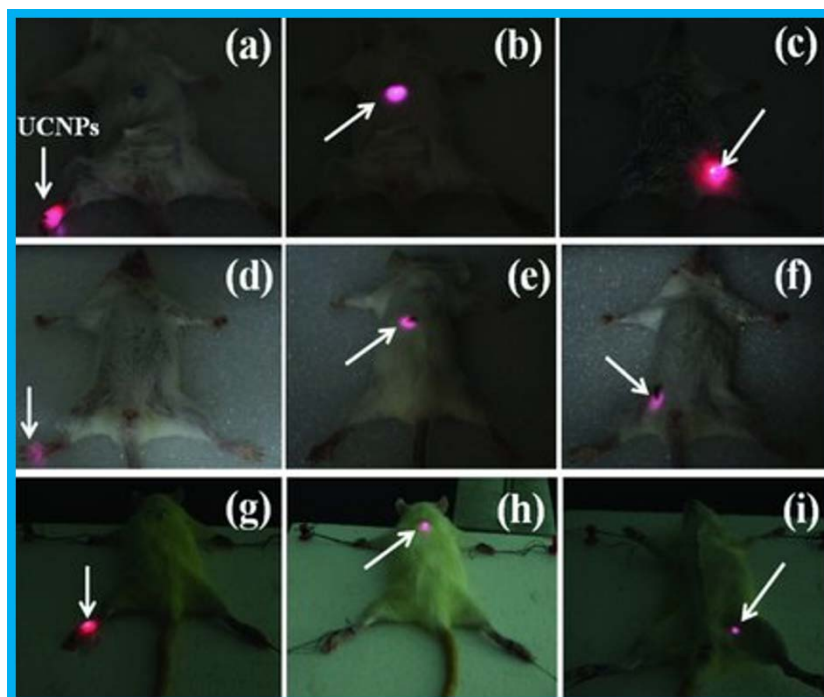


Figure 29. In vivo UCL-based animal imaging studies. PEG-UCNPs were injected into the (a, d, g) translucent foot, (b, e, h) below skin of back or (c, f, i) tight muscles of mice show effective luminescence. Images (a-c) represent Kunming mouse with 100 uL of 2.0 mg/mL PEG-UCNPs; images (d-f) represent Kunming mouse with 100 uL of 0.5mg/mL PEG-UCNPs and images (g-i) represent S. D. rat with 100 uL of 2.0 mg/mL PEG-UCNPs. Reprint with permission of [166].

cells not only exhibited normal early proliferation, but were also able to undergo osteogenic and adipogenic differentiation upon in vitro induction. Moreover, Lee's group monitored and observed the spatiotemporal distribution of UCNPs in single living HeLa cells.[163] It was confirmed that the UCNPs were internalized through endocytosis, transported by microtubule-dependent motor proteins (dyneins), accumulated at the perinuclear region, transported by another type of motor proteins (kinesins), and finally released out of the cells through exocytosis. Importantly, the non-bleaching property of Ln^{3+} -UCNPs provides potential to unveil the temporal interaction between the UCNPs and biological systems at cell level or subcellular level. However, it has been noted that non-specific endocytosis usually occurs when hydrophilic Ln^{3+} -UCNPs are exposed to cultured cells. Therefore, Ln^{3+} -UCNPs are often modified with polymers such as PEG, PEI, PAA and PVP to improve their hydrophilicity and biocompatibility for cell uptake. Importantly, targeted cellular labelling or uptake is the most commonly used method for bioimaging of Ln^{3+} -UCNPs. It requires that the Ln^{3+} -UCNPs be modified with various biological substances including peptides and antibodies for specific functions. $\text{NaGdF}_4\text{:Yb,Er}$ UCNPs modified with cyclin D-specific

peptides (can specifically target the CDK4/cyclin D complex) can cause cancer cell cycle disruption.[164] Moreover, a DNA-modified NaYF₄:18%Yb,2%Er UCNP was developed for DNA delivery and targeted binding to a breast cancer cell line MCF-7. (Figure 28)[165]

In vivo imaging. Due to their remarkable penetration depth, high signal-to-noise ratio, and low toxicity, Ln³⁺-UCNPs are quite promising biomarkers for in vivo imaging.[159] There are various biological models that have been employed for in vivo imaging studies based on Ln³⁺-UCNPs, including mice, zebrafish, and some other uncommon models (such as bacteria, *Caenorhabditis elegans*, rabbits and even plants). Most Ln³⁺-UCNPs based animal in vivo imaging studies that have been conducted to date are in rats. For example, a PEGylated manganese ion (Mn²⁺) -doped NaYF₄:Yb,Er UCNPs loaded with commonly used chemotherapeutic drug (doxorubicin, DOX) for cancer therapy. (Figure 29)[166] The results showed that DOX was effectively transported into cells by this PEG-UCNP drug delivery system. Furthermore, the as prepared PEG-UCNPs with Mn²⁺ doping not only exhibited enhanced upconversion luminescence (red emission), but also could be used as paramagnetic resonance (MR) imaging probes.[167–170] Thus, these UCNPs are promising to be utilized as multifunctional drug delivery platform for simultaneous diagnosis and therapy.

1.4.5.2 Ln³⁺-UCNPs for Drug Delivery

In past decades, the development of multifunctional Ln³⁺-UCNP-based drug delivery platforms is rapid and continually attracting intensive interest. The aim is to bridge the gap between materials science and clinical theranostics, combining disease diagnosis and therapy within a single nanocarrier. To meet this requirement, various UCNP-based nanocomposites have been developed as a drug delivery system for multifunctional upconversion fluorescence bioimaging, drug delivery, and monitoring of drugs by fluorescence imaging in real time. In this section, it mainly described recent progress in various chemical fabrication of Ln³⁺-UCNPs, with typical emphasis on their application in targeted drug release and subsequent therapy. Functional groups that are introduced for targeting processes, which can regulate the movement of the pharmaceutical cargo and release the drug at a desired region. This is significant to boost drug efficacy in CNS diseases while minimizing the side effects. Many multifunctional (upconversion luminescence/

paramagnetic and porous shell) composite materials based on Ln^{3+} have been designed for targeted and controlled drug delivery.

One of the key advantages of UCNP-based drug carriers is that UCNPs will enable tracking and efficient evaluation of drug release in real time due to their advantages of photo-stability and deep tissue penetration. A multifunctional core-shell structured nanocomposites $\text{Fe}_3\text{O}_4@\text{SiO}_2@\text{mSiO}_2@\text{NaYF}_4:\text{Yb/Er}$ loaded with ibuprofen (IBU) was fabricated to investigate the relationship between the cumulative release of IBU and the UC luminescence intensity of nanocomposites.[171] The result showed that with the increase in cumulative IBU release, luminescence intensity of nanocomposites increases as well due to a reduction in the quenching effect. Therefore, the drug release process could be monitored by the change in UC luminescence intensity.[172] There are several other Ln^{3+} -UCNPs-based nanocarriers developed for multimodal bioimaging and in vivo drug delivery. This correlation between the extent of the drug release and the UC luminescence intensity can be potentially used as a probe for monitoring the drug release actions during disease therapy. However, this strategy is limited to certain drugs whose properties can affect the luminescence of Ln^{3+} -UCNPs.

Furthermore, a key challenge for efficient drug delivery system is to selectively release the therapeutic agents at specific sites. There are two main strategies to achieve site-specific drug transport: (a) magnetic field-guided for targeted drug delivery; (b) specific molecules attached onto the surface of nanoparticles for targeted drug delivery.

Magnetic field-guided for targeted drug delivery. The magnetic-field-guided drug delivery is a convenient and attractive method for delivering therapeutic agents to the area of interest. One of the most popular nanomaterials used in this strategy is iron oxide (Fe_3O_4) due to its prominent advantages such as being biocompatible, responsive and biodegradable. There are a variety of magneto-optical multifunctional nanocarriers by integrating Ln^{3+} -UCNPs and Fe_3O_4 into a single nanocomposite for simultaneous diagnosis and therapeutic purposes.[173–176] The targeted delivery of these magnetic-sensitive particles can be selectively localized to the target regions by exposure to a strong magnetic field. For instance, dual modal optical and magnetic resonance imaging of mice reveals that by placing a magnet nearby the tumor, multifunctional nanoparticles tend to migrate toward the tumor

after intravenous injection and show high tumor accumulation, which is ~ 8 folds higher than that without magnetic targeting.[177]

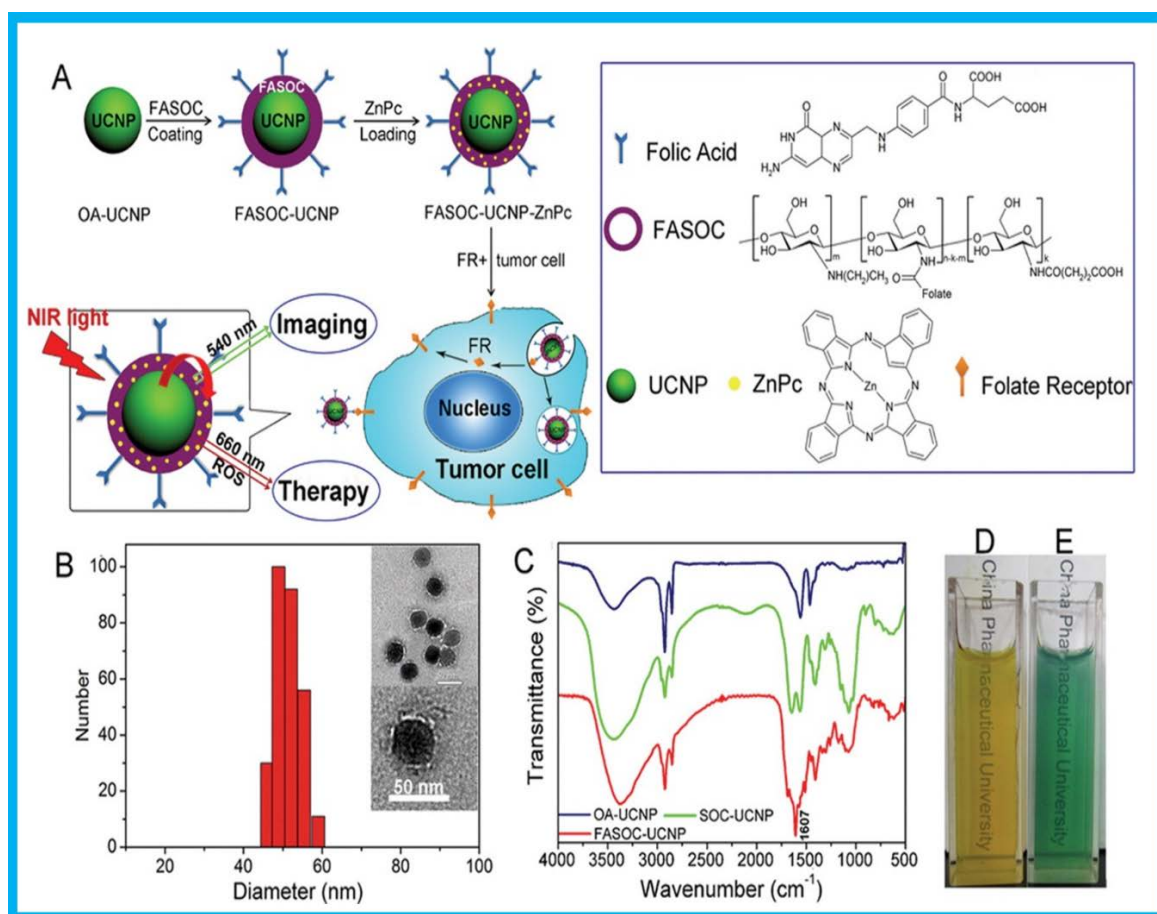


Figure 30. Preparation and characterization of FASOC-UCNP-ZnPc nanoconstruct. (A) Schematic of the fabrication of FASOC-UCNP-ZnPc nanoconstruct and folate receptor-mediated endocytosis of tumor cells; (B) particle size distribution of the prepared nanoconstruct by DLS and TEM imaging; (C) Fourier transform infrared (FTIR) spectra of OA-UCNP, SOC, and FASOC-UCNP; (D) photographs of FASOC-UCNP, and (E) ZnPc-loaded FASOC-UCNP in PBS under ambient light. Copy with permission from ref. [186].

Specific molecule utilized to targeted drug delivery. Non-invasive target-specific recognition is an attractive and popular approach for targeted drug delivery with the aid of specific targeting ligands or biomolecules (such as transferrin,[178] peptide,[178,179]FA[180–185] and TAT[177, 185]. These ligand-combined nanocarriers can be specifically recognized by the appropriate receptors on the surface of the target cells. Therefore, a receptor-mediated endocytosis pathway is used in this site-specific drug delivery strategy. Typically, folic acid (FA) is an attractive agent for targeted anticancer drug release due to the overexpressed folate receptors (FR) in numerous types of human cancer

cells but absent in normal cells, including cancers of the ovary, lung, breast, kidney, brain and colon. For example, Gu's group developed a multifunctional nanoconstruct, FA-chitosan-coated UCNPs (FASOCUCNPs) loaded with photosensitizer zinc (II) phthalocyanine (ZnPc) as carriers for in vivo targeted deep-tissue imaging and photodynamic therapy. (Figure 31)[186] UCNPs in this nanocomposite not only transfer near-infrared (NIR) light to visible light, but also transfer energy to ZnPc. The result showed that the tumor-selectivity of the nanoconstructs to cancer cells that overexpressed folate receptor was enhanced. Furthermore, reactive oxygen species (ROS) generation in cancer cells under a 1cm tissue was higher upon excitation of UCNPs with the 980 nm light than that with 660 nm irradiation. Generally, this strategy for Ln^{3+} -UCNPs based on specific ligands or biological molecules has the capability of selective recognition and imaging of cancer cells, controllable and effective activation of the photosensitizer, and increased therapeutic effect.

1.5 Conclusions and Outlook

In summary, Ln^{3+} -UCNPs have attracted much interest for biomedical applications due to their high resistance to photobleaching, negligible photoblinking, cross-talked emission, low signal-to-noise ratio and deeper tissue penetration. Furthermore, their tunable size, morphology and surface chemistry support in vivo and in vitro studies. In addition, Ln^{3+} -UCNPs can serve as multifunctional platform for bioapplication through doping and surface functionalization. The recent progress of bioimaging and therapeutic applications of Ln^{3+} -UCNPs have been discussed in this introduction. Ln^{3+} -UCNPs exhibit great promise for theranostics as they provide numerous advantages over conventional biomarkers due to their unique optical properties and biocompatibility with the aid of intrinsic merits of being a nanoscale substance. However, there are some important issues that need to be addressed to improve their future biomedical applications:

(a) Higher luminescence efficiency is required. The upconversion emission of Ln^{3+} is indeed high, but their relatively low quantum yield hinders the wide application of Ln^{3+} -UCNPs, such as imaging to tissue depth of more than 2cm.

(b) Improving the safety of bioimaging and therapy. Most UCNPs-based bioimaging and therapy investigations to date have utilized 980nm laser as the excitation source, which can

easily lead to an overheating effect in the tissue which can be damaging. This challenge can be overcome by replacing 980nm to 808nm NIR light for triggering Ln^{3+} -based UCNPs, minimizing tissue absorption and therefore heat generation.

(c) Monochromatic emissions. Ln^{3+} -based UCNPs are promising for multicolor imaging and multiplexed detections due to their sharp emission bands. Currently, the protocols for encoding samples utilize the differences in their upconversion emission ratios. Nevertheless, the emission ratio depends on various factors such as the surface properties of the UCNPs and the solvents involved. UCNPs with monochromatic emissions may further afford more convenient encoding, but there is lack of general synthetic approaches. Meanwhile, minimization of deleterious cross-deleterious must be considered when investigate tailoring the local coordination structure and the incorporation of the proper activators.

(d) Nanotoxicity of Ln^{3+} -based UCNPs. Nanotoxicity assessments of lanthanide UCNPs with tunable sizes, various surface coating species and different morphologies are essential before their further application. Typically, the development of smaller biocompatible Ln^{3+} -based UCNPs is needed to overcome nonspecific organ uptake and monocyte/macrophage system scavenging. Moreover, aggregation of Ln^{3+} -based UCNPs in biological media is a major challenge (as it is for most nanoparticles) and the interaction between lanthanide UCNPs and proteins in the blood is still poorly understood. Importantly, a safe dose of Ln^{3+} -based UCNPs is urgently needed to lay the foundation for future theranostic applications.

1.6 Thesis Aims

The aim of this study was to demonstrate a new generation of upconversion nanoparticles suitable for tracking the biological process (such as cellular uptake or BBB penetration) how the nanoparticles are selected to pass the BBB. The ultimate aim of this project is to discovery and control the key biophysical characteristic (like surface engineering, shape, aspect ratios) to produce a library of specific nanoparticles for nanoscale drug delivery. Specifically, this study has three objectives:

1. To synthesize and functionalise the UCNPs with a variety of surface modification to improve their hydrophobicity and biocompatibility, ultimately identify the preferable surfaces for biological and therapeutic applications. (achieved in Chapter 3)

These surface modified nanoparticles should avoid the aggregation of nanoparticles and survive in the complicated body fluid. We will demonstrate the optimum surfaces for nanoparticles internalization by brain endothelial cells.

2. To synthesize and identify the optimal nanoparticles with shape range that can efficiently pass the BBB. (studied in Chapter 4)

Identification of the desired morphology that can rapidly achieve BBB penetration is particularly significant, since the larger penetrative nanoparticles tend to be more uniform, longer-lasting with stronger concentrations and specificity for delivery of drugs into the brain.

3. To investigate whether the aspect ratios (ARs) of rod-shaped particles alters their biocompatibility and cellular uptake. (investigated in Chapter 5)

From the study at previous chapters, it was confirmed that rod-shaped UCNPs coated with transferrin tend to be the superior UCNPs for delivery into the brain. Typically, aspect ratios (ARs) seems a likely character profoundly influence the biocompatibility and cellular uptake of rod-shaped nanoparticles.

1.7 Reference

- [1] S. Sidney, C.P. Quesenberry, M.G. Jaffe, M. Sorel, M.N. Nguyen-Huynh, L.H. Kushi, A.S. Go, J.S. Rana, Recent Trends in Cardiovascular Mortality in the United States and Public Health Goals, *JAMA Cardiol.* 1 (2016) 594. doi:10.1001/jamacardio.2016.1326.
- [2] S. National Center for Health, Table A-3. Cancer among adults aged 18 and over, by selected characteristics: United States, 2014, *Heal. United States, 2014 With Spec. Featur. Adults Aged 55-64.* 6 (2015) 1–9. doi:papers3://publication/uuid/9CD98A3C-7533-4BCF-8A11-74733653C53D.
- [3] A. Association, 2013 Alzheimer's disease facts and figures, *Alzheimer's Dement.* 9 (2013) 208–245. doi:10.1016/j.jalz.2013.02.003.
- [4] K.K. Jain, Nanobiotechnology-based drug delivery to the central nervous system, *Neurodegener. Dis.* 4 (2007) 287–291. doi:10.1159/000101884.
- [5] S. Tiwari, M. Amiji, A Review of Nanocarrier-Based CNS Delivery Systems, *Curr.*

- Drug Deliv. 3 (2006) 219–232. doi:10.2174/156720106776359230.
- [6] D. Yang, P. Ma, Z. Hou, Z. Cheng, C. Li, J. Lin, Current advances in lanthanide ion (Ln(3+))-based upconversion nanomaterials for drug delivery., 2014. doi:10.1039/c4cs00155a.
- [7] N.M. Idris, M.K. Gnanasammandhan, J. Zhang, P.C. Ho, R. Mahendran, Y. Zhang, In vivo photodynamic therapy using upconversion nanoparticles as remote-controlled nanotransducers, *Nat. Med.* 18 (2012) 1580–1585. doi:10.1038/nm.2933.
- [8] Y. Yang, Q. Shao, R. Deng, C. Wang, X. Teng, K. Cheng, Z. Cheng, L. Huang, Z. Liu, X. Liu, B. Xing, In vitro and in vivo uncaging and bioluminescence imaging by using photocaged upconversion nanoparticles, *Angew. Chemie - Int. Ed.* 51 (2012) 3125–3129. doi:10.1002/anie.201107919.
- [9] X. Xie, N. Gao, R. Deng, Q. Sun, Q. Xu, X. Liu, Mechanistic investigation of photon upconversion in Nd(3+)-sensitized core-shell nanoparticles., *J. Am. Chem. Soc.* 135 (2013) 12608–11. doi:10.1021/ja4075002.
- [10] B. Kerrey, C. Cassel, S.E. Hyman, M. McClellan, S.D.O. Connor, Alzheimer ' s Strategic Plan : The RepoRT of The Alzheimer ' s sTudy GRoup, *Natl. Alzheimer's Strateg. Plan.* (2011) 1–52.
- [11] M.D. Hurd, P. Martorell, A. Delavande, K.J. Mullen, K.M. Langa, Monetary Costs of Dementia in the United States, *N. Engl. J. Med.* 368 (2013) 1326–1334. doi:10.1056/NEJMSa1204629.
- [12] W.M. Pardridge, Why is the global CNS pharmaceutical market so under-penetrated?, *Drug Discov. Today.* 7 (2002) 5–7. doi:10.1016/S1359-6446(01)02082-7.
- [13] S. Wohlfart, S. Gelperina, J. Kreuter, Transport of drugs across the blood-brain barrier by nanoparticles, *J. Control. Release.* 161 (2012) 264–273. doi:10.1016/j.jconrel.2011.08.017.
- [14] B. Engelhardt, Development of the blood-brain barrier, *Cell Tissue Res.* 314 (2003) 119–129. doi:10.1007/s00441-003-0751-z.
- [15] D.J. Begley, M.W. Brightman, Structural and functional aspects of the blood-brain barrier, in: *Pept. Transp. Deliv. into Cent. Nerv. Syst.*, 2003: pp. 39–78. doi:10.1007/978-3-0348-8049-7_2.
- [16] N.J. Abbott, Astrocyte-endothelial interactions and blood-brain barrier permeability, *J. Anat.* 200 (2002) 629–638. doi:10.1046/j.1469-7580.2002.00064.x.
- [17] B.T. Hawkins, *The Blood-Brain Barrier/Neurovascular Unit in Health and Disease*,

- Pharmacol. Rev. 57 (2005) 173–185. doi:10.1124/pr.57.2.4.
- [18] U. Kniesel, H. Wolburg, Tight junctions of the blood-brain barrier., *Cell. Mol. Neurobiol.* 20 (2000) 57–76. doi:10.1023/A:1006995910836.
- [19] N.J. Abbott, Evidence for bulk flow of brain interstitial fluid: Significance for physiology and pathology, *Neurochem. Int.* 45 (2004) 545–552. doi:10.1016/j.neuint.2003.11.006.
- [20] K.K. Jain, Nanobiotechnology-based strategies for crossing the blood-brain barrier., *Nanomedicine (Lond).* 7 (2012) 1225–33. doi:10.2217/nnm.12.86.
- [21] N.J. Abbott, L. Rönnbäck, E. Hansson, Astrocyte–endothelial interactions at the blood–brain barrier, *Nat. Rev. Neurosci.* 7 (2006) 41–53. doi:10.1038/nrn1824.
- [22] Y. Igarashi, H. Utsumi, H. Chiba, Y. Yamada-Sasamori, H. Tobioka, Y. Kamimura, K. Furuuchi, Y. Kokai, T. Nakagawa, M. Mori, N. Sawada, Glial cell line-derived neurotrophic factor induces barrier function of endothelial cells forming the blood-brain barrier., *Biochem. Biophys. Res. Commun.* 261 (1999) 108–12. doi:10.1006/bbrc.1999.0992.
- [23] H. Mi, H. Haeberle, B. a Barres, Induction of astrocyte differentiation by endothelial cells., *J. Neurosci.* 21 (2001) 1538–1547. doi:21/5/1538 [pii].
- [24] S.-W. Lee, W.J. Kim, Y.K. Choi, H.S. Song, M.J. Son, I.H. Gelman, Y.-J. Kim, K.-W. Kim, SSeCKS regulates angiogenesis and tight junction formation in blood-brain barrier, *Nat. Med.* 9 (2003) 900–906. doi:10.1038/nm889.
- [25] R.A. Kroll, E.A. Neuwelt, Outwitting the blood-brain barrier for therapeutic purposes: Osmotic opening and other means, *Neurosurgery.* 42 (1998) 1083–1100. doi:10.1097/00006123-199805000-00082.
- [26] K. Matsukado, T. Inamura, S. Nakano, M. Fukui, R.T. Bartus, K.L. Black, Enhanced tumor uptake of carboplatin and survival in glioma-bearing rats by intracarotid infusion of bradykinin analog, RMP-7, *Neurosurgery.* 39 (1996) 125–134. doi:10.1097/00006123-199607000-00025.
- [27] G. Miller, DRUG TARGETING: Breaking Down Barriers, *Science* (80-.). 297 (2002) 1116–1118. doi:10.1126/science.297.5584.1116.
- [28] P. Blasi, S. Giovagnoli, A. Schoubben, M. Ricci, C. Rossi, Solid lipid nanoparticles for targeted brain drug delivery, *Adv. Drug Deliv. Rev.* 59 (2007) 454–477. doi:10.1016/j.addr.2007.04.011.
- [29] S.J. Madsen, H. Hirschberg, Site-specific opening of the blood-brain barrier, *J.*

- Biophotonics. 3 (2010) 356–367. doi:10.1002/jbio.200900095.
- [30] M.M. Patel, B.R. Goyal, S. V. Bhadada, J.S. Bhatt, A.F. Amin, Getting into the brain: Approaches to enhance brain drug delivery, *CNS Drugs*. 23 (2009) 35–58. doi:10.2165/0023210-200923010-00003.
- [31] I. Brasnjevic, H.W.M. Steinbusch, C. Schmitz, P. Martinez-Martinez, Delivery of peptide and protein drugs over the blood-brain barrier, *Prog. Neurobiol.* 87 (2009) 212–251. doi:10.1016/j.pneurobio.2008.12.002.
- [32] B.C. Masi, B.M. Tyler, H. Bow, R.T. Wicks, Y. Xue, H. Brem, R. Langer, M.J. Cima, Intracranial MEMS based temozolomide delivery in a 9L rat gliosarcoma model, *Biomaterials*. 33 (2012) 5768–5775. doi:10.1016/j.biomaterials.2012.04.048.
- [33] D.J. Begley, ABC transporters and the blood-brain barrier., *Curr. Pharm. Des.* 10 (2004) 1295–312. doi:10.2174/1381612043384844.
- [34] A. Rice, Y. Liu, M. Lou Michaelis, R.H. Himes, G.I. Georg, K.L. Audus, Chemical modification of paclitaxel (taxol) reduces P-glycoprotein interactions and increases permeation across the blood-brain barrier in vitro and in situ, *J. Med. Chem.* 48 (2005) 832–838. doi:10.1021/jm040114b.
- [35] W.M. Pardridge, Molecular Trojan horses for blood-brain barrier drug delivery, *Curr. Opin. Pharmacol.* 6 (2006) 494–500. doi:10.1016/j.coph.2006.06.001.
- [36] K.A. Witt, T.J. Gillespie, J.D. Huber, R.D. Egleton, T.P. Davis, Peptide drug modifications to enhance bioavailability and blood-brain barrier permeability, *Peptides*. 22 (2001) 2329–2343. doi:10.1016/S0196-9781(01)00537-X.
- [37] P. Vlieghe, M. Khrestchatisky, Medicinal Chemistry Based Approaches and Nanotechnology-Based Systems to Improve CNS Drug Targeting and Delivery, *Med. Res. Rev.* 33 (2013) 457–516. doi:10.1002/med.21252.
- [38] D.S. Kern, K.N. Maclean, H. Jiang, E.Y. Synder, J.R. Sladek, K.B. Bjugstad, Neural stem cells reduce hippocampal tau and reelin accumulation in aged Ts65Dn down syndrome mice, *Cell Transplant.* 20 (2011) 371–379. doi:10.3727/096368910X528085.
- [39] H. Taki, T. Kanazawa, F. Akiyama, Y. Takashima, Intranasal Delivery of Camptothecin-Loaded Tat-Modified, *Pharmaceuticals*. 5 (2012) 1092–1102. doi:10.3390/ph5101092.
- [40] D. Liu, B. Lin, W. Shao, Z. Zhu, T. Ji, C. Yang, In Vitro and in Vivo Studies on the Transport of PEGylated Silica Nanoparticles across the Blood–Brain Barrier, *ACS*

- Appl. Mater. Interfaces. 6 (2014) 2131–2136. doi:10.1021/am405219u.
- [41] X. Gao, J. Qian, S. Zheng, Y. Changyi, J. Zhang, S. Ju, J. Zhu, C. Li, Overcoming the blood-brain barrier for delivering drugs into the brain by using adenosine receptor nanoagonist, *ACS Nano*. 8 (2014) 3678–3689. doi:10.1021/nn5003375.
- [42] Y.C. Kuo, C.Y. Shih-Huang, Solid lipid nanoparticles carrying chemotherapeutic drug across the blood-brain barrier through insulin receptor-mediated pathway, *J. Drug Target*. 21 (2013) 730–738. doi:10.3109/1061186X.2013.812094.
- [43] S. Ruan, X. Cao, X. Cun, G. Hu, Y. Zhou, Y. Zhang, L. Lu, Q. He, H. Gao, Matrix metalloproteinase-sensitive size-shrinkable nanoparticles for deep tumor penetration and pH triggered doxorubicin release, *Biomaterials*. 60 (2015) 100–110. doi:10.1016/j.biomaterials.2015.05.006.
- [44] H. Xin, X. Jiang, J. Gu, X. Sha, L. Chen, K. Law, Y. Chen, X. Wang, Y. Jiang, X. Fang, Angiopep-conjugated poly(ethylene glycol)-co-poly(ϵ -caprolactone) nanoparticles as dual-targeting drug delivery system for brain glioma, *Biomaterials*. 32 (2011) 4293–4305. doi:10.1016/j.biomaterials.2011.02.044.
- [45] H. Yan, L. Wang, J. Wang, X. Weng, H. Lei, X. Wang, L. Jiang, J. Zhu, W. Lu, X. Wei, C. Li, Two-order targeted brain tumor imaging by using an optical/paramagnetic nanoprobe across the blood brain barrier, *ACS Nano*. 6 (2012) 410–420. doi:10.1021/nn203749v.
- [46] C. Saraiva, C. Praça, R. Ferreira, T. Santos, L. Ferreira, L. Bernardino, Nanoparticle-mediated brain drug delivery: Overcoming blood-brain barrier to treat neurodegenerative diseases, *J. Control. Release*. 235 (2016) 34–47. doi:10.1016/j.jconrel.2016.05.044.
- [47] J. Kreuter, Drug delivery to the central nervous system by polymeric nanoparticles: What do we know?, *Adv. Drug Deliv. Rev.* 71 (2014) 2–14. doi:10.1016/j.addr.2013.08.008.
- [48] X. Duan, Y. Li, Physicochemical characteristics of nanoparticles affect circulation, biodistribution, cellular internalization, and trafficking, *Small*. 9 (2013) 1521–1532. doi:10.1002/sml.201201390.
- [49] F. Alexis, E. Pridgen, L.K. Molnar, O.C. Farokhzad, Factors affecting the clearance and biodistribution of polymeric nanoparticles, in: *Mol. Pharm.*, 2008: pp. 505–515. doi:10.1021/mp800051m.
- [50] A. Albanese, P.S. Tang, W.C.W. Chan, The effect of nanoparticle size, shape, and

- surface chemistry on biological systems., *Annu. Rev. Biomed. Eng.* 14 (2012) 1–16. doi:10.1146/annurev-bioeng-071811-150124.
- [51] M.L. Schipper, G. Iyer, A.L. Koh, Z. Cheng, Y. Ebenstein, A. Aharoni, S. Keren, L.A. Bentolila, J. Li, J. Rao, X. Chen, U. Banin, A.M. Wu, R. Sinclair, S. Weiss, S.S. Gambhir, Particle size, surface coating, and PEGylation influence the biodistribution of quantum dots in living mice, *Small*. 5 (2009) 126–134. doi:10.1002/smll.200800003.
- [52] H. Hillaireau, P. Couvreur, Nanocarriers' entry into the cell: Relevance to drug delivery, *Cell. Mol. Life Sci.* 66 (2009) 2873–2896. doi:10.1007/s00018-009-0053-z.
- [53] K. Yin Win, S.-S. Feng, Effects of particle size and surface coating on cellular uptake of polymeric nanoparticles for oral delivery of anticancer drugs, *Biomaterials*. 26 (2005) 2713–2722. doi:10.1016/j.biomaterials.2004.07.050.
- [54] E. Fröhlich, The role of surface charge in cellular uptake and cytotoxicity of medical nanoparticles, *Int. J. Nanomedicine*. 7 (2012) 5577–5591. doi:10.2147/IJN.S36111.
- [55] A. Lankoff, M. Arabski, A. Wegierek-Ciuk, M. Kruszewski, H. Lisowska, A. Banasik-Nowak, K. Rozga-Wijas, M. Wojewodzka, S. Slomkowski, Effect of surface modification of silica nanoparticles on toxicity and cellular uptake by human peripheral blood lymphocytes in vitro, *Nanotoxicology*. 7 (2013) 235–250. doi:10.3109/17435390.2011.649796.
- [56] A. Verma, F. Stellacci, Effect of surface properties on nanoparticle-cell interactions, *Small*. 6 (2010) 12–21. doi:10.1002/smll.200901158.
- [57] Z.G. Yue, W. Wei, P.P. Lv, H. Yue, L.Y. Wang, Z.G. Su, G.H. Ma, Surface charge affects cellular uptake and intracellular trafficking of chitosan-based nanoparticles, *Biomacromolecules*. 12 (2011) 2440–2446. doi:10.1021/bm101482r.
- [58] B.D. Chithrani, W.C.W. Chan, Elucidating the mechanism of cellular uptake and removal of protein-coated gold nanoparticles of different sizes and shapes, *Nano Lett.* 7 (2007) 1542–1550. doi:10.1021/nl070363y.
- [59] X. Huang, X. Teng, D. Chen, F. Tang, J. He, The effect of the shape of mesoporous silica nanoparticles on cellular uptake and cell function, *Biomaterials*. 31 (2010) 438–448. doi:10.1016/j.biomaterials.2009.09.060.
- [60] V. Ayala, A.P. Herrera, M. Latorre-Esteves, M. Torres-Lugo, C. Rinaldi, Effect of surface charge on the colloidal stability and in vitro uptake of carboxymethyl dextran-coated iron oxide nanoparticles, *J. Nanoparticle Res.* 15 (2013). doi:10.1007/s11051-

013-1874-0.

- [61] N.L. Rosi, Oligonucleotide-Modified Gold Nanoparticles for Intracellular Gene Regulation, *Science* (80-.). 312 (2006) 1027–1030. doi:10.1126/science.1125559.
- [62] D.A. Giljohann, D.S. Seferos, P.C. Patel, J.E. Millstone, N.L. Rosi, C.A. Mirkin, Oligonucleotide loading determines cellular uptake of DNA-modified gold nanoparticles, *Nano Lett.* 7 (2007) 3818–3821. doi:10.1021/nl072471q.
- [63] J. Voigt, J. Christensen, V.P. Shastri, Differential uptake of nanoparticles by endothelial cells through polyelectrolytes with affinity for caveolae, *Proc. Natl. Acad. Sci.* 111 (2014) 2942–2947. doi:10.1073/pnas.1322356111.
- [64] H. Takahashi, T. Niidome, T. Kawano, S. Yamada, Y. Niidome, Surface modification of gold nanorods using layer-by-layer technique for cellular uptake, *J. Nanoparticle Res.* 10 (2008) 221–228. doi:10.1007/s11051-007-9227-5.
- [65] M.H. El-Shabouri, Positively charged nanoparticles for improving the oral bioavailability of cyclosporin-A, *Int. J. Pharm.* 249 (2002) 101–108. doi:10.1016/S0378-5173(02)00461-1.
- [66] J. Yu, H. Zhao, L. Ye, H. Yang, S. Ku, N. Yang, N. Xiao, Effect of surface functionality of magnetic silica nanoparticles on the cellular uptake by glioma cells in vitro, *J. Mater. Chem.* 19 (2009) 1265. doi:10.1039/b816157g.
- [67] G. Storm, S.O. Belliot, T. Daemen, D.D. Lasic, Surface modification of nanoparticles to oppose uptake by the mononuclear phagocyte system, *Adv. Drug Deliv. Rev.* 17 (1995) 31–48. doi:10.1016/0169-409X(95)00039-A.
- [68] J. V Jokerst, T. Lobovkina, R.N. Zare, S.S. Gambhir, Nanoparticle PEGylation for imaging and therapy, *Nanomedicine.* 6 (2011) 715–728. doi:10.2217/nmm.11.19.
- [69] G. Prencipe, S.M. Tabakman, K. Welsher, Z. Liu, A.P. Goodwin, L. Zhang, J. Henry, H. Dai, PEG branched polymer for functionalization of nanomaterials with ultralong blood circulation, *J. Am. Chem. Soc.* 131 (2009) 4783–4787. doi:10.1021/ja809086q.
- [70] G. Von Maltzahn, J.H. Park, A. Agrawal, N.K. Bandaru, S.K. Das, M.J. Sailor, S.N. Bhatia, Computationally guided photothermal tumor therapy using long-circulating gold nanorod antennas, *Cancer Res.* 69 (2009) 3892–3900. doi:10.1158/0008-5472.CAN-08-4242.
- [71] X. He, H. Nie, K. Wang, W. Tan, X. Wu, P. Zhang, In vivo study of biodistribution and urinary excretion of surface-modified silica nanoparticles, *Anal. Chem.* 80 (2008) 9597–9603. doi:10.1021/ac801882g.

- [72] T.J. Daou, L. Li, P. Reiss, V. Josserand, I. Texier, Effect of poly(ethylene glycol) length on the in vivo behavior of coated quantum dots, *Langmuir*. 25 (2009) 3040–3044. doi:10.1021/la8035083.
- [73] Y. Sadzuka, A. Nakade, R. Hirama, A. Miyagishima, Y. Nozawa, S. Hirota, T. Sonobe, Effects of mixed polyethyleneglycol modification on fixed aqueous layer thickness and antitumor activity of doxorubicin containing liposome, *Int. J. Pharm.* 238 (2002) 171–180. doi:10.1016/S0378-5173(02)00075-3.
- [74] F. Lu, S.H. Wu, Y. Hung, C.Y. Mou, Size effect on cell uptake in well-suspended, uniform mesoporous silica nanoparticles, *Small*. 5 (2009) 1408–1413. doi:10.1002/smll.200900005.
- [75] D.P.K. Lankveld, A.G. Oomen, P. Krystek, A. Neigh, A. Troost - de Jong, C.W. Noorlander, J.C.H. Van Eijkeren, R.E. Geertsma, W.H. De Jong, The kinetics of the tissue distribution of silver nanoparticles of different sizes, *Biomaterials*. 31 (2010) 8350–8361. doi:10.1016/j.biomaterials.2010.07.045.
- [76] F. Osaki, T. Kanamori, S. Sando, T. Sera, Y. Aoyama, A quantum dot conjugated sugar ball and its cellular uptake. On the size effects of endocytosis in the subviral region, *J. Am. Chem. Soc.* 126 (2004) 6520–6521. doi:10.1021/ja048792a.
- [77] A. Lankoff, W.J. Sandberg, A. Wegierek-Ciuk, H. Lisowska, M. Refsnes, B. Sartowska, P.E. Schwarze, S. Meczynska-Wielgosz, M. Wojewodzka, M. Kruszewski, The effect of agglomeration state of silver and titanium dioxide nanoparticles on cellular response of HepG2, A549 and THP-1 cells, *Toxicol. Lett.* 208 (2012) 197–213. doi:10.1016/j.toxlet.2011.11.006.
- [78] H.S. Choi, W. Liu, P. Misra, E. Tanaka, J.P. Zimmer, B. Itty Ipe, M.G. Bawendi, J. V Frangioni, Renal clearance of nanoparticles, *Nat. Biotechnol.* 25 (2007) 1165–1170. doi:10.1038/nbt1340.Renal.
- [79] C. Foged, B. Brodin, S. Frokjaer, A. Sundblad, Particle size and surface charge affect particle uptake by human dendritic cells in an in vitro model, in: *Int. J. Pharm.*, 2005: pp. 315–322. doi:10.1016/j.ijpharm.2005.03.035.
- [80] J. Huang, L. Bu, J. Xie, K. Chen, Z. Cheng, X. Li, X. Chen, Effects of nanoparticle size on cellular uptake and liver MRI with polyvinylpyrrolidone-coated iron oxide nanoparticles, *ACS Nano*. 4 (2010) 7151–7160. doi:10.1021/nn101643u.
- [81] S. Zhang, J. Li, G. Lykotrafitis, G. Bao, S. Suresh, Size-dependent endocytosis of nanoparticles, *Adv. Mater.* 21 (2009) 419–424. doi:10.1002/adma.200801393.

- [82] W. Jiang, B.Y.S. Kim, J.T. Rutka, W.C.W. Chan, Nanoparticle-mediated cellular response is size-dependent, *Nat. Nanotechnol.* 3 (2008) 145–150. doi:10.1038/nnano.2008.30.
- [83] B.D. Chithrani, A.A. Ghazani, W.C.W. Chan, Determining the size and shape dependence of gold nanoparticle uptake into mammalian cells, *Nano Lett.* 6 (2006) 662–668. doi:10.1021/nl052396o.
- [84] J. REJMAN, V. OBERLE, I.S. ZUHORN, D. HOEKSTRA, Size-dependent internalization of particles via the pathways of clathrin- and caveolae-mediated endocytosis, *Biochem. J.* 377 (2004) 159–169. doi:10.1042/bj20031253.
- [85] N. Doshi, A.S. Zahr, S. Bhaskar, J. Lahann, S. Mitragotri, Red blood cell-mimicking synthetic biomaterial particles, *Proc. Natl. Acad. Sci.* 106 (2009) 21495–21499. doi:10.1073/pnas.0907127106.
- [86] Y. Geng, P. Dalhaimer, S. Cai, R. Tsai, M. Tewari, T. Minko, D.E. Discher, Shape effects of filaments versus spherical particles in flow and drug delivery, *Nat. Nanotechnol.* 2 (2007) 249–255. doi:10.1038/nnano.2007.70.
- [87] J.H. Park, G. Von Maltzahn, E. Ruoslahti, S.N. Bhatia, M.J. Sailor, Micellar hybrid nanoparticles for simultaneous magnetofluorescent imaging and drug delivery, *Angew. Chemie - Int. Ed.* 47 (2008) 7284–7288. doi:10.1002/anie.200801810.
- [88] S. Muro, C. Garnacho, J.A. Champion, J. Leferovich, C. Gajewski, E.H. Schuchman, S. Mitragotri, V.R. Muzykantov, Control of Endothelial Targeting and Intracellular Delivery of Therapeutic Enzymes by Modulating the Size and Shape of ICAM-1-targeted Carriers, *Mol. Ther.* 16 (2008) 1450–1458. doi:10.1038/mt.2008.127.
- [89] G. Sharma, D.T. Valenta, Y. Altman, S. Harvey, H. Xie, S. Mitragotri, J.W. Smith, Polymer particle shape independently influences binding and internalization by macrophages, *J. Control. Release.* 147 (2010) 408–412. doi:10.1016/j.jconrel.2010.07.116.
- [90] J.A. Champion, S. Mitragotri, Role of target geometry in phagocytosis, *Proc. Natl. Acad. Sci.* 103 (2006) 4930–4934. doi:10.1073/pnas.0600997103.
- [91] R.A. Petros, J.M. DeSimone, Strategies in the design of nanoparticles for therapeutic applications, *Nat. Rev. Drug Discov.* 9 (2010) 615–627. doi:10.1038/nrd2591.
- [92] P. Kolhar, A.C. Anselmo, V. Gupta, K. Pant, B. Prabhakarapandian, E. Ruoslahti, S. Mitragotri, Using shape effects to target antibody-coated nanoparticles to lung and brain endothelium, *Proc. Natl. Acad. Sci.* 110 (2013) 10753–10758.

- doi:10.1073/pnas.1308345110.
- [93] R. Agarwal, V. Singh, P. Journey, L. Shi, S. V. Sreenivasan, K. Roy, Mammalian cells preferentially internalize hydrogel nanodiscs over nanorods and use shape-specific uptake mechanisms, *Proc. Natl. Acad. Sci.* 110 (2013) 17247–17252. doi:10.1073/pnas.1305000110.
- [94] X. Huang, X. Teng, D. Chen, F. Tang, J. He, The effect of the shape of mesoporous silica nanoparticles on cellular uptake and cell function, *Biomaterials*. 31 (2010) 438–448. doi:10.1016/j.biomaterials.2009.09.060.
- [95] S.E.A. Gratton, P.A. Ropp, P.D. Pohlhaus, J.C. Luft, V.J. Madden, M.E. Napier, J.M. DeSimone, The effect of particle design on cellular internalization pathways, *Proc. Natl. Acad. Sci.* 105 (2008) 11613–11618. doi:10.1073/pnas.0801763105.
- [96] K.C.L. Black, Y. Wang, H.P. Luehmann, X. Cai, W. Xing, B. Pang, Y. Zhao, C.S. Cutler, L. V. Wang, Y. Liu, Y. Xia, Radioactive ^{198}Au -doped nanostructures with different shapes for in vivo analyses of their biodistribution, tumor uptake, and intratumoral distribution, *ACS Nano*. 8 (2014) 4385–4394. doi:10.1021/nn406258m.
- [97] W.H. Reino, *Letters, J. Chem. Educ.* 29 (1952) 581. doi:10.1021/ed029p581.2.
- [98] M.R. Macdonald, J.E. Bates, J.W. Ziller, F. Furche, W.J. Evans, Completing the series of +2 ions for the lanthanide elements: Synthesis of molecular complexes of Pr^{2+} , Gd^{2+} , Tb^{2+} , and Lu^{2+} , *J. Am. Chem. Soc.* 135 (2013) 9857–9868. doi:10.1021/ja403753j.
- [99] J.-C.G. Bünzli, C. Piguet, Taking advantage of luminescent lanthanide ions, *Chem. Soc. Rev.* 34 (2005) 1048. doi:10.1039/b406082m.
- [100] J.C.G. Bünzli, S. Comby, A.S. Chauvin, C.D.B. Vandevyver, New Opportunities for Lanthanide Luminescence, *J. Rare Earths*. 25 (2007) 257–274. doi:10.1016/S1002-0721(07)60420-7.
- [101] S. V. Eliseeva, J.-C.G. Bünzli, Lanthanide luminescence for functional materials and bio-sciences, *Chem. Soc. Rev.* 39 (2010) 189–227. doi:10.1039/B905604C.
- [102] K. Binnemans, Lanthanide-based luminescent hybrid materials, *Chem. Rev.* 109 (2009) 4283–4374. doi:10.1021/cr8003983.
- [103] Y. Liu, S. Zhou, D. Tu, Z. Chen, M. Huang, H. Zhu, E. Ma, X. Chen, Amine-functionalized lanthanide-doped zirconia nanoparticles: Optical spectroscopy, time-resolved fluorescence resonance energy transfer biodetection, and targeted imaging, *J. Am. Chem. Soc.* 134 (2012) 15083–15090. doi:10.1021/ja306066a.

- [104] J. Shen, L.-D. Sun, C.-H. Yan, Luminescent rare earth nanomaterials for bioprobe applications, *Dalt. Trans.* (2008) 5687. doi:10.1039/b805306e.
- [105] N.M. Idris, M.K.G. Jayakumar, A. Bansal, Y. Zhang, Upconversion nanoparticles as versatile light nanotransducers for photoactivation applications, *Chem. Soc. Rev.* 44 (2015) 1449–1478. doi:10.1039/C4CS00158C.
- [106] X. Huang, S. Han, W. Huang, X. Liu, Enhancing solar cell efficiency: the search for luminescent materials as spectral converters, *Chem. Soc. Rev.* 42 (2013) 173–201. doi:10.1039/C2CS35288E.
- [107] F. Auzel, Upconversion and Anti-Stokes Processes with f and d Ions in Solids, *Chem. Rev.* 104 (2004) 139–173. doi:10.1021/cr020357g.
- [108] H. Dong, S.R. Du, X.Y. Zheng, G.M. Lyu, L.D. Sun, L.D. Li, P.Z. Zhang, C. Zhang, C.H. Yan, Lanthanide Nanoparticles: From Design toward Bioimaging and Therapy, *Chem. Rev.* 115 (2015) 10725–10815. doi:10.1021/acs.chemrev.5b00091.
- [109] F. Wang, R. Deng, J. Wang, Q. Wang, Y. Han, H. Zhu, X. Chen, X. Liu, Tuning upconversion through energy migration in core–shell nanoparticles, *Nat. Mater.* 10 (2011) 968–973. doi:10.1038/nmat3149.
- [110] S. Wu, G. Han, D.J. Milliron, S. Aloni, V. Altoe, D. V Talapin, B.E. Cohen, Non-blinking and photostable upconverted luminescence from single lanthanide- doped nanocrystals, *Proc. Natl. Acad. Sci. U. S. A.* 106 (2009) 1–5. doi:10.1073/pnas.0904792106.
- [111] A. Stepuk, D. Mohn, R.N. Grass, M. Zehnder, K.W. Krämer, F. Pellé, A. Ferrier, W.J. Stark, Use of NIR light and upconversion phosphors in light-curable polymers, *Dent. Mater.* 28 (2012) 304–311. doi:10.1016/j.dental.2011.11.018.
- [112] C. Zhang, Y. Yuan, S. Zhang, Y. Wang, Z. Liu, Biosensing platform based on fluorescence resonance energy transfer from upconverting nanocrystals to graphene oxide, *Angew. Chemie - Int. Ed.* 50 (2011) 6851–6854. doi:10.1002/anie.201100769.
- [113] M. Wang, C.-C. Mi, W.-X. Wang, C.-H. Liu, Y.-F. Wu, Z.-R. Xu, C.-B. Mao, S.-K. Xu, Immunolabeling and NIR-Excited Fluorescent Imaging of HeLa Cells by Using NaYF₄:Yb,Er Upconversion Nanoparticles, *ACS Nano.* 3 (2009) 1580–1586. doi:10.1021/Nn900491j.
- [114] F. Wang, X. Liu, Upconversion multicolor fine-tuning: Visible to near-infrared emission from lanthanide-doped NaYF₄ nanoparticles, *J. Am. Chem. Soc.* 130 (2008) 5642–5643. doi:10.1021/ja800868a.

- [115] H. Zhang, Y. Li, Y. Lin, Y. Huang, X. Duan, Composition tuning the upconversion emission in NaYF₄:Yb/Tm hexaplate nanocrystals, *Nanoscale*. 3 (2011) 963. doi:10.1039/c0nr00823k.
- [116] V. Mahalingam, F. Vetrone, R. Naccache, A. Speghini, J.A. Capobianco, Colloidal Tm³⁺/Yb³⁺-Doped LiYF₄ nanocrystals: Multiple luminescence spanning the UV to NIR regions via low-energy excitation, *Adv. Mater.* 21 (2009). doi:10.1002/adma.200901174.
- [117] A. Yin, Y. Zhang, L. Sun, C. Yan, Colloidal synthesis and blue based multicolor upconversion emissions of size and composition controlled monodisperse hexagonal NaYF₄: Yb,Tm nanocrystals, *Nanoscale*. 2 (2010) 953. doi:10.1039/b9nr00397e.
- [118] J. Zhao, D. Jin, E.P. Schartner, Y. Lu, Y. Liu, A. V. Zvyagin, L. Zhang, J.M. Dawes, P. Xi, J.A. Piper, E.M. Goldys, T.M. Monro, Single-nanocrystal sensitivity achieved by enhanced upconversion luminescence, *Nat. Nanotechnol.* 8 (2013) 729–734. doi:10.1038/nnano.2013.171.
- [119] E.P. Schartner, H. Ebendorff-Heidepriem, S.C. Warren-Smith, R.T. White, T.M. Monro, Driving down the detection limit in microstructured fiber-based chemical dip sensors, *Sensors*. 11 (2011) 2961–2971. doi:10.3390/s110302961.
- [120] M. Misiak, K. Prorok, B. Cichy, A. Bednarkiewicz, W. Stręk, Thulium concentration quenching in the up-converting α -Tm³⁺/Yb³⁺ NaYF₄ colloidal nanocrystals, *Opt. Mater. (Amst)*. 35 (2013) 1124–1128. doi:10.1016/j.optmat.2013.01.002.
- [121] S.K.W. MacDougall, A. Ivaturi, J. Marques-Hueso, K.W. Krämer, B.S. Richards, Ultra-high photoluminescent quantum yield of β -NaYF₄: 10% Er³⁺ via broadband excitation of upconversion for photovoltaic devices, *Opt. Express*. 20 (2012) A879. doi:10.1364/OE.20.00A879.
- [122] C. Drees, A.N. Raj, R. Kurre, K.B. Busch, M. Haase, J. Piehler, Engineered Upconversion Nanoparticles for Resolving Protein Interactions inside Living Cells, *Angew. Chemie - Int. Ed.* 55 (2016) 11668–11672. doi:10.1002/anie.201603028.
- [123] H.S. Qian, Y. Zhang, Synthesis of hexagonal-phase core-shell NaYF₄ nanocrystals with tunable upconversion fluorescence, *Langmuir*. 24 (2008) 12123–12125. doi:10.1021/la802343f.
- [124] Q. Dou, N.M. Idris, Y. Zhang, Sandwich-structured upconversion nanoparticles with tunable color for multiplexed cell labeling, *Biomaterials*. 34 (2013) 1722–1731. doi:10.1016/j.biomaterials.2012.11.011.

- [125] G. Chen, H. Qiu, P.N. Prasad, X. Chen, Upconversion nanoparticles: Design, nanochemistry, and applications in Theranostics, *Chem. Rev.* 114 (2014) 5161–5214. doi:10.1021/cr400425h.
- [126] N. Bogdan, F. Vetrone, G.A. Ozin, J.A. Capobianco, Synthesis of ligand-free colloiddally stable water dispersible brightly luminescent lanthanide-doped upconverting nanoparticles, *Nano Lett.* 11 (2011) 835–840. doi:10.1021/nl1041929.
- [127] Z. Li, Y. Li, Y. Wang, H. Miao, Y. Du, H. Liu, A general strategy to fabricate ligand-free water-soluble up-conversion nanoparticles, *J. Alloys Compd.* 613 (2014) 18–24. doi:10.1016/j.jallcom.2014.05.152.
- [128] N. Bogdan, E.M. Rodriguez, F. Sanz-Rodriguez, M.C. de la Cruz, A. Juarranz, D. Jaque, J.G. Sole, J.A. Capobianco, Bio-functionalization of ligand-free upconverting lanthanide doped nanoparticles for bio-imaging and cell targeting, *Nanoscale.* 4 (2012) 3647–3650. doi:10.1039/c2nr30982c.
- [129] J.C. Boyer, M.P. Manseau, J.I. Murray, F.C.J.M. Van Veggel, Surface modification of upconverting NaYF₄ nanoparticles with PEG-phosphate ligands for NIR (800 nm) biolabeling within the biological window, *Langmuir.* 26 (2010) 1157–1164. doi:10.1021/la902260j.
- [130] G. Chen, T.Y. Ohulchanskyy, W.C. Law, H. Ågren, P.N. Prasad, Monodisperse NaYbF₄: Tm³⁺/NaGdF₄ core/shell nanocrystals with near-infrared to near-infrared upconversion photoluminescence and magnetic resonance properties, *Nanoscale.* 3 (2011) 2003. doi:10.1039/c0nr01018a.
- [131] R.R. and J.A.C. Nicoleta Bogdan, Fiorenzo Vetrone, Carbohydrate-coated lanthanide-doped upconverting nanoparticles for lectin recognition, *J. Mater. Chem.* 20 (2010) 7543–7550. doi:10.1039/C0JM01617A.
- [132] A. Dong, X. Ye, J. Chen, Y. Kang, T. Gordon, J.M. Kikkawa, C.B. Murray, A Generalized Ligand-Exchange Strategy Enabling Sequential Surface Functionalization of Colloidal Nanocrystals, (2011) 998–1006. doi:10.1021/ja108948z.
- [133] J. Shan, Y. Ju, Controlled synthesis of lanthanide-doped NaYF₄ upconversion nanocrystals via ligand induced crystal phase transition and silica coating, *Appl. Phys. Lett.* 91 (2007). doi:10.1063/1.2783476.
- [134] N.M. Idris, Z. Li, L. Ye, E.K. Wei Sim, R. Mahendran, P.C.L. Ho, Y. Zhang, Tracking transplanted cells in live animal using upconversion fluorescent nanoparticles,

- Biomaterials. 30 (2009) 5104–5113. doi:10.1016/j.biomaterials.2009.05.062.
- [135] Z. Lu, J. Dai, X. Song, G. Wang, W. Yang, Facile synthesis of Fe₃O₄/SiO₂ composite nanoparticles from primary silica particles, *Colloids Surfaces A Physicochem. Eng. Asp.* 317 (2008) 450–456. doi:10.1016/j.colsurfa.2007.11.020.
- [136] H. Hu, L. Xiong, J. Zhou, F. Li, T. Cao, C. Huang, Multimodal-luminescence core-shell nanocomposites for targeted imaging of tumor cells, *Chem. - A Eur. J.* 15 (2009) 3577–3584. doi:10.1002/chem.200802261.
- [137] T. Nann, P. Mulvaney, Single quantum dots in spherical silica particles, *Angew. Chemie - Int. Ed.* 43 (2004) 5393–5396. doi:10.1002/anie.200460752.
- [138] A.-L. Morel, S.I. Nikitenko, K. Gionnet, A. Wattiaux, J. Lai-Kee-Him, C. Labrugere, B. Chevalier, G. Deleris, C. Petibois, A. Brisson, M. Simonoff, Sonochemical Approach to the Synthesis of Fe₃O₄@SiO₂ Core–Shell Nanoparticles with Tunable Properties, *ACS Nano.* 2 (2008) 847–856. doi:10.1021/nn800091q.
- [139] Z. Hou, C. Li, P. Ma, G. Li, Z. Cheng, C. Peng, D. Yang, P. Yang, J. Lin, Electrospinning preparation and drug-delivery properties of an Up-conversion Luminescent Porous NaYF₄:Yb³⁺, Er³⁺@silica fiber nanocomposite, *Adv. Funct. Mater.* 21 (2011) 2356–2365. doi:10.1002/adfm.201100193.
- [140] R.P. Bagwe, L.R. Hilliard, W. Tan, Surface modification of silica nanoparticles to reduce aggregation and nonspecific binding, *Langmuir.* 22 (2006) 4357–4362. doi:10.1021/la052797j.
- [141] G. Chen, H. Qiu, P.N. Prasad, X. Chen, Upconversion nanoparticles: Design, nanochemistry, and applications in Theranostics, *Chem. Rev.* 114 (2014) 5161–5214. doi:10.1021/cr400425h.
- [142] G. Chen, T.Y. Ohulchanskyy, A. Kachynski, H. Ågren, P.N. Prasad, Intense visible and near-infrared upconversion photoluminescence in colloidal LiYF₄:Er³⁺ nanocrystals under excitation at 1490 nm, *ACS Nano.* 5 (2011) 4981–4986. doi:10.1021/nn201083j.
- [143] X. Teng, Y.H. Zhu, W. Wei, S.C. Wang, J.F. Huang, R. Naccache, W.B. Hu, a I.Y. Tok, Y. Han, Q.C. Zhang, Q.L. Fan, W. Huang, J. a Capobianco, L. Huang, Lanthanide-Doped Na_xScF_{3+x} Nanocrystals: Crystal Structure Evolution and Multicolor Tuning, *J. Am. Chem. Soc.* 134 (2012) 8340–8343. doi:10.1021/Ja3016236.
- [144] G. Chen, H. Qiu, R. Fan, S. Hao, S. Tan, C. Yang, G. Han, Lanthanide-doped

- ultrasmall yttrium fluoride nanoparticles with enhanced multicolor upconversion photoluminescence, *J. Mater. Chem.* 22 (2012) 20190. doi:10.1039/c2jm32298f.
- [145] X. Sun, Y.W. Zhang, Y.P. Du, Z.G. Yan, R. Si, L.P. You, C.H. Yan, From trifluoroacetate complex precursors to monodisperse rare-earth fluoride and oxyfluoride nanocrystals with diverse shapes through controlled fluorination in solution phase, *Chem. - A Eur. J.* 13 (2007) 2320–2332. doi:10.1002/chem.200601072.
- [146] D. Liu, X. Xu, Y. Du, X. Qin, Y. Zhang, C. Ma, S. Wen, W. Ren, E.M. Goldys, J.A. Piper, S. Dou, X. Liu, D. Jin, Three-dimensional controlled growth of monodisperse sub-50 nm heterogeneous nanocrystals, *Nat. Commun.* 7 (2016) 10254. doi:10.1038/ncomms10254.
- [147] H. Qiu, G. Chen, L. Sun, S. Hao, G. Han, C. Yang, Ethylenediaminetetraacetic acid (EDTA)-controlled synthesis of multicolor lanthanide doped BaYF₅ upconversion nanocrystals, *J. Mater. Chem.* 21 (2011) 17202. doi:10.1039/c1jm12950c.
- [148] J.H. Zeng, J. Su, Z.H. Li, R.X. Yan, Y.D. Li, Synthesis and upconversion luminescence of hexagonal-phase NaYF₄:Yb, Er³⁺ phosphors of controlled size and morphology, *Adv. Mater.* 17 (2005) 2119–2123. doi:10.1002/adma.200402046.
- [149] L. Wang, P. Li, Y. Li, Down- and up-conversion luminescent nanorods, *Adv. Mater.* 19 (2007) 3304–3307. doi:10.1002/adma.200700144.
- [150] P.W. Voorhees, The theory of Ostwald ripening, *J. Stat. Phys.* 38 (1985) 231–252. doi:10.1007/BF01017860.
- [151] J. Wang, F. Wang, J. Xu, Y. Wang, Y. Liu, X. Chen, H. Chen, X. Liu, Lanthanide-doped LiYF₄ nanoparticles: Synthesis and multicolor upconversion tuning, *Comptes Rendus Chim.* 13 (2010) 731–736. doi:10.1016/j.crci.2010.03.021.
- [152] Y. Liu, D. Tu, H. Zhu, R. Li, W. Luo, X. Chen, A strategy to achieve efficient dual-mode luminescence of Eu³⁺ in lanthanides doped multifunctional NaGdF₄ nanocrystals, *Adv. Mater.* 22 (2010) 3266–3271. doi:10.1002/adma.201000128.
- [153] W. Zheng, S. Zhou, Z. Chen, P. Hu, Y. Liu, D. Tu, H. Zhu, R. Li, M. Huang, X. Chen, Sub-10 nm lanthanide-doped CaF₂ nanoprobe for time-resolved luminescent biodetection, *Angew. Chemie - Int. Ed.* 52 (2013) 6671–6676. doi:10.1002/anie.201302481.
- [154] M. Yu, F. Li, Z. Chen, H. Hu, C. Zhan, H. Yang, C. Huang, Laser scanning up-conversion luminescence microscopy for imaging cells labeled with rare-earth

- nanophosphors, *Anal. Chem.* 81 (2009) 930–935. doi:10.1021/ac802072d.
- [155] M. Wang, G. Abbineni, A. Clevenger, C. Mao, S. Xu, Upconversion nanoparticles: Synthesis, surface modification and biological applications, *Nanomedicine Nanotechnology, Biol. Med.* 7 (2011) 710–729. doi:10.1016/j.nano.2011.02.013.
- [156] Q. Zhan, J. Qian, H. Liang, G. Somesfalean, D. Wang, S. He, Z. Zhang, S. Andersson-Engels, Using 915 nm laser excited Tm³⁺/Er³⁺/Ho³⁺-doped NaYbF₄ upconversion nanoparticles for in vitro and deeper in vivo bioimaging without overheating irradiation, *ACS Nano*. 5 (2011) 3744–3757. doi:10.1021/nn200110j.
- [157] O.S. Kwon, H.S. Song, J. Conde, H. Il Kim, N. Artzi, J.H. Kim, Dual-color emissive upconversion nanocapsules for differential cancer bioimaging in vivo, *ACS Nano*. 10 (2016) 1512–1521. doi:10.1021/acsnano.5b07075.
- [158] Q. Liu, T. Yang, W. Feng, F. Li, Blue-emissive upconversion nanoparticles for low-power-excited bioimaging in vivo, *J. Am. Chem. Soc.* 134 (2012) 5390–5397. doi:10.1021/ja3003638.
- [159] J. Zhou, Z. Liu, F. Li, Upconversion nanophosphors for small-animal imaging, *Chem. Soc. Rev.* 41 (2012) 1323–1349. doi:10.1039/C1CS15187H.
- [160] F. Wang, D. Banerjee, Y. Liu, X. Chen, X. Liu, Upconversion nanoparticles in biological labeling, imaging, and therapy, *Analyst*. 135 (2010) 1839. doi:10.1039/c0an00144a.
- [161] D. Tu, Y. Liu, H. Zhu, X. Chen, Optical/magnetic multimodal bioprobes based on lanthanide-doped inorganic nanocrystals, *Chem. - A Eur. J.* 19 (2013) 5516–5527. doi:10.1002/chem.201204640.
- [162] Z. Gu, L. Yan, G. Tian, S. Li, Z. Chai, Y. Zhao, Recent advances in design and fabrication of upconversion nanoparticles and their safe theranostic applications, *Adv. Mater.* 25 (2013) 3758–3779. doi:10.1002/adma.201301197.
- [163] Y.M. Bae, Y. Il Park, S.H. Nam, J.H. Kim, K. Lee, H.M. Kim, B. Yoo, J.S. Choi, K.T. Lee, T. Hyeon, Y.D. Suh, Endocytosis, intracellular transport, and exocytosis of lanthanide-doped upconverting nanoparticles in single living cells, *Biomaterials*. 33 (2012) 9080–9086. doi:10.1016/j.biomaterials.2012.08.039.
- [164] C.-F. Chan, M.-K. Tsang, H. Li, R. Lan, F.L. Chadbourne, W.-L. Chan, G.-L. Law, S.L. Cobb, J. Hao, W.-T. Wong, K.-L. Wong, Bifunctional up-converting lanthanide nanoparticles for selective in vitro imaging and inhibition of cyclin D as anti-cancer agents, *J. Mater. Chem. B*. 2 (2014) 84–91. doi:10.1039/C3TB21034K.

- [165] L. Le Li, P. Wu, K. Hwang, Y. Lu, An exceptionally simple strategy for DNA-functionalized Up-conversion nanoparticles as biocompatible agents for nanoassembly, DNA delivery, and imaging, *J. Am. Chem. Soc.* 135 (2013) 2411–2414. doi:10.1021/ja310432u.
- [166] G. Tian, Z. Gu, L. Zhou, W. Yin, X. Liu, L. Yan, S. Jin, W. Ren, G. Xing, S. Li, Y. Zhao, Mn²⁺ dopant-controlled synthesis of NaYF₄:Yb/Er upconversion nanoparticles for in vivo imaging and drug delivery., *Adv. Mater.* 24 (2012) 1226–1231. doi:10.1002/adma.201104741.
- [167] J. Kim, Y. Piao, T. Hyeon, Multifunctional nanostructured materials for multimodal imaging, and simultaneous imaging and therapy., *Chem. Soc. Rev.* 38 (2009) 372–390. doi:10.1039/b709883a.
- [168] H. Bin Na, J.H. Lee, K. An, Y. Il Park, M. Park, I.S. Lee, D.H. Nam, S.T. Kim, S.H. Kim, S.W. Kim, K.H. Lim, K.S. Kim, S.O. Kim, T. Hyeon, Development of a T1 contrast agent for magnetic resonance imaging using MnO nanoparticles, *Angew. Chemie - Int. Ed.* 46 (2007) 5397–5401. doi:10.1002/anie.200604775.
- [169] H. Bin Na, I.C. Song, T. Hyeon, Inorganic nanoparticles for MRI contrast agents, *Adv. Mater.* 21 (2009) 2133–2148. doi:10.1002/adma.200802366.
- [170] H. Yang, Y. Zhuang, H. Hu, X. Du, C. Zhang, X. Shi, H. Wu, S. Yang, Silica-coated manganese oxide nanoparticles as a platform for targeted magnetic resonance and fluorescence imaging of cancer cells, *Adv. Funct. Mater.* 20 (2010) 1733–1741. doi:10.1002/adfm.200902445.
- [171] S. Gai, P. Yang, C. Li, W. Wang, Y. Dai, N. Niu, J. Lin, Synthesis of magnetic, up-conversion luminescent, and mesoporous core-shell-structured nanocomposites as drug carriers, *Adv. Funct. Mater.* 20 (2010) 1166–1172. doi:10.1002/adfm.200902274.
- [172] C. Zhang, C. Li, S. Huang, Z. Hou, Z. Cheng, P. Yang, C. Peng, J. Lin, Self-activated luminescent and mesoporous strontium hydroxyapatite nanorods for drug delivery, *Biomaterials.* 31 (2010) 3374–3383. doi:10.1016/j.biomaterials.2010.01.044.
- [173] D. Pan, H. Zhang, T. Fan, J. Chen, X. Duan, Nearly monodispersed core-shell structural Fe₃O₄@DFUR-LDH submicro particles for magnetically controlled drug delivery and release, *Chem. Commun.* 47 (2011) 908–910. doi:10.1039/C0CC01313G.
- [174] W. Zhao, H. Chen, Y. Li, A. Li, M. Lang, J. Shi, Uniform rattle-type hollow magnetic

- mesoporous spheres as drug delivery carriers and their sustained-release property, *Adv. Funct. Mater.* 18 (2008) 2780–2788. doi:10.1002/adfm.200701317.
- [175] L. Cheng, K. Yang, Y. Li, X. Zeng, M. Shao, S.T. Lee, Z. Liu, Multifunctional nanoparticles for upconversion luminescence/MR multimodal imaging and magnetically targeted photothermal therapy, *Biomaterials*. 33 (2012) 2215–2222. doi:10.1016/j.biomaterials.2011.11.069.
- [176] V. V. Mody, A. Cox, S. Shah, A. Singh, W. Bevins, H. Parihar, Magnetic nanoparticle drug delivery systems for targeting tumor, *Appl. Nanosci.* 4 (2013) 385–392. doi:10.1007/s13204-013-0216-y.
- [177] L. Pan, J. Liu, Q. He, L. Wang, J. Shi, Overcoming multidrug resistance of cancer cells by direct intranuclear drug delivery using TAT-conjugated mesoporous silica nanoparticles, *Biomaterials*. 34 (2013) 2719–2730. doi:10.1016/j.biomaterials.2012.12.040.
- [178] J. Chang, Y. Jallouli, M. Kroubi, X. bo Yuan, W. Feng, C. sheng Kang, P. yu Pu, D. Betbeder, Characterization of endocytosis of transferrin-coated PLGA nanoparticles by the blood-brain barrier, *Int. J. Pharm.* 379 (2009) 285–292. doi:10.1016/j.ijpharm.2009.04.035.
- [179] Z. Xiao, O.C. Farokhzad, Aptamer-functionalized nanoparticles for medical applications: Challenges and opportunities, *ACS Nano*. 6 (2012) 3670–3676. doi:10.1021/nn301869z.
- [180] F. Porta, G.E.M. Lamers, J. Morrhayim, A. Chatzopoulou, M. Schaaf, H. den Dulk, C. Backendorf, J.I. Zink, A. Kros, Folic Acid-Modified Mesoporous Silica Nanoparticles for Cellular and Nuclear Targeted Drug Delivery, *Adv. Healthc. Mater.* 2 (2013) 281–286. doi:10.1002/adhm.201200176.
- [181] M. Heidari Majd, D. Asgari, J. Barar, H. Valizadeh, V. Kafil, A. Abadpour, E. Moumivand, J.S. Mojarad, M.R. Rashidi, G. Coukos, Y. Omid, Tamoxifen loaded folic acid armed PEGylated magnetic nanoparticles for targeted imaging and therapy of cancer, *Colloids Surfaces B Biointerfaces*. 106 (2013) 117–125. doi:10.1016/j.colsurfb.2013.01.051.
- [182] P.S. Low, W.A. Henne, D.D. Doorneweerd, Discovery and Development of Folic-Acid-Based Receptor Targeting for Imaging and Therapy of Cancer and Inflammatory Diseases, *Acc. Chem. Res.* 41 (2008) 120–129. doi:10.1021/ar7000815 [doi].
- [183] P. Huang, L. Bao, C. Zhang, J. Lin, T. Luo, D. Yang, M. He, Z. Li, G. Gao, B. Gao,

- S. Fu, D. Cui, Folic acid-conjugated Silica-modified gold nanorods for X-ray/CT imaging-guided dual-mode radiation and photo-thermal therapy, *Biomaterials*. 32 (2011) 9796–9809. doi:10.1016/j.biomaterials.2011.08.086.
- [184] P. Huang, C. Xu, J. Lin, C. Wang, X. Wang, C. Zhang, X. Zhou, S. Guo, D. Cui, Folic Acid-conjugated Graphene Oxide loaded with Photosensitizers for Targeting Photodynamic Therapy., *Theranostics*. 1 (2011) 240–50. doi:10.7150/thno/v01p0240.
- [185] A.R. Hilgenbrink, P.S. Low, Folate receptor-mediated drug targeting: From therapeutics to diagnostics, *J. Pharm. Sci.* 94 (2005) 2135–2146. doi:10.1002/jps.20457.
- [186] S. Cui, D. Yin, Y. Chen, Y. Di, H. Chen, Y. Ma, S. Achilefu, Y. Gu, In vivo targeted deep-tissue photodynamic therapy based on near-infrared light triggered upconversion nanoconstruct, *ACS Nano*. 7 (2013) 676–688. doi:10.1021/nn304872n.
- [187] N.J. Abbott, I.A. Romero, Transporting therapeutics across the blood-brain barrier, *Mol. Med. Today*. 2 (1996) 106–113. doi:10.1016/1357-4310(96)88720-X.
- [188] A.H. Schinkel, P-Glycoprotein, a gatekeeper in the blood-brain barrier, *Adv. Drug Deliv. Rev.* 36 (1999) 179–194. doi:10.1016/S0169-409X(98)00085-4.
- [189] R.A. Hawkins, D.R. Peterson, J.R. Viña, The complementary membranes forming the blood-brain barrier, *IUBMB Life*. 54 (2002) 101–107. doi:10.1080/15216540214541.
- [190] R.L. O’Kane, I. Martínez-López, M.R. DeJoseph, J.R. Viña, R.A. Hawkins, Na⁺-dependent glutamate transporters (EAAT1, EAAT2, and EAAT3) of the blood-brain barrier. A mechanism for glutamate removal, *J. Biol. Chem.* 274 (1999) 31891–31895. doi:10.1074/jbc.274.45.31891.
- [191] M.S. McAllister, L. Krizanac-Bengez, F. Macchia, R.J. Naftalin, K.C. Pedley, M.R. Mayberg, M. Marroni, S. Leaman, K.A. Stanness, D. Janigro, Mechanisms of glucose transport at the blood-brain barrier: An in vitro study, *Brain Res.* 904 (2001) 20–30. doi:10.1016/S0006-8993(01)02418-0.

Chapter 2: Protocol Development and Optimization

This chapter described the main experimental approaches that were developed and optimized for use in this thesis. At the start of this project, there were numerous methodologies available in the laboratory for the generation of a standard set of lanthanide-doped upconversion nanoparticles with luminescent emission at 800nm. However, there were no procedures in place ready for the fabrication of high-lanthanide doped UCNPs ($\text{NaYF}_4:20\% \text{Yb}, 4\% \text{Tm}$) and the biophysical modification of these UCNPs. Therefore, in this project, a considerable amount of optimization was undertaken to prepared high lanthanide-doped UCNPs and modify the as-prepared UCNPs with various methods, such as acid treatment, one-step ligand exchange and reverse microemulsion to form UCNPs with different surface-modifications (OA-free, DNA-modified, silica-coating and PEG capping). During the development of these controlled preparation of UCNPs, the methods reported previously were not feasible for directly employment. Thus, several experimental conditions were adjusted and tuned to controlled fabrication of UCNPs as required in this project (different shapes with similar size and various ARs of nanorods for systematic study). In addition, some technical challenges were encountered during the development of these surface-modification strategies. For example, it was difficult to control the ratio of silica precursor (tetraethyl orthosilicate, TEOS) and UCNPs to form a thin and uniform layer on the surface of UCNPs. Moreover, it was not easy to strictly control the longitudinal growth of UCNPs to generate nanorods of various aspect ratios (length/width, L/W) of 1, 2, 3 and 4. While published literature suggested that this can be achieved by step-by-step growth to produce longer rod-like UCNPs, however it is difficult to be reproduced or controlled. However, after optimization during this project, a new protocol was developed that supports nanorod growth to any desired length using a one-pot seed-mediated approach through hot injection. Furthermore, protocols were established in this project that allowed reproducibility and high purity production of UCNPs with various shapes.

Furthermore, new techniques were established for nanoparticle microinjection into zebrafish (undertaken by Dr. Marco Morsch) and in vivo microscopy for UCNP-tracking in zebrafish. This project developed an integrated experimental workflow to evaluate the cellular uptake and bio-distribution capabilities of UCNPs, using cell culture and zebrafish experiments, bioimaging and analysis with confocal microscope and Imaris software. To the best of my knowledge, this is the first time that UCNPs have been injected into the spinal cord and blood vessels of zebrafish to evaluate their bioavailability and biodistribution. The process of optimizing these techniques involved identification of appropriate concentrations of UCNPs for microinjection directly into the spinal cord, as well as optimizing the microscopy techniques for detection of the UCNPs. Furthermore, a technique was developed for administration into the bloodstream of zebrafish, to track their uptake across the BBB and into the brain. To confidently confirm this occurred, transgenic zebrafish that express a fluorophore in the endothelial cells that line the blood vessels were used – and this required optimization of the imaging techniques to confidently confirm that UCNPs had indeed passed out of the blood vessel and into the brain.

In summary, this chapter presents data that demonstrates the optimization of the key experimental models and techniques that were used in this project. Because this thesis is presented in a “thesis-by-publication” format, these data did not logically fit within the structure of the manuscript chapters, but are crucial for demonstrating the robustness of the assays that were used for this project.

2.1 Developing a production strategy to allow highly-controlled size and shape of high lanthanide-doped upconversion nanoparticles

In this section, the synthesis conditions for production of unmodified OA-capped UCNPs to form high quality OA-UCNPs with uniform shape and size are presented. As upconversion luminescence can be significantly influenced by the shape and size of nanoparticles, the aim was to synthesise a series of OA-UCNPs with different shape and size through optimization of experimental conditions such as heating-up speed, temperature and argon (Ar) flow-speed.

2.1.1 Synthesis of spherical OA-capped UCNPs

Method

The OA-capped high lanthanide ions-doped UCNPs ($\text{NaYF}_4\text{:20\%Yb,4\%Tm, Ln}^{3+}$ -UCNPs) were fabricated according to a modified oxygen-free approach based on the literature.[1] Specifically, 0.76 mmol $\text{YCl}_3 \cdot 6\text{H}_2\text{O}$, 0.2 mmol $\text{YbCl}_3 \cdot 6\text{H}_2\text{O}$ and 0.04 mmol $\text{TmCl}_3 \cdot 6\text{H}_2\text{O}$

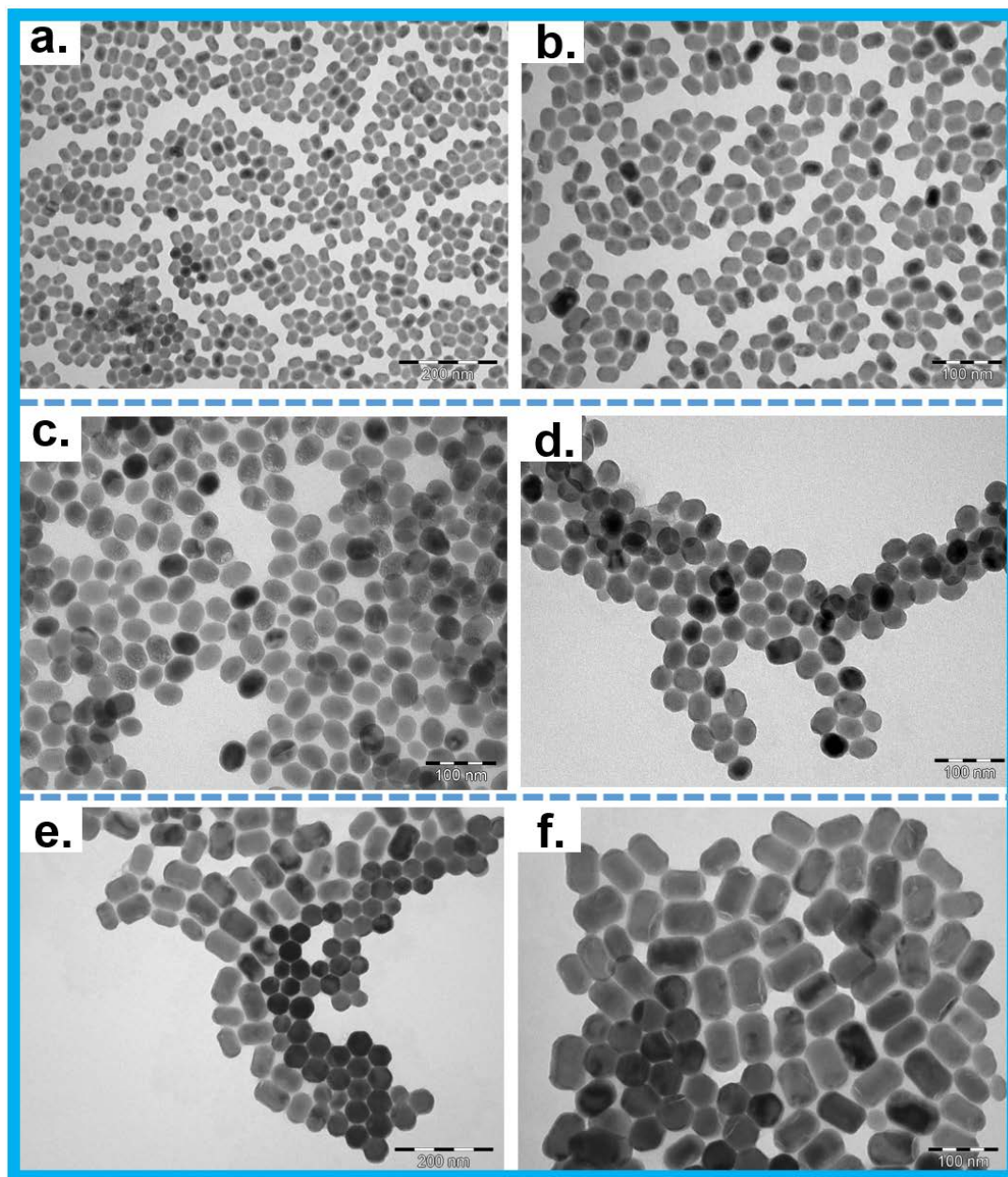


Figure 2. TEM images of UCNRs (NaYF₄:20%Yb,4%Tm). Images of a and b represent UCNRs at first step; images c and d mean the UCNRs synthesized at the second step; e and f represent UCNRs prepared at the third step. (Scale bar of image a and e is 200 nm, scale bar in image b, c, d and f is 100 nm)

Result and Discussion:

In Figure 2, TEM images show representative examples of the OA-UCNRs prepared according to the above method at various steps, resulting in nanorod sizes of $23.4 \text{ nm} \times$

33.9nm, 33.1 nm \times 42.3 nm and 40.5 nm \times 55.2 nm, respectively (all aspect ratios of less than 1:2). The size of the original spherical UCNP core at the first step is \sim 20nm. These results indicated that both width and length of the core grow at the same time, despite it being hoped that only length would elongate. Therefore, the protocol that has been reported for production of NaYF₄ nanorods does not appear to work for Ln³⁺-UCNRs synthesis. Therefore, new techniques had to be developed for synthesis of Ln³⁺-UCNRs with high ARs.

Method (B): One-pot Hot-injection Approach

The NaYF₄:20%Yb,4%Tm upconversion nanorods with various ARs were produced with a one-pot synthesis approach through successive layer-by-layer hot-injection modified and optimized from our previous work.[2, 3] First, the shell precursors were prepared. 0.76mmol YCl₃·6H₂O, 0.2mmol YbCl₃ and 0.04mmol TmCl₃·6H₂O were added to a 50 mL-flask containing 6.5mL oleic acid and 15mL 1-octadecene. The mixture solution was heated to 160 °C for 30 min with protection of argon flow and then cooled down to room temperature (RT), followed by the addition of 4.0mmol NH₄F, 2.5mmol NaOH and 2.0mmol KOH in 8 mL methanol. After stirring for 30 min at RT, the solution was heated to 80 °C with argon flow for 20 min to remove methanol, and then the react system was continually heated to 150 °C for another 30 min to remove water in the solution. Finally, the reaction solution was cooled down to room temperature and labeled as 1mmol NaYF₄:Yb,Tm shell precursors for further use.

For the longitudinal growth of NaYF₄:Yb,Tm with AR=2, 0.2 mmol NaYF₄:Yb,Tm core particles in cyclohexane were added to a 50 mL three-neck flask containing 1.3mL OA and 3 mL ODE. The mixture solution was heated to 160 °C under protection of argon flow for 30 min to remove cyclohexane, and then the solution was continually heated to 310 °C. Followed with that, 0.2 mmol of as-prepared NaYF₄:Yb,Tm shell precursors were injected into the reaction mixture at the speed of 0.1 mL per 10 min and followed by another 0.5 h reaction time at 310 °C. Finally, the formed solution was gradually cooled

down to room temperature and the formed upconversion nanorods with AR=2 were purified according to the procedures employed for the purification of NaYF₄:Yb,Tm core particles. For fabrication of UCNRs with other ARs (ARs= 3, 4), it was found that this could be controlled through the ratio of core and shell precursors to 1:2 and 1:3, respectively.

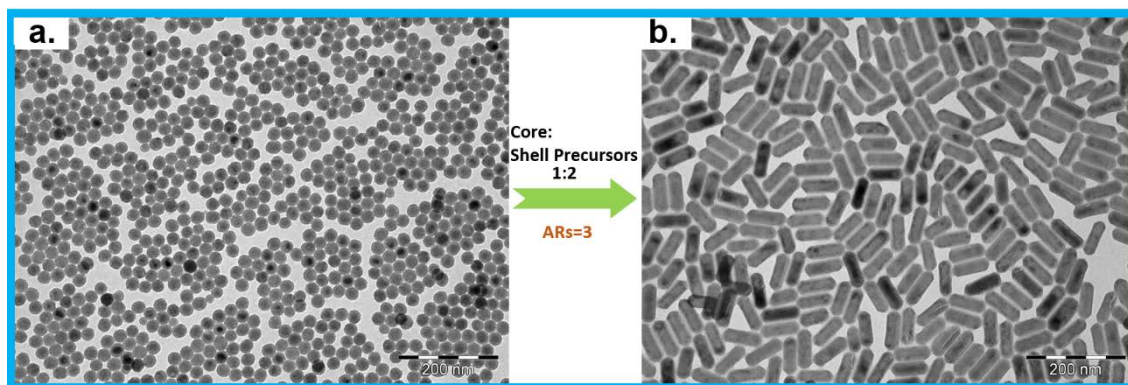


Figure 3. TEM images of spherical UCNPs (NaYF₄:20% Yb,4% Tm) as the core (a) and the as-prepared UCNR (ARs=3). (Scale bar of images is 200 nm)

Result and Discussion

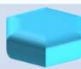
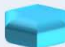


In Figure 3, TEM images showed the spherical OA-UCNPs that formed the core starting material, prepared according to the protocol described above (B). The diameter of the original core in this system was ~26 nm. In this synthesis procedure, the ratio of core and shell precursors was controlled to be 1:2. Therefore, the ARs of as-prepared OA-UCNRs is 3 with the size of 26 nm × 76.5 nm. It showed that the width of nanorods did not show any growth as expected. Therefore, it indicated that the ARs of nanorods could be precisely controlled for Ln³⁺-UCNRs-based drug delivery system design. The further study of Ln³⁺-UCNRs with various ARs is presented in the Chapter five.

2.1.3 Synthesis of Upconversion Nanodisks

Method

The small disk-shaped UCNPs were fabricated using an modified and optimized oxygen-free protocol based on the literature[3]. Specifically, 3.5 mL of methanol solution (containing 0.76mmol YCl_3 , 0.2mmol YbCl_3 and 0.04mmol Tm) was magnetically mixed with 15 mL OA and 16 mL ODE in a 100mL flask. The mixture was degassed under Ar flow and heated to 150 °C for 30 min, then cooled to room temperature. 3.8mmol NH_4F and 2.5mmol NaOH in 5 mL of methanol solution was added into the reaction system and kept stirring for 30 min at room temperature. The methanol and water in the system were removed by keeping the mixture solution at 110 °C for 30 min. Then the formed mixture solution was slowly heated to reaction temperature 310°C and remain for 1.5 h. Ethanol was added to precipitate the nanocrystals after the solution cooled down to room temperature. Finally, the resultant nanoparticles were collected by centrifugation, washed with cyclohexane, ethanol and methanol for three times, the final disk-shaped $\text{NaYF}_4\text{:20%Yb,4%Tm}$ nanocrystals were re-dispersed in 10mL cyclohexane at 4°C for further experiment.

Table 1. Summary of the disk-shaped and rod-like Ln^{3+} -UCNPs ($\text{NaYF}_4\text{:20%Yb,4%Tm}$).

NPs No.	NaOH	NH_4F	Shape	Model	Size (width×height)
1	2.5	3.2	disk		105nm × 280nm
2	2.5	3.6	disk		55nm × 112nm
3	2.5	3.8	disk		45nm × 45nm
4	2.5	4	rod		23nm × 36nm

Result and Discussion

As shown in Table 1, UCNP shape mainly depends upon the ratio between NaOH and NH_4F . With the increasing ratio value of $\text{NH}_4\text{F}/\text{NaOH}$, the size of as-prepared Ln^{3+} -UCNPs decreased from 105 nm×280 nm to 23 nm× 36 nm, turning the shape from big disk to small rod. Accordingly, in order to synthesize small disks within 50 nm, the ratio

of $\text{NH}_4\text{F}/\text{NaOH}$ was adjusted to between 3.6/2.5 and 3.8/2.5. Furthermore, the size of as-synthesized Ln^{3+} -UCNPs was also significantly affected by the heating up speed, with lower heating up speed leading to the production of smaller size Ln^{3+} -UCNPs. The disk-shaped Ln^{3+} -UCNPs with specific size were fabricated and used in Chapter four.

2.2 Development of a standard protocol for surface modification of upconversion nanoparticles

To date, there are numerous published methods to modify Ln^{3+} -UCNPs to improve their hydrophilicity and biocompatibility. However, some of these modified Ln^{3+} -UCNPs are not stable in biological media and easily aggregate together to form clusters. Therefore, a Ln^{3+} -UCNPs-based platform was presented to evaluate the surface effect characteristics and identify which type of surface modification is preferable for neuron cells uptake and ultimately internalized by neurons. The as-prepared Ln^{3+} -UCNPs are generally coated with surfactants such as oleic acid or oleic acid molecules on the surface to avoid aggregation of Ln^{3+} -UCNPs during synthesis process. Thus, in order to further utilize Ln^{3+} -UCNPs for biological application, it is essential to increase the hydrophilicity of Ln^{3+} -UCNPs. Several different methods were tested, including OA removal, DNA conjugation, silica coating and PEGylation. However, the most challenge modification method was silica coating with amino groups on the surface. In this section, the optimization for preparing silica coating and controlling the thickness of silica layer outside the Ln^{3+} -UCNPs is presented. There are two popular methods (Stöber method and reverse microemulsion) used for silica coating on the surface of Ln^{3+} -UCNPs and the results have been compared with each other.

2.2.1 Stöber Method for Silica Coating of Ln^{3+} -UCNPs

Method

The Stöber method can be used to coat silica on the surface of hydrophilic Ln^{3+} -

UCNPs.[4] Accordingly, 1mL of 0.1mmol OA-capped Ln^{3+} -UCNPs were mixed with 1mL ethanol before separate via centrifugation. The pellet was sonicated with 1 mL hydrochloride (pH=2) and 1mL ethanol for 10min to remove the OA on the surface of Ln^{3+} -UCNPs. Then the OA-free Ln^{3+} -UCNPs were separated after centrifugation. Then 0.2 g PVP-40 was added into a 50 mL flask with 4 mL MiliQ water before 1mL of 0.1mmol OA-free Ln^{3+} -UCNPs with sonication for 0.5h and kept stirring for 4h to make sure PVP complete covers all of Ln^{3+} -UCNPs. Then 0.8 mL 30% NH_4OH was added into the reaction system followed with sonication for 10 min. Finally, 200 μL TEOS was rapidly added into the solution and kept stirring for 12h. The as-prepared silica-coated Ln^{3+} -UCNPs were washed by ethanol and MiliQ water for three time.

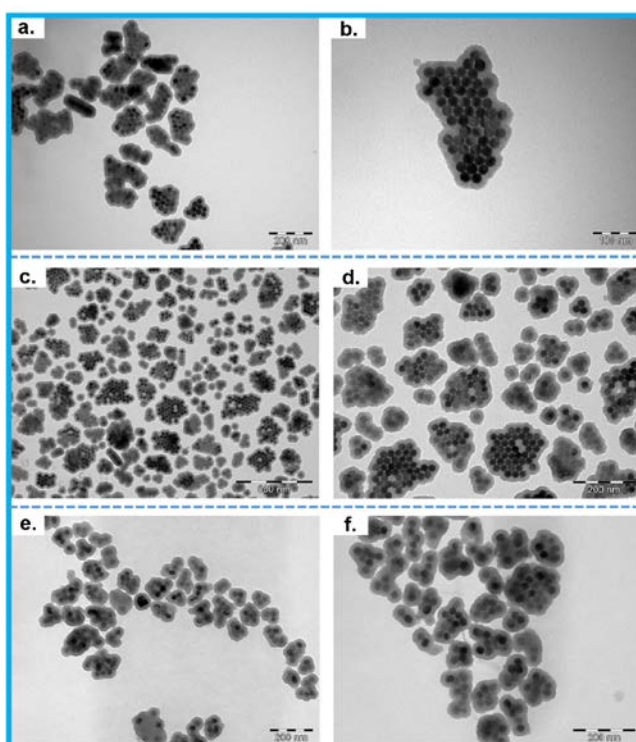


Figure 4. TEM images of OA-coated Ln^{3+} -UCNPs (NaYF_4 :20%Yb,4%Tm). Image a and b, c and d, e and f represent three batches of silica coating modification. (Scale bars of image a, d, e and f are 200 nm, scale bar in image b and c are 100 nm and 500 nm, respectively.)

Result and Discussion

As shown in Figure 4, images 4a and 4b are taken from the same batch of silica-coated

Ln^{3+} -UCNPs following synthesis via the method above. The image showed that most UCNPs had aggregated together before being capped by silica. Modification of the synthesis procedure by removal of the OA from the surface prior to silica coating was able to reduce this aggregation (Figures 4c-f). It was found that three rounds of OA removal resulted in the optimum batch of small silica-coated non-aggregated UCNPs (Figures 4e, 4f). A challenge with this method is that it is hard to confirm if the OA on the surface of Ln^{3+} -UCNPs was removed completely or not. Therefore, an alternate approach was sought to achieve a uniform silica coating layer on the surface of each nanoparticle.

2.2.2 Reverse Microemulsion for Silica Coating of Ln^{3+} -UCNPs

Method

To fabricate SiO_2 -coated UCNPs, an optimized and facile water-in-cyclohexane (W/C) reverse microemulsion coating approach was used in this experiment.[4] Firstly, 1 mL cyclohexane dispersion of NaYF_4 :20% Yb,4% Tm nanocrystals (0.1 mmol mL^{-1}), 1 mL IGPAL CO-520 and 20 mL cyclohexane was magnetically mixed in a glass flask for 30 min. Then, 35 μL of ammonia (30 wt%) was injected into the solution and a transparent emulsion formed after sonicating for 40 minutes. Thereafter, 100 μL of TEOS was added as the silica shell precursor and the solution was kept under gentle stirring at the speed of 600 rpm at room temperature for two days. After that, 10 ml acetone was added to precipitate the silica-coated UCNPs from the micro-emulsion. The nanoparticles were centrifugally washed with ethanol two times to remove the excess surfactant, and then washed with water to remove ethanol, and finally redispersed in water for use.

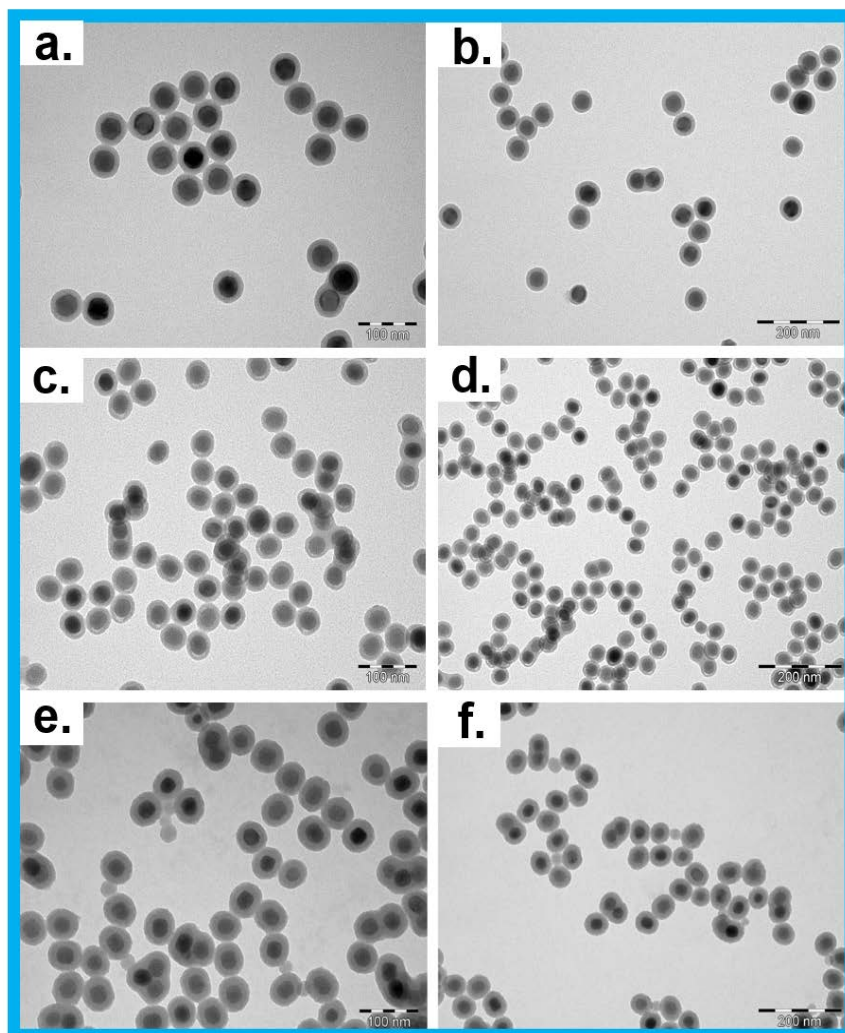


Figure 5. TEM images of OA-coated Ln^{3+} -UCNPs ($\text{NaYF}_4\text{:20\% Yb,4\% Tm}$). Image a and b, c and d, e and f represent three batches of silica coating modification. (Scale bar of image a, c and e are 200 nm, scale bar in image b, d and f is 200 nm.)

Result and Discussion

As shown in Figure 5, successful silica coating could be achieved via this reverse microemulsion protocol. Furthermore, the thickness of silica layer on the surface of Ln^{3+} -UCNPs could be tuned via precisely controlling the amount of TEOS in the reaction mix. Another factor that affects the thickness of the silica layer is the size of the nanoparticles themselves, as this directly determines the surface area at the same volume. It is essential

to reduce the thickness of silica layer on the surface of Ln^{3+} -UCNPs to as small as possible, as the thick silica layer significantly increases the size of each nanoparticles, which is likely to influence the cellular uptake of nanoparticles. The thickness of the silica coating layer is also likely to interfere with the optical properties of the Ln^{3+} -UCNPs. The thickness of silica layer of these three samples are 9.8nm, 7.5nm and 12.7nm. The diameter of the core of those three samples are 35.4 nm, 29.3 nm and 26.5 nm. The comparison of second and third sample indicated that the smaller core of Ln^{3+} -UCNPs, the thicker silica coating layer is when using the same amount of TEOS (silica precursors) to coat. Furthermore, when the core diameter of two samples is similar, the reducing TEOS used will decrease the thickness of silica coating layer. Actually, the thickness of silica layer can be controlled to be as low as ~6nm as shown in the Chapter three in this thesis.

Therefore, it was found that the reverse microemulsion method is most suitable to achieve silica coating on the hydrophobic Ln^{3+} -UCNPs. An additional benefit is that it saved one step (and therefore reducing one variable in the production workflow) of having to remove the hydrophobic surfactant (OA) when using the Stöber Method for silica coating. Furthermore, the thickness of the silica layer using the reverse microemulsion approach can be precisely controlled for further applications.

2.3 Development of a methodology for high resolution fluorescent imaging of UCNPs in cultured cells

Traditionally, the quantitative measurement of intracellular uptake of nanoparticles is conducted with flow-cytometry for systematic measurement. However, this may not be able to accurately determine whether a nanoparticle is simply bound to the surface of the cell, or truly internalised. Furthermore, because of the unique spectral properties of the UCNPs (ie: illumination with 980nm laser) a standard flow cytometer does not have the necessary laser line for detection. Therefore, in order to get an accurate endocytosis

efficiency measurement of Ln^{3+} -UCNPs, it is necessary to distinguish between nanoparticle attachment on the surface of the cell, and true uptake by the cells. To achieve this, methods were developed for high resolution fluorescent imaging and image analysis.

Method 1

Previously, silica-coated Ln^{3+} -UCNPs were employed to do the cellular experiment. Firstly, hydrophilic Ln^{3+} -UCNPs with silica coating were dispersed in cell culture media (DMEM + 10% FBS) to make the concentration about 50ug/mL. 1×10^4 cells/well NSC-34 neuron-like cells were seeded into the 12-well plate at 37 °C under 5% CO_2 for 24h. Then 150uL 50ug/mL cell culture media suspension with silica-coated Ln^{3+} -UCNPs was added to each well and incubated for 4h in the 37°C incubator with 5% CO_2 according to the method in our previous report.[5] This was followed by washing with PBS three times, cells were fixed in 4% paraformaldehyde for 30 min at room temperature. The fixed cells were rinsed with PBS and mounted with Vector Vectashield mounting media (USA) before the coverslips were sealed. The imaging procedure was performed using the Olympus FV1200 confocal microscope with a custom-added 980 nm laser. The highest amplification objective (63 \times oil objective) was employed to observe the cell samples with silica-coated Ln^{3+} -UCNPs.

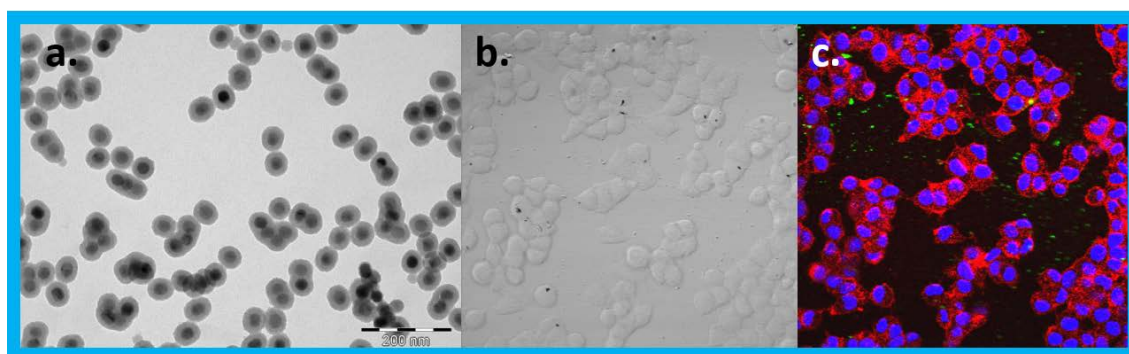


Figure 6. TEM images of silica-coated Ln^{3+} -UCNPs (NaYF_4 :20% Yb,4% Tm) (a), bright field image of NSC-34 cells treated with 50ug/mL silica-coated Ln^{3+} -UCNPs (b) and the merge of upconversion emission of silica-coated Ln^{3+} -UCNPs and cells (nucleus stained with DAPI and membrane stained with deep red plasma membrane stain) under 980nm excitation.

Method 2

During this project, a new microscope became available. Therefore, subsequent experiments were performed using a Zeiss 880 confocal minicroscope which had a higher magnification oil objective ($100\times$ oil objective) with a factory-installed 980nm laser as one of its excitation resource. Furthermore, PEGylated Ln^{3+} -UCNPs were utilized to perform the method optimisation of cellular uptake quantification due to their excellent hydrophilicity and outstanding biocompatibility in cell culture media. The following process is similar as “method 1” except for new additional cell membrane and cell nucleus-staining steps. Typically, the fixed cells were washed with PBS buffer and incubated with $1.5\times$ deep red plasma membrane stain and $2\ \mu\text{M}$ Hoechst 33342 for 10 min at $37\ ^\circ\text{C}$. The labelled cells were rinsed with PBS and mounted with Vector Vectashield mounting media (USA) before the coverslips were sealed.

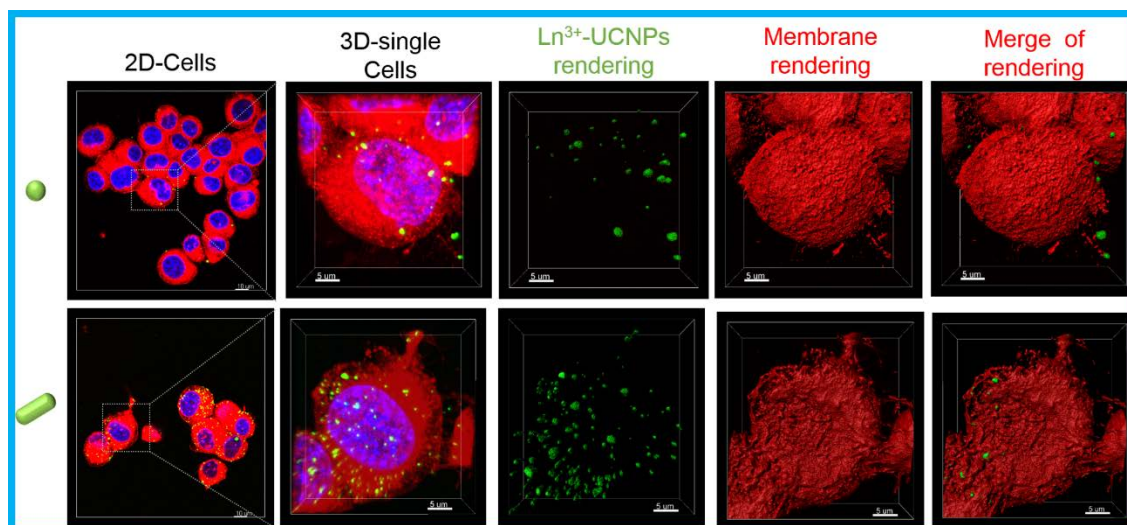


Figure 7. TEM images of PEGylated UCNPs ($\text{NaYF}_4:20\% \text{Yb}, 4\% \text{Tm}$) internalized by NSC-34 neuron like cells. The concentration of PEG-UCNPs at 50ug/mL was used in this experiment under the excitation of a 980nm laser.

Result and Discussion

As shown in the Figure 6, although the brightness of silica-coated Ln^{3+} -UCNPs was strong enough to be detected. However, the bright field image of cells seemed too blurry. Compare with Figure 6, the Figure 7 demonstrated much higher resolution with aid of

100× oil objective. Furthermore, the biodistribution of PEGylated Ln^{3+} -UCNPs is much better than silica-coated ones. Moreover, I can precisely quantify the signal of UCNPs via Imaris software to do cell membrane rendering and nanoparticle rendering. Therefore, after the optimization of imaging conditions greatly improve the imaging quality and is available for further quantification analysis.

2.4 Development of a protocol for quantification analysis of UCNPs internalized by cultured cells

Method

The high-resolution 3-D images of single cell treated with UCNPs are further employed to quantification of modified Ln^{3+} -UCNPs internalized by cells. In this study, I employed 3-dimensional (3D) rendering to precisely analyse the distribution of the surface functionalized UCNPs in the neuron-like cells. Accordingly, the z-stack confocal images of individual NSC-34 cells were processed through Imaris (Bitplane) to generate individual 3D renderings of the cell membrane and UCNP distribution (Figure 8a). Typically, mask selection method was used to identify the nanoparticles inside the cell (Figure 8b). The main steps of mask selection protocol to separate the nanoparticles inside the cells or just close to the cell were shown in Figure 9 to Figure 11. Firstly, I need to create a new surface rendering for cell membrane, then use this whole cell as a base to do the mask selection of the signal from UCNPs. Ultimately, it will form a new signal channel that represents the signal of UCNPs just inside the cells. Additionally, main factors that significantly affect the output of rendering is the value of threshold. Therefore, I need to keep the threshold value consistent when do the membrane rendering of various cells. Only in this way, the value of calculated cellular uptake efficiency of various nanoparticles can be further compared.

Result and Discussion

After the rendering, the volume and intensity of the fluorescence signal of UCNPs inside or outside of a single cell were collected, analysed and 3D-rendered using Imaris software. Subsequently, the fluorescence signal of the cell membrane dye was 3D rendered and used as a mask within Imaris software, which allowed the determination of the volume of the UCNP signal that was either inside the cell, or outside of the cell membrane. This information was used to determine the volume ratio of UCNPs within NSC-34 cells (Vinside) versus the total distribution of UCNPs detected in proximity to the cell (Ventire). The value of Vinside and Ventire was acquired by calculating UCNP uptake in 6 individual cells from confocal microscopy images captured under the same conditions. The average volume of UCNPs identified in association with individual NSC-34 cells (Ventire). Therefore, the value of Vinside/Ventire ratio was regarded as the cellular uptake efficiency of Ln^{3+} -UCNPs.

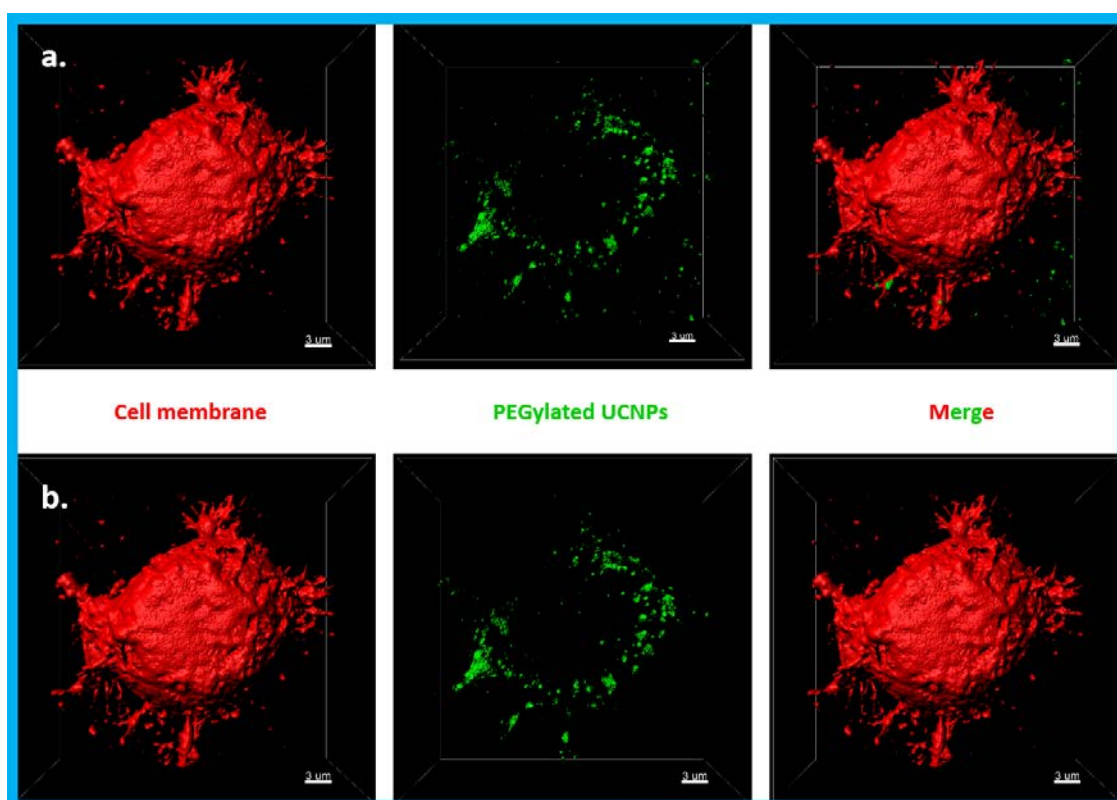


Figure 8. 3D rendering of confocal z-stacks to quantitate the cellular uptake of surface-modified UCNPs. These images represent 3D rendering using Imaris software of PEG-UCNP (green) distribution in an individual NSC-34 cell. Both UCNP and membrane signals were individually

3D-rendered (before, row a), and then the masks overlaid to isolate and exclude any UCNPs signal (after, row b) that is outside of the cell membrane mask (and therefore outside of the cell).

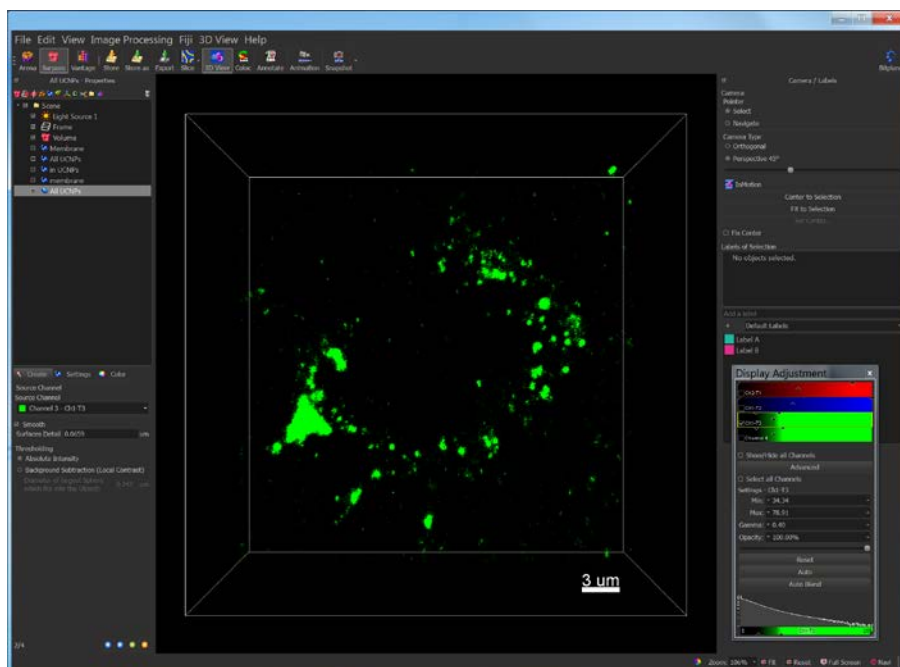


Figure 9. 3-D confocal microscope image of all UCNPs in or outside one single NSC-34 cell.

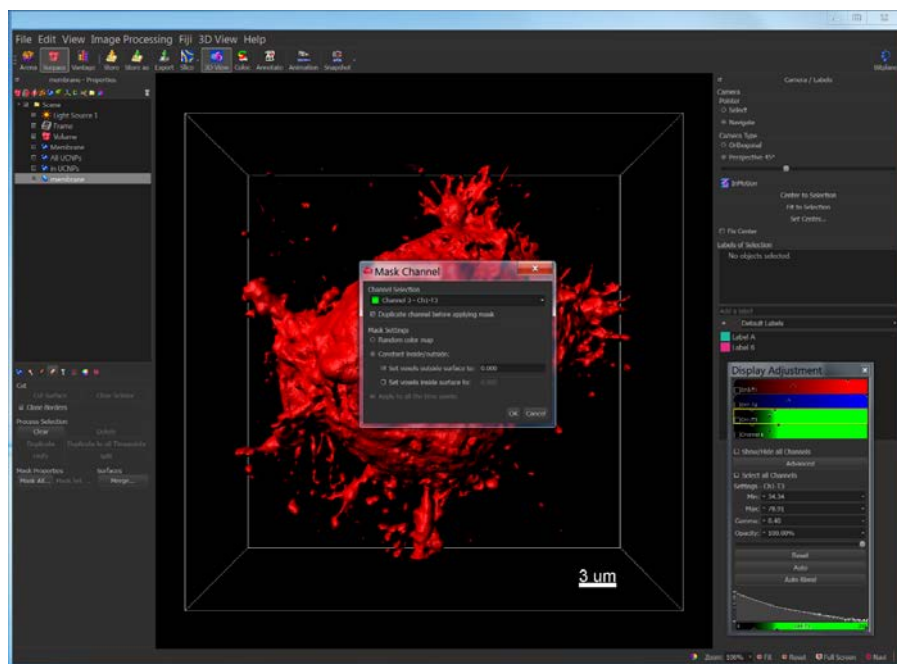


Figure 10. 3-D confocal microscope image of cell membrane rendering used to mask selection for UCNPs inside one single NSC-34 cell.

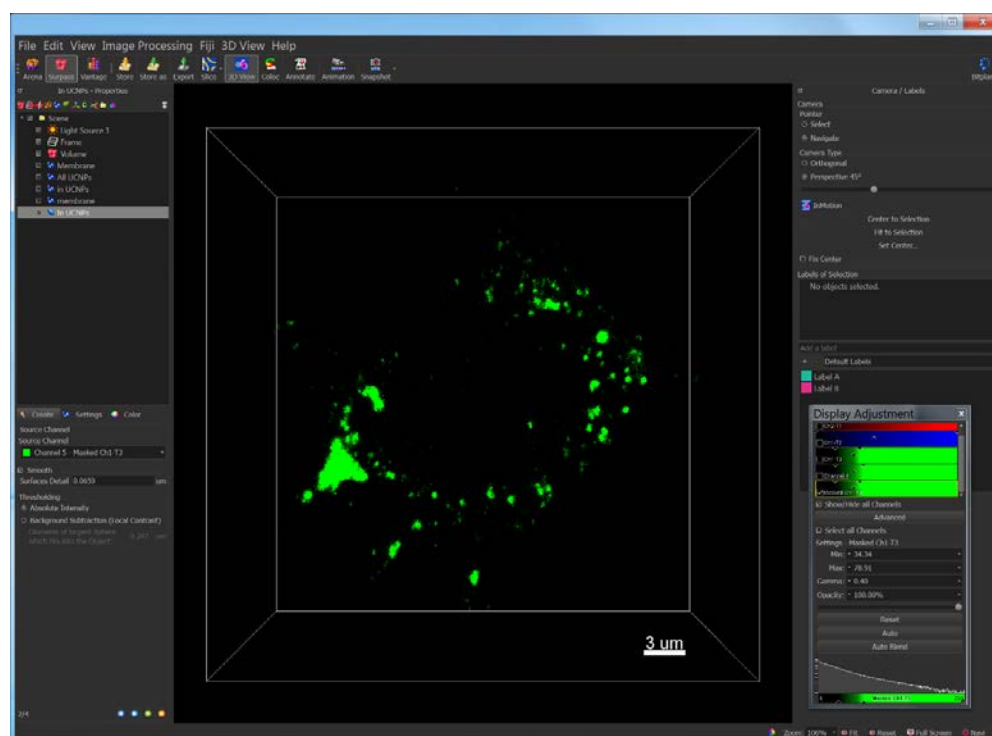


Figure 11. 3-D confocal microscope image of all UCNPs inside one single NSC-34 cell after mask selection (ie: all UCNPs outside of the cell have been subtracted as per Figure 10).

2.5 Development of a protocol for high resolution real-time confocal microscopy of UCNPs in zebrafish

Animal model studies are essential for nanoparticles ultimately applied for clinical application. The zebrafish model is regarded as one of the most suitable models for animal studies, particularly because of their transparent body when young (up to 5 days of age), that allows relatively easy microscopy evaluation of bio-distribution of administered UCNPs. Note that all microinjections of UCNPs into living zebrafish were performed by Dr. Marco Morsch. Imaging in fixed zebrafish was performed by myself.

Method 1 – direct injection into the spinal cord

A first set of optimisation experiments were conducted using 3mg/mL of PEGylated

rod-shaped UCNPs that were directly microinjected into the spinal cord of zebrafish. The biodistribution of UCNPs-PEG was then investigated *in vivo* using optically transparent zebrafish larvae. Five-day-old zebrafish larvae were mounted in 1% low melting agarose before microinjection and imaged as previously described.[6, 7] A suspension of 3 mg mL⁻¹ UCNPs was injected into the spinal cord (labelled with blue fluorescent protein; Tg(-3mnx1:TagBFP)) of five-day-old zebrafish larvae. Approximately, 5 nL solution was injected into the spinal cord and luminescence images were acquired at 2 h after injection. Upon excitation at 980 nm, the distribution of the nanoparticles in the zebrafish could be clearly visualized by confocal microscopy.

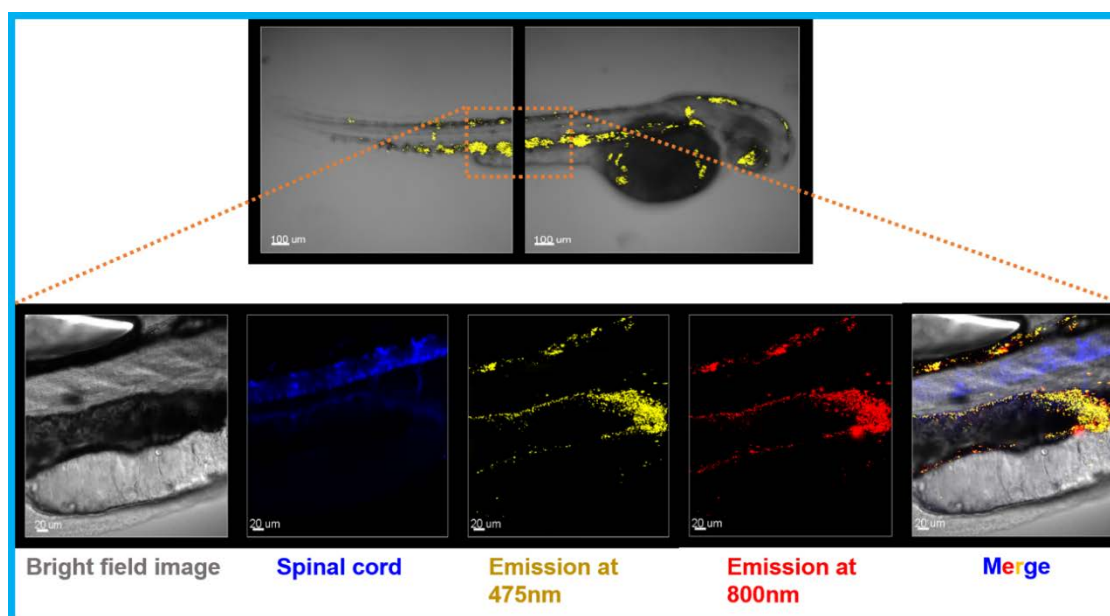


Figure 12. Confocal microscope images of zebrafish injected with PEGylated UCNPs (NaYF₄:20% Yb,4% Tm) into the spinal cord. The concentration of PEG-UCNPs at 3 mg/mL was used in this experiment under the excitation of a 980nm laser.

Method 2 – direct injection into the bloodstream

To visualise UCNPs in the blood stream and subsequently test our particles for uptake into the brain (through the BBB) I first tested different concentrations of UCNPs. To control for the correct uptake of UCNPs specifically into the blood vessels we used transgenic zebrafish (Tg(fli1a:EGFP)) that express GFP in the vasculature.[8] 5 day old

fish were mounted as described above and 3.0 & 1mg/mL injections performed. 5 nL solution was injected into the spinal cord and luminescence images were acquired at 6 h after injection (fed into the fish water in a 28 °C incubator). The concentrations were optimised to test for toxicity and distribution. Here I present the data for 3.0 & 1mg/mL injections. Furthermore, different injection sites were tested to ensure suitable circulation of nanoparticles in the blood stream. Specifically, injections into the dorsal aorta and the caudal vein of zebrafish were compared. Lastly, I compared the spherical and the rod-like Tf-UCNPs at the same concentration (1 mg/mL).

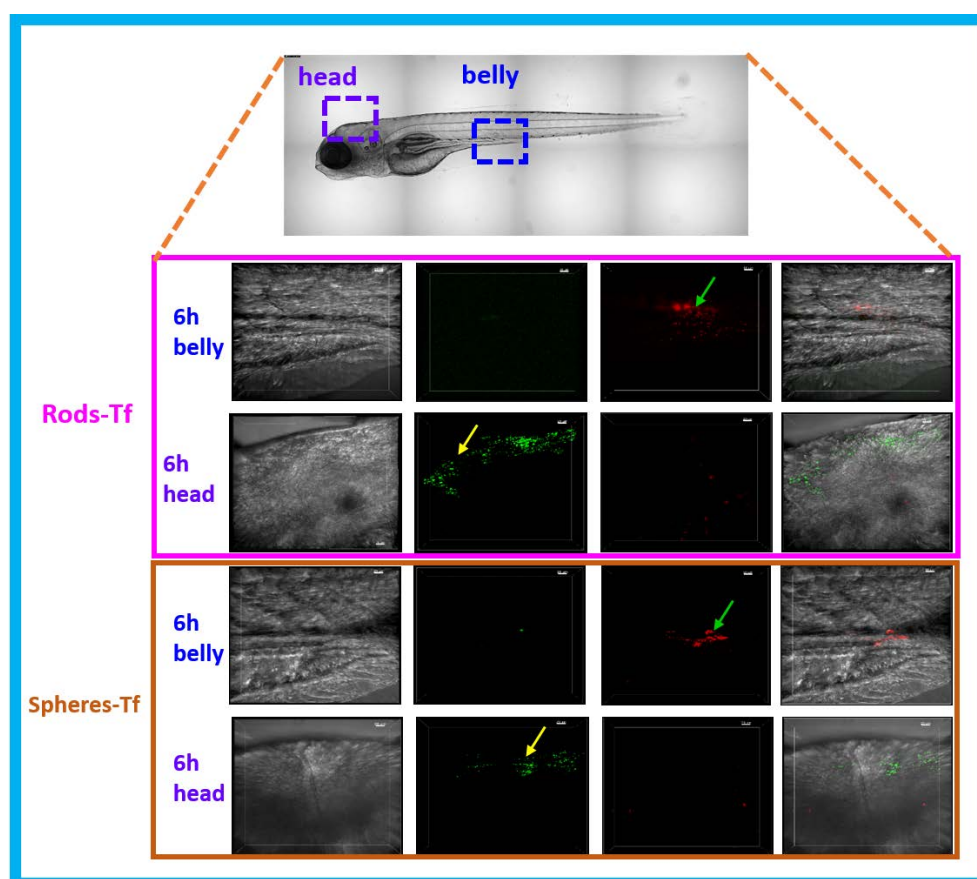


Figure 13. Confocal microscope images of zebrafish injected with rod-like and spherical Tf-UCNPs ($\text{NaYF}_4\text{:}20\%\text{Yb},4\%\text{Tm}$) into the blood vessel and were observe after 6h. The concentration of Tf-UCNPs at 1mg/mL was used in this experiment under the excitation of a 980nm laser.

Result and Discussion

Upon excitation at 980 nm, the distribution of the nanoparticles in the zebrafish spinal cord and vasculature could be clearly visualized. In Figure 12, I present an unsuccessful injection of PEGylated UCNPs into the spinal cord. The image shows that the UCNPs have diffused into the periphery including the gut (no overlap of blue fluorescence (spinal motor neurons) and red or yellow colours (UCNPs)). Further, a concentration of 3mg/mL of nanoparticles was too high and resulted in forming large clusters outside the spinal cord injection site. This was also true for blood vessel injection, 1mg/mL injections showed a far more homogeneous distribution throughout the vasculature. Successful examples of these injections are presented in Figure 8 from paper 1 (attached in Chapter 3) and Figure 7 and Figure 8 from manuscript 2 (shown in Chapter 4). Comparison of injections into the dorsal aorta and caudal vein revealed a higher success rate of circulating NPs for the caudal vein injections and were the preferred method of vascular injection hereafter. (data not shown)

Images in Figure 13 were all observed at 6h after microinjection. At the site of zebrafish belly, the negligible of green signal from both rod and spherical Tf-UCNPs remain in this injection site after 6h. However, the red signal from commercial microbeads which is employed to visual control the microinjection seemed still have quite a lot left at the site where injected. Compared with the spherical Tf-UCNPs observed in the brain, rod-shaped Tf-UCNPs seemed accumulated to be a greater extent than the spherical ones. It confirmed that the rod-shaped Tf-UCNPs exhibited superior BBB penetration capability compared to the spherical ones, and this result was consistent with the cellular experiment result.

2.6 Conclusion

In summary, the optimization of the methodologies and techniques were described and discussed in this chapter. It specifically figured out a standard approach to generate a set of high lanthanide-doped upconversion nanoparticles with uniform morphology. Moreover, it further studied the modification methods and investigated the appropriate

methods to fabricate upconversion nanoparticles with various shapes. Furthermore, the techniques of upconversion nanoparticles detection in vivo and in vitro were established and optimized for first time this work. This chapter represents a significant support part of this project”.

2.7 Reference

- [1] D. Liu, X. Xu, Y. Du, X. Qin, Y. Zhang, C. Ma, S. Wen, W. Ren, E.M. Goldys, J.A. Piper, S. Dou, X. Liu, D. Jin, Three-dimensional controlled growth of monodisperse sub-50 nm heterogeneous nanocrystals, *Nat. Commun.* 7 (2016) 10254. doi:10.1038/ncomms10254.
- [2] S. Wen, D. Li, D. Liu, X. Xu, Y. Du, D.R.G. Mitchell, B. Shi, X. Shi, D. Jin, Seed mediated one-pot growth of versatile heterogeneous upconversion nanocrystals for multimodal bioimaging, *10013* (2016) 1001315. doi:10.1117/12.2245172.
- [3] C. Liu, Z. Gao, J. Zeng, Y. Hou, F. Fang, Y. Li, R. Qiao, L. Shen, H. Lei, W. Yang, M. Gao, Magnetic/upconversion fluorescent NaGdF₄:Yb,Er nanoparticle-based dual-modal molecular probes for imaging tiny tumors in vivo, *ACS Nano*. 7 (2013) 7227–7240. doi:10.1021/nn4030898.
- [4] S. Sivakumar, P.R. Diamente, F.C.J.M. van Veggel, Silica-coated Ln³⁺-Doped LaF₃ nanoparticles as robust down- and upconverting biolabels., *Chemistry*. 12 (2006) 5878–5884. doi:10.1002/chem.200600224.
- [5] B. Shi, H. Zhang, S.Z. Qiao, J. Bi, S. Dai, Intracellular Microenvironment-Responsive Label-Free Autofluorescent Nanogels for Traceable Gene Delivery, *Adv. Healthc. Mater.* 3 (2014) 1839–1848. doi:10.1002/adhm.201400187.
- [6] M. Morsch, R. Radford, A. Lee, E.K. Don, A.P. Badrock, T.E. Hall, N.J. Cole, R. Chung, In vivo characterization of microglial engulfment of dying neurons in the zebrafish spinal cord, *Front. Cell. Neurosci.* 9 (2015). doi:10.3389/fncel.2015.00321.
- [7] D. Cheng, G.J. Shami, M. Morsch, R.S. Chung, F. Braet, Ultrastructural Mapping

of the Zebrafish Gastrointestinal System as a Basis for Experimental Drug Studies, *Biomed Res. Int.* 2016 (2016). doi:10.1155/2016/8758460.

- [8] L. Chen, C. Watson, M. Morsch, N.J. Cole, R.S. Chung, D.N. Saunders, J.J. Yerbury, K.L. Vine, Improving the Delivery of SOD1 Antisense Oligonucleotides to Motor Neurons Using Calcium Phosphate-Lipid Nanoparticles, *Front. Neurosci.* 11 (2017) 1–12. doi:10.3389/fnins.2017.00476.

Chapter 3: A Versatile Upconversion Surface Evaluation Platform for Bio-nano Surface Selection for the Nervous System

This chapter addresses Aim 1 of this thesis, which was to identify a suitable surface modification of lanthanide ions-doped upconversion nanoparticles (Ln^{3+} -UCNPs) to improve their hydrophobicity and biocompatibility for biological applications. The specific goal was to identify a suitably modified UCNP that could be internalized by neurons. At the commencement of this project, the as-prepared unmodified UCNPs were coated with oleic acid on the surface to avoid aggregation, providing a hydrophobic surface that ensures good solubility in organic solvents (such as cyclohexane). However, it became immediately apparent that this surface was not suitable for biological applications, as these OA-capped UCNPs were found to rapidly aggregate in water or cell culture media. Therefore, this chapter describes the workflow that I developed to evaluate the effectiveness of several popular approaches for surface modification of nanoparticles for improving the bioavailability of UCNPs. It turned out that most of these surface modifications resulted in Ln^{3+} -UCNPs readily aggregating and/or exhibiting low biocompatibility with cultured cells (either cytotoxicity or poor cell uptake). However, I was successful in identifying a superior surface modification protocol (PEGylation) which not only prevented UCNP aggregation, but also profoundly increased the biocompatibility of Ln^{3+} -UCNPs with neurons.

In this Chapter, I have presented the development of a nano-bio surface evaluation platform to systematically evaluate the biophysical characteristics of Ln^{3+} -UCNPs with various surface modifications (OA removal, DNA-conjugated, Silica coating and PEG capping), and the subsequent biocompatibility of these UCNPs with cultured neuron-like cells and within the living zebrafish. The results showed that PEG is a preferable surface modification for further applications of Ln^{3+} -UCNPs in

vitro and in vivo. Furthermore, this study demonstrates that Ln^{3+} -UCNPs provide a versatile platform for systematic evaluation of nanoparticle surface modifications, which may have future applications for selecting appropriate surfaces for nanoparticle-based theranostic applications in CNS disorders.

The results generated from this body of research were reported in a first-author peer-reviewed paper “A Versatile Upconversion Surface Evaluation Platform for Bio-nano Surface Selection for the Nervous System”.

3.1 Contribution to Paper 1

	L.F	M.M	B.S	G.W	A.L	R.R	Y.L	D.J	R.C
Experiment Design	●		●						●
Sample Preparation	●	●		●					
Data Collection	●								
Analysis	●			●		●	●		
Manuscript	●		●		●	●	●	●	●

I undertook the majority of work towards this publication (approximately 80%), demonstrating my capability and independence in conducting research from concept development, experimental design, sample preparations, data collections and analysis, to the final stage of publication preparation.

3.2 Paper 1



Nanoscale

PAPER

 View Article Online
 View Journal | View Issue
Cite this: *Nanoscale*, 2017, 9, 13683

A versatile upconversion surface evaluation platform for bio–nano surface selection for the nervous system†

 Libing Fu,^{a,b,c} Marco Morsch,^b Bingyang Shi,^{a,b,c} Guoying Wang,^b Albert Lee,^b Rowan Radford,^b Yiqing Lu,^{a,c,d} Dayong Jin^e and Roger Chung^b

There is considerable interest in developing diagnostic nanotools for early detection and delivery of various therapeutic agents for treatment of neurodegenerative diseases. However, a key challenge remains in the selection of suitable surfaces to overcome the nano–bio interface issue, namely that many nanoparticle surfaces demonstrate instability when administered into biological environments and show substantial cytotoxicity to the central nervous system. In this study, we fabricated an evaluation platform for bio–nano surface selection based on the combination of upconversion nanoparticles (UCNPs), cultured neural cells and zebra fish, and systemically demonstrated how it can evaluate the suitability of nanoparticle surfaces for applications in the central nervous system. Firstly, we fabricated highly lanthanide-doped UCNPs, which generate the strongest tissue penetrable emission at 800 nm. We then functionalized these UCNPs with four popular surfaces for evaluation. Next, we systematically evaluated the spectral emission properties, biophysical stability, cytotoxicity and cell uptake capability of these surface-functionalized UCNPs in biological solutions or with cultured NSC-34 cells. Through these studies, PEG–COOH proved to be the superior surface modification. Accordingly, we further confirmed the bioavailability of unmodified and surface modified UCNPs in the spinal cord of living zebrafish. As predicted, PEG–UCNPs displayed excellent dispersal and uptake into spinal motor neurons in living zebrafish. Collectively, this study developed a versatile upconversion platform for systematic evaluation of nanoparticle surfaces, which can provide valuable information via systemic surface evaluation *in vitro* and *in vivo* for future construction of multifunctional nanosystems for theranostic applications in neurodegenerative diseases.

 Received 18th May 2017,
 Accepted 13th August 2017
 DOI: 10.1039/c7nr03557h
 rsc.li/nanoscale

Introduction

Neurodegenerative diseases including Alzheimer's disease (AD), Parkinson's disease (PD), Huntington's disease (HD) and amyotrophic lateral sclerosis (ALS) have been perplexing physicians and scientists for many years. Recent advances in the development of nanotechnology systems have provided great

potential for diagnostic and therapeutic applications in these disorders – the combination of which is collectively termed “theranostics”. Over the past decade, a variety of functional nanoparticle-based systems have been developed and evaluated for theranostic use in neurodegenerative diseases, including gold nanoparticles for AD diagnostics,^{1,2} cerium oxide nanoparticles for the treatment of oxidative stress-induced damage which occurs in neurodegenerative disorders,^{3,4} PEG–PLGA nanoparticles for the delivery of therapeutic agents across the BBB,^{5–7} silica–DNA nanocomplexes for HD gene therapy,^{8,9} and solid–lipid nanoparticles and carbon nanotubes for the treatment of ALS.^{10,11} These systems have demonstrated the promising potential for theranostics in neurodegenerative diseases. However, there are limitations to these strategies with a key challenge being the requirement to overcome the nano–bio interface, meaning that many nanoparticles are unstable when administered into biological environments and show cytotoxicity to the central nervous system.^{12,13} Furthermore, many of these particles cannot be readily detected in living animals. The nano–bio interface comprises

^aInternational Joint Centre for Biomedical Innovations, School of Life Sciences, Henan University, Jin Ming Avenue, Kaifeng, Henan, 475004, China

^bMotor Neuron Disease Research Centre, Department of Biomedical Sciences, Faculty of Medicine & Health Sciences, Macquarie University, Sydney, NSW, Australia. E-mail: bingyang.shi@mq.edu.au

^cARC Centre of Nanoscale Biophotonics, Macquarie University, Sydney, NSW 2109, Australia

^dDepartment of Physics and Astronomy, Faculty of Sciences and Engineering, Macquarie University, Sydney, NSW, Australia

^eInstitute for Biomedical Materials and Devices (IBMD), Faculty of Science, University of Technology Sydney, Sydney, NSW 2007, Australia

†Electronic supplementary information (ESI) available. See DOI: 10.1039/c7nr03557h

Paper

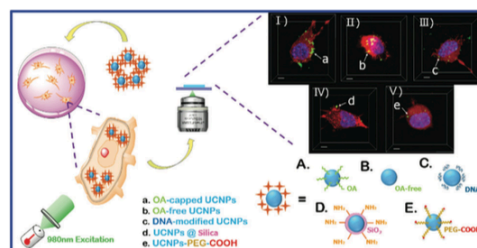
View Article Online

Nanoscale

a dynamic series of interactions between the nanomaterial surface and the interface with biomolecules, which are governed by a variety of forces including long-range forces arising from attractive van der Waals and repulsive electrostatic double-layer interactions, and short-range forces arising from charge, steric, depletion and solvent interactions. These interactions determine processes such as the formation of the protein corona, cellular contact, endocytosis and intracellular transport.¹⁴ Clearly, the selection of a NP surface for a suitable nano-bio interface is of essential importance in the design of NPs that can ultimately be used for neurodegenerative disease theranostics. However, there is no standardized methodology pipeline for systematic surface selection/evaluation for application in the central nervous system.

Upconversion nanoparticles (UCNPs) are nanoscale crystals doped with rare earth ions, which demonstrate stepwise absorption of two (or more) low-energy photons in near infrared (NIR) before emitting one high-energy photon in the UV, visible or NIR spectrum *via* an up-conversion mechanism.^{15–20} In recent years, UCNPs have attracted scientific interest because of their experimental advantages, including non-photobleaching, non-photoblinking, and tunable emission and lifetime, which allow UCNPs to generate stable, background-free signals in complex biological systems where non-specific background “noise” is problematic. Most recently, we developed a new generation of UCNPs *via* a high doping and high power excitation strategy, which leads to significantly enhanced luminescence signals (by up to a factor of 70), allowing the detection of UCNPs at the single nanocrystal level using fluorescence microscopy.²¹ Furthermore, both the excitation (980 nm) and emission (800 nm) of thulium (Tm) doped UCNPs are within the “tissue transparent window”, which presents benefits for their use in bio-imaging applications in living animals where penetration through tissue is required. Importantly, UCNPs have a readily-modifiable surface that can be manipulated for further biomedical applications. The kinds of UCNP surfaces that can be achieved *via* various modification approaches include ligand exchange,^{22–25} ligand interaction,^{26–29} chemical reaction of surface ligands^{30–33} and salinization.^{34–37} These superior properties make UCNPs a suitable potential platform for systemic evaluation of the nano-bio surface interaction for the central nervous system.

In this study, we fabricated a upconversion nano-bio surface evaluation platform based upon the surface modification of a new generation of UCNPs, evaluated for the first time through a pipeline of cultured neural cells and living zebrafish, to systematically demonstrate how suitable nanoparticle surfaces can be selected for further theranostic applications in the nervous system. Firstly, we synthesized highly doped UCNPs (β -NaYF₄:20%Yb,4% Tm) with tissue penetrative emission (800 nm). And then we functionalized the UCNPs with various modification strategies, generating four popular hydrophilic surfaces (OA-free, DNA, silica and PEG-COOH) for evaluation. Secondly, we compared the biophysical characteristics of the functionalized UCNPs including luminescence spectral



Scheme 1 Overview of UCNP fabrication and evaluation of biocompatibility with neurons. UCNPs with different surface modifications are produced, incubated with NSC-34 cells and cell uptake into neurons evaluated *via* confocal microscopy: (A) OA-capped; (B) OA-removed; (C) DNA-conjugated; (D) silica-coated; (E) PEG-modified. The representative confocal microscopy images of I–V are corresponding to UCNPs of types a–e respectively. The nucleus (blue) of cells is stained with DAPI, and the membrane (red) of cells is labelled with deep red plasma. The UCNPs (shown in green, indicated by arrows) are photo-excited using a 980 nm laser (scale bars = 5 nm).

properties and brightness, size, surface charge, aqueous stability and cytotoxicity. Next, we evaluated the cellular uptake and bio-distribution of these surface-modified UCNPs with cultured neural cells using confocal microscopy and Imaris software (Scheme 1). This systematic evaluation identified that the surface priorities for neural cells are PEG-COOH > DNA > OA-free > silica-NH₂ in terms of stability, low cytotoxicity and high cell uptake efficiency. Finally, we confirmed that PEG is a preferable surface for nanoparticle applications in the nervous system *via* evaluating the dispersion and bioavailability of PEG-UCNPs in the spinal cord of living zebrafish.

Results and discussion

Fabrication and characterization of upconversion nanoparticles with various surfaces

To produce luminescent nanoparticles for surface evaluation, we firstly synthesized an improved version of UCNPs (β -NaYF₄:20%Yb,4% Tm) from our prior studies.^{38,39} These UCNPs were subjected to a different rare-earth-metal doping strategy that yields higher photo-emission properties.⁴⁰ Transmission Electron Microscopy (TEM) revealed that the UCNPs were spherical with a uniform size (Fig. 1A). Dynamic light scattering (DLS) measurements demonstrated that they have a uniform size distribution (summarised in Fig. 1f). We then functionalised the surface of UCNPs with four established hydrophilic surfaces (OA-free, DNA, silica-NH₂ and PEG-COOH), using various surface modification strategies (see details in Fig. S1†). As shown in Fig. 1b–e, TEM images demonstrate that all of the surface-modified UCNPs displayed a relatively uniform spherical shape with a narrow size distribution (details shown in Fig. S2†).

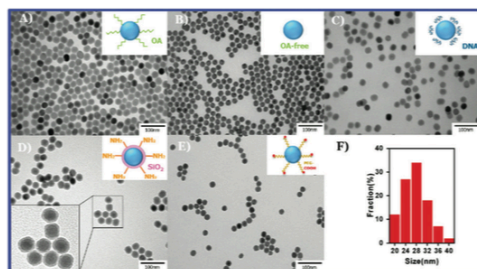


Fig. 1 Transmission electron microscopy (TEM) images of spherical $\text{NaYF}_4:20\%\text{Yb},4\%\text{Tm}$ nanoparticles (UCNPs) with different surface modifications. i.e., unmodified (A), OA-free (B), DNA-functionalized (C), silica-coated (D), PEG-COOH-modified (E) and the size distribution of unmodified UCNPs (F).

To systematically verify the biocompatibility properties introduced by the various surface modifications upon UCNPs, the physico-chemical properties of the modified UCNPs in water and cell culture media (DMEM, 10% FBS) were characterized by DLS. As summarized in Table 1, unmodified UCNPs displayed the largest average hydrodynamic diameter (408 nm) in water, presumably because their hydrophobic surface caused aggregation. After modification, all functionalized UCNPs demonstrated good water solubility with diameters within the range of 33.98 to 40.65 nm (single non-aggregated particles). The amine-functionalized UCNPs@silica are susceptible to aggregation in water because the positively charged amines and the negatively charged silicate surface lead to electrostatic attraction at physiological pH 7.0.⁴¹ The hydrodynamic diameter of all functionalized UCNPs increased slightly in the cell culture media compared to those in water due to the formation of a protein corona. Furthermore, zeta potential measurements demonstrated that the surface charge of unmodified UCNPs was negative (-9.31 mV) and significantly increased after surface modification including OA-removal (0.03 mV), DNA (15.71 mV), silica- NH_2 (7.55 mV) and PEG-COOH (-6.32 mV). The zeta potential of all the UCNPs decreased when dispersed in cell culture media compared to those in water because of the absorption of negatively charged serum proteins onto the nanoparticles.⁴² Altogether, these changes in the zeta potential indicated the success of surface

modifications to alter the hydrophobicity and make these particles more readily biocompatible (i.e. water soluble) compared to unmodified UCNPs.

Upconversion photoluminescence spectral properties of surface functionalized UCNPs

To investigate the influence of surface modification on the optical properties of UCNPs, the upconversion photoluminescence (UC PL) properties of unmodified UCNPs (OA-UCNPs) in cyclohexane and surface-modified UCNPs dispersed in MilliQ water at the same concentration (1 mg mL^{-1}) were evaluated under exposure to continuous wave (CW) excitation at 980 nm (1.6 W cm^{-2}). The upconversion fluorescence spectra exhibited three major emission peaks at 475 nm, 700 nm and 800 nm, which are attributed to the $^1\text{D}_2 \rightarrow ^3\text{H}_6$, $^3\text{F}_{2,3} \rightarrow ^3\text{H}_6$ and $^3\text{H}_4 \rightarrow ^3\text{H}_6$ transitions, respectively (Fig. 2A).⁴³ The emission intensity at 800 nm is much higher than the other emissions, suggesting that the UCNPs have high tissue penetrative properties. While the peak emission wavelengths remained unchanged following surface modification, the fluorescence signal intensity of functionalized UCNPs was lower in comparison to the unmodified UCNPs (Fig. 2B and Fig. S4†). However, the luminescence intensity of the OA-free UCNPs dispersed in water is higher compared to that of the OA-capped UCNPs dispersed in cyclohexane. The results indicated that the OA-layer covered on the surface of $\text{NaYF}_4:\text{Yb}^{3+},\text{Tm}^{3+}$ nanocrystals affects the fluorescence emission. In summary, although the UC PL slightly decreased after modification

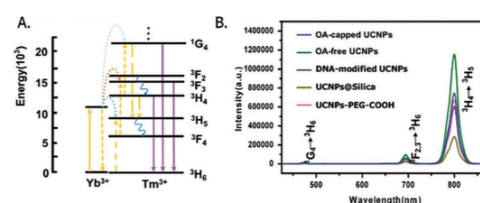


Fig. 2 (A) Overview of the upconversion photoluminescence (UCPL) properties of $\text{Yb}^{3+}-\text{Tm}^{3+}$ mediated photo-emissions of UCNPs. (B) Comparison of the UCPL spectra of colloidal UCNPs with various surface modifications (OA-capped, OA-free, DNA-modified, silica-coated and PEG-COOH functionalized UCNPs) under CW excitation of a 980 nm laser.

Table 1 Summary of the biophysical properties of unmodified and surface-modified UCNPs dispersed in water and cell culture media (DMEM, 10% FBS)

Surface modification of UCNPs	Surface moiety	Method	Solubility	Size(nm)		ζ -Potential (mV)	
				MilliQ water	Cell culture media	MilliQ water	Cell culture media
OA-capped UCNPs	OA	Oxygen-free	Hydrophobic	408.03 ± 3.51	417.71 ± 4.94	-9.31 ± 0.18	-12.08 ± 0.16
OA-free UCNPs	RE cations	Acid treatment	Hydrophilic	40.65 ± 0.36	41.94 ± 0.76	0.03 ± 0.01	-1.07 ± 0.11
DNA-modified UCNPs	DNA	One-step ligand exchange	Hydrophilic	39.42 ± 0.23	43.81 ± 0.51	15.71 ± 0.34	-18.95 ± 0.24
UCNPs@ SiO_2	SiO_2	Reverse microemulsion	Poor hydrophilic	206.95 ± 1.99	217.01 ± 4.24	7.55 ± 0.08	2.48 ± 0.01
UCNPs-PEG-COOH	PEG-COOH	Ligand exchange	Hydrophilic	37.98 ± 0.27	40.19 ± 0.52	-6.32 ± 0.09	-8.91 ± 0.08

(except for OA-free UCNPs), the emission at 800 nm is still of sufficient intensity to be highly detectable in biological environments.

Biostability of functionalized UCNPs with various surfaces in cell culture medium

The physical stability of functionalized UCNPs was assessed in cell culture medium (DMEM, 10% FBS) according to standard methods.⁴⁴ Utilizing dynamic light scattering, we observed an initial increase in the size of all UCNPs within the first 2 h of exposure to cell culture medium, presumably due to protein corona formation. The size of UCNPs remained stable over the following 10 h in the cell culture medium (Fig. 3). The relative biostability of UCNPs in culture medium was confirmed using a TEM and confocal microscope (under 980 nm laser excitation), with a size distribution of surface-modified UCNPs in the order of (from the largest to the smallest) unmodified > silica-NH₂ > DNA > OA-free > PEG-COOH (as shown in Fig. S3†). This result conforms to the data in Fig. 3. According to the results above, it may be advantageous to pre-incubate the UCNPs in culture medium for 2 h to form a stable conformation prior to further use in biological experiments.

Cytotoxicity evaluation of functionalized UCNPs with various surfaces with cultured neural cells

The cytotoxicity of UCNPs with different surface modifications was investigated with motor neuron-like cells (NSC-34) in the concentration range from 1 to 100 $\mu\text{g mL}^{-1}$ using a standard MTT viability assay (which detects living cells based upon their metabolic activity). As shown in Fig. 4A, OA-capped and silica-coated UCNPs displayed a significant cytotoxicity (at 50–100 $\mu\text{g mL}^{-1}$ concentrations), leading to 20–30% reduction in cell viability after 24 h of exposure to UCNPs. In contrast, the other three types of UCNPs (OA-free, DNA-modified and PEG-COOH functionalized UCNPs) displayed minimal cytotoxicity (<10% reduction in cell viability) under the same con-

ditions. To confirm these cytotoxicity results, we used a second viability assay which detects the number of dying cells by the accumulation of lactate dehydrogenase (LDH) into the culture medium (LDH is only released from dying cells). The result of the LDH assay confirmed that OA-free, DNA-modified and PEG-COOH functionalized UCNPs all display a reduced cytotoxic effect upon NSC-34 cells compared to silica-coated and unmodified UCNPs (Fig. 4B). Notably, PEG-COOH UCNPs displayed the least amount of cytotoxicity in both cell viability assays, indicating that PEG-COOH is a preferable surface modification for neuronal delivery of UCNPs. For comparison, the UCNP surface modifications displaying low to high cytotoxicity are in the order of PEG-COOH > DNA > OA-free > silica-NH₂.

Evaluation of neuronal uptake capability of the modified UCNPs with various surfaces

The functionalized UCNPs with various surfaces were further evaluated for their cellular uptake capability and distribution with NSC-34 cells using confocal microscopy. Firstly, we determined the optimal concentration of UCNPs to be applied to NSC-34 cells to allow confident detection and quantitation (see details in Fig. S5†). In the tested range from 20–500 $\mu\text{g mL}^{-1}$, we identified 20 $\mu\text{g mL}^{-1}$ as the suitable concentration due to better uptake. To confidently visualize the internalization of UCNPs (emission at 800 nm, green) and distinguish them from particles that are stuck on the membrane and not actually internalised, the cell membrane was stained with plasma membrane stains (red) and the nucleus was labelled with Hoechst dye (blue). The non-modified UCNPs (OA-capped) and surface-functionalized UCNPs (OA-free, DNA, silica-NH₂, PEG-COOH) were preincubated with cell culture medium for 2 h to form stable colloidal nanoparticles and then incubated with NSC-34 cells for 4 h. As shown in Fig. 5, the OA-capped UCNPs formed large aggregates that adhered onto the outer cell surface (Fig. 5A). After modification, the OA-free, DNA and PEG-COOH functionalized UCNPs all showed some uptake

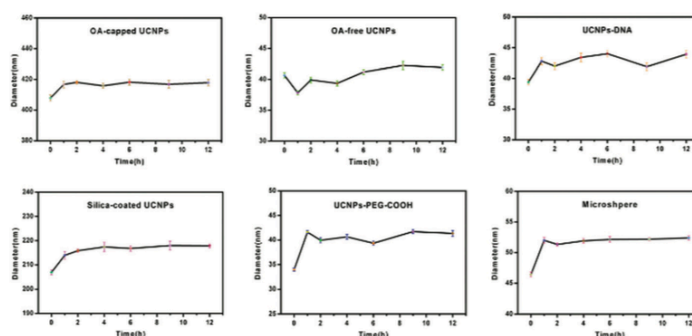


Fig. 3 Assessment of the biostability of UCNPs in cell culture medium (DMEM, 10%FBS). Surface-functionalized UCNPs were incubated in the cell culture medium at 37 °C up to 12 hours, and dynamic light scattering was used to determine the particle size at 0, 1, 2, 4, 6, 9, 12 h post-incubation. There was no significant change in the size of UCNPs after 2 h incubation, indicating that they have reached a biostable equilibrium in the cell culture medium.

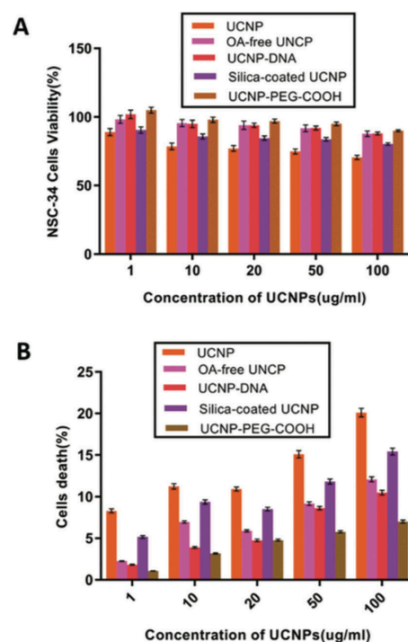


Fig. 4 Cell viability analysis of NSC-34 cells following treatment with surface-modified UCNP. Surface-modified UCNP (OA-free UCNP, UCNP-DNA, silica-coated UCNP and UCNP-PEG-COOH) were applied in the cell culture medium across a broad concentration range (1, 10, 20, 50 and 100 $\mu\text{g mL}^{-1}$) for 24 h. (A) Results from the MTT assay; (B) results from the LDH assay.

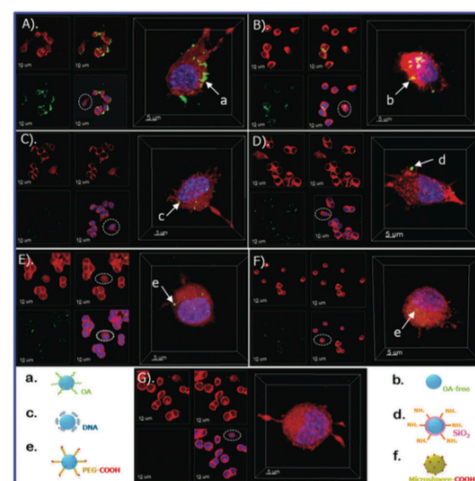


Fig. 5 Confocal microscopy evaluation of UCNP uptake into NSC-34 cells. Surface-modified UCNP were applied to cultured cells for 4 hours ($20 \mu\text{g mL}^{-1}$ concentration), followed by fixation and confocal imaging. (A) OA-capped UCNP, (B) OA-free UCNP, (C) UCNP-DNA, (D) silica-coated UCNP, (E) UCNP-PEG-COOH, (F) commercial fluorescent microspheres with the carboxyl group on the surface (positive control, 580/605 nm) and (G) untreated cells. The upconversion luminescence from UCNP is shown in green, the cell membrane dye in red, and the cell nucleus in blue. Each of the surface-modified UCNP is marked as a–e and their formulation is illustrated in the lower panels. The high magnification insert in each panel is a 3D-reconstruction of one representative cell (white dotted circle).

into NSC-34 cells (Fig. 5B, C and E respectively). The silica-coated UCNP were also found to aggregate and form large clusters on the cell membrane (Fig. 5D). We employed fluorescently-labelled commercial microspheres as a positive experimental control, which were readily internalized by NSC-34 cells under the same experimental conditions (Fig. 5F).

To further confirm whether UCNP were internalized by NSC-34 cells, we used high-resolution confocal imaging and 3-dimensional (3D) rendering to precisely analyse the distribution of the surface functionalized UCNP in the motor neuron-like cells. In Fig. 6A, the 3D-simulation of PEG-UCNP (green) distribution in an individual NSC-34 cell demonstrates that the signals of UCNP-PEG-COOH are localised inside the single cell after signal-selection rendering. Accordingly, the z-stack confocal images of individual NSC-34 cells were processed through Imaris (Bitplane) to generate individual 3D renderings of the cell membrane and UCNP distribution (Fig. 6A). Firstly, the volume and intensity of the fluorescence signal of UCNP inside or outside of a single cell were collected, analysed and 3D-rendered using Imaris software. Subsequently, the fluorescence signal of the cell membrane dye was 3D rendered and used as a mask within Imaris soft-

ware, which allowed the determination of the volume of the UCNP signal that was either inside the cell, or outside of the cell membrane. This information was used to determine the volume ratio of UCNP within NSC-34 cells (V_{inside}) versus the total distribution of UCNP detected in proximity to the cell (V_{entire}). The value of V_{inside} and V_{entire} was acquired by calculating UCNP uptake in 6 individual cells from confocal microscopy images captured under the same conditions. The average volume of UCNP identified in association with individual NSC-34 cells (V_{entire}) and the volume of UCNP inside the cell (V_{inside}) demonstrate clearly that PEG-COOH UCNP display superior cellular uptake capability – and therefore the $V_{\text{inside}}/V_{\text{entire}}$ ratio for PEG-COOH UCNP was set to 100%. As shown in Fig. 6B, the cell uptake ratios of unmodified UCNP and surface-modified UCNP (OA-free, DNA and silica-coated UCNP) were 4.8%, 38.7%, 48.4% and 9.7% respectively, which is accordingly substantially lower than the uptake capability of PEG-functionalized UCNP. As expected, the commercial microspheres demonstrated good cell uptake (87.2%), although this was slightly lower than the uptake of PEG-UCNP. The calculated average volume of PEG-COOH functionalized UCNP internalized by cells was 561.0 cm^3 per cell. This was substantially greater than the minimal uptake

View Article Online

Nanoscale

Paper

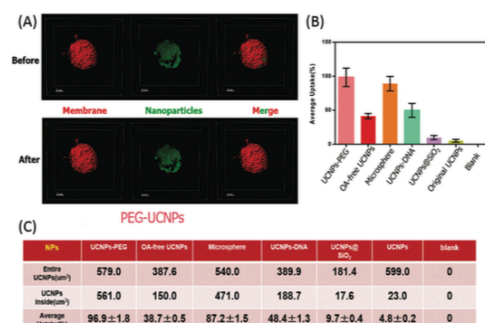


Fig. 6 3D rendering of confocal z-stacks to quantitate the neuronal uptake of surface-modified UCNPs. (A) 3D rendering using Imaris software of PEG-UCNP (green) distribution in an individual NSC-34 cell. Both UCNP and membrane signals were individually 3D-rendered (before), and then the masks overlaid to isolate and exclude any UCNP signal (after) that is outside of the cell membrane mask (and therefore outside of the cell). (B) The average volume ratio ($V_{\text{inside}}/V_{\text{entrance}}$) of cellular uptake into individual NSC-34 cells for the surface-modified UCNPs. All values have been normalized against the uptake of PEG-COOH functionalized UCNPs. (C) The average volume of UCNPs identified in association with an individual NSC-34 cell (V_{entrance}) and the volume of UCNP inside the cell (V_{inside}) demonstrates clearly that PEG-COOH UCNPs display superior cellular uptake capability. The values of V_{inside} and V_{entrance} were the average of 6 cells analyses.

like the UCNPs@silica (only 17.6 cm³ per cell, as shown in Fig. 6C). These data indicate that PEG-COOH-modified UCNPs display superior uptake capability to other surface modified UCNPs and even commercially available nanoparticles.

Photostability evaluation of surface-modified UCNPs

A particular advantage of UCNPs is their photostability; we have previously demonstrated that such rare-metal doped NPs display inextinguishable photoluminescence.⁴⁵ To confirm that this property is maintained following application to NSC-34 cells, we undertook a characterization study on the photoquenching of the signal. Here, silica-UCNPs were used as representative functionalized UCNPs because they form reasonably large aggregates that readily adhere to the cell surface, in comparison to commercial fluorescent microspheres (FM). The silica-UCNPs were incubated with NSC-34 cells at 37 °C for 4 h, followed by regular confocal image capture and photo-stability evaluation over a 12-h period. To confirm the proximity of UCNPs to cells, we performed membrane and nuclear labelling with deep red plasma (red, membrane) and Hoechst dye (blue, nucleus) as described in Fig. 6. As shown in Fig. 7A and C, both silica-UCNPs and FMs display a strong and readily detectable signal at the start of the imaging sequence. Notably, despite 12 h of continuous 980 nm laser excitation, the silica-UCNPs maintained their emission intensity (Fig. 7B). However, the fluorescence signal

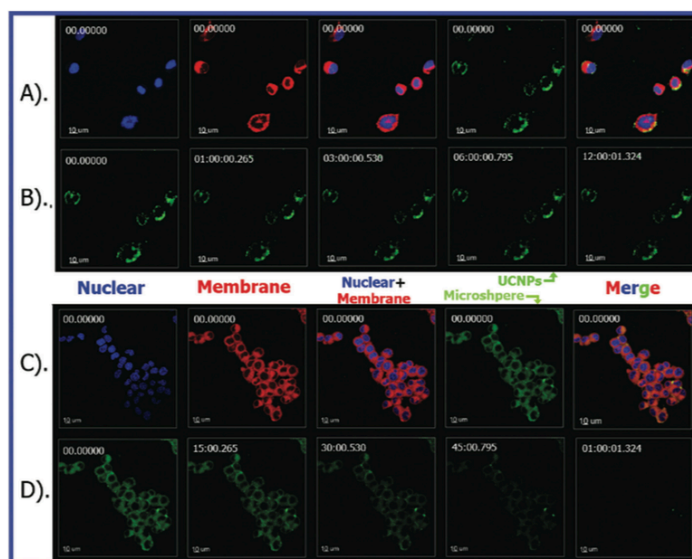


Fig. 7 The photo-stability evaluation of functionalized UCNPs. (A) Confocal images of NSC-34 cells treated with 20 μg mL⁻¹ commercial fluorescent microspheres; (B) fluorescent signals of microspheres at various times (0, 15 min, 30 min, 45 min and 1 h) under continuous excitation; (C) confocal images of NSC-34 cells treated with 20 μg mL⁻¹ PEG-UCNPs; (D) luminescent signals of functionalized UCNPs at different times (0, 1 h, 3 h, 6 h and 12 h) under continuous excitation. The number at the top left of each image means the relative time of every image captured.

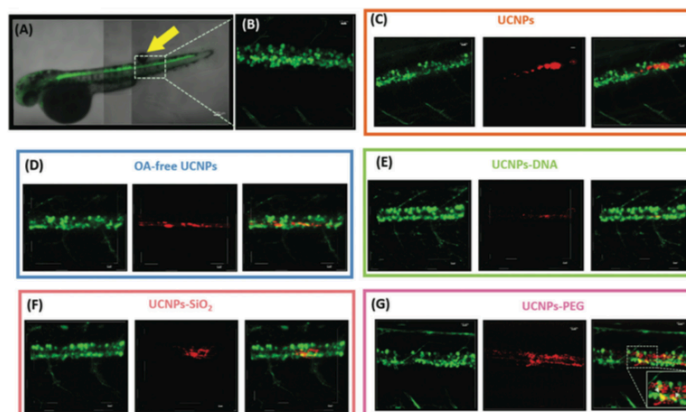


Fig. 8 Evaluation of NP uptake in the zebrafish spinal cord. (A) A transgenic zebrafish with BFP tagged motor neurons in the spinal cord (pseudocoloured in green). The injection site is marked by a yellow arrow. (B) The amplified image of the fluorescent section of spinal cord motor neurons. (C–G) Confocal images of unmodified, OA-free, DNA-modified, silica-coated and PEG-capped UCNPs in the spinal cord of zebrafish. These images in figures C–G were captured at 2 h after nanoparticle injection, in which the nanoparticles are red and motor neurons were tagged with blue fluorescent protein.

of FMs displayed rapid photobleaching, fading after only 15 minutes of excitation at 561 nm, and almost fully absent after a further 30 min of photo-illumination (Fig. 7D). The results demonstrated that the developed upconversion nanoparticle platform is able to provide a reliable fluorescence signal for further evaluation in the biological environment.

Evaluation of UCNP's bioavailability and distribution in living zebrafish

To further investigate the distribution of unmodified and surface modified UCNP in living animals, we used transparent zebrafish larvae at 5 days post fertilisation. Moreover, their rapid development and feasible size allowed us to readily inject UCNP directly into the spinal cord to evaluate neuronal uptake. A further advantage is that we have generated a transgenic zebrafish that specifically expresses blue fluorescent protein (BFP) in spinal motor neurons, this allows us to visualize these motor neurons and track UCNP uptake in real time in living animals. The unmodified and surface modified UCNP were microinjected directly into the spinal cord of the transgenic zebrafish expressing blue fluorescent protein (see Fig. 8A and B). Following UCNP injection, the zebrafish were observed under a confocal microscope with a 980 nm laser at 2 h post-injection (Fig. 8C–G). Over this experimental course, the unmodified UCNP dispersed poorly from the initial injection site, and were visualized as large extracellular structures (Fig. 8C). This correlates with the rapid aggregation of unmodified UCNP that was observed in cell culture studies (Fig. 3 and 6). Similarly, the silica-coated UCNP demonstrated poor diffusion from the initial injection site into the spinal cord,

although slightly better diffusion than unmodified UCNP (Fig. 8F). On the contrary, we observed rapid dispersal of the PEG-UCNP throughout the spinal cord from the initial injection site (Fig. 8G). Notably, we observed some specific neuronal uptake of PEG-UCNP in the spinal cord (these are identified as yellow cells demonstrating co-localisation between PEG-UCNP and BFP-labelled motor neurons, which are marked by arrows in Fig. 8G). The OA-free and DNA-modified UCNP demonstrated some diffusion from the initial injection site into the spinal cord, although this was less than the PEG-UCNP. There was also minimal evidence of the neuronal uptake of OA-free and DNA-modified UCNP, despite these particles displaying good diffusion capability following injection into the spinal cord of zebrafish.

Conclusions

In this study, we have developed a versatile nanoparticle surface evaluation platform based upon the use of easy-to-modify new-generation UCNP, tested through a pipeline of biophysical characterisation, cultured motor neuron like cells and zebrafish models as a process for nano-bio surface selection for nervous system application. The developed upconversion platform is able to precisely select biocompatible and stable nanoparticle surfaces for further application in neurodegenerative diseases *via* systemically comparing the physicochemical properties (upconversion emission, nanoparticle size, surface zeta potentials and stability) and evaluating their biocompatibility (cytotoxicity, cell uptake and biophotonic stability) in mouse NSC-34 motor neuron cells, and dispersion and neuron internalization in the spinal cord of living zebra-

View Article Online

Paper

Nanoscale

fish. Our results suggest that the surface of nanoparticles plays a key role in the bio-nano interface (such as the hydrophobicity, stability and aggregation), which further affects the *in vitro* cytotoxicity and cell uptake efficiency. For example, the silica-NH₂ surface resulted in an unstable bio-nano interface and aggregated clusters (large size), leading to higher cytotoxicity and weaker cellular uptake in neuron-like cells compared with other modified UCNPs. In summary, this study provides important information on nanoparticle surface selection for applications in the central nervous system, towards constructing multifunctional nanosystems that can overcome nano-bio challenges for future theranostic use in neurodegenerative diseases.

Experimental

Materials and methods

Yttrium chloride hexahydrate (YCl₃·6H₂O, 99.99%), ytterbium chloride hexahydrate (YbCl₃·6H₂O, 99.99%), thulium chloride hexahydrate (TmCl₃·6H₂O, 99.99%), sodium hydroxide (NaOH, 99%), ammonium fluoride (NH₄F, 99%), oleic acid (OA, 90%), 1-octadecene (ODE, 90%), tetraethyl orthosilicate (TEOS), (3-aminopropyl)triethoxysilane (APTES, 99%), IGEPAL® CO-520, and ammonium hydroxide solution (NH₄OH, 30%) were all purchased from Sigma-Aldrich and used as received without further purification. The DNA linkers (5'-TTC CTC CAG ACT GAG GTC TTC-3') with amine and thiol modifications were obtained from Integrated DNA Technologies. Dulbecco's modified Eagle's medium (DMEM), fetal bovine serum (FBS), DAPI, Hoechst 3342, and deep red plasma membrane stain were obtained from Invitrogen Life Technologies (Mulgrave, Australia).

Ligand-exchange bio-conjugation for DNA-modified UCNPs. 46 10 µl of 10 mg mL⁻¹ original UCNPs were added into 400 µl chloroform, and then mixed with 300 µl ultrapure H₂O solution containing purified DNA-protein conjugates. After two hour incubation on a mixer (details see Fig. S6†), the upper layer solution was taken out and then centrifuged twice at 14 000 rpm for 5 min. The final settlement was dissolved in 100 µl ultrapure H₂O with sonication for 5 seconds. The UCNPs-DNA were dispersed in MilliQ-water for further use.

Silica coating on UCNPs. To fabricate SiO₂-coated UCNPs, we used a modified water-in-cyclohexane (W/C) reverse micro-emulsion coating approach.⁴⁷ Firstly, a cyclohexane dispersion of NaYF₄:Yb,Tm nanocrystals (0.1 mmol mL⁻¹, 1 mL), IGEPAL CO-520 (1 mL) and cyclohexane (20 mL) was magnetically mixed in a glass flask for 30 min. Then, 35 mL of ammonia (30 wt%) was injected into the solution and a transparent emulsion formed after sonicating for 40 minutes. Thereafter, 100 µL of TEOS was added as the silica shell precursor and the solution was kept under gentle stirring (controlled at 600 rpm) at room temperature for two days. After that, 10 mL acetone was added to precipitate the silica-coated UCNPs from the micro-emulsion. The nanoparticles were centrifugally washed with ethanol two times to remove the excess surfactant, and

then washed with water to remove ethanol, and finally redispersed in water for use.

Synthesis of UCNPs-PEG-COOH. Firstly, a dichloromethane solution of NOBF₄ was used to turn UCNPs hydrophilic according to the literature.⁴⁸ In a typical process, 5 mL of cyclohexane (containing UCNPs ~5 mg mL⁻¹) was combined with 5 mL of dichloromethane (DCM) solution of NOBF₄ (0.01 M) at room temperature. The mixture was shaken overnight to transfer UCNPs from the upper cyclohexane layer to the bottom DCM layer. After centrifugation to remove the supernatant, the pellet (UCNPs) was redispersed in DMF at the concentration of 10 mg mL⁻¹. Then, 200 µL of solution (~2 mg UCNPs) was taken into a bottle and 2 mL of 100% ethanol was added and stirred, followed by 10 mg PEG dispersed in 1 mL water. The mixture solution became cloudy. Then water (~3 mL) was added until the solution became clear and stirred for 48 h. Finally, the UCNPs-PEG-COOH were washed with water 5 times.

Size, zeta potential, absorption spectrum and emission spectrum measurements. The as-synthesized UCNPs were characterized by transmission electron microscopy (TEM). 10 µl of aqueous dispersion of UCNPs was placed on a formvar-coated copper grid (300 meshes), dried and measured with a Philips CM10 TEM with Olympus Sis Megaview G2 Digital Camera. ImageJ freeware was employed for the UCNPs size distribution analysis. The sizes and zeta-potentials of the modified UCNPs were measured using a Zetasizer Nano ZS (Malvern Instruments, U.K.) at 25 °C in two different solutions. UCNPs size and zeta potential measurements by dynamic light scattering were carried out in MilliQ water and DMEM cell culture media (including 10% FBS and 1% p/s). The Thermo Scientific Nanodrop 2000 Spectrophotometer was used to measure the spectrum profiles of the DNA-modified UCNPs, as well as the pure DNA. Two microliters of each sample were placed on the lower measurement pedestal to obtain the spectrum profiles. The HORIBA Scientific FluoroLog spectrofluorometer with 980 nm laser excitation was employed to obtain the emission spectrum of the as-synthesized UCNPs.

Cell imaging with confocal microscopy. Surface-modified UCNPs at the concentration of 0, 20, 50, 100 and 500 µg mL⁻¹ were incubated with NSC-34 cells at 37 °C for 4 h under 5% CO₂ according to our well-established method.⁴⁹ After washing with PBS three times, cells were fixed in 4% paraformaldehyde for 30 min at room temperature. The fixed cells were washed with PBS and incubated with 1.5× deep red plasma membrane stain and 2 µM Hoechst 33342 for 10 min at 37 °C. The labelled cells were rinsed with PBS and mounted with Vector Vectashield mounting media (USA) before the coverslips were sealed. The cells without UCNPs served as the blank control. Furthermore, a commercial fluorescent microsphere was employed as the positive control and the OA-capped UCNPs served as the negative control in this process. Confocal microscopy measurement was performed in order to confirm internalization and quantification of the localized UCNPs using a laser-scanning fluorescence confocal microscope (ZEISS LSM 880 with Airyscan) illuminated with a custom-built

View Article Online

Paper

Nanoscale

980 nm laser module. The oil-immersions of 40× and 100× were used in this imaging process. The excitation intensity was set to $9.8 \times 10^7 \text{ W cm}^{-2}$. For each cell culture, a minimum of three different cell areas was imaged.

Quantification of UCNP uptake in NSC-34 cells. Nanoparticle uptake was quantitatively calculated using the Imaris software. For each cell culture slide, a minimum of three different cell areas was imaged. For the image analysis, stains for the nucleus and membranes were used to outline single cells, cell clusters, or a monolayer region within the excitation spot. The signal from the pixels of the same area in the PL images was processed by subtracting the background and correcting for the exposure time. The resulting UCNP signals were quantified as a mean UCNP signal per area, which was a measure of the mean cellular uptake of UCNPs. The relative intensity of the UCNP PL signal was recorded and normalized with respect to the largest cellular uptake level observed (that of UCNPs-PEG-COOH; see Fig. 6), which was set to 100%.

Comparison of the signal between the commercial fluorescent microspheres (FM) and UCNPs. To further confirm the nonphotobleaching optical properties provided by UCNPs, the comparison of fluorescence between the commercial fluorescent microspheres and silica-coated UCNPs was conducted in this experiment. NSC-34 cells were seeded on coverslips in 24-well plates overnight. The FM and silica-coated UCNPs were blocked with cell culture media (DMEM, 10% FBS) for 2 h. Then, the cells were incubated with 0.02 mg mL^{-1} pretreated FM and 0.02 mg mL^{-1} silica-coated UCNPs for 4 h at 37 °C, respectively. Then, the coverslips were washed with PBS to remove extra FM and UCNPs before staining with Hoechst and deep red plasma membrane stain. Finally, the cells were fixed and treated with mounting media to prepare detectable slides. The images were captured under 580 nm⁵⁰ and 980 nm⁵¹ excitation at various times. For FM, the images were obtained at 0, 15, 30, 45 and 60 min. For silica-coated UCNPs, the confocal microscopy images were acquired at 0, 1, 3, 6 and 12 h, because the UCNPs were far more stable than commercial fluorescent materials.

Zebrafish microinjection. The biodistribution of UCNPs-PEG was then investigated *in vivo* using optically transparent zebrafish larvae. Five-day-old zebrafish larvae were mounted in 1% low melting agarose before microinjection and imaging as previously described.^{52,53} A suspension of UCNPs (1 mg mL^{-1}), UCNP-PEG (1 mg mL^{-1}) and microbeads (1 mg mL^{-1}) was injected into the spinal cord (labelled with blue fluorescent protein; Tg (-3mnx1:TagBFP)) of five-day-old zebrafish larvae.⁵⁴ Approximately, 5 nL solution was injected into the spinal cord and luminescence images were acquired at 0 and 2 h after injection (fed into the fish water in a 28 °C incubator). Upon excitation at 980 nm, the distribution of the nanoparticles in the zebrafish can be clearly visualized.

Conflicts of interest

There are no conflicts to declare.

Acknowledgements

We gratefully acknowledge the financial support of the National Natural Science Foundation of China (NSFC 31640027, 31600809 and U1604177), the Programme of China's 1000-talents Plan, the Macquarie University Research Fellowship, the National Health and Medical Research Council (NHMRC) dementia fellowship (APP1111611), the 2014–2016 Discovery Project-Grant (DP140103233) and the China Scholarship Council (CSC)–Macquarie University joint scholarship. We would also like to thank Xianlin Zheng for assisting with confocal microscopy imaging, and Serene Gwee and Stephanie Rayner helped with the neuron cells culture.

References

- 1 C. Zhang, X. Wan, X. Zheng, X. Shao, Q. Liu, Q. Zhang and Y. Qian, *Biomaterials*, 2014, **35**, 456–465.
- 2 N. Xia, B. Zhou, N. Huang, M. Jiang, J. Zhang and L. Liu, *Biosens. Bioelectron.*, 2016, **85**, 625–632.
- 3 A. Y. Estevez and J. S. Erlichman, *Nanomedicine*, 2014, **9**, 1437–1440.
- 4 R. N. Mitra, S. M. Conley and M. I. Naash, *Adv. Exp. Med. Biol.*, 2016, **854**, 463–469.
- 5 S. Wohlfart, S. Gelperina and J. Kreuter, *J. Controlled Release*, 2012, **161**, 264–273.
- 6 J. K. Saucier-Sawyer, Y. Deng, Y. E. Seo, C. J. Cheng, J. Zhang, E. Quijano and W. M. Saltzman, *J. Drug Targeting*, 2015, **23**, 736–749.
- 7 K. Liu, X. Jiang and P. Hunziker, *Nanoscale*, 2016, **8**, 16091–16156.
- 8 C. Hom, J. Lu and F. Tamanoi, *J. Mater. Chem.*, 2009, **19**, 6308–6316.
- 9 A. Suwalski, H. Dabboue, A. Delalande, S. F. Bensamoun, F. Canon, P. Midoux, G. Saillant, D. Klatzmann, J. P. Salvétat and C. Pichon, *Biomaterials*, 2010, **31**, 5237–5245.
- 10 M. Srikanth and J. A. Kessler, *Nat. Rev. Neurol.*, 2012, **8**, 307–318.
- 11 B. Shi, X. Du, J. Chen, L. Fu, M. Morsch, A. Lee, Y. Liu, N. Cole and R. Chung, *Small*, 2017, **13**, 1603966.
- 12 H. Koo, M. S. Huh, I. C. Sun, S. H. Yuk, K. Choi, K. Kim and I. C. Kwon, *Acc. Chem. Res.*, 2011, **44**, 1018–1028.
- 13 J. M. Caster, M. Sethi, S. Kowalczyk, E. Wang, X. Tian, S. Nabeel Hyder, K. T. Wagner, Y. A. Zhang, C. Kapadia, K. Man Au and A. Z. Wang, *Nanoscale*, 2015, **7**, 2805–2811.
- 14 A. E. Nel, L. Madler, D. Velegol, T. Xia, E. M. Hoek, P. Somasundaran, F. Klaessig, V. Castranova and M. Thompson, *Nat. Mater.*, 2009, **8**, 543–557.
- 15 Q. S. Qin, P. Z. Zhang, L. D. Sun, S. Shi, N. X. Chen, H. Dong, X. Y. Zheng, L. M. Li and C. H. Yan, *Nanoscale*, 2017, **9**, 4660–4664.
- 16 J. Yu, Y. Yang, R. Fan, P. Wang and Y. Dong, *Nanoscale*, 2016, **8**, 4173–4180.
- 17 B. Zhou, B. Shi, D. Jin and X. Liu, *Nat. Nanotechnol.*, 2015, **10**, 924–936.

View Article Online

Paper

Nanoscale

- 18 N. Bogdan, F. Vetrone, G. A. Ozin and J. A. Capobianco, *Nano Lett.*, 2011, **11**, 835–840.
- 19 L. Wang, R. Yan, Z. Huo, L. Wang, J. Zeng, J. Bao, X. Wang, Q. Peng and Y. Li, *Angew. Chem., Int. Ed.*, 2005, **44**, 6054–6057.
- 20 C. Wang, H. Tao, L. Cheng and Z. Liu, *Biomaterials*, 2011, **32**, 6145–6154.
- 21 D. J. Gargas, E. M. Chan, A. D. Ostrowski, S. Aloni, M. V. Altoe, E. S. Barnard, B. Sanii, J. J. Urban, D. J. Milliron, B. E. Cohen and P. J. Schuck, *Nat. Nanotechnol.*, 2014, **9**, 300–305.
- 22 Q. Liu, Y. Sun, T. Yang, W. Feng, C. Li and F. Li, *J. Am. Chem. Soc.*, 2011, **133**, 17122–17125.
- 23 H. Q. Wang and T. Nann, *ACS Nano*, 2009, **3**, 3804–3808.
- 24 J. Peng, Y. Sun, L. Zhao, Y. Wu, W. Feng, Y. Gao and F. Li, *Biomaterials*, 2013, **34**, 9535–9544.
- 25 L. Wang, R. Yan, Z. Huo, L. Wang, J. Zeng, J. Bao, X. Wang, Q. Peng and Y. Li, *Angew. Chem., Int. Ed.*, 2005, **44**, 6054–6057.
- 26 Q. Liu, M. Chen, Y. Sun, G. Chen, T. Yang, Y. Gao, X. Zhang and F. Li, *Biomaterials*, 2011, **32**, 8243–8253.
- 27 L. L. Li, R. Zhang, L. Yin, K. Zheng, W. Qin, P. R. Selvin and Y. Lu, *Angew. Chem., Int. Ed.*, 2012, **51**, 6121–6125.
- 28 L. M. Yao, J. Zhou, J. L. Liu, W. Feng and F. Y. Li, *Adv. Funct. Mater.*, 2012, **22**, 2667–2672.
- 29 M. A. White, J. A. Johnson, J. T. Koberstein and N. J. Turro, *J. Am. Chem. Soc.*, 2006, **128**, 11356–11357.
- 30 Z. Chen, H. Chen, H. Hu, M. Yu, F. Li, Q. Zhang, Z. Zhou, T. Yi and C. Huang, *J. Am. Chem. Soc.*, 2008, **130**, 3023–3029.
- 31 T. Yi and C. Huang, *J. Am. Chem. Soc.*, 2008, **130**, 3023–3029.
- 32 N. Niwa, Y. Yamagishi, H. Murakami and H. Suga, *Bioorg. Med. Chem. Lett.*, 2009, **19**, 3892–3894.
- 33 H. Zhang, Y. Li, I. A. Ivanov, Y. Qu, Y. Huang and X. Duan, *Angew. Chem., Int. Ed.*, 2010, **49**, 2865–2868.
- 34 Y. Yang, Q. Shao, R. Deng, C. Wang, X. Teng, K. Cheng, Z. Cheng, L. Huang, Z. Liu, X. Liu and B. Xing, *Angew. Chem., Int. Ed.*, 2012, **51**, 3125–3129.
- 35 O. Ehlert, R. Thomann, M. Darbandi and T. Nann, *ACS Nano*, 2008, **2**, 120–124.
- 36 G. S. Yi, H. C. Lu, S. Y. Zhao, G. Yue, W. J. Yang, D. P. Chen and L. H. Guo, *Nano Lett.*, 2004, **4**, 2191–2196.
- 37 Z. Y. Hou, C. X. Li, P. A. Ma, G. G. Li, Z. Y. Cheng, C. Peng, D. M. Yang, P. P. Yang and J. Lin, *Adv. Funct. Mater.*, 2011, **21**, 2356–2365.
- 38 A. Albanese, P. S. Tang and W. C. Chan, *Annu. Rev. Biomed. Eng.*, 2012, **14**, 1–16.
- 39 Y. Q. Lu, J. B. Zhao, R. Zhang, Y. J. Liu, D. M. Liu, E. M. Goldys, X. S. Yang, P. Xi, A. Sunna, J. Lu, Y. Shi, R. C. Leif, Y. J. Huo, J. Shen, J. A. Piper, J. P. Robinson and D. Y. Jin, *Nat. Photonics*, 2014, **8**, 32–36.
- 40 D. Liu, X. Xu, Y. Du, X. Qin, Y. Zhang, C. Ma, S. Wen, W. Ren, E. M. Goldys, J. A. Piper, S. Dou, X. Liu and D. Jin, *Nat. Commun.*, 2016, **7**, 10254.
- 41 J. Zhao, D. Jin, E. P. Schartner, Y. Lu, Y. Liu, A. V. Zvyagin, L. Zhang, J. M. Dawes, P. Xi, J. A. Piper, E. M. Goldys and T. M. Monro, *Nat. Nanotechnol.*, 2013, **8**, 729–734.
- 42 F. Liu, Q. Zhao, H. You and Z. Wang, *Nanoscale*, 2013, **5**, 1047–1053.
- 43 E. C. Cho, Q. Zhang and Y. Xia, *Nat. Nanotechnol.*, 2011, **6**, 385–391.
- 44 Y. Liu, Y. Lu, X. Yang, X. Zheng, S. Wen, F. Wang, X. Vidal, J. Zhao, D. Liu, Z. Zhou, C. Ma, J. Zhou, J. A. Piper, P. Xi and D. Jin, *Nature*, 2017, **543**, 229–233.
- 45 S. Lazzari, D. Moscatelli, F. Codari, M. Salmona, M. Morbidelli and L. Diomedea, *J. Nanopart. Res.*, 2012, **14**, 920–929.
- 46 Y. Shi, B. Shi, A. V. Dass, Y. Lu, N. Sayyadi, L. Kautto, R. D. Willows, R. Chung, J. Piper, H. Nevalainen, B. Walsh, D. Jin and N. H. Packer, *Sci. Rep.*, 2016, **6**, 37533.
- 47 J. Lu, Y. Chen, D. Liu, W. Ren, Y. Lu, Y. Shi, J. Piper, I. Paulsen and D. Jin, *Anal. Chem.*, 2015, **87**, 10406–10413.
- 48 D. K. Yi, S. T. Selvan, S. S. Lee, G. C. Papaefthymiou, D. Kundaliya and J. Y. Ying, *J. Am. Chem. Soc.*, 2005, **127**, 4990–4991.
- 49 B. Shi, H. Zhang, S. Z. Qiao, J. Bi and S. Dai, *Adv. Healthcare Mater.*, 2014, **3**, 1839–1848.
- 50 Y. Q. Wang, C. J. Xu and H. Ow, *Theranostics*, 2013, **3**, 544–560.
- 51 G. S. Yi and G. M. Chow, *Adv. Funct. Mater.*, 2006, **16**, 2324–2329.
- 52 M. Morsch, R. Radford, A. Lee, E. K. Don, A. P. Badrock, T. E. Hall, N. J. Cole and R. Chung, *Front. Cell. Neurosci.*, 2015, **9**, 321.
- 53 D. Cheng, G. J. Shami, M. Morsch, R. S. Chung and F. Braet, *BioMed Res. Int.*, 2016, **2016**, 1–13.
- 54 E. K. Don, I. Formella, A. P. Badrock, T. E. Hall, M. Morsch, E. Hurtle, A. Hogan, S. Chow, S. S. L. Gwee, J. J. Stoddart, G. Nicholson, R. Chung and N. J. Cole, *Zebrafish*, 2017, **14**, 69–72.

Electronic Supplementary Material (ESI) for Nanoscale.
This journal is © The Royal Society of Chemistry 2017

Electronic Supplementary Information (ESI) for Nanoscale
This journal is © The Royal Society of Chemistry 2017

Versatile Upconversion Surface Evaluation Platform for Bio-nano Surface Selection for Nervous System

*Libing Fu,^{a,b,c} Marco Morsch,^b Bingyang Shi,^{*a,b,c} Guoying Wang,^b Albert Lee,^b Rowan Radford,^b Yiqing Lu,^{a,c,d} Dayong Jin,^e and Roger Chung^b*

^a International Joint Center for Biomedical Innovation, School of Life Sciences, Henan University, Jin Ming Avenue, Kaifeng, Henan, 457004, China

^b Department of Biomedical Sciences, Faculty of Medicine & Health Sciences, Macquarie University, Sydney, NSW 2109, Australia

^c ARC Centre for Nanoscale Biophotonics, Macquarie University, Sydney, NSW 2109, Australia

^d Department of Physics and Astronomy, Faculty of Sciences & Engineering, Macquarie University, Sydney, NSW 2109, Australia

^e Institute for Biomedical Materials and Devices (IBMD), Faculty of Science, University of Technology Sydney, Sydney, NSW2007, Australia

E-mail: bingyang.shi@mq.edu.au

Methods:**Synthesis of the Original NaYF₄:20%Yb,4%Tm upconversion nanocrystals (UCNPs).**

The original UCNPs were synthesized following an oxygen-free protocol described in the literature.¹ In a typical procedure, 3.5 mL of methanol solution (0.76mmol YCl₃, 0.2mmol YbCl₃ and 0.04mmol Tm) was magnetically mixed with OA (6.5 mL) and ODE (15 mL) in a 100 mL three-neck round-bottom flask. The mixture was degassed under Ar flow and heated to 150 °C for 30 min to form a clear solution, then cooled to room temperature. 5 mL of methanol solution containing NH₄F (4 mmol) and NaOH (2.5 mmol) was added into the solution of YCl₃ in ODE and stirred for 30 min at room temperature. The mixture solution was slowly heated up to 110 °C and kept at 110 °C for 30 min to remove methanol and water completely. Then the mixture solution was quickly heated to reaction temperature 310°C and aged for 1.5 h. After the solution cooled down to room temperature, ethanol was added to precipitate the nanocrystals. After the product was washed with cyclohexane, ethanol and methanol for 3 times, the final NaYF₄ nanocrystals were re-dispersed in 10mL cyclohexane at 4°C for further use.

Synthesis of OA-free UCNPs. OA ligand on the UCNPs surface was removed according to literatures²⁻⁴ with modifications. 1ml of cyclohexane containing oleate-capped UCNPs (20 mg/ml) was added into 4ml absolute ethanol and performed with sonicating for 10min. The solution turned to be cloudy, because the UCNPs were participated. Then the solution was centrifuge for 10min at 10000 rpm to separate UCNPs. The as prepared UCNPs was dispersed in aqueous solution (5 mL) and the pH was adjusted to 2 by adding 0.5 M HCl solution. The reaction was performed with sonication for 10min. During this reaction the carboxylate groups of the oleate ligand were protonated (to yield oleic acid). The UCNPs in the solution were recuperated and treated with 5ml HCl solution (pH 4) by sonicating for 20 min. Afterwards, the particles were recuperated and washed with ethanol for three times. Finally, the particles were dispersed in water.

NSC-34 Cell Culture. Mouse NSC-34 hybrid cell line (NSC-34; kindly provided by Dr. Vinod, University of Macquarie) were cultured in Dulbecco's modified Eagle's medium (DMEM), including 10% fetal bovine serum (FBS) and 1% penicillin/streptomycin solution (P/S).⁵ Cells were maintained under standard conditions (humidified, 5% CO₂, 37°C). Cells were subcultured every 3-4 days. The in vitro experiments were designed at different concentrations of UCNPs and different incubation time. After the incubation the cells were washed with phosphate buffered saline (PBS) buffer for three times. Control experiments were performed with growth medium without nanoparticles.

Cell viability assays. For the viability assays, 1.0×10^4 NSC-34 cells were seeded into a 96-well plate (200μL medium/well) and incubated overnight at 37 °C with 5% CO₂. The media was replaced with increasing UCNPs concentrations (0, 1, 10, 20, 50 and 100mg/ml). The plates were incubated for 24 h. a) A colorimetric MTT assay with minor modifications was conducted by adding 10uL of the 3-[4,5-dimethylthiazol-2-yl]-2,5-diphenyltetrazolium-bromide (MTT, 5.0 mg/mL in PBS) to each well. Cells were further incubated at 37 °C for 4 h to allow precipitation of insoluble purple formazan crystals. Then, the supernatant was carefully removed, and 150uL dimethyl sulfoxide (DMSO) was added to the wells and left for 2h in the dark at room temperature. Finally, the absorbance was measured using the Biotek Microplate Reader (Biotek, U.S.A.) at a wavelength of 570 nm. The control well was assumed have 100% viability. Therefore, the viable cells number was calculated based on the absorbance of the control cultures. b) LDH assay followed the LDH Assay Kit (601170): 1.0×10^4 of cells

at a density of 5×10^5 cells/ml (DMEM containing 10% FBS) were seeded in each well of 96-well plates and grown for 24 h before NP incubation. The cells were washed with PBS three times and dosed with different concentrations of NPs (0, 1, 10, 20, 50 and 100mg/ml) in DMEM medium containing 10% FBS. After 24 h incubation, 20ul of Triton X-100(10%) solution was added to three wells and 20ul of Assay Buffer was added to another three wells before incubation at room temperature for one hour. Transfer 100ul of cell supernatant to a new 96-well assay plate. 100ul of Reaction Solution was added to each well. After that, the plate was incubated with gentle shaking on an orbital shaker (150rpm) for 30 minutes at 37 degrees. Finally, the absorbance of the plate was measured at 490nm with Biotek Microplate Reader (Biotek, U.S.A.). The LDH activity of the samples was obtained by measuring the decreasing rate of NADH absorbance over time.

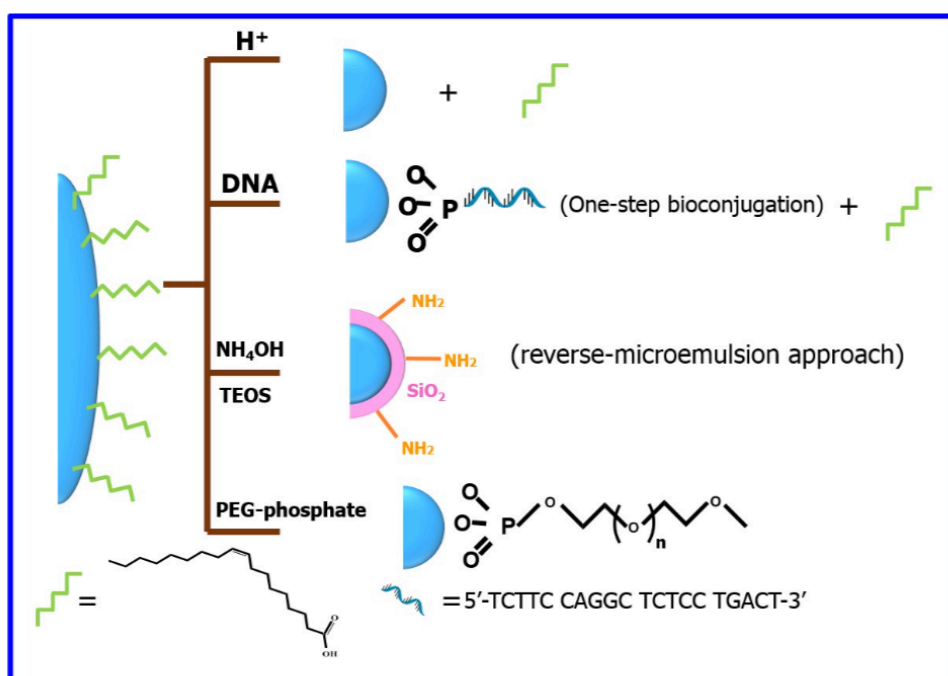


Fig. S1 Schematic illustration showing the fabrication of the surface-modified UCNPs: OA-free (employing acid to remove OA on the surface), DNA-modified (using one-step bioconjugation approach), Silica-coated (utilizing reverse-microemulsion method) and PEG-COOH functionalized (ligand exchange approach) UCNPs.

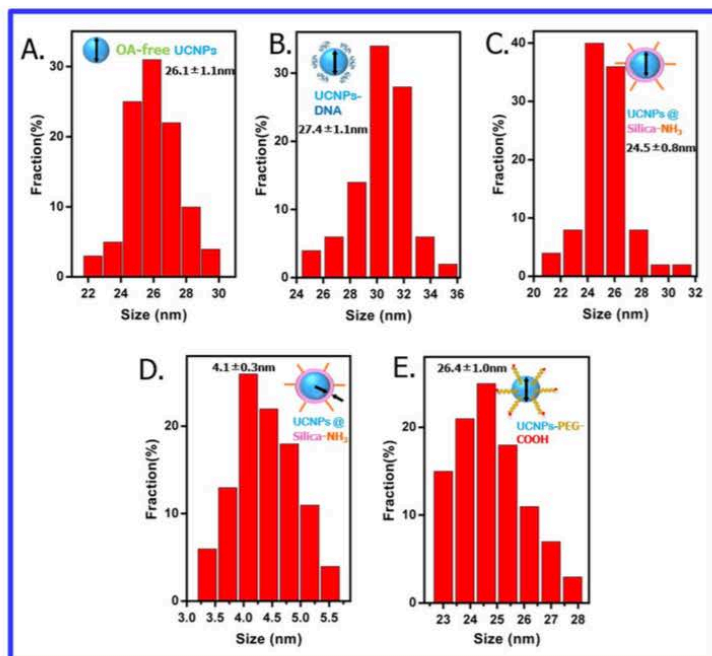


Fig S2. The size distribution characterization of the UCNPs core. A) OA-free, B) DNA-modified, C) silica-coated, D) silica layer of (C) and E) PEG-capped UCNPs. The size of upconversion core of these types of modified UCNPs are similar (about 26nm~28nm).

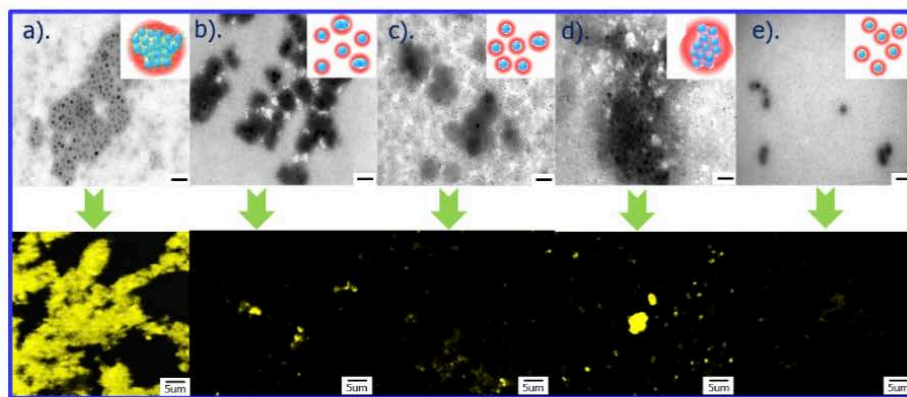


Fig. S3 TEM images of the UCNPs (the upper row): unmodified (a), DNA-modified (b), OA-free (c), Silica-coated (d) and PEG-COOH functionalized UCNPs dispersed in cell culture media for 4h at 37 °C. The corresponding UCNPs (the bottom row) imaged with confocal microscope under 980nm laser excitation.

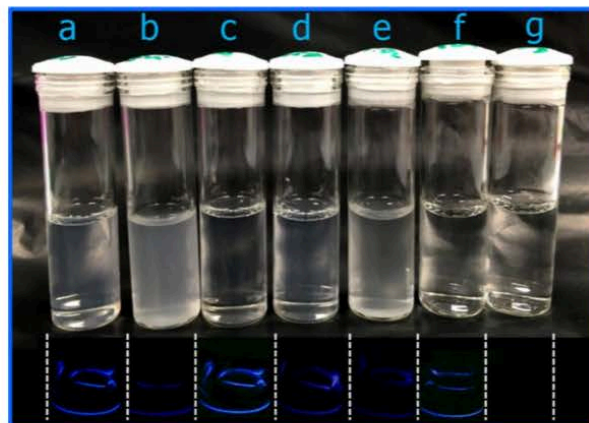


Fig. S4 The photograph of the upconversion nanoparticles: a) OA-capped UCNPs in 1wt% cyclohexane solution (as the positive control for comparison); b) OA-capped UCNPs, c) OA-free UCNPs, d) UCNPs-DNA, e)UCNPs@Silica-NH₂, f) UCNPs-PEG-COOH (b-f were dispersed in 1wt% water) and MiliQ water (as the blank control). The bottom row showed the upconversion fluorescence (blue) of corresponding UCNPs under 980nm NIR excitation. Note the NIR emission of NaYF₄:20%Yb,4%Tm at 800nm is invisible to both the human eye and the camera.

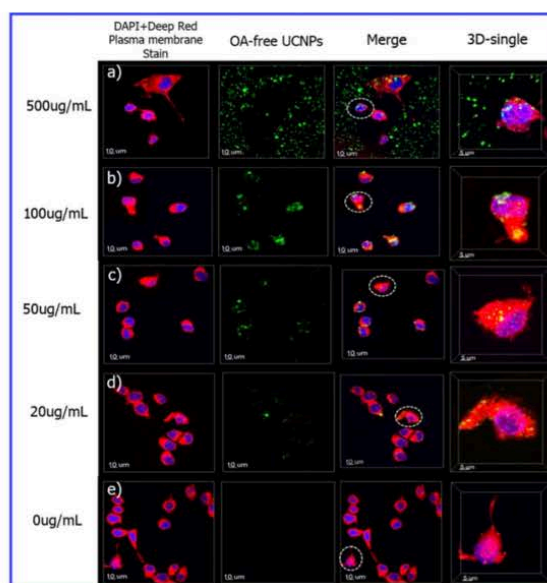


Fig. S5 Confocal microscopy images of NSC-34 cells after 4h incubation at 37°C with OA-free UCNPs at different concentrations (a-e: 500ug/ml, 100ug/ml, 50ug/ml, 20ug/ml and 0ug/ml): Fluorescent images of cell nucleus (blue, stained with Hoechst), cell membrane (red, labeled with deep red plasma membrane stain) and OA-free UCNPs (set to green, upconversion luminescence of UCNPs collected at 800nm), overlays of cell images & OA-free UCNPs and 3D-single cell with OA-free UCNPs. The OA-free UCNPs were utilized as sample for optimization the concentration of UCNPs used for cell uptake experiment.

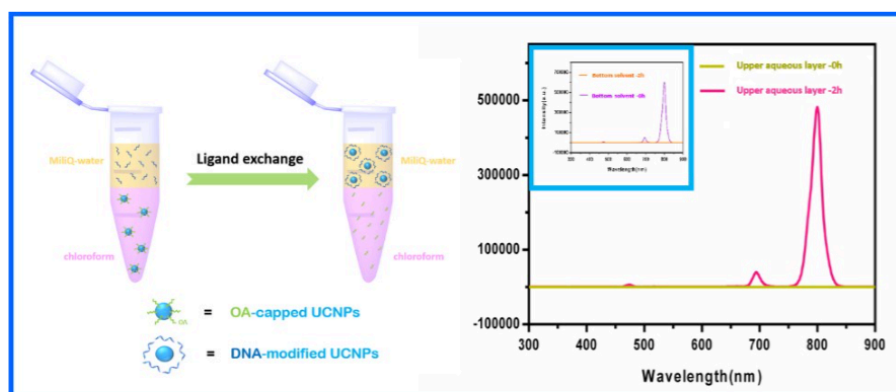


Fig. S6 The change of emission spectrum in the upper aqueous layer after and before 2h-incubation of original UCNPs with ssDNA. The inset figure shows the change of UCNPs-containing organic solvent before and after incubation with ssDNA. The negligible spectrum cure after incubation suggests that nearly all the UCNPs were successfully transferred out from the bottom solvent layer to the upper aqueous layer.

Supplementary References

- [1] Z. Q. Li, Y. Zhang and S. Jiang, *Adv. Mater.*, 2008, **20**, 4765-4769.
- [2] Z. Yu, Q. Sun, W. Pan, N. Li and B. Tang, *ACS nano*, 2015, **9**, 11064-11074.
- [3] L. Zhao, J. Peng, Q. Huang and C. Li, *Adv. Funct. Mater.*, 2014, **24**, 363-371.
- [4] N. Bogdan, F. Vetrone, G. A. Ozin and J. A. Capobianco, *Nano letters*, 2011, **11**, 835-840.
- [5] N. R. Cashman, H. D. Durham, J. K. Blusztajn, K. Oda, T. Tabira, I. T. Shaw, S. Dahrouge and J. P. Antel, *Dev. Dyn.*, 1992, **194**, 209-221.
- [6] D. K. Yi, S. T. Selvan, S. S. Lee, G. C. Papaefthymiou, D. Kundaliya and J. Y. Ying, *J. Am. Chem. Soc.*, 2005, **127**, 4990-4991.

3.3 Remarks

The key findings of this paper: (i) that PEGylation provides the superior surface for biocompatibility and neuronal cellular uptake properties of lanthanide ion-doped upconversion nanoparticles (NaYF₄:20% Yb,4% Tm); (ii) that the spectral properties of these UCNPs supports high resolution in vivo imaging in zebrafish; (iii). Ln³⁺-UCNPs can be used as a platform for systematic surface evaluation and identification of suitable surface for nanoparticle-based drug delivery for the treatment of CNS diseases.

Limitations and future directions: It is likely that other biophysical properties of UCNPs, in addition to surface, will influence the biocompatibility of UCNPs (such as size and shape etc.) - these will be studied in following chapters of this thesis, using the knowledge gained from this Chapter that PEGylation represents the superior surface modification.

In this study, it was found that a protein corona was formed on the surface of all types of surface-modified Ln³⁺-UCNPs when incubated in cell culture media (see Figure X). It is likely that the composition of the protein corona may affect the biological properties of the UCNPs. Attempts were made to evaluate the composition of the protein corona formed on the various surface of Ln³⁺-UCNPs using proteomic mass spectrometry approaches. However, these were unsuccessful, because of the presence of detergents (such as PEG) that interfered with the mass spectrometry analysis (data not shown). Future studies will need to optimise this for improved proteomic characterisation of the composition of the protein corona.

Chapter 4: Evaluation of the Effect of Shape upon Endocytosis of Transferrin-coated Upconversion nanoparticles, and their Ability to cross the Blood-brain Barrier

The blood-brain barrier (BBB) is a major challenge for the treatment of central nervous system (CNS) diseases. The BBB strictly regulates the movement of molecules into and out of the brain, and therefore protects the brain from noxious agents. However, for this reason the BBB also acts as a major obstacle that prevents most therapeutic molecules from getting into the target site of the brain. Therefore, it is essential to develop an efficient and general approach to overcome the BBB and transport the drug to the targeted region. Nanoparticle-based drug delivery systems are emerging as a promising drug delivery platform, due to their distinct advantages of tunable biophysical properties such as surface chemistry, size and shape leading to various biological actions (like clearance, biodistribution and biocompatibility) in the body. Therefore, it was hypothesized that the shape of nanoparticles will influence their BBB permeation efficiency (Aim 2 of this thesis).

In this report, a series of transferrin-coated upconversion nanoparticles (Tf-UCNPs) with various shapes were generated, including sphere, rod, disk and dumbbell. The cellular uptake ability, biodistribution and BBB penetration of those different-shaped Tf-UCNPs were assessed in cultured cells (brain endothelial cells, modeling the BBB) and in vivo. The results revealed that rod-shaped Tf-UCNPs were the superior shape to mediate low cytotoxicity and maximal cellular uptake among sphere-, disk- and dumbbell-like Tf-UCNPs. Furthermore, transferrin profoundly improves the cellular uptake efficiency of the UCNPs in brain endothelial cells. Zebrafish were employed to study the BBB penetration ability of nanoparticles in vivo, where it was confirmed that rod-shaped UCNPs provide the most effective BBB permeation compared to other shapes (such as spherical, disc and dumbbell-like). In summary, this provides important information for

structure design of high-efficiency nanoparticle-based vector to delivery drugs across the BBB for neurodegenerative disorder therapy.

The methodology that was developed and optimised during this project for reproducible synthesis of the various shapes of UCNPs is presented in Chapter 2. Analysis of the biophysical and biocompatibility of the UCNPs is presented in this Chapter in the form of a draft manuscript entitled “Evaluation of the Effect of Shape upon Endocytosis of Transferrin-coated UCNPs, and their Ability to cross the Blood-brain Barrier”. This manuscript has been prepared for submission to *ACS nano*, with submission expected within several weeks after submission of this thesis.

4.1 Contribution to Manuscript 2

	L.F	B.S	M.M	G.W	Y.L	D.J	R.C
Experiment Design	●	●					●
Sample Preparation	●		●	●			
Data Collection	●						
Analysis	●			●	●		
Manuscript	●	●	●		●	●	●

The experimental aspects of this project were mostly performed by myself (90%), except the microinjection of UCNPs into the zebrafish (performed by Dr. M. Morsch).

4.2 Manuscript 2

Evaluation of the Effect of Shape upon Endocytosis of Transferrin-coated UCNPs, and their Ability to cross the Blood-brain Barrier

L. B. Fu¹, B. Y. Shi^{*1}, M. Morsch¹, G. Y. Wang,¹ Y. Q. Lu², D. Y. Jin,³ R. Chung^{*1}

¹Department of Biomedical Sciences, Faculty of Medicine & Health Sciences, Macquarie University, Sydney, NSW 2109, Australia. Email: roger.chung@mq.edu.au, bingyang.shi@mq.edu.au

² Department of Physics and Astronomy, Macquarie University, Sydney, NSW 2109, Australia

³Institute for Biomedical Materials and Devices (IBMD), Faculty of Science, University of Technology Sydney, Sydney, NSW 2007, Australia

Abstract

Sustained and effective delivery of therapeutic agents across the blood-brain barrier (BBB) remains a key bottleneck for successful therapeutic treatment of neurodegenerative diseases. Nanoparticles have become a popular choice for evaluation as drug carriers. To design an efficient nanoparticle-based carrier, nanoparticle shape has emerged as a significant parameter that can influence the success of targeted drug delivery. In this study, we fabricated a series of transferrin-coated upconversion nanoparticles (Tf-UCNPs) with various shapes, including sphere, rod, disk and dumbbell. Thereafter, we systematically characterized the biophysical properties of these different-shaped Tf-UCNPs including their morphology, surface conjugation, cytotoxicity and cell uptake capability in biological solutions or with cultured hCMEC/D3 brain endothelial cells. Through these studies, rod-shaped Tf-UCNPs proved to be the superior morphology for greatest bioavailability and cell uptake capacity amongst sphere-, disk- and dumbbell-like UCNPs. To further investigate how nanoparticle shape influences BBB permeability, each shape of Tf-UCNPs was microinjected into the blood vessels of juvenile zebrafish. As predicted, rod-shaped Tf-UCNPs displayed excellent dispersal and uptake into the brain in living zebrafish, while other shapes of Tf-UCNPs were either aggregation prone and/or displayed poor uptake into the brain. Thus, NP shape plays a crucial role in mediating bioavailability and cellular endocytosis and transport of transferrin-coated UCNPs in vivo. Further, our data suggests that rod-shaped UCNPs might have potential future applications as a drug loading nano-system with high efficacy for use in delivering therapeutics into the brain. These results provide valuable information towards designing nanoparticle-based vectors for the delivery of drugs across the blood-brain barrier for

future theranostic applications in neurodegenerative disorders.

Introduction

Neurodegenerative diseases including dementia and motor neuron disease (MND) destroy the nerve cells that control cognitive and/or motor function, with no effective long-term therapies available. A major challenge is to develop strategies for effective and efficient systematic administration of therapeutic compounds across the blood brain barrier (BBB). The blood-brain barrier (BBB) is a unique physiological barrier between blood capillary and central nervous system (CNS) in the brain. It strictly regulates the passage of ions and molecules to maintain the homeostasis of the cellular environment within the brain.¹ Therefore, the BBB represents a major hurdle to effective drug delivery via blood circulation to treat brain diseases, as it is well described that it excludes many therapeutic compounds from directly entering the brain. For example, a large-scale evaluation of over 7000 drugs measured in the Comprehensive Medicinal Chemistry (CMC) database, revealed that only 1% of these drugs can cross the BBB at detectable levels.² To overcome this issue, an increasing number of strategies have been tested to overcome this hurdle, with two major approaches being either non-invasive or invasive delivery of drugs cross the BBB. The non-invasive method refers to the typical application of drug carriers via a receptor or adsorptive mediated transcytosis mechanism,³ or more recently through intranasal delivery.⁴ However, those methods are profoundly restricted by the chemical structure of the drug delivery vector and the presence of efflux pumps.^{5,6} Invasive strategies involve direct administration including intracranial injection such as convection-enhanced delivery (CED)^{7,8} or directly injecting the drug through intraventricular or intracerebral administration. However invasive delivery techniques impose direct physical injury to the brain, and can have limitations on the spread of the injected compound. Therefore, there is strong interest in identifying an effective and secure strategy to enhance brain delivery of drugs to the specific target site in the brain, and to control the delivery of the drug to the appropriate cellular, subcellular and temporal location for it to exert its therapeutic functions.

In order to enhance BBB penetration, the drug delivery system should escape clearance through the reticuloendothelial system to ensure sustained presence at effective concentrations.⁹ In principle, there are three pathways that support delivery past the BBB.

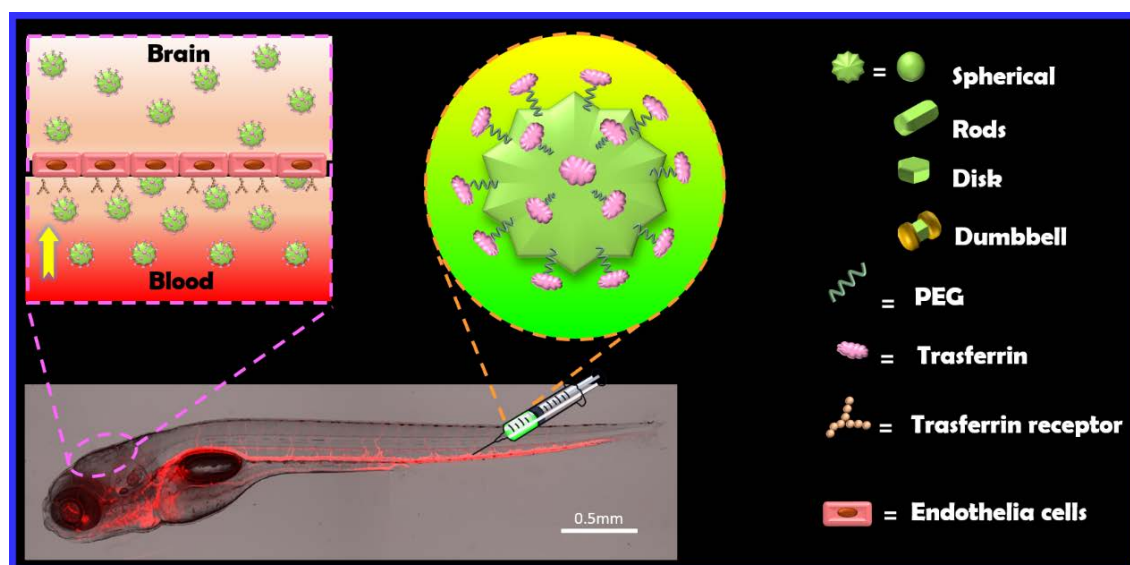
Firstly, surface ligands of carrier-systems which bind to surface receptors abundant on the surface of endothelial cells that form the BBB facilitate binding and uptake into the brain.^{10–12} Specific peptides targeting certain receptors such as the transferrin receptor or lipoprotein receptors might help to deliver cargoes across the BBB via receptor-mediated endocytosis. Secondly, certain physicochemical characteristics of delivery systems are suitable for crossing BBB. For example, it was reported that gold nanoparticles (20nm) were found in the retina after intravenous injection.¹³ In addition, some pathological conditions in the brain (such as brain tumors, or injury to brain such as traumatic brain injury or stroke) lead to an abnormal increase in the permeability of the BBB vasculature. Thirdly, surface modification can improve the BBB permeability of therapeutic compounds. For instance, partial capping of delivery systems with polysorbate 80 or chitosan increased the targeting transport of drugs into the deep brain.^{14–16} This combination of characteristics of the delivery system and pathological vasculatures would make BBB more readily to drug-loaded delivery system penetration.

Employing nanoparticles as carriers to transport drugs across the BBB is an emerging approach in the nanotechnology field. The distinct advantage of nano-enabled drug delivery systems is that the biophysical properties of nanoparticles can be readily modified based upon size, shape and surface, resulting in striking changes in the clearance, biodistribution and biocompatibility of nanoparticles *in vivo*.¹⁷ In terms of that, some studies have showed that the effect of size and surface modification of nanoparticles on biological actions *in vivo*^{18, 19} and *in vitro*.^{20, 21} For instance, Chan's group reported the membrane receptor internalization of silver nanoparticles and Au particles with diameters range from 2 to 100 nm, and found the preferable efficient uptake was within 25-50nm size range. Moreover, Zuhorn et al. exploited uncoated, cationic polymer polyethyleneimine (PEI)-attached and prion proteins-functionalized 500 nm beads to investigate their intracellular processing in an *in vitro* BBB model. They demonstrated that surface modifications of nanoparticles (like charge and protein ligands) affect their mode of internalization by brain endothelial cells and further subcellular fate and transcytosis potential. Meanwhile, the shape is also most likely a key factor of NPs for BBB penetration. However, there are few reports related to the effect of nanoparticles shape on cellular internalization and subsequent intracellular transport across the BBB.²² This might be because of the limited availability of approaches and the complexity to

synthesize nonspherical biocompatible nanoparticles.²³

Upconversion nanoparticles (UCNPs) consist of a crystalline host (like NaYF₄ or NaGdF₄) together with a low concentration metal-dopant (generally lanthanide ions). UCNPs processes unique optical properties, which can emit shorter visible light under near infrared long-wavelength excitation through a process known as the anti-Stokes principal. This is particularly valuable for biological applications, as long-wavelength excitation penetrates more deeply into tissue and yields lower phototoxicity than more common forms of excitation. Moreover, UCNPs exhibit other technical advantages, including high photo-stability, low auto-fluorescence background, narrow emission bandwidths, high penetration depth and low toxicity.^{24–27} Therefore, recent decades have witnessed substantial growth in the UCNP field, particularly exploring the fabrication and bio-application of UCNPs as a new class of luminescent optical labels and drug delivery vehicles for therapeutic applications and biological imaging.^{28–30} Importantly, the size, lifetime and shape of UCNPs are adjustable via controlling the synthesis conditions (heating up speed, reaction temperature and chemical ratio) and composition parameters (percentage of host and lanthanide ions).

In this study, we developed a library of UCNPs with various shapes as we have described previously.³¹, to evaluate the effect of shape upon BBB penetration. First, we fabricated a batch of high-doped UCNPs (β-NaYF₄: 20% Yb, 4% Tm) with different shapes, such as sphere, rod, disk and dumbbells. And then we functionalized these UCNPs via transferrin bioconjugation, forming four types of different-shaped transferrin-modified UCNPs for morphology evaluation. (Scheme 1 and S1) Second, we compared the biophysical characteristics of the functionalized UCNPs, including particle size, surface charge, UVvis absorbance, cytotoxicity and brightness. Furthermore, we measured the cellular uptake and BBB penetration of these transferrin-UCNPs with cultured brain endothelial cells (BBB hCMEC/D3) and injection into the bloodstream of living zebrafish, utilizing confocal microscopy and Imaris software. This systematic evaluation identified that the shape priorities for brain endothelial cell is rod > disk > sphere > dumbbell in terms of low cytotoxicity, high cell uptake efficiency and BBB penetration. Further, we confirmed that rod-shaped Tf-UCNPs display the best ability to cross the BBB and enter the brain



Scheme1. Illustration of microinjection of different-shaped Tf-UCNPs fabrication into the blood vessel of zebrafish. Tf-UCNPs with different shapes: sphere, rod, disk and dumbbell. Inset image of zebrafish represents the fli zebrafish with GFP labelled vessels (set to red in this image). (Scale bar = 0.5mm)

following bloodstream injection. Our result therefore demonstrates that morphology of nanoparticles plays a crucial role in BBB penetration and cellular uptake properties.

Results and Discussion

Fabrication of UCNPs with Various Shapes. To provide superior luminescent nanoparticles as the nano-platform for shape evaluation, we synthesized a series of UCNPs (β -NaYF₄: 20% Yb, 4% Tm) with different shapes (including spheres, rods, disks and dumbbells) based on our prior studies.^{31, 32} The as-synthesized UCNPs were originally dispersed in the organic solvent (chloroform), capped with the unsaturated fatty acid (oleic acid) on the surface. The oleic acid is used as the surface ligand to control the growth of UCNPs and subsequently stabilize the resultant UCNPs against agglomeration.³³ Transmission Electron Microscopy (TEM) results showed that we were able to generate highly consistent shapes of UCNPs such as spherical, rod, hexagonal prism and dumbbell-shaped with uniform size (details see Figure 1a-1d) and all well-

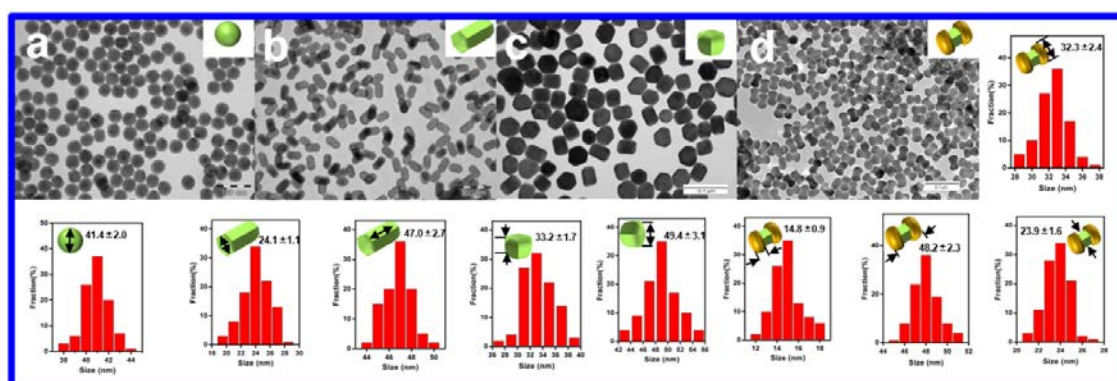


Figure 1. Transmission electron microscopy (TEM) images and size distribution of as-prepared β -NaYF₄: 20% Yb, 4% Tm nanoparticles (UCNPs) with different shapes, i.e., spheres (a), rods (b), disk (c) and dumbbell (d) dispersed in cyclohexane.

dispersed in cyclohexane (hydrophobic solvent). The calculated size of the as-prepared UCNPs was acquired with Image J by counting 100 particles from their corresponding TEM images. The size distribution images in Figure 1 suggested that the original UCNPs with various shapes were relatively uniform with narrow size variation.

Tf Modification and Characterization of Tf-modified UCNPs. To transfer the hydrophobic OA-capped as-prepared UCNPs into a hydrophilic intermediate compatible for bio-application, we functionalized the UCNPs with PEG-COOH and modified them with a highly water-dispersible surface based upon a multi-step ligand exchange strategy.

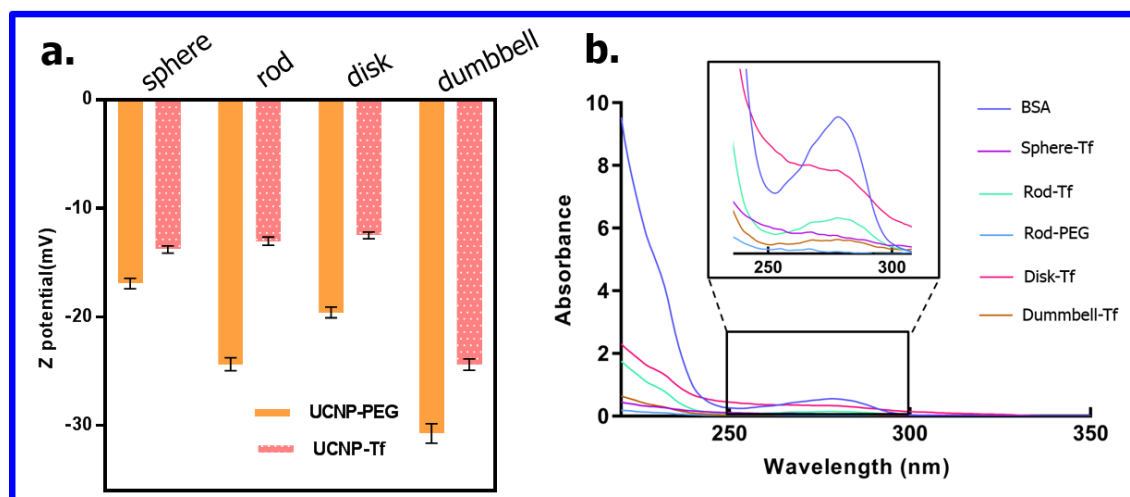


Figure 2. The Z-potential of UCNPs-PEG versus UCNPs-Tf (a) and comparison of absorbance of transferrin-capped UCNPs with different shapes, including: sphere-Tf, rods-Tf, disk-Tf, dumbbell-Tf, PEG-rod and pure BSA (b).

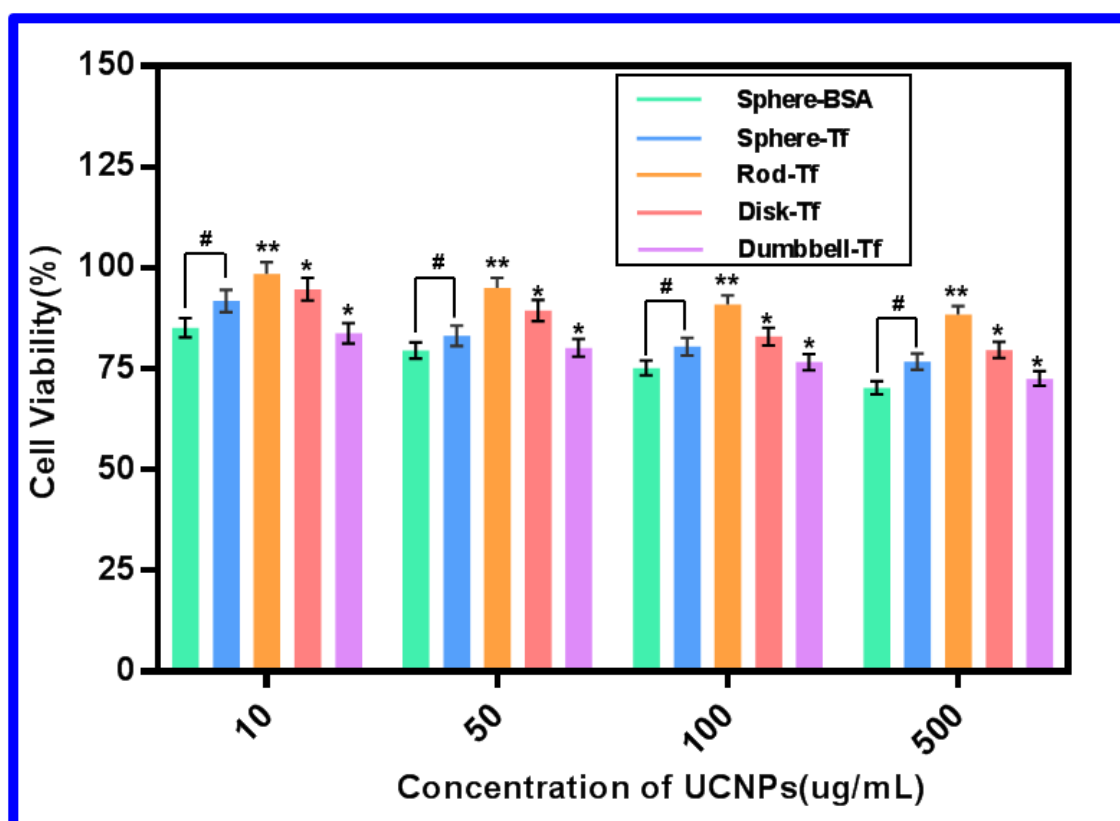


Figure 3. In vitro cell viabilities of hCMEC/D3 cells after incubation with 10, 50, 100 and 500ug/mL of 5 types of UCNPs (e.g. sphere-BSA, sphere-Tf, Rod-Tf, Disk-Tf and Dumbbell-Tf) for 24 h. A significant difference when compared to the sphere-Tf is indicated by “* $P < 0.05$ and ** $P < 0.01$ ”, and “#” indicates a significant difference when compared to the sphere-BSA.

Firstly, NOBF_4^- was introduced to replace the OA on the surface of UCNPs, forming an intermediate of NOBF_4^- -UCNPs.^{33, 34} Thereafter, we further replaced NOBF_4^- with a PEG linker (PHOS-PEG3500-COOH), due to the NOBF_4^- having a lower binding affinity than the phosphates. The PEG linker modification was used to provide a linker for biological functionalization. Finally, we conjugated the PEG-COOH modified UCNPs with transferrin (Tf) to facilitate transport across the BBB, as transferrin has been reported as a suitable substrate for this purpose. (as shown in S2) Furthermore, transferrin can also enhance the distinction among those Tf-modified UCNPs with various shapes. This conjugation was based upon EDC chemistry with the formation of amide bonds between the carboxyl groups of UCNP-PEG-COOH and primary amine groups of transferrin. The Z-potential change of this step was verified by dynamic light scattering (DLS).

As shown in Figure 2a, the Z-potential of various shapes of UCNP-PEG-Tf all increased significantly compared to their corresponding UCNP-PEG-COOH, which is expected

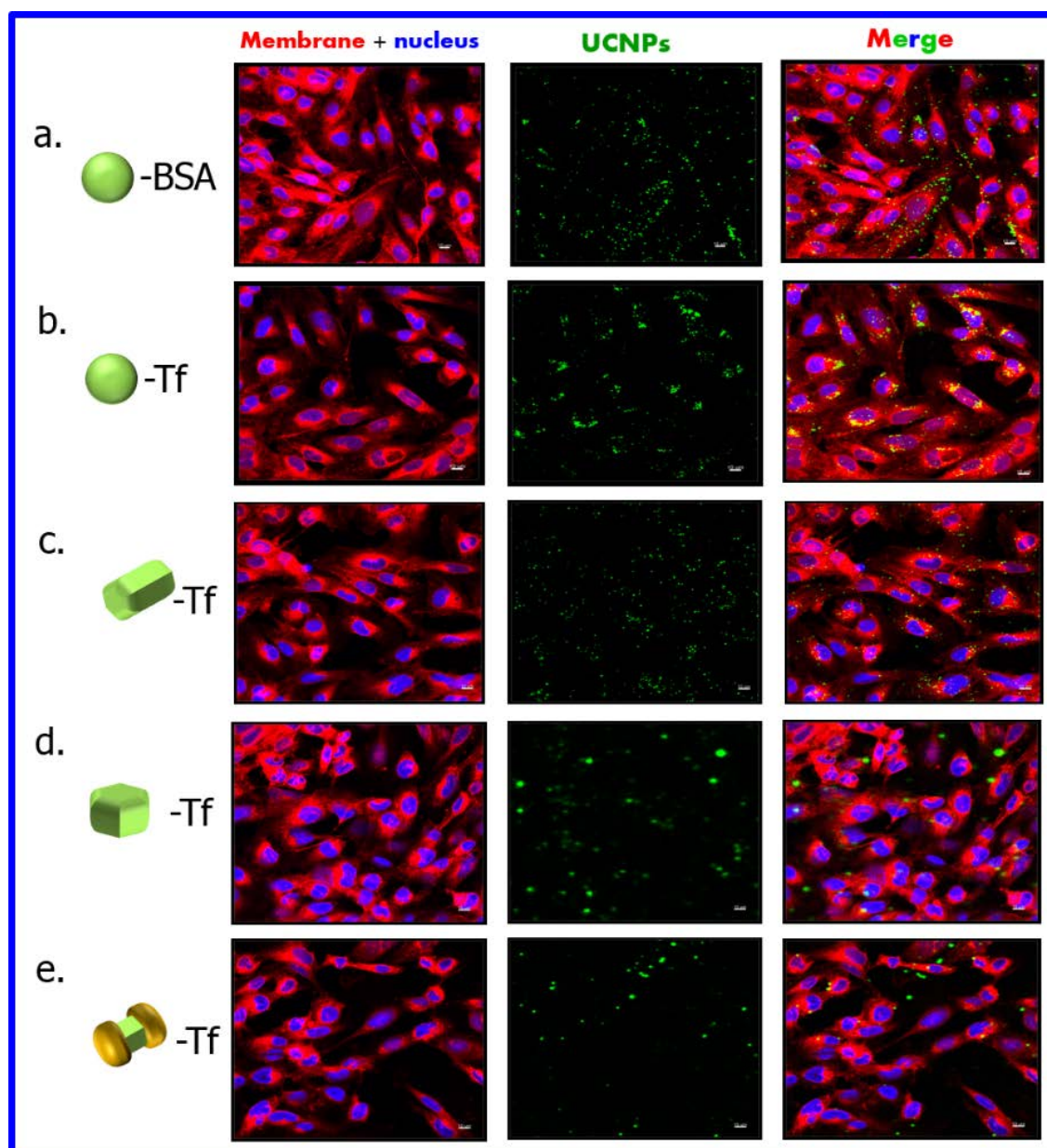


Figure 4. Representative confocal microscopy images of UCNPs-Tf endocytosis on BBB endothelial cells after 4 h co-incubation at 37°C (at the concentration of 50ug/mL): spherical UCNPs-BSA (a), spherical UCNPs-Tf (b), rod UCNPs-Tf (c), disk UCNPs-Tf (d) and dumbbell UCNPs-Tf (e). The images show the upconversion luminescence (green, 980/800nm), the corresponding hCMEC/D3 cells (red membrane labeled with deep red plasma membrane stain, 649/666nm; blue nuclear stained with DAPI, 405/461nm), the overlay of the upconversion luminescent images and the hCMEC/D3 cells. Each shape of UCNPs is labeled as a-e and their formulation are illustrated in the left column, respectively.

because of the reduction of carboxyl groups binding with amine groups of Tf. Furthermore, the confirmation of successful conjugation of Tf to the UCNPs-PEG-Tf conjugates was further confirmed by measuring the OD280 absorbance peak with a

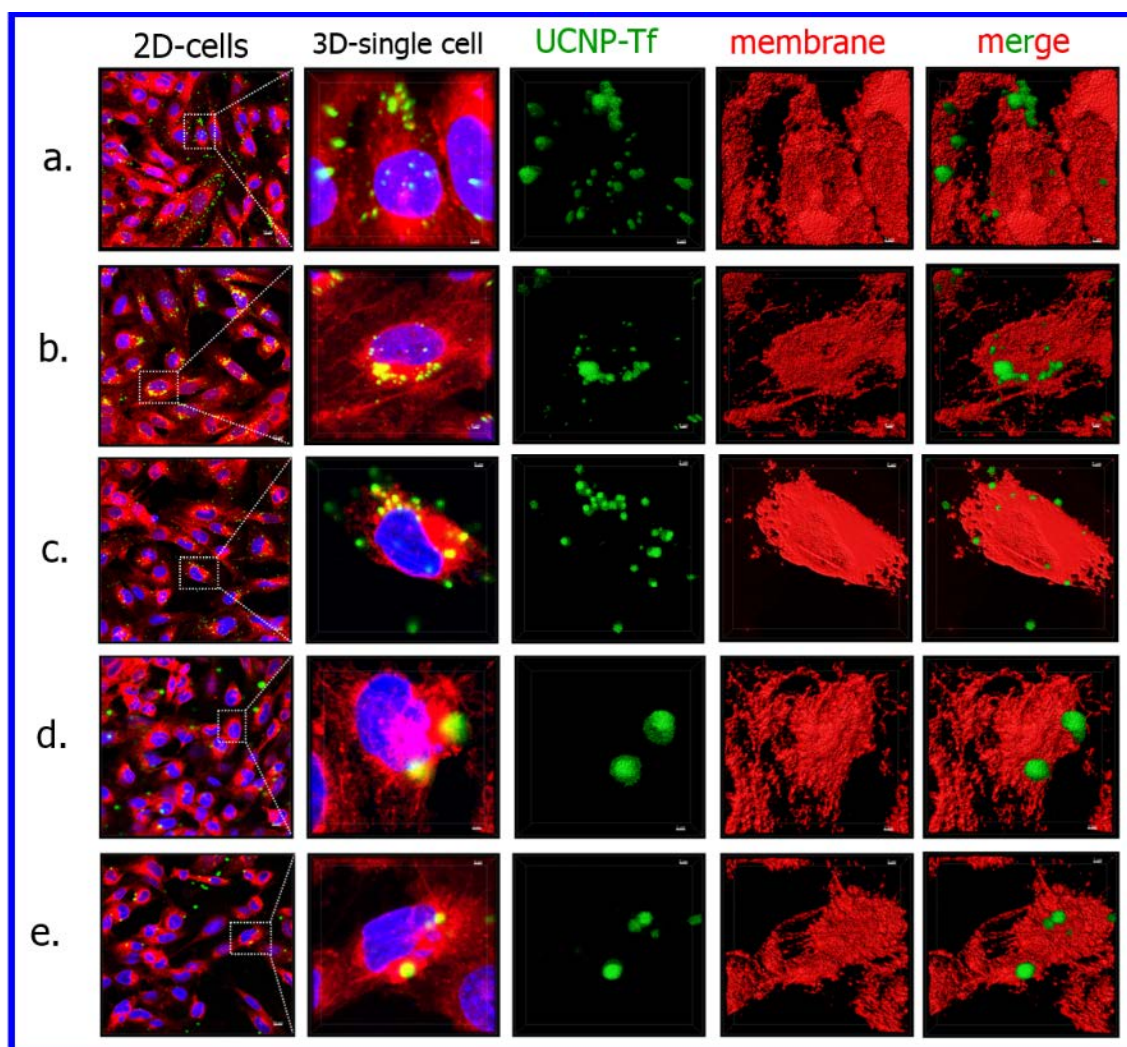


Figure 5. Luminescent microscopy images of five types of UCNP-Tf internalized by hCMEC/D3 cells and their corresponding Imaris software processed 3D single-cell images after 4 h incubation at 37°C (at the concentration of 50ug/mL): spherical UCNPs-Tf (a), spherical UCNPs-Tf (b), rod UCNPs-Tf (c), disk UCNPs-Tf (d) and dumbbell UCNPs-Tf (e). Specifically, the left two rows of images represent original 2D and their magnified 3D single cell images. The right three columns of images showed the luminescent signal of each types of UCNP-Tf, the cell membranes and their overlay. The average cell uptake value can be analyzed by collecting the volume of UCNP-Tf inside the cells.

Nanodrop spectrophotometer (Figure 2b). Pure Tf shows strong ultraviolet (UV) absorption peak at 280nm, while spherical UCNPs-PEG-COOH does not have such a typical absorbance. After conjugation, the absorbance peak of spherical UCNPs-PEG-Tf displays an obvious increase in absorbance at 280nm. Similarly, the other shapes of UCNPs-PEG-Tf showed a distinct absorbance peak at the wavelength of 280nm. The significant change of surface property (Z potential) and the UV absorbance spectra

indicate the success of surface functionalization with Tf.

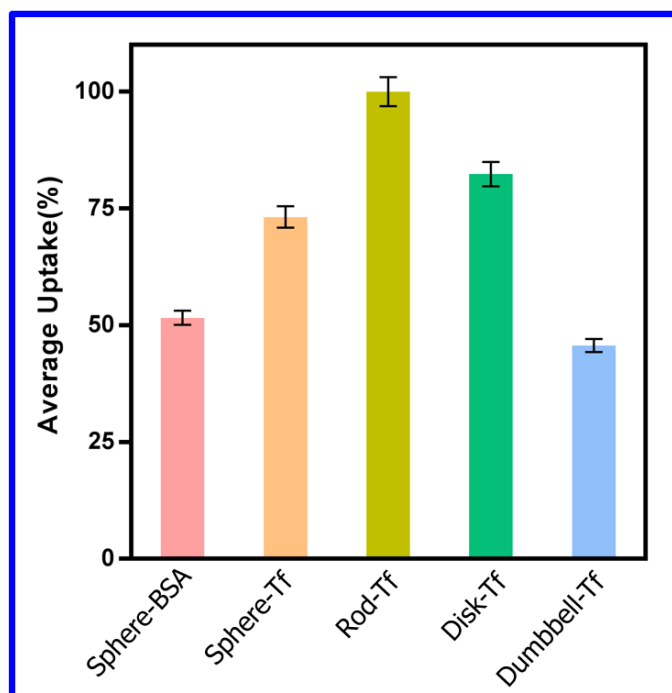


Figure 6. The cellular uptake of modified UCNP with various shapes, including sphere-BSA, sphere-Tf, rod-Tf, disk-Tf and dumbbell-Tf by brain endothelial cells after 4h incubation at 37°C. The average uptake value corresponded to the mean value of ratio between NPs inside and entire ($V_{\text{inside}}/V_{\text{entire}}$) was normalized such that rod-Tf uptake was 100%. UCNPs were employed at a concentration of 50ug/mL.

Cytotoxicity: The cytotoxicity of the Tf-coated UCNPs with different shapes were firstly studied against hCMEC/D3 cells at a concentration range from 10 to 500ug/mL using the MTT assay (Figure 3). Treatment with most shapes of nanoparticles maintained cell survival above 75%, even at high concentration (500μg/mL) of Tf-modified UCNPs for 24h, indicating the low cytotoxicity of these types of UCNPs in vitro. A direct comparison of the cytotoxicity of these three different shapes (rod, dumbbell and disk) of Tf-coated UCNPs and the spheres, it revealed that the dumbbell-shaped UCNPs-Tf both displayed the greatest degree of relative toxicity (* $p < 0.05$) than the spherical UCNPs-Tf, leading to 22% reduction in cell viability after 24h co-incubation with 100μg/mL UCNPs. In contrast, the rod-Tf demonstrated the least cytotoxicity (** $p < 0.01$) even at the highest concentration of 500μg/mL, indicating that rod-shaped UCNPs-Tf are the preferable shape for exposure to cultured cells.

To confirm the successful conjugation of Tf and that this surface modification has improved the bioactivity of the UCNPs, we compared the cytotoxicity of BSA-capped spherical UCNPs against Tf-modified spherical UCNPs under the same experimental concentrations. We found that Tf-capped spherical UCNPs displayed less cytotoxicity than BSA-capped spherical UCNPs at all concentrations tested. ($p < 0.01$, Figure 3)

UCNP-Tf Endocytosis by hCMEC/D3 cells: The targeting functionalized UCNPs-Tf with various shapes were further investigated for their cellular uptake capability and distribution with cultured brain endothelial cells (hCMEC/D3 cells). These cells were selected as they are the cells that form the BBB between blood vessels and the brain tissue, and therefore molecules must be internalized by these cells for them to be transported across the BBB and into the brain. First, as an experimental control to confirm bioactivity of transferrin conjugation onto the surface of UCNPs (we expect that it will

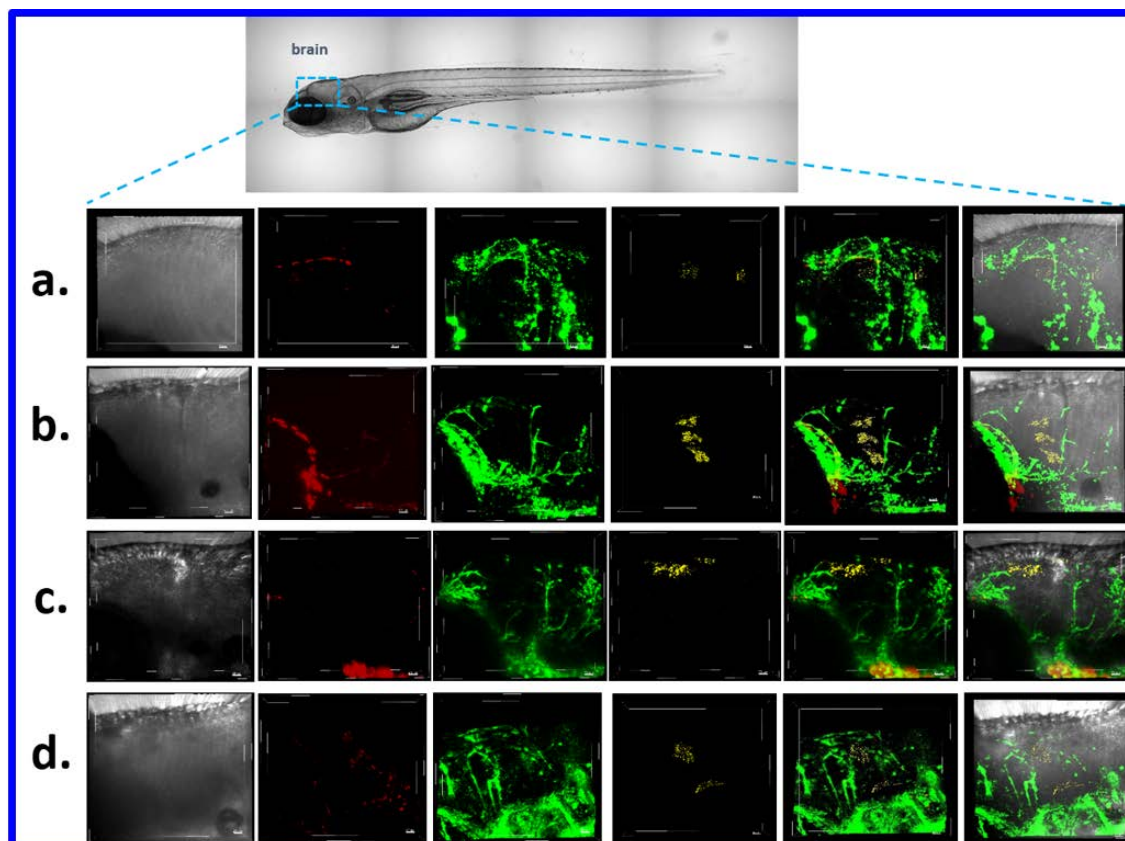


Figure 7. Evaluation of different-shaped UCNPs-Tf uptake in the brain of fli zebrafish. The 3-D confocal microscope images (columns from left to right) represent the bright field images, commercial microbeads (red), GFP labelled blood vessel (green) and Tf-UCNPs (yellow) with various shapes, including spheres (row a), rod (row b), disk (row c) and dumbbell (row d). Those images were captured at 2h after nanoparticle injection.

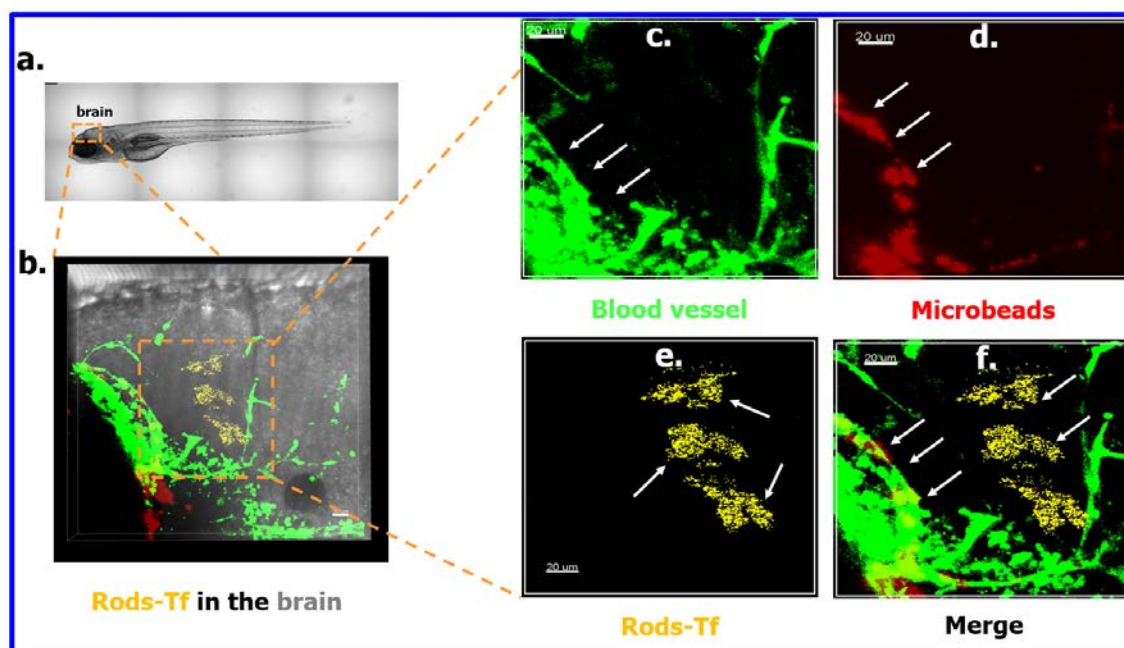


Figure 8. Illustration of rod-shaped UCNPs-Tf uptake in the brain of fli zebrafish. a. The bright field image of fli zebrafish; b. the merged 3-D confocal microscope images of zebrafish brain; c. GFP labelled green blood vessel; d. microbeads in red; e. rod-shaped UCNPs-Tf in yellow and the merged images of c, d and e.

improve cellular uptake of UCNPs), we compared the uptake capacity of spherical UCNPs-Tf and spherical UCNPs-BSA (Figure 4a and b). The luminescent microscopy showed that UCNPs-Tf present significantly higher uptake than UCNPs-BSA. Subsequently, we compared the cellular uptake of UCNPs-Tf with different shapes, such as sphere, rod, disk and dumbbells, finding that all displayed substantial uptake into the cultured endothelial cells (Figure 4b-e). Notably, different shapes of UCNPs-Tf showed obvious differences in their endocytic capability. Specifically, the rod-shaped UCNPs-Tf displayed the homogenous distribution of small UCNPs (presumably single nanoparticles) and good endocytosis by cultured endothelial cells in comparison to other shapes of UCNPs-Tf. In contrast, disk and dumbbell shaped UCNPs-Tf formed large aggregates, which often stuck to the surface of cultured endothelial cells.

To quantitatively measure UCNPs uptake into cultured endothelial cells and distinguish from UCNPs that are stuck on the membrane of cells not actually endocytosed, 3D cell analysis was performed. Accordingly, the cell membrane was stained with deep red membrane dye (red) and the nucleus labelled with DAPI (blue). High resolution z-stack

confocal imaging and 3-dimensional (3D) rendering of the cells (membrane and nucleus) together with visualisation of the UCNP (980nm excitation) was performed, and UCNPs distribution calculated with Imaris (Bitplane) (Figure 5) to precisely analyse the subcellular distribution of UCNP in the cultured endothelial cells. The 3D-rendering of UCNPs (green) distribution in an individual hCMEC/D3 cell was collected as the total volume of UCNP associated with the cell (V_{entire}). The cellular uptake was determined by calculating the volume of UCNPs localised within a single hCMEC/D3 cell (V_{inside}) as determined by masking of the cell membrane versus V_{entire} . Using this approach, we found that all rod-shaped UCNPs-Tf that were associated with an individual hCMEC/D3 cell were fully internalized and therefore the $V_{\text{inside}}/V_{\text{entire}}$ ratio for rod UCNPs-Tf was set to 100%. As shown in Figure 6, the endocytosis value of transferrin modified UCNP was about 2-fold greater than UCNP-BSA. This confirms the successful bioavailability of the UCNPs-Tf. The cell uptake ratios of UCNPs-Tf (sphere, disk and dumbbell) were 38.7%, 48.4% and 9.7% respectively, which is substantially lower than the uptake capability of rod-shaped UCNPs-Tf. These results demonstrate that the shape of UCNP plays an important role in the biostability and cellular uptake properties of UCNPs-Tf. Specifically, we show that the preferable shape for bioavailability and cell uptake in brain endothelial cells is rod > disk > spherical > dumbbell.

Evaluation of UCNPs-Tf bioavailability and distribution in living zebrafish Our cell-culture results indicated that rod-shaped UCNPs-Tf displays the greatest likelihood for BBB crossing and imaging studies in living animals. To confirm this, we investigated the ability of UCNPs-Tf to enter the brain following systemic administration into zebrafish larvae, taking advantage of the ability to readily image the brain of these animals as they are transparent during their first five days of life. (see S3 and S4) To confidently visualize the transport of UCNP into the brain, we used transgenic zebrafish that specifically express green fluorescent protein (GFP) in blood vessels (fli-GFP zebrafish) – this allows us to confirm that the UCNP is not in the small blood vessels in the brain or on the blood-side of the BBB. All four shapes of UCNPs-Tf (sphere, rod, disk and dumbbell) were microinjected directly into the blood vessel of Fli-GFP-zebrafish larvae, followed by confocal imaging in zebrafish at 6h post-injection (Figure 7). In Figure 7a-d, we observed that all shapes of UCNPs-Tf displayed some accumulation within the brain

region of zebrafish larva. Notably, rod-shaped UCNPs-Tf showed the greatest accumulation, while spherical UCNPs-Tf displayed the lowest amount of brain localization. The enlarged fluorescent images of rod-like UCNPs-Tf uptake by the brain is shown in the Figure 8. It showed that most of red microbeads remained in the blood vessels, because most of red-colour overlap with green blood vessels in Figure 8f. However, the yellow-colour of rod-like UCNPs-Tf were hardly observe in the green blood vessel, which means that nanorods may pass the BBB and accumulate in the brain. These results above were consistent with the cellular uptake capability of UCNPs-Tf in cell culture medium studies. On the contrary, the fluorescent microbeads (FM, visual control for microinjection) still mainly remained in the blood vessel after injection for 6h, demonstrating more difficult to across BBB than UCNPs-Tf. Due to the FMs without Tf targeting modification, FMs processed no specific BBB transport ability. The volume of those types of UCNPs-Tf accumulated in the brain were measured via the Imaris software. The accumulated volume of UCNPs-Tf (sphere, disk and dumbbell) were $152 \pm 4 \text{ um}^3$, $217 \pm 6 \text{ um}^3$ and $69 \pm 2 \text{ um}^3$ respectively, which is substantially lower than the uptake capability of rod-shaped UCNPs-Tf ($264 \pm 8 \text{ um}^3$). This result indicated that the BBB transport ability of various-shaped UCNPs-Tf was as the order rod > disk > dumbbell > spheres.

Conclusions

In this paper, we systemically investigated the effect of nanoparticle shape upon the biophysical properties of UCNPs, and the influence of this upon cellular uptake in cultured cells and brain uptake in vivo. Firstly, we synthesized a series of lanthanide-doped $\beta\text{-NaYF}_4$: 20% Yb, 4% Tm UCNPs with different shapes, such as sphere, disk, rod and dumbbell. Thereafter, those types of UCNPs were further modified with transferrin, which was demonstrated to enable significant nanoparticles transport across the BBB into the brain by Tf receptor-mediated endocytosis by the brain capillary endothelial cells (Jiang Chang et al. International Journal of Pharmaceutics 2009). Followed with that, we characterize the modification process and measured the internalization behaviour with hCMEC/D3 cells. The result showed that Tf was successfully modified on the surface of UCNPs by the Z-potential change on the surface and the typical absorbance peak at 280nm of UCNPs-Tf. Furthermore, the Tf-modified spherical UCNPs showed higher cell

uptake efficiency compared to the BSA-capped UCNPs. This indicated that the transferrin-conjugation to the UCNPs facilitates improved uptake into the endothelial cells. We also investigated the transport efficiency of UCNPs-Tf with different shapes across the BBB in living zebrafish. Both cellular and zebrafish microinjection results suggested that all types of UCNP-Tf with different shapes can cross the BBB by receptor-mediated transcytosis and subsequently accumulated in the brain. Moreover, we have found that the priorities are rod > disk > sphere > dumbbell. Therefore, those UCNPs-Tf has potential application as excellent carriers for the transport of drugs crossing the BBB.

Materials and Methods:

Chemicals. The following materials were obtained from Sigma-Aldrich (St. Louis, MO, USA): Yttrium chloride hexahydrate ($\text{YCl}_3 \cdot 6\text{H}_2\text{O}$, 99.99%), gadolinium chloride hexahydrate ($\text{GdCl}_3 \cdot 6\text{H}_2\text{O}$, 99.99%) ytterbium chloride hexahydrate ($\text{YbCl}_3 \cdot 6\text{H}_2\text{O}$, 99.99%), thulium chloride hexahydrate ($\text{TmCl}_3 \cdot 6\text{H}_2\text{O}$, 99.99%), sodium hydroxide (NaOH, 99%), ammonium fluoride (NH_4F , 99%), oleic acid (OA, 90%), 1-octadecene (ODE, 90%), cyclohexane, ethanol, ammonium hydroxide solution (NH_4OH , 30%) and 3-[4,5-dimeethylthiazol-2-yl]-2,5-diphenyl tetrazolium bromide (MTT). Fetal bovine serum (FBS), Hoechst 3342, and deep red plasma membrane stain were purchased from Invitrogen Life Technologies (Mulgrave, Australia). PHOS-PEG-COOH (MW3500) was synthesized by JenKem technology Co. Ltd (Beijing China).

Synthesis of sphere-like UCNPs: The spherical UCNPs ($\beta\text{-NaYF}_4\text{:20\%Yb,4\%Tm}$) were synthesized following a nominally oxygen-free protocol according to previously reported literature.^{31, 35} Generally, YCl_3 (0.76 mmol), YbCl_3 (0.2 mmol) and TmCl_3 (0.04 mmol) were mixed with 6 mL oleic acid (OA) and 15 mL octadecene (ODE) in a 50 mL two-neck round-bottom flask. Thereafter, the above mixture was degassed under Ar flow and heated to 160 °C to form a homogeneous solution, then cooled down to room temperature. Five mL methanol solution containing NH_4F (4 mmol) and NaOH (2.5 mmol) was slowly added into the flask and stirred for 30 min at room temperature. Subsequently, the mixture solution was slowly heated up to 110 °C for 15min to remove methanol, and continually heated to 150 °C for 15 min to remove water completely. Finally, the mixture solution was quickly heated to 310°C and maintained for 1.5 h under Ar protection. Followed with that, the solution was cooled down to room temperature

naturally, ethanol was added to precipitate the nanocrystals. After the product was washed with cyclohexane/ethanol/methanol (2:9:3 v/v/v) for three times, the final spherical NaYF₄:20% Yb,4% Tm nanocrystals were stored in 2mL cyclohexane at 4°C.

Synthesis of rod-like UCNPs: The longitudinal shell growth of UCNPs onto the core of spherical β -NaYF₄:20% Yb,4% Tm NPs was conducted via a hot seed-injection protocol.³⁶ Firstly, 2mL methanol (containing 0.76 mmol YCl₃, 0.2mmol YbCl₃ and 0.02mmol TmCl₃) were added to a 50 mL three-neck round-bottom flask containing 3.25mL oleic acid and 7.5mL 1-octadecene. The mixture solution was heated to 150 °C under argon protection for 30 min to generate a clear solution and then cooled down naturally to below 50 °C (labeled as UCNPs shell precursors). Afterwards, 2.5mL methanol solution containing NH₄F (2 mmol) and NaOH (1.25mmol) and two mL methanol solution of KOH (0.5mmol). After stirring for 30 min, the solution was heated to 80 °C under argon for 15 min to remove methanol, and then the reaction solution was further heated to 150 °C for another 20min. For the longitudinal shell growth of UCNPs, 0.5 mmol as-prepared spherical NaYF₄:20% Yb,4% Tm core particles were added to the 50 mL-flask. The mixture was heated to 150 °C under argon for 20 min, and then the solution was quickly heated to 310 °C for 1h. Lastly, the solution was gradually cooled down to room temperature and the prepared UCNPs nanorods were washed via the procedures used for the purification of spherical β -NaYF₄:Yb,Tm particles.

The NaYF₄:20% Yb,4% Tm upconversion nanorods with ARs = 2 were conducted with a one-pot hot-injection approach modified and optimized on the base of our previous work.^{31, 36} First, shell precursors were prepared. 0.76mmol YCl₃·6H₂O, 0.2mmol YbCl₃ and 0.04mmol TmCl₃·6H₂O were mixed into a 50 mL-flask containing 6.5mL oleic acid and 15mL 1-octadecene. The mixture solution was heated to 160 °C for 30 min with under argon flow and then cooled down to room temperature (RT), followed by the addition of 4.0mmol NH₄F, 2.5mmol NaOH and 2.0mmol KOH in 8 mL methanol. After stirring for 30 min at RT, the solution was heated to 80 °C with argon flow for 20 min, and then the react system was continually heated to 150 °C for another 30 min. Finally, the reaction solution was cooled down to room temperature and labeled as 1mmol NaYF₄:Yb,Tm shell precursors for further use.

For the longitudinal growth of NaYF₄:Yb,Tm with AR=2, 0.2 mmol spherical

NaYF₄:Yb,Tm core particles in cyclohexane were added to a 50 mL three-neck flask containing 1.3mL OA and 3 mL ODE. The mixture solution was heated to 160 °C under argon flow for 30 min, and then the solution was continually heated to 310 °C. Followed with that, 0.2 mmol of as-prepared NaYF₄:Yb,Tm shell precursors were injected into the reaction mixture at the speed of 0.1 mL per 10 min and followed by another 0.5 h reaction time at 310 °C. Finally, the formed solution was gradually cooled down to room temperature and the formed upconversion nanorods with AR=2 were purified according to the procedures employed for the purification of NaYF₄:Yb,Tm core particles.

Synthesis of disk-like UCNPs: The disk-shaped UCNPs were fabricated using an oxygen-free protocol described in the literature³⁷. Specifically, 3.5 mL of methanol solution (containing 0.76mmol YCl₃, 0.2mmol YbCl₃ and 0.04mmol Tm) was magnetically mixed with 15 mL OA and 16 mL ODE in a 100 mL-flask. The resultant mixture was degassed under Ar flow and heated to 150 °C for 30 min to form a clear solution, then stopped heating and cooled to room temperature. 3.7mmol NH₄F and 2.5mmol NaOH in 5 mL of methanol solution was added into the reaction system and kept stirring for 30 min at room temperature. The methanol and water in the system were removed by keeping the mixture solution at 110 °C for 30 min. Then the formed mixture solution was slowly heated to reaction temperature 310°C and remain for 1.5 h. Ethanol was added to precipitate the nanocrystals after the solution cooled down to room temperature. Finally, the resultant nanoparticles were collected by centrifugation, washed with cyclohexane, ethanol and methanol for three times, the final spherical NaYF₄:20%Yb,4%Tm nanocrystals were re-dispersed in 10mL cyclohexane at 4°C for further experiment.

Synthesis of dumbbell-like UCNPs: The dumbbell-shaped UCNPs were prepared according to an approach previously reported in the literature³¹. Typically, 1mL of methanol solution (containing 0.2mmol GdCl₃) was magnetically mixed with 3.5 mL OA and 9 mL ODE in a 50 mL three-neck round-bottom flask. The reaction system was protected under Ar flow and heated to 150 °C for 30 min to generate a homogeneous solution before it was cooled down to room temperature naturally. Methanol solution (4mL) containing NH₄F (0.8 mmol) and NaOH (0.5 mmol) was added into the solution of OA and ODE and kept stirring for 30 min at room temperature. Subsequently, the

formed solution was slowly heated up and kept at 110 °C for 30 min to remove methanol and the remaining water completely. Followed with that, 0.2mmol of nanorod UCNPs core in cyclohexane was injected into the reaction system. After keeping the reaction temperature at 110 °C for further 10 min to evaporate all cyclohexane, the mixture solution was quickly heated to reaction temperature 310°C and kept for 1.5 h. After the formed solution cooled down to room temperature, ethanol was added to precipitate the as-prepared UCNPs. After the particles was washed with cyclohexane, ethanol and methanol for 3 times, the final dumbbell-like UCNPs were re-dispersed in 10mL cyclohexane for further application.

Synthesis of PEGylated UCNPs with Various Shapes To functionalize UCNPs with carboxyl group, we employed PHOS-PEG-COOH (MW3500) to ligand exchange with OA on the surface of as-prepared UCNPs with various shapes. Firstly, dichloromethane solution of NOBF₄ was used to transfer various-shaped UCNPs to hydrophilic according to the literatures.^{38–40} Typically, 5mL of cyclohexane (containing UCNPs ~5 mg/mL) was added into 0.05mol NOBF₄ in 5 mL dichloromethane (DCM) solution and kept vigorously shaking until UCNPs were transferred from the upper cyclohexane layer to the bottom DCM layer. The surface modified UCNPs were purified by precipitation with the addition of toluene and cyclohexane (1:1 by volume), then the precipitated PEGylated UCNPs with various shapes were re-dispersed in DMF at the concentration of 10 mg/mL, respectively. Furthermore, take 500 µL of solution (~5mg UCNPs) into a glass bottle. Followed with that, 25 mg PEG dispersed in 2.5 mL MiliQ water was added into the bottle, causing white precipitation on the bottom of the glass bottle. Then, 2mL absolute ethanol was also added into the mixture solution, leading to the solution becoming clear. The reaction system was kept stirring for 48 h. Finally, the UCNPs-PEG-COOH were washed by water for 5 times and stored at 4°C for further use.

Bioconjugation of UCNPs with Various Shapes To conjugate transferrin or bovine serum albumin (BSA) to PEGylated UCNPs (spherical), primary amines of transferrin or BSA were linked with PEGylated UCNPs with carboxyl group via EDC/NHS chemistry.³⁹ 5 mg PEGylated UCNPs was suspended in 500 µ L MES buffer (500 mM, pH 5.5) to form a 10 mg/mL solution. The solution was mixed well with 25 mg/mL EDC and 90 mg/mL NHS in MES solution and left to react for 15 min at room temperature.

Ultrafiltration was performed by Vivaspin 20 (MWCO 3000) spin columns to remove excess EDC and NHS following buffer exchange into PBS (0.1 M, pH 8.0). The carboxyl activated solution was mixed with 1 mL of 2 mg/mL transferrin in PBS (transferrin: PEGylated UCNPs= 1:50) to react at room temperature for 2 h. The as-prepared Transferrin-functionalized UCNPs were collected by centrifugation and then washed three times with water. Finally, the formed spherical Transferrin-UCNPs were re-dispersed in MiliQ water and stored at 4°C for further use. For the transferrin functionalization of other shapes of UCNPs (rod, disk and dumbbell), the same approach above was used for bioconjugation.

Blood-Brain Barrier hCMEC/D3 Cell Culture: Blood-Brain Barrier (BBB) hCMEC/D3 cell line (purchased from Merck Millipore) were grown in EBM-2 medium (Lonza, Basel, Switzerland) supplemented with 5% ultralow IgG FBS, 10 mM HEPES, 1 ng/ml basic FGF (bFGF), 1.4 μ M hydrocortisone and 1% penicillin–streptomycin.⁴¹ The cells were incubated at 37 °C, 5% CO₂/saturated humidity according to established procedure. Cells were subcultured every 3-4 days.

Cell Cytotoxicity Assay: To measure the cell cytotoxicity, 3-[4,5-dimethylthiazol-2-yl]-2,5-diphenyltetrazolium-bromide (MTT) proliferation assay was used in this experiment. The MTT assay is based on the protocol firstly described by Mossmann (1983).⁴² The assay was optimized for the cell lines used in the experiments. Briefly, 2.0×10^3 hCMEC/D3 BBB cells in cell culture media introduced above were seeded into a 96-well microplate (200 μ L/well) and incubated for 24h at 37 °C. Followed with that, the growth media was replaced with 200 μ L fresh cell culture media containing increasing transferrin-functionalized UCNPs concentrations (0, 1, 10, 20, 50 and 100mg/ml). The plates were incubated for 24 h before 10 μ L of the MTT (5.0 mg/mL in phosphate buffered saline solution) was added to each well for evaluation of cell viability. Cells were further incubated at 37 °C for four h to allow precipitation of insoluble purple formazan crystals. Subsequently, the supernatant was carefully removed, and 150 μ L dimethyl sulfoxide was added to each well and left for 2h in the dark at room temperature to dissolve the formed formazan crystals. Finally, the absorbance was measured using the Biotek Microplate Reader (Biotek, U.S.A.) at a wavelength of 570 nm.^{43, 44} The control wells were assumed to have 100% viability. Thus, the viable cells number was calculated based on the absorbance of the control cultures. For analysis, 3 wells per treatment were repeated in

this experiment.

Size, Zeta Potential, Absorption Spectrum Measurements. The as-prepared UCNPs with various shapes (including sphere, rod, disk and dumbbell) were characterized with transmission electron microscopy (TEM). 8 μ l of an aqueous dispersion of UCNPs in cyclohexane was placed on a copper grid and measured with a Philips CM10 TEM with Olympus Sis Megaview G2 Digital Camera. ImageJ software was used for the UCNP size distribution analysis. Furthermore, the zeta-potentials of PEGylated UCNPs and transferrin-coated UCNPs were measured using a Zeta sizer Nano ZS (Malvern Instruments, U.K.) at 25 °C in cell culture media. Since transferrin has a typical absorption peak at 280nm, the Thermo Scientific Nanodrop 2000 Spectrophotometer was used to determine the transferrin conjugation with PEGylated UCNPs. Thus, the absorption of the PEGylated UCNPs, transferrin-modified UCNPs and the pure transferrin were obtained at 1mg/ml in water, respectively. Two microliters of each sample were dipped on the lower measurement pedestal to generate the spectrum profiles.

Cell and zebrafish imaging with confocal microscopy BBB hCMEC/D3 cells at 4×10^4 cells/well were cultured in glass chamber slide (8 chambers) for 24h. 200 μ L transferrin-modified UCNPs with various shapes at the concentration of 50 μ g/mL was added into each chamber and incubated with hCMEC/D3 cells at 37 °C for four h under 5% CO₂. After washing with PBS for three times, cells were further fixed in 4% paraformaldehyde in the dark for 30 min at room temperature. The fixed cells were washed with PBS for three times and labelled by $2 \times$ deep red plasma membrane stain and 2 μ M Hoechst 33342 for 15min in the dark at 37°C. The stained cells were rinsed with PBS for three times and mounted with Vector Vectashield fluorescent mounting media (USA) before the coverslips were sealed with nail polish. The cultured cells without UCNPs served as the blank control. Furthermore, BSA-modified spherical UCNPs was employed as negative control compared with transferrin-functionalized spherical UCNPs in this process. Z-stack imaging with a confocal microscope (ZEISS LSM 880 with Airyscan and 980nm laser) was performed in order to confirm internalization and quantification of the transferrin-functionalized UCNPs. The oil-immersions 40 \times objective was used for zebrafish imaging and 100 \times objective for cells imaging process to obtain high resolution

fluorescent images. The excitation intensity was set to 9.8×10^7 W/cm². For each cell culture, a minimum of three different cell areas was imaged to reduce noise.

Zebrafish microinjection. The BBB penetration of Tf-UCNPs was then investigated in vivo using fli zebrafish that express GFP in the vasculature.⁴⁵ Five-day-old zebrafish were mounted in 1% low melting agarose before microinjection and imaging as previously described. A suspension of Tf-UCNPs (1 mg ml⁻¹) with various shapes mixed with 1 mg ml⁻¹ microbeads (as visual control) was injected into the blood vessel (labelled with green fluorescent protein; Tg (fli1a:EGFP)) of five-day-old zebrafish. Approximately, 5 nL solution was injected into the blood stream and luminescence images were acquired at 6 h after injection (fed into the fish water in a 28 °C incubator). Upon excitation at 980 nm, the transferrin-functionalized nanoparticles entered the zebrafish brain can be clearly visualized.

Evaluation of internalized transferrin-modified UCNPs To evaluate the uptake capacity of transferrin-modified UCNPs with various shapes, Imaris software was used in this process for quantitative analyzation. For each cell culture slide chamber, a minimum of three different cell areas was observed. For the image analysis, the labelling of membranes and nuclear were used to outline single cells, cell clusters, or a monolayer region within the excitation spot. The obtained UCNP signals were quantified as a mean UCNP signal per cell, which was a measure of the mean cellular uptake of transferrin-modified UCNPs. The relative intensity of PEGylated and transferrin-conjugated UCNPs signal were recorded and normalized with respect to the largest cellular uptake level observed (that of rod transferrin-functionalized UCNPs), which was set to 100%.

Luminescent Intensity Comparison different-shaped transferrin-UCNPs To further confirm the optical property of each shape of UCNPs for quantification use, the comparison of the luminescent intensity of single transferrin-UCNPs with various morphology was conducted in this experiment. 100uL of 0.5mg/mL spherical (or rod, or disk, or dumbbell) transferrin-UCNPs in water were used to rinse the coverslip, then it was upside down attached (sealed with nail polish) on a glass slide after it dried. The luminescent intensity of each shape of transferrin-UCNPs was measured by homemade microscopy (built in 980nm laser). The intensity of each shape of transferrin-UCNPs was measured three times and the average value was obtained for comparison.

References

- (1) Bradbury, M. Why a Blood-Brain Barrier? *Trends Neurosci.* **1979**, 2, 36–38.
- (2) Ghose, A. K.; Viswanadhan, V. N.; Wendoloski, J. J. A Knowledge-Based Approach in Designing Combinatorial or Medicinal Chemistry Libraries for Drug Discovery. 1. A Qualitative and Quantitative Characterization of Known Drug Databases. *J. Comb. Chem.* **1999**, 1, 55–68.
- (3) Kreuter, J. Nanoparticulate Systems for Brain Delivery of Drugs. *Adv. Drug Deliv. Rev.* **2001**, 47, 65–81.
- (4) Dhuria, S. V.; Hanson, L. R.; Frey, W. H. Intranasal Delivery to the Central Nervous System: Mechanisms and Experimental Considerations. *Journal of Pharmaceutical Sciences*, 2010, 99, 1654–1673.
- (5) Sanovich, E.; Bartus, R. T.; Friden, P. M.; Dean, R. L.; Le, H. Q.; Brightman, M. W. Pathway across Blood-Brain Barrier Opened by the Bradykinin Agonist, RMP-7. *Brain Res.* **1995**, 705, 125–135.
- (6) Tang, S. C.; Lankheet, N. A. G.; Poller, B.; Wagenaar, E.; Beijnen, J. H.; Schinkel, A. H. P-Glycoprotein (ABCB1) and Breast Cancer Resistance Protein (ABCG2) Restrict Brain Accumulation of the Active Sunitinib Metabolite N-Desethyl Sunitinib. *J. Pharmacol. Exp. Ther.* **2012**, 341, 164–173.
- (7) Bobo, R. H.; Laske, D. W.; Akbasak, A.; Morrison, P. F.; Dedrick, R. L.; Oldfield, E. H. Convection-Enhanced Delivery of Macromolecules in the Brain. *Proc Natl Acad Sci U S A* **1994**, 91, 2076–2080.
- (8) Allard, E.; Passirani, C.; Benoit, J. P. Convection-Enhanced Delivery of Nanocarriers for the Treatment of Brain Tumors. *Biomaterials* **2009**, 30, 2302–2318.
- (9) Petros, R. A.; DeSimone, J. M. Strategies in the Design of Nanoparticles for Therapeutic Applications. *Nat. Rev. Drug Discov.* **2010**, 9, 615–627.
- (10) Kuang, Y.; An, S.; Guo, Y.; Huang, S.; Shao, K.; Liu, Y.; Li, J.; Ma, H.; Jiang, C. T7 Peptide-Functionalized Nanoparticles Utilizing RNA Interference for Glioma Dual Targeting. *Int. J. Pharm.* **2013**, 454, 11–20.
- (11) Singh, S. R.; Grossniklaus, H. E.; Kang, S. J.; Edelhauser, H. F.; Ambati, B. K.; Kompella, U. B. Intravenous Transferrin, RGD Peptide and Dual-Targeted Nanoparticles Enhance Anti-VEGF Intracellular Gene Delivery to Laser-Induced CNV. *Gene Ther.* **2009**, 16, 645–659.
- (12) Zhang, B.; Sun, X.; Mei, H.; Wang, Y.; Liao, Z.; Chen, J.; Zhang, Q.; Hu, Y.; Pang, Z.; Jiang, X. LDLR-Mediated Peptide-22-Conjugated Nanoparticles for Dual-Targeting Therapy of Brain Glioma. *Biomaterials* **2013**, 34, 9171–9182.
- (13) Kim, J. H.; Kim, J. H.; Kim, K.-W.; Kim, M. H.; Yu, Y. S. Intravenously Administered Gold Nanoparticles Pass through the Blood–retinal Barrier Depending on the Particle Size, and Induce No Retinal Toxicity. *Nanotechnology* **2009**, 20, 505101.
- (14) Kurakhmaeva, K. B.; Djindjikhshvili, I. A.; Petrov, V. E.; Balabanyan, V. U.; Voronina, T. A.; Trofimov, S. S.; Kreuter, J.; Gelperina, S.; Begley, D.; Alyautdin, R. N. Brain Targeting of Nerve Growth Factor Using Poly(butyl Cyanoacrylate) Nanoparticles. *J. Drug Target.* **2009**, 17, 564–574.
- (15) Sun, W.; Xie, C.; Wang, H.; Hu, Y. Specific Role of Polysorbate 80 Coating on the Targeting of Nanoparticles to the Brain. *Biomaterials* **2004**, 25, 3065–3071.
- (16) Mistry, A.; Stolnik, S.; Illum, L. Nanoparticles for Direct Nose-to-Brain Delivery

- of Drugs. *International Journal of Pharmaceutics*, 2009, 379, 146–157.
- (17) Masserini, M. Nanoparticles for Brain Drug Delivery. *ISRN Biochem.* **2013**, 2013, 1–8.
- (18) Lin, Y.-S.; Haynes, C. L. Impacts of Mesoporous Silica Nanoparticle Size, Pore Ordering, and Pore Integrity on Hemolytic Activity. *J Am Chem Soc* **2010**, 132, 4834–4842.
- (19) Choi, H. S.; Ipe, B. I.; Misra, P.; Lee, J. H.; Bawendi, M. G.; Frangioni, J. V. Tissue- and Organ-Selective Biodistribution of NIR Fluorescent Quantum Dots. *Nano Lett.* **2009**, 9, 2354–2359.
- (20) Chithrani, B. D.; Ghazani, A. A.; Chan, W. C. W. Determining the Size and Shape Dependence of Gold Nanoparticle Uptake into Mammalian Cells. *Nano Lett.* **2006**, 6, 662–668.
- (21) Chung, T. H.; Wu, S. H.; Yao, M.; Lu, C. W.; Lin, Y. S.; Hung, Y.; Mou, C. Y.; Chen, Y. C.; Huang, D. M. The Effect of Surface Charge on the Uptake and Biological Function of Mesoporous Silica Nanoparticles in 3T3-L1 Cells and Human Mesenchymal Stem Cells. *Biomaterials* **2007**, 28, 2959–2966.
- (22) Jiang, W.; Kim, B. Y. S.; Rutka, J. T.; Chan, W. C. W. Nanoparticle-Mediated Cellular Response Is Size-Dependent. *Nat. Nanotechnol.* **2008**, 3, 145–150.
- (23) Champion, J. A.; Katare, Y. K.; Mitragotri, S. Particle Shape: A New Design Parameter for Micro- and Nanoscale Drug Delivery Carriers. *Journal of Controlled Release*, 2007, 121, 3–9.
- (24) Yi, Z.; Lu, W.; Xu, Y.; Yang, J.; Deng, L.; Qian, C.; Zeng, T.; Wang, H.; Rao, L.; Liu, H.; *et al.* PEGylated NaLuF₄: Yb/Er Upconversion Nanophosphors for In vivo Synergistic fluorescence/X-Ray Bioimaging and Long-Lasting, Real-Time Tracking. *Biomaterials* **2014**, 35, 9689–9697.
- (25) Liu, L.; Venkatraman, S. S.; Yang, Y. Y.; Guo, K.; Lu, J.; He, B.; Mookhala, S.; Kan, L. Polymeric Micelles Anchored with TAT for Delivery of Antibiotics across the Blood-Brain Barrier. In *Biopolymers - Peptide Science Section*; 2008; Vol. 90, pp. 617–623.
- (26) Yang, D.; Ma, P.; Hou, Z.; Cheng, Z.; Li, C.; Lin, J. *Current Advances in Lanthanide Ion (Ln(3+))-Based Upconversion Nanomaterials for Drug Delivery*; 2014; Vol. 44.
- (27) Ge, X.; Dong, L.; Sun, L.; Song, Z.; Wei, R.; Shi, L.; Chen, H. New Nanoplatforms Based on UCNP_s Linking with Polyhedral Oligomeric Silsesquioxane (POSS) for Multimodal Bioimaging. *Nanoscale* **2015**, 7, 7206–7215.
- (28) Auzel, F. Upconversion and Anti-Stokes Processes with F and D Ions in Solids. *Chemical Reviews*, 2004, 104, 139–173.
- (29) Wang, F.; Liu, X. Recent Advances in the Chemistry of Lanthanide-Doped Upconversion Nanocrystals. *Chem. Soc. Rev.* **2009**, 38, 976.
- (30) Haase, M.; Schäfer, H. Upconverting Nanoparticles. *Angew. Chemie - Int. Ed.* **2011**, 50, 5808–5829.
- (31) Liu, D.; Xu, X.; Du, Y.; Qin, X.; Zhang, Y.; Ma, C.; Wen, S.; Ren, W.; Goldys, E. M.; Piper, J. A.; *et al.* Three-Dimensional Controlled Growth of Monodisperse Sub-50 nm Heterogeneous Nanocrystals. *Nat. Commun.* **2016**, 7, 10254.
- (32) Lu, Y.; Zhao, J.; Zhang, R.; Liu, Y.; Liu, D.; Goldys, E. M.; Yang, X.; Xi, P.; Sunna, A.; Lu, J.; *et al.* Tunable Lifetime Multiplexing Using Luminescent Nanocrystals. *Nat. Photonics* **2013**, 8, 32–36.
- (33) Wang, F.; Deng, R.; Liu, X. Preparation of Core-Shell NaGdF₄ Nanoparticles

- Doped with Luminescent Lanthanide Ions to Be Used as Upconversion-Based Probes. *Nat. Protoc.* **2014**, *9*, 1634–1644.
- (34) Huang, X.; Teng, X.; Chen, D.; Tang, F.; He, J. The Effect of the Shape of Mesoporous Silica Nanoparticles on Cellular Uptake and Cell Function. *Biomaterials* **2010**, *31*, 438–448.
- (35) Zhao, J.; Lu, Z.; Yin, Y.; McRae, C.; Piper, J. A.; Dawes, J. M.; Jin, D.; Goldys, E. M. Upconversion Luminescence with Tunable Lifetime in NaYF₄:Yb,Er Nanocrystals: Role of Nanocrystal Size. *Nanoscale* **2013**, *5*, 944–952.
- (36) Wen, S.; Li, D.; Liu, D.; Xu, X.; Du, Y.; Mitchell, D. R. G.; Shi, B.; Shi, X.; Jin, D. Seed Mediated One-Pot Growth of Versatile Heterogeneous Upconversion Nanocrystals for Multimodal Bioimaging. **2016**, *10013*, 1001315.
- (37) Liu, C.; Gao, Z.; Zeng, J.; Hou, Y.; Fang, F.; Li, Y.; Qiao, R.; Shen, L.; Lei, H.; Yang, W.; *et al.* Magnetic / Upconversion Fluorescent Dual-Modal Molecular Probes for Imaging Tiny Tumors in Vivo. *ACS Nano* **2013**, *7*, 7227–7240.
- (38) Chen, Q.; Wang, C.; Cheng, L.; He, W.; Cheng, Z.; Liu, Z. Protein Modified Upconversion Nanoparticles for Imaging-Guided Combined Photothermal and Photodynamic Therapy. *Biomaterials* **2014**, *35*, 2915–2923.
- (39) Shi, Y.; Shi, B.; Dass, A. V. E.; Lu, Y.; Sayyadi, N.; Kautto, L.; Willows, R. D.; Chung, R.; Piper, J.; Nevalainen, H.; *et al.* Stable Upconversion Nanohybrid Particles for Specific Prostate Cancer Cell Immunodetection. *Sci. Rep.* **2016**, *6*, 37533.
- (40) Dong, A.; Ye, X.; Chen, J.; Kang, Y.; Gordon, T.; Kikkawa, J. M.; Murray, C. B. A Generalized Ligand-Exchange Strategy Enabling Sequential Surface Functionalization of Colloidal Nanocrystals. **2011**, 998–1006.
- (41) Markoutsas, E.; Pampalakis, G.; Niarakis, A.; Romero, I. A.; Weksler, B.; Couraud, P. O.; Antimisiaris, S. G. Uptake and Permeability Studies of BBB-Targeting Immunoliposomes Using the hCMEC/D3 Cell Line. *Eur. J. Pharm. Biopharm.* **2011**, *77*, 265–274.
- (42) Mosmann, T. Rapid Colorimetric Assay for Cellular Growth and Survival: Application to Proliferation and Cytotoxicity Assays. *J. Immunol. Methods* **1983**, *65*, 55–63.
- (43) Shi, B.; Zhang, H.; Bi, J.; Dai, S. Endosomal pH Responsive Polymers for Efficient Cancer Targeted Gene Therapy. *Colloids Surfaces B Biointerfaces* **2014**, *119*, 55–65.
- (44) Shen, Z.; Bi, J.; Shi, B.; Nguyen, D.; Xian, C. J.; Zhang, H.; Dai, S. Exploring Thermal Reversible Hydrogels for Stem Cell Expansion in Three-Dimensions. *Soft Matter* **2012**, *8*, 7250.
- (45) Chen, L.; Watson, C.; Morsch, M.; Cole, N. J.; Chung, R. S.; Saunders, D. N.; Yerbury, J. J.; Vine, K. L. Improving the Delivery of SOD1 Antisense Oligonucleotides to Motor Neurons Using Calcium Phosphate-Lipid Nanoparticles. *Front. Neurosci.* **2017**, *11*, 1–12.

Electronic Supplementary Information (ESI)

Evaluation of the Effect of Shape upon Endocytosis of Transferrin-coated Upconversion nanoparticles, and their Ability to cross the Blood-brain Barrier

*Libing Fu,^{a,b} Bingyang Shi,^{*a,b} Marco Morsch,^a Guoying Wang,^{a,b} Yiqing Lu,^{b,c} Dayong Jin,^d and Roger Chung^{*a}*

^a Department of Biomedical Sciences, Faculty of Medicine & Health Sciences, Macquarie University, Sydney, NSW 2109, Australia

^b ARC Centre for Nanoscale Biophotonics, Macquarie University, Sydney, NSW 2109, Australia

^c Department of Chemistry and Biochemistry, Concordia University, 7141 Sherbrooke Street West, Montreal, QC H4B 1R6, Canada

^d Institute for Biomedical Materials and Devices (IBMD), Faculty of Science, University of Technology Sydney, Sydney, NSW2007, Australia

E-mail: roger.chung@mq.edu.au; bingyang.shi@mq.edu.au.

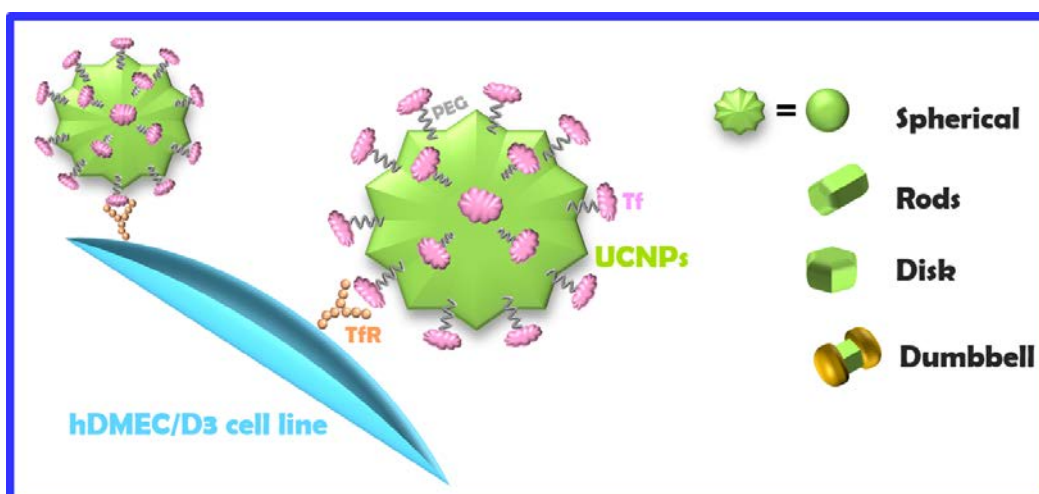


Figure. S1 The illustration of the internalization of UCNPs by hDMEC/D3 endothelial cells via receptor-mediated pathway.

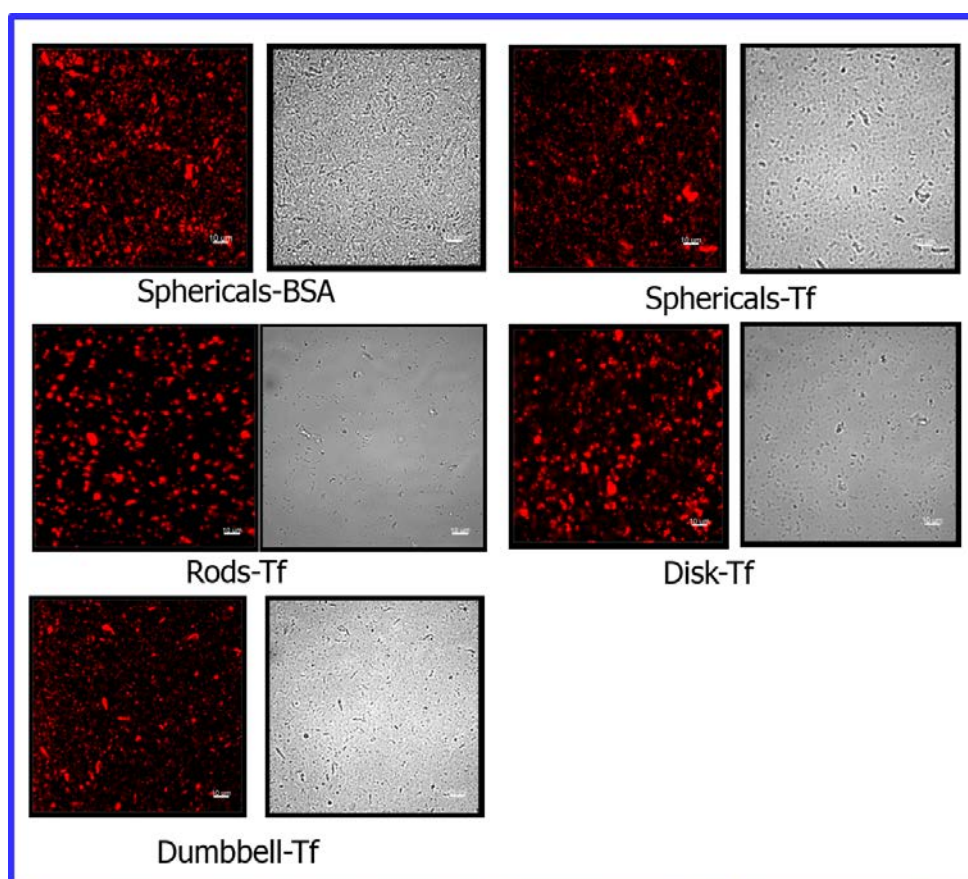


Fig S2. Confocal microscope images (emission at 800nm) and corresponding bright field images of spherical UCNPs-BSA, spherical UCNPs-Tf, rods-Tf, disk-Tf and dumbbell-Tf.

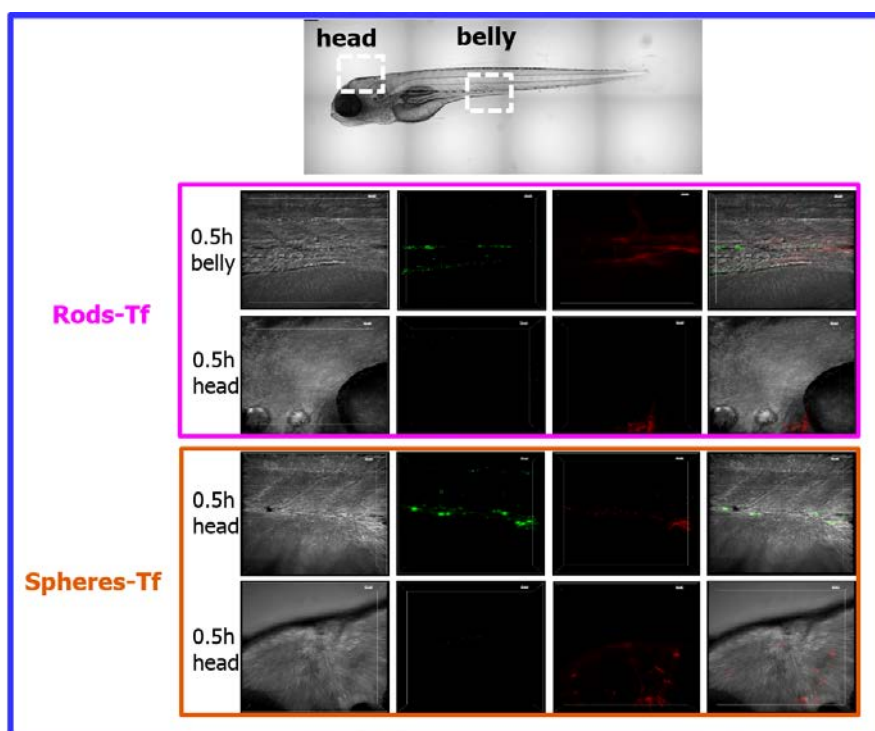


Fig S3. Confocal microscope images and corresponding bright field images of spherical UCNPs-Tf, rods-Tf, (emission at 800nm, green) and microbeads (red) after microinjection after 0.5h.

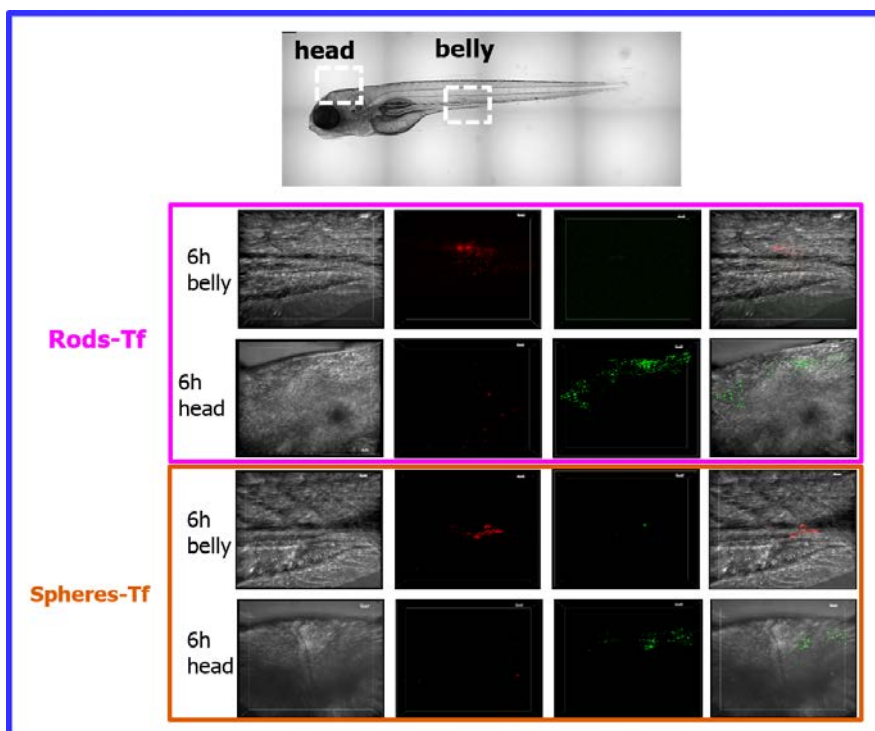


Fig S4. Confocal microscope images and corresponding bright field images of spherical UCNPs-Tf, rods-Tf, (emission at 800nm, green) and microbeads (red) after microinjection after 6h.

4.3 Remarks of Manuscript 2

The key findings of this manuscript: (i) A robust and reproducible UCNP fabrication protocol was developed that was able to achieve controlled epitaxial growth of the core-shell structure of spherical UCNPs to form rod-, disk- and dumbbell-shaped nanoparticles; (ii) Conjugation of transferrin onto the surface of the UCNPs significantly improved their uptake by cultured brain endothelial cells; (iii) Transgenic zebrafish with Tg(fli1a:EGFP) that specifically express a genetic fluorophore in the blood vessels provides a valuable animal model for investigation of the BBB penetration. Using this model, it was found that rod-shaped UCNPs display the most effective uptake by cultured brain endothelial cells, and the greatest uptake into the brain in zebrafish.

Limitations and future directions: Even though the Tf-UCNPs were found to pass the BBB and enter the brain, it is not clear where the nanoparticles finally localized. Therefore, future studies are required to investigate the fate of those Tf-UCNPs entering the brain, and their interactions with cells in the brain. This can be conducted using immunohistochemical identification of different brain cell types (neurons, glia etc.) and determining co-localisation of UCNPs within these cells. Alternatively, using genetically-modified zebrafish expressing fluorophores specifically in different cell types in the brain (neurons, glia etc.) could be used for studies to track the cellular fate of Tf-UCNPs in the brain.

Chapter 5: The Effect of Modifying the Aspect Ratio of PEGylated UCNPs upon their Cellular Uptake

Previous chapters of this thesis investigated the effect of manipulation of several physicochemical properties of UCNPs (such as surface charge, surface functionalization, size and shape) on their cellular uptake in cultured cells and following administration into zebrafish. In these previous chapters, it was identified that rod-shaped UCNPs coated with transferrin appear to be the superior UCNP for delivery into the brain and in vivo imaging applications. This Chapter extends upon this work, by investigating whether the aspect ratio (AR) of rod-shaped particles alters their biocompatibility and cellular uptake (Aim 3 of this thesis).

In this study, a series of PEGylated lanthanide-doped unconversion nanorods (Ln^{3+} -UCNRs, $\text{NaYF}_4:20\% \text{Yb}, 4\% \text{Tm}$) with various aspect ratios ($\text{ARs} = 2, 3$ and 4) was generated (optimization of this fabrication process is described in Chapter 2), and their cell uptake capability evaluated in cultured hCMEC/D3 brain endothelial cells, NSC-34 neurons-like cells and primary neurons. Nanorods with an AR of 2 displayed superior cellular uptake capability and lower cytotoxicity than nanorods with other ARs or spherical UCNPs. In particular, UCNRs with greater length 75nm ($\text{AR}=3$) to 96nm ($\text{AR}=4$) showed decreased cellular uptake and increased cytotoxicity in all three types of cells. Furthermore, a protocol was developed and optimized to measure the luminescent intensity of single UCNPs- using this approach it was possible to confirm that the luminescent intensity significantly depends on the ARs of nanorods. Accordingly, higher ARs is associated with stronger luminescent intensity. Apart from that, the PEGylated UCNRs decreased a little bit compared to the unmodified UCNRs. This characterization protocol of single-nanoparticle also provide possibility to future single-nanoparticle tracking at cellular or subcellular level.

The optimisation of nanorod fabrication is described in Chapter 2. The experimental

results are presented in a draft manuscript format, entitled “The Effect of Modifying the Aspect Ratio of PEGylated UCNPs upon their Cellular Uptake”. This manuscript has been prepared for submission to *Biomaterials*, and it is expected that it will be submitted for review soon after submission of this thesis for examination.

5.1 Contribution to Manuscript 3

	L.F	B.S	G.W	D. L	D.J	R.C
Experiment Design	●	●	●	●		●
Sample Preparation	●					
Data Collection	●					
Analysis	●	●				
Manuscript	●	●		●	●	●

I performed a majority of this study (90%) including fabrication of upconversion nanorods and their surface modification. Furthermore, I collected the experimental data of cell culture experiments, in vitro cytotoxicity measurement and microscopy characterization of nanoparticle cell uptake. Finally, I summarised the data and wrote the manuscript.

5.2 Manuscript 3

The Effect of Aspect Ratio of PEGylated Upconversion Nanocrystals upon the Cellular Uptake

Libing Fu, Bingyang Shi, Guoying Wang, Deming Liu, Dayong Jin and Roger Chung**

Department of Biomedical Sciences, Faculty of Medicine & Health Sciences, Macquarie University, Sydney, NSW, Australia

Email: bingyang.shi@mq.edu.au; roger.chung@mq.edu.au

Abstract

The central nervous system (CNS) is protected by the blood-brain barrier (BBB), which acts as a physical barrier to regulate and/or prevent the uptake of endogenous metabolites and xenobiotics. However, the BBB also prevents most non-lipophilic drugs from reaching the CNS following systematic administration. Therefore, there is considerable interest in identifying drug carriers that can maintain the biostability of therapeutic molecules and target their transport across the BBB. In this regard, upconversion nanoparticles (UCNPs) have become popular as a nanoparticle-based solution to this problem, with the additional benefit that they display excellent properties for in vivo visualisation. The majority of studies to date has explored basic spherical UCNPs for drug delivery applications. However, the biophysical properties of UCNPs their cell uptake and BBB transport have not been fully explored. Therefore, in this study we have systematically evaluated the effect of the physical aspect ratio of UCNPs on cellular uptake. We used a one-pot seed-mediated approach to precisely control longitudinal growth to produce bright upconversion nanorods (UCNRs) with various aspect ratios. Then we PEGylated the as-prepared UCNRs to enhance their biostability and cell uptake capacity. We identify an optimal aspect ratio for UCNR uptake into several different types of cultured cells, finding that this is generally in the ratio of 2 (length/width). This data provides a crucial clue for further optimisation of UCNRs as a drug carrier to deliver therapeutic agents into the CNS.

KEYWORDS: upconversion nanorod, aspect ratio, PEG modification, cellular uptake, primary neurons

Introduction

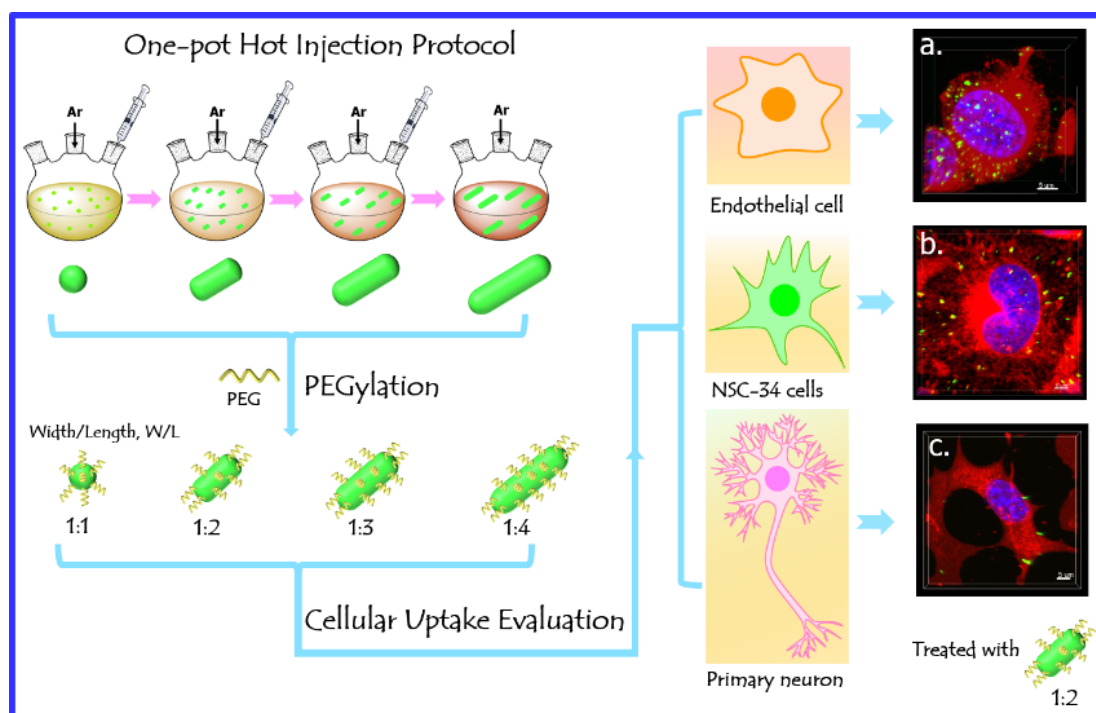
Despite enormous development in brain research, central nervous system (CNS) diseases remain the world's leading cause of disability. There is no effective therapy for most of these diseases, including neurodegenerative disorders such as Alzheimer's disease and Huntington's disease. A major challenge is that there is a lack of high-performance carriers to deliver drugs across the blood-brain barrier (BBB). The BBB is crucial for maintaining the homeostasis of the CNS by regulating the flow of water and molecules into and out of the brain. However, this hinders the successful transport of most therapeutic agents into the brain. This biological barrier consists of a cellular tight junction between the brain capillary endothelial cells that line the blood vessels that feed the brain, and therefore it is uptake and transport across the endothelial cell barrier and into the CNS that represents the major goal for identification of suitable drug carriers. Nanoparticles have become a popular method for developing drug carriers for the CNS, with considerable evidence demonstrating that the cell uptake properties of nanoparticles are strongly influenced by their physicochemical properties (ie. size,¹⁻³ shape,^{4,5} and surface modification⁶⁻⁹ etc.).

The aspect ratio (AR) of nanoparticles is regarded as a significant factor that can influence their cellular uptake.¹⁰⁻¹² Therefore, adjusting the AR of nanoparticles is able to improve their bio-distribution^{13, 14} and tumor internalization.¹⁵ However, systematic evaluation of the impact of AR upon nanoparticle cell uptake is difficult because of the inherent challenges in controlling AR during the nanoparticle synthesis process. For instance, spherical ($390 \pm 40\text{nm}$) disulfide-stabilized poly(methacrylic acid) hydrogel capsules (PMA HCs) being internalized faster and more than rod-like capsules with higher AR up to 3.8 (length $1290 \pm 140\text{ nm}$, width $340 \pm 60\text{ nm}$) in HeLa cells.¹⁶ To the contrary, the PRINT (Particle Replication In Non-wetting Templates) hydrogel rods consist of cross-linked poly(ethylene glycol) hydrogels with $\text{AR}=3$ ($d = 150\text{ nm}$, $h = 450\text{ nm}$) occurs much more efficient and faster internalization than a spherical particles ($d = 200\text{ nm}$) counterpart, even though both particles are treated with HeLa cells at the same volume.¹⁶ Furthermore, PEGylated nucleoprotein rods made of tobacco mosaic virus (TMV) protein and various RNA scaffolds with lowest aspect ratio ($d = 18\text{ nm}$, h

= 60 nm, AR = 3.5) exhibit the most passive tumor-homing capability due to their high diffusion ability, whereas RGD-labeled rods with a medium aspect ratio ($d = 18\text{ nm}$, $h = 130\text{ nm}$, AR = 7) show more efficient at tumor targeting result from a balance between infusibility and ligand-receptor interactions.¹⁷ Compare those types of nanomaterials with upconversion nanoparticles, the aspect ratio of nanomaterials can just be controlled roughly like from 2.6 to 3.6.¹⁸ However, the aspect ratio of UCNPs can be strictly tuned exactly in a much wide range from 1 up to 4 or more. The different influence of ARs on cellular uptake found in those studies likely due to the different cellular uptake pathways administrating the response of various structure of particles. It indicates that the interaction between cellular endocytosis and particle shape (like ARs) is complexed and poor understood.

In the past few decades, lanthanide-doped upconversion nanoparticles (UCNPs) have become popular as luminescent probes and drug carriers. This is due to their tunable physicochemical properties (ie. size, shape, lifetime, multiple-dopant and surface modification)¹⁹⁻²¹ and unique optical characteristics, such as low auto-fluorescence background, sharp emission bandwidths, negligible photobleaching, and high penetration depth under near-infrared radiation(NIR).²²⁻²⁵ With these modifiable features, UCNPs are a promising nano-platform to investigate interrelationship between the physicochemical properties of UCNPs (ie. size, shape and surface chemistry) and their cellular permeability.

Herein, we describe the development of a protocol to produce $\text{NaYF}_4\text{:}20\%\text{Yb}$, $4\%\text{Tm}$ UCNPs with a precise series of width/length aspect ratios (ie: ARs of 1:1, 1:2, 1:3 and 1:4), and systematically evaluate their cellular uptake properties. We found that cellular endocytosis of UCNPs is significantly affected by their aspect ratio in a cultured neuronal cell line (NSC-34), endothelial cells (hCMEC/D3) and primary neurons. Notably, an aspect ratio of 1:2 consistently provided superior cellular uptake efficiency and lower cytotoxicity than other ARs. Through this study, we have identified that the aspect ratio of UCNPs provides substantial control over their cell uptake properties, providing crucial information for future optimization of UCNP-based drug carriers for use to treat CNS diseases.



Scheme1. Illustration of PEGylated UCNRs fabrication and cellular uptake evaluations. UCNRs with different ARs: 1:1, 1:2, 1:3 and 1:4 and confocal imaging (under 980nm laser excitation) after incubation with hCMEC/D3 endothelial cells, NSC-34 neuron like cells and primary neurons for 4h at 37°C. The 3D confocal microscopy images of a-c are corresponding to endothelial cells, NSC-34 cells and primary treated with PEGylated UCNRs with ARs of 1:2, respectively. The nucleus (blue) of cells is stained with Hoechst 33342 for nuclear and deep red plasma for membrane. The UCNRs (been set to green) are excited by high power 980nm laser. (Scale bars = 5nm)

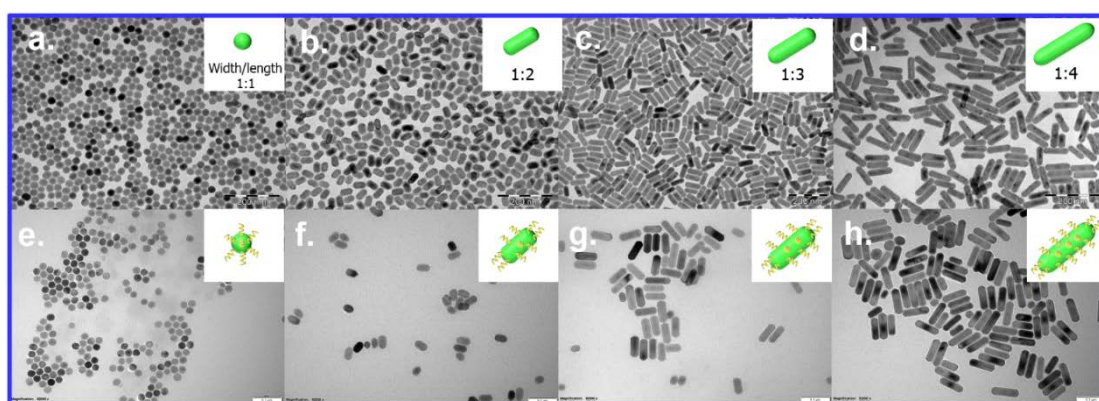


Figure 1. Transmission electron microscopy (TEM) images of as-prepared β -NaYF₄: 20% Yb, 4% Tm UCNRs with different ARs, including 1:1 (a), 1:2 (b), 1:3 (c) and 1:4 (d) dispersed in cyclohexane. The TEM images of corresponding PEGylated UCNRs suspended in MilliQ water were also showed in the images e-h.

Results and Discussion

Production and biophysical characterization of UCNRs with various ARs We developed a highly reproducible protocol for generation of a series of UCNRs (β -NaYF₄: 20%Yb, 4%Tm) with tightly controlled ARs (including 1:1, 1:2, 1:3 and 1:4)

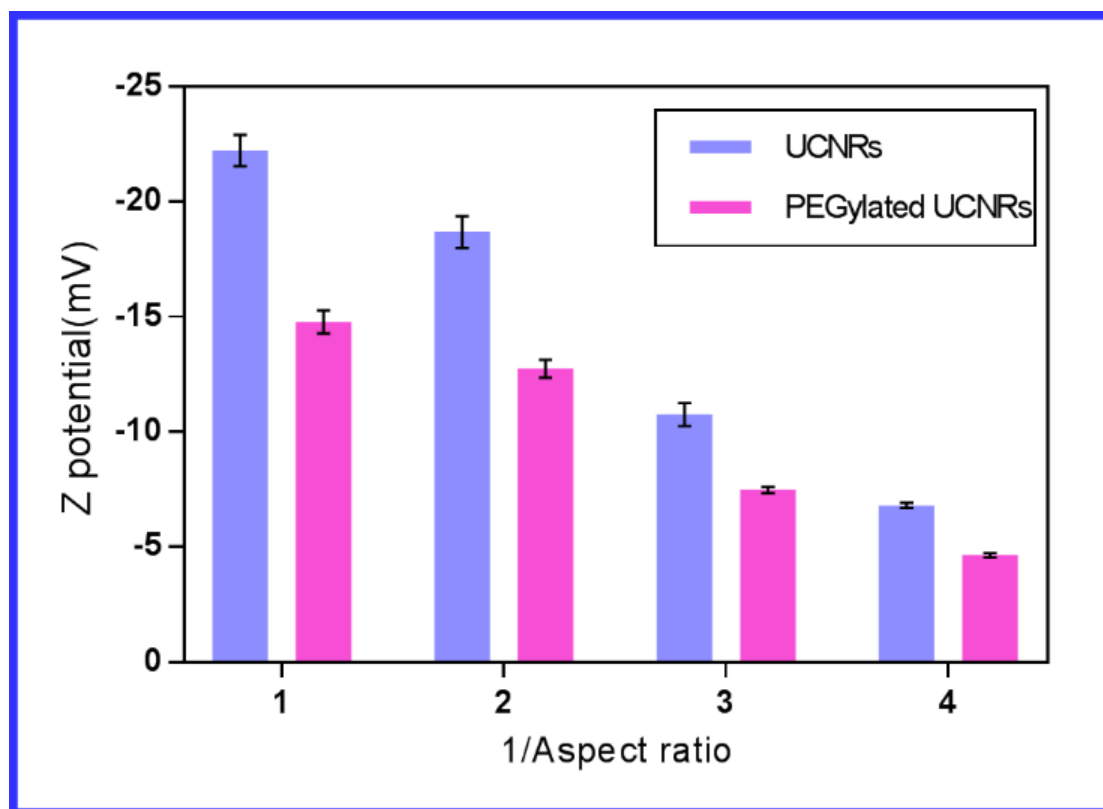


Figure 2. Comparison of z-potential of original UCNPs with various ARs (including 1:1 1:2, 1:3 and 1:4) suspended in cyclohexane and corresponding PEGylated UCNPs dispersed in MilliQ water at 1mg/mL.

based upon modifications to our previously published protocols.^{20, 21, 26} Firstly, we synthesized spherical upconversion nanoparticles (UCNPs) as the basic core (ie: 1:1 AR ratio) according to our recent previous report.²⁷ UCNPs were dispersed in cyclohexane, and capped with oleic acid molecules (OAH) and oleic acid ions (OA⁻) on their surface. Next, the UCNRs were prepared via a one-pot synthesis through a successive layer-by-layer hot-injection protocol. To generate and control longitudinal epitaxial growth of the UCNPs to the desired aspect ratios (ARs, which is width/length, W/L), we manipulated the ratio of OA⁻ to OAH by adding KOH (to transfer more OAH

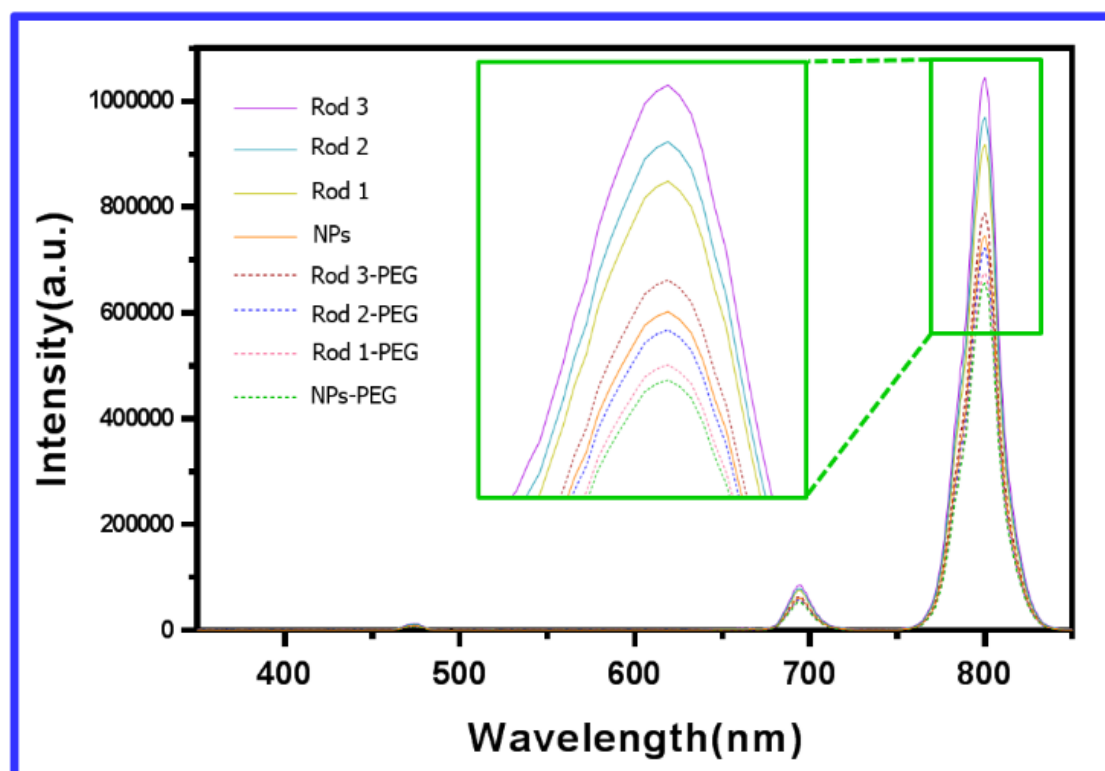


Figure 3. Comparison of the upconversion photoluminescent spectra of original upconversion nanoparticles, including spherical NPs, AR2 (W/L, 1:2), AR3 (W/L, 1:3) and AR4 (W/L, 1:2) in cyclohexane and their corresponding PEG-COOH functionalized UCNPs in water under excitation of a 980nm laser. (All nanoparticles are at the concentration of 1mg/mL)

into OA-) and together with alteration in synthesis time (is this correct, or was it only OA-/OAH ratio that was changed) this allowed us to generate UCNRs with tightly controlled ARs. Transmission Electron Microscopy (TEM) of these UCNRs (Figure 1a-d) revealed UCNP cores (1:1 AR) of approximately ~26 nm diameter and UCNRs representing an ordered increase in AR (46nm, 75nm and 96nm). The size of the as-prepared UCNPs was calculated using Image J software by randomly picking 100 particles from their corresponding TEM images. The size distribution of UCNPs (see Figure S1) demonstrates that they all display relatively uniform size distribution.

Next, we introduced a PEGylation surface modification to the UCNPs, to enhance the biostability of the nanoparticles. Successful PEGylation was determined by measuring the Z-potential of the UCNPs in MilliQ water using a Zeta sizer (Nano ZS; Malvern Instruments, U.K.). The Z-potential measurements showed that the surface charge of unmodified UCNPs displayed a negative value (because of the presence of OA⁻ ions)

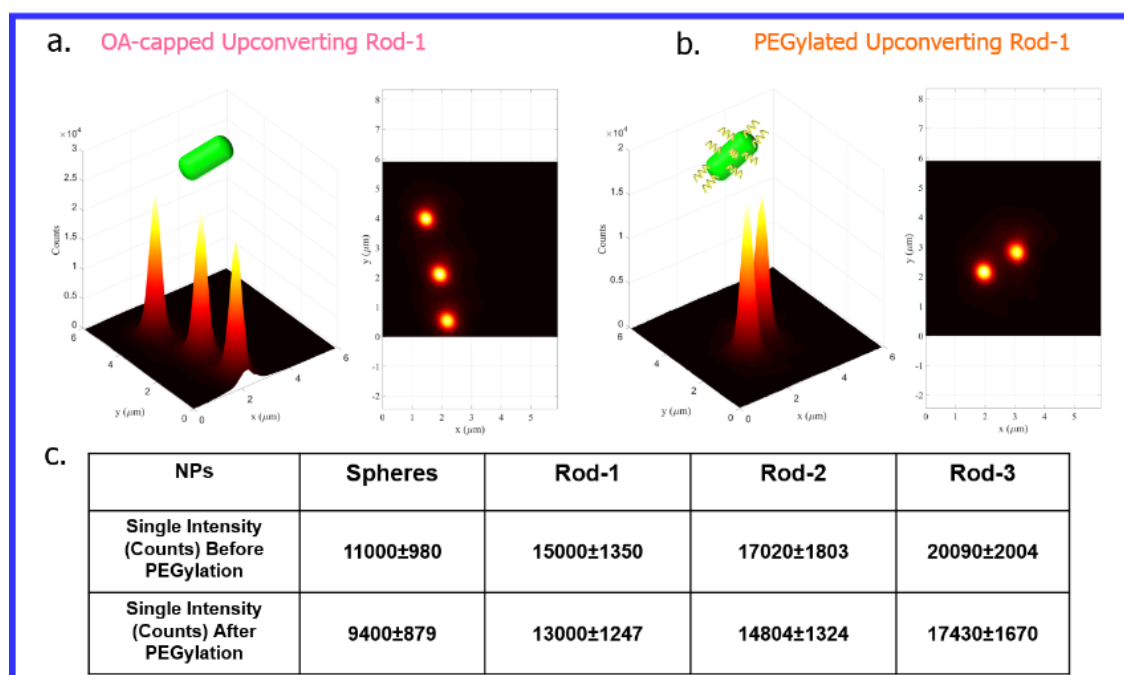


Figure 4. The emission intensity of single UCNPs of original AR2 with ARs of 1:2 (a) and PEGylated AR2 (b). Summary of single emission intensity of spheres, AR2, AR3 and AR4 under excitation of 980nm laser. Confocal microscopy quantitative measurement of whole spectrum luminescence emission of single

and increased concordant with greater AR from -12.23mV (AR=1) to -6.01mV (AR=4). This may due to the decreased surface area of upconversion nanoparticles following the increase of ARs value at the same weight. Thus, the Z-potential increase along with the decrease of oleic acid ions (attached on the surface of original UCNPs) in the solution. Furthermore, the PEGylated UCNPs were negatively charged because of the carboxyl group at the terminal of grafted PEG on the surface of UCNPs. Specifically, the Z-potential variation of UCNPs PEGylation with various ARs (including 1, 2, 3 and 4) were 9.75mV, 7.05mV, 5.48mV and 4.65mV. The decreased trend of PEGylated UCNPs Z-potential may also result from reduction of surface area of UCNPs with different ARs range from 1 to 4 at the same concentration (that means at the same volume). Therefore, these changes in the Z-potential demonstrated that the success of PEGylation to enhance the biocompatible (ie: water soluble) of UCNPs compared to original UCNPs with OA⁻ on the surface.

Evaluation of the effect of aspect ratio upon the photoluminescence spectral properties of UCNPs To verify the optical properties of UCNRs, the upconversion photoluminescence (UC PL) properties of UCNPs were detected under 1.6 W cm^{-2}

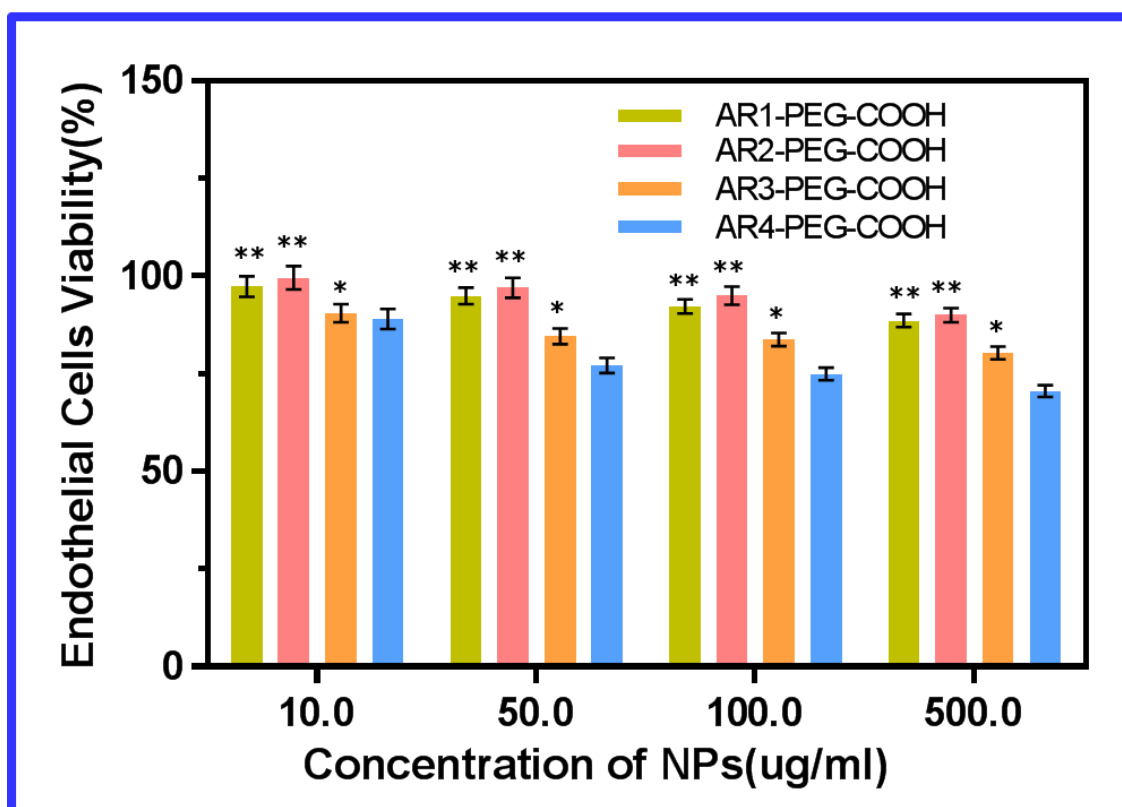


Figure 5. Cytotoxicity evaluation of PEGylated UCNPs (spheres), AR2 (ARs, 1:2), AR3 (ARs, 1:3) and AR4 (ARs, 1:4) treated with NSC-34 neuron like cells across a broad concentration range (10, 50, 100 and 500 $\mu\text{g mL}^{-1}$) for 24 h at 37 °C. A significant difference when compared to the most toxic AR4-PEG-COOH is indicated by “* $P < 0.05$ and ** $P < 0.01$ ”

980nm laser excitation. As shown in Figure 3, the as-designed UCNPs showed emission at three distinct wavelengths at 475 nm, 700 nm and 800 nm, which correspond to the $^1\text{D} \rightarrow ^3\text{H}$, $46\ ^3\text{F}_{2,3} \rightarrow ^3\text{H}_6$ and $^3\text{H}_4 \rightarrow ^3\text{H}_6$ transitions, respectively.(Figure 3)²⁸ Emission intensity was greatest at 800nm, indicating that the UCNPs have high tissue penetration spectral properties with low auto-fluorescence background (ie: minimal emission in the 350nm wavelength). Specifically, the emission at 800nm of AR1, AR2, AR3 and AR4 were 787774.5, 917590.7, 969811.3 and 1044412 (a.u.) respectively. Notably, the emission wavelengths were consistent for both PEGylated and non-PEGylated UCNPs, the signal intensity was mildly reduced in PEGylated UCNPs, presumably because of the spectral interference caused by the PEG surface-coating. The reduction percentage of each type of UCNPs-PEG were 16.7%, 26.3%, 25.5% and 28.6%, respectively. Importantly, the intensity of photoemission increased in a linear manner in accordance with the increase in AR of the UCNPs (from AR1 to AR4).

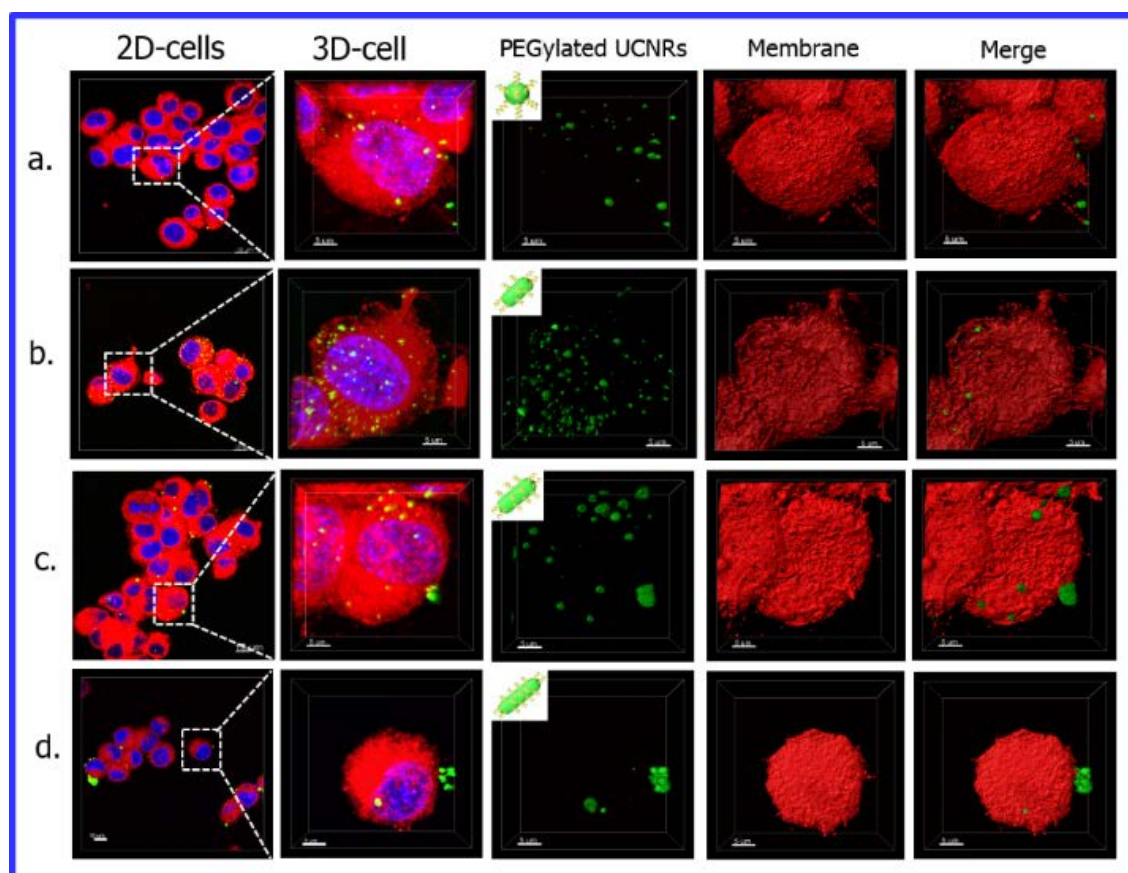


Figure 6-1. Luminescent microscopy images of PEGylated UCNPs internalized by NSC-34 cells and their corresponding Imaris software processed 3D single-cell images after 4 h incubation at 37°C (at the concentration of 50ug/mL): spheres (a), AR2 with ARs 1:2 (b), AR3 with ARs 1:3 (c) and AR4 with ARs 1:4 (d). Specifically, the left two rows of images represent original 2D and their magnified 3D single cell images. The right three columns of images showed the luminescent signal of each types of UCNPs, the cell membranes and their overlay. The average cell uptake value can be analyzed by collecting the volume of UCNPs inside the cells.

Measurement of the photoluminescence intensity of single UCNPs We measured the brightness of individual UCNPs using a self-built confocal microscope (the illustration of system layout is shown in Figure S2).^{19, 28} A 976 nm single mode diode laser was used as the excitation source, which focused onto the sample via a 100× objective lens (NA 1.4). The emission signal of the sample is collected by the same objective lens before being projected into an optical fiber. A Single Photon Counting Avalanche Diode (SPAD) detector connected to the collection optical fiber is employed to detect the emission intensity. As we expect there to be uniformity in the emission intensity for each individual UCNP from the same batch (based upon the tight consistency in UCNP

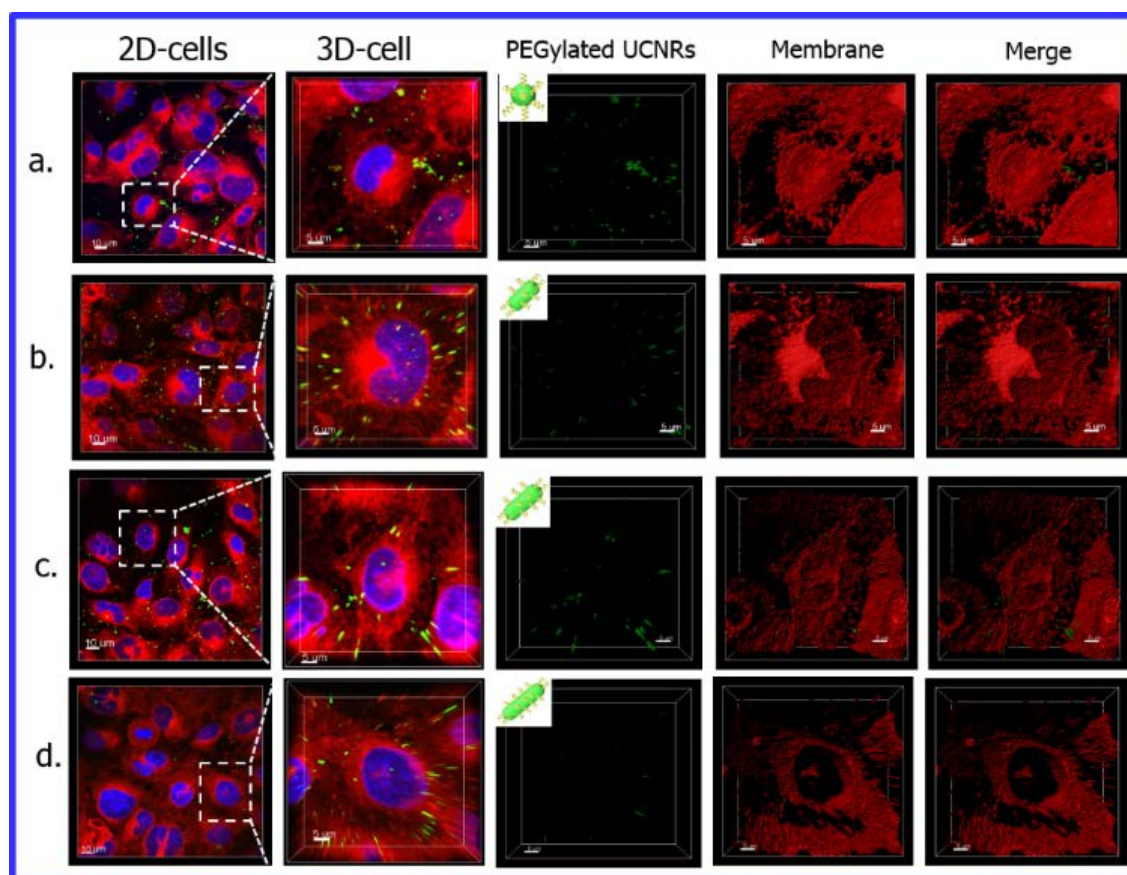


Figure 6-2. Luminescent microscopy images of PEGylated UCNRs internalized by hCMEC/D3 cells and their corresponding Imaris software processed 3D single-cell images after 4 h incubation at 37°C (at the concentration of 50ug/mL): spheres (a), AR2 with ARs 1:2 (b), AR3 with ARs 1:3 (c) and AR4 with ARs 1:4 (d).

size demonstrated in Figure S1), we can confirm the monodispersity of each sample. The brightness of each single particle was represented by a single Gaussian spot, with the maximum pixel value of each Gaussian spot representing the brightness of that individual nanoparticle. We found a linear increase in the brightness of individual UCNRs in accordance with the linear increase in their aspect ratio, providing an important baseline for subsequent visualization of individual UCNRs following cellular uptake.

Cytotoxicity evaluation of PEGylated UCNRs with various ARs Prior to employing PEGylated UCNRs for in vitro imaging, the influence of the ARs on cytotoxicity against NSC-34 neuron like cells was observed at a concentration range from 10 to 500ug/mL via MTT (methyl thiazolyl tetrazolium) assay. Typically, the NSC-34 cells were not hindered by our spherical UCNP-PEG-COOH and AR2-PEG-COOH up to an extremely

high concentration (500 μ g/mL) even after incubation for 24h, indicating the dramatically low cytotoxicity of spherical and short rod-like UCNPs in vitro compared to AR4-PEG-COOH (**P<0.01, Figure 5) However, AR3-PEG-COOH exhibited slightly more cytotoxic than AR4-PEG-COOH under the same concentrations due to the remarkably increasing length of rod up to 75nm (*P<0.05). Specifically, AR3-PEG-COOH revealed a relatively high cytotoxicity at 500 μ g/mL concentration in NSC-34 cells, leading to 25% decrease cell viability after 24h co-incubation in NSC-34 cells. In comparison of these four different ARs of PEGylated UCNPs, the longest AR4-PEG-COOH showed most toxic, causing 30% reduction in cell viability after 24h incubation. Interestingly, the AR2-PEG-COOH revealed much less cytotoxicity (~90% cells survival) compared to AR4-PEG-COOH even at the highest concentration of 500 μ g/mL(**P<0.01), indicating that ARs of 1:2 PEGylated UCNRs is a

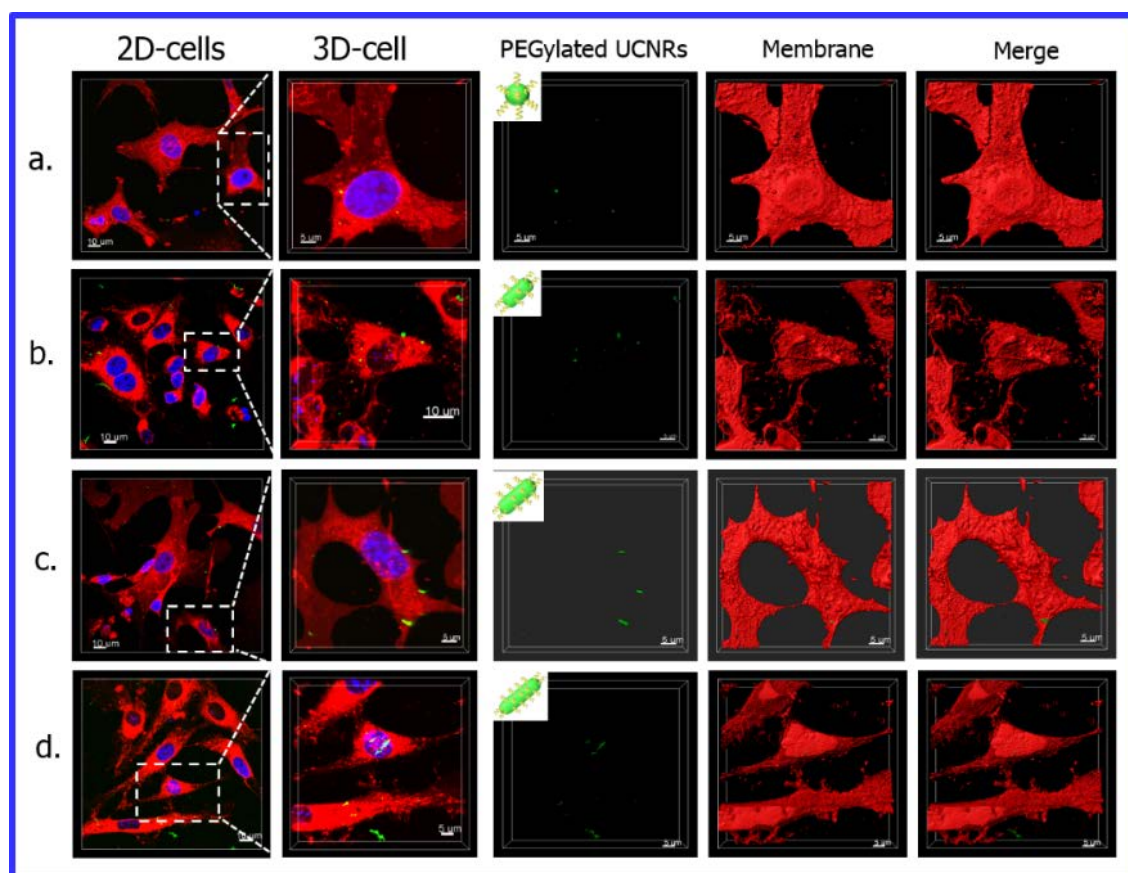


Figure 6-3. Luminescent microscopy images of PEGylated UCNPs internalized by primary neurons and their corresponding Imaris software processed 3D single-cell images after 4 h incubation at 37°C (at the concentration of 50 μ g/mL): spheres (a), AR2 with ARs 1:2 (b), AR3 with ARs 1:3 (c) and AR4 with ARs 1:4 (d).

preferable ARs for neuron like cellular internalization. In summary, the result of MTT assay suggested that the cytotoxicity reduced along with the ARs (from 1 to 2) of PEGylated UCNPs, while suddenly went up with ARs (from 3 to 4) of PEGylated UCNPs in NSC-34 cells. For the comparison, these different ARs of PEGylated UCNPs showing low to high cytotoxicity are in the order of $AR2 < AR1 < AR3 < AR4$. Therefore, the result indicated that the ARs of 1:2 revealed the most readily and feasibility for NSC-34 neuron like cells uptake analysis and imaging investigation.

Imaging of PEGylated UCNP uptake by NSC-34 cells, endothelial cells and primary neurons To investigate the influence of AR of PEGylated UCNPs on their cellular internalization, we acquired confocal microscope images of cellular uptake of the UCNPs in NSC-34 cells (neuron-like), hCMEC/D3 (endothelial cells) and primary

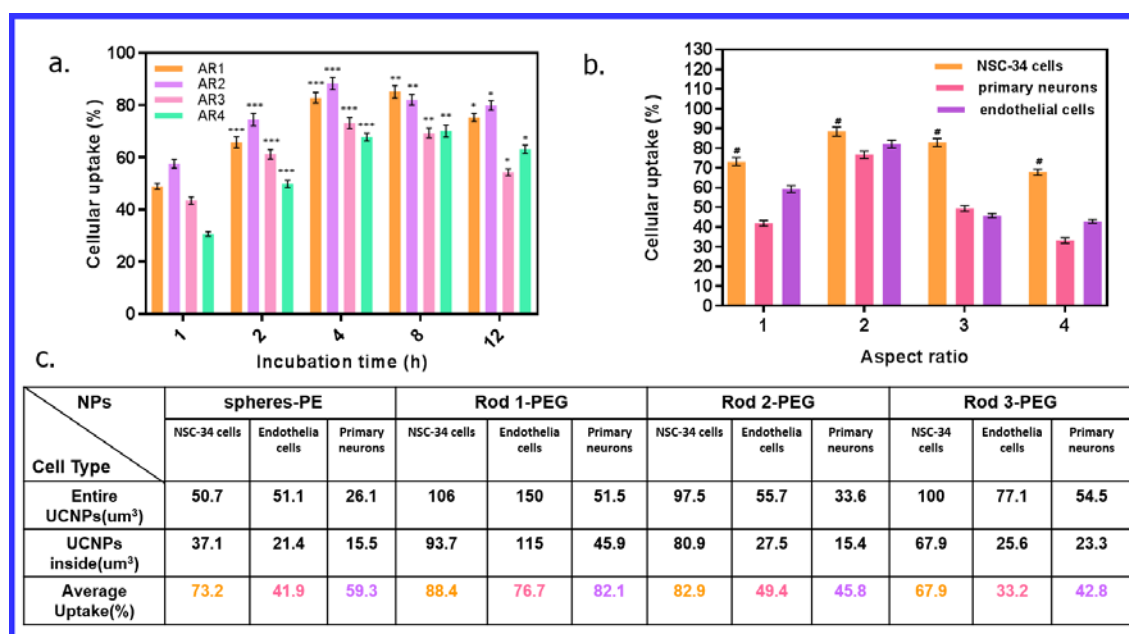


Figure 7. Optimization of incubation time of PEGylated UCNRs with various ARs (including 1:1, 1:2, 1:3 and 1:4) in NSC-34 cells and the quantification of cellular uptake. (a) 1h, 2h, 4h, 8h and 12h Cell uptake analysis of PEGylated upconversion spheres and nanorods (AR2 with ARs 1:2, AR3 with ARs 1:3 and AR4 with ARs 1:4) incubated with NSC-34 cells across the time range (1h, 2h, 4h, 8h and 12h). A significant difference when compared to 1h-incubation time is indicated by “*P < 0.05, **P < 0.01 and ***P < 0.001”. (b) Relationship between cellular uptake of PEGylated UCNPs with various aspect ratio in NSC-34 cells, endothelial cells and primary neurons. A significant difference when compared to the UCNPs-PEG-COOH incubated with primary neurons is indicated by #P < 0.05. (c) Summary of calculated PEGylated UCNPs internalized by NSC-34 cells, endothelial cells and primary neurons via Imaris software simulation.

neurons. (Figure 6-1, 6-2 and 6-3) The cultured cells were incubated with 50ug/mL of PEGylated UCNPs with varying ARs for 4h at 37 °C (5% CO₂). (Figure 7a) Following fixation, the cell membrane was stained with deep red plasma membrane stain (excitation/emission 649/666 nm) and the nucleus was labelled with Hoechst dye (excitation/emission 350/461nm) and imaged by confocal microscopy (Zeiss 880). We identified that AR had a significant impact upon the endocytosis of PEGylated UCNPs. While the spherical UCNPs displayed some cellular uptake, AR2 UCNRs displayed a homogenous distribution and superior endocytosis by NSC-34 cells, hCMEC/D3 endothelial cells compared to the spherical UCNPs and nanorods with different ARs (ie: AR3 and AR4). Furthermore, AR3 and AR4 UCNPs displayed substantial aggregation, leading to accumulation on the surface of cultured cells and lower uptake efficiency. Notably, all UCNPs displayed significantly lower uptake into cultured primary neurons, with AR2 UCNRs displaying the best uptake. As expected, PEG-coated UCNPs displayed superior uptake than unmodified UCNPs.

Quantification of cellular uptake capability of the PEGylated UCNPs The incubation time was optimized respectively for further cellular uptake measurement. (Figure 7a) The cellular uptake efficiency of PEGylated UCNPs incubated with those three types of cells for 1 h is the least. Moreover, the 4 h-incubation time showed significantly different with 1 h-incubation treatment ($***P < 0.001$), indicating 4 h incubation time gets much higher internalization efficiency compared with 1 h co-incubation time. While, the incubation time of 8 h ($**P < 0.01$) and 12 h ($*P < 0.05$) demonstrated slightly better than 1 h. Therefore, 4h was chosen as incubation time in this experiment. To precisely quantify the uptake efficiency of PEGylated UCNPs with various ARs, we utilized high resolution z-stack confocal imaging and 3-dimensional (3D) rendering of their cellular distribution (Figure 7b and 7c) in NSC-34 cells, hCMEC/D3 brain endothelia cells and primary neurons. The volumetric rendering of PEGylated UCNP (green) internalized in an individual cell was regarded as the entire volume of UCNPs (V_{entire}). The cellular uptake efficiency was calculated by then specifically selecting the volume of PEGylated UCNP located within the single cell (V_{inside}) versus V_{entire} . With this protocol, we found that cellular uptake of PEGylated UCNPs by NSC-34 cells were obviously higher than the other two types of cells (endothelial cells and primary neurons).

Interestingly, PEGylated upconversion sphere, AR2 and AR4 revealed the cellular uptake efficiency in the order of NSC-34 cells > endothelial cells > primary neurons. However, PEGylated AR3 exhibited much higher cell internalization in NSC-34 cells than primary neurons and endothelial cells (AR3 cellular uptake by in primary neurons is slightly higher than in endothelial cells). Typically, the endocytosis value of PEGylated AR2 was greater than spheres in these three types of cells. It demonstrated that the ARs (from 1 to 2) facilitated the internalization of PEGylated UCNPs. However, the cellular uptake tended to decrease from ARs of 2 to 3. These results showed that AR2 display superior uptake capability to other ARs of PEGylated UCNPs. Totally, the ARs priority for cell bioavailability and cell uptake is AR2 > AR1 > AR3 > AR4. Thus, the result suggested that ARs of PEGylated UCNPs exhibited significantly impacts their cell internalization behavior.

Conclusion

In this study, we investigated the ARs influence during cellular internalization for further drug carrier design for neuron disease therapy. Specifically, we successfully fabricated a series of high lanthanide-doped β -NaYF₄: 20%Yb, 4%Tm UCNRs with various ARs via one-pot hot-injection method, which enable the strictly control of longitudinal growth of UCNRs. These types of UCNRs were further modified with PEG-COOH, which was confirmed to be able to increase the biocompatibility of nanoparticles and their cellular uptake capability according to our previous work. Thereafter, we employed as model systems to investigate the effect of ARs on cellular uptake among endothelial cells, NSC-34 cells and primary neurons. The results showed that the ARs of PEGylated UCNRs play a significant role on cellular uptake capability. Specifically, the ARs of 2 is dramatically superior to other ARs for cellular internalization efficiency. In contrast, the highest ARs of 3.6 revealed the lowest cellular uptake capability and meanwhile provided the most toxic to the cells in this study. Importantly, the result also demonstrated that UCNRs with ARs of 2 process obvious higher cellular uptake efficiency than spherical upconversion nanoparticles with ARs of 1. Therefore, the PEGylated UCNRs with aspect ratio of 2 have a bright future as a safe and high efficient drug carrier for further potential application in the therapy of

neurodegenerative diseases.

Methods

Reagents and materials Yttrium chloride hexahydrate ($\text{YCl}_3 \cdot 6\text{H}_2\text{O}$), ytterbium chloride hexahydrate ($\text{YbCl}_3 \cdot 6\text{H}_2\text{O}$), thulium chloride hexahydrate ($\text{TmCl}_3 \cdot 6\text{H}_2\text{O}$), oleic acid (OA) and 1-octadecene (ODE), sodium hydroxide (NaOH), potassium hydroxide (KOH), ammonium fluoride (NH_4F), 3-[4,5-dimethylthiazol-2-yl]-2,5-diphenyl tetrazolium bromide (MTT) and nitrosyl tetrafluoroborate (NOBF_4) were all purchased from Sigma-Aldrich and used as received. Dulbecco's modified Eagle's medium (DMEM), EBM-2 basal medium, Hoechst 33342, Deep red plasma membrane stain, fetal bovine serum (FBS), penicillin-streptomycin, hydrocortisone, HEPES buffer and bFGF were obtained from Invitrogen Life Technologies (Mulgrave, Australia). PHSO-PEG_{3.5k}-COOH was acquired from JenKem Co., Ltd. All reagents were of analytical grade and used without any further purification.

Synthesis of Original $\text{NaYF}_4\text{:20\%Yb,4\%Tm}$ Upconversion Nanoparticle as the

Core The core of high lanthanide-doped upconversion nanoparticles (spherical) were synthesized according to an oxygen-free protocol described in our previous work.^{29, 30} Specifically, 0.76mmol $\text{YCl}_3 \cdot 6\text{H}_2\text{O}$, 0.2mmol YbCl_3 and 0.04mmol $\text{TmCl}_3 \cdot 6\text{H}_2\text{O}$ were added into a 100 mL two-neck round-bottom flask and was magnetically mixed with OA (6.5 mL) and ODE (15 mL). The mixture was protected with Ar flow and heated to 150 °C for 30 min before cooling to room temperature (RT). 4mmol NH_4F and 2.5mmol NaOH in 5 mL of methanol solution was added into the solution and kept stirring for 30 min at RT. The reaction solution was slowly heated up to 110 °C and kept at 110°C for 30 min to remove methanol and water completely under the protection of Ar. Following with that, the mixture solution was quickly heated to 310°C and reacted for 1.5 h. After the solution cooled down to RT, ethanol was added to precipitate the UCNPs. After the nanoparticles were washed with cyclohexane, ethanol and methanol (2:9:3, v:v:v) for 3 times, the final $\text{NaYF}_4\text{:20\%Yb,4\%Tm}$ nanocrystals were re-dispersed in 10mL cyclohexane at 4°C for further use.

Synthesis of the Original Upconversion Nanorod (UCNRs) with various ARs

The longitudinal growth of $\text{NaYF}_4\text{:Yb,Tm}$ onto the core of $\text{NaYF}_4\text{:Yb,Tm}$ upconversion

nanoparticles was conducted with a one-pot through successive layer-by-layer hot-injection approach modified from our previous work.³¹ In this work, to generate longitudinal epitaxial growth of upconversion nanoparticles, we increased the ratio of OA^- to OAH by adding KOH to lead to the conversion of more OAH into OA^- and to lead to form UCNRs with various aspect ratio (ARs, which is width/length, W/L). First, shell precursors were prepared. 0.76mmol $\text{YCl}_3 \cdot 6\text{H}_2\text{O}$, 0.2mmol YbCl_3 and 0.04mmol $\text{TmCl}_3 \cdot 6\text{H}_2\text{O}$ were added to a 50mL flask containing 6.5mL oleic acid and 15mL 1-octadecene. The mixture solution was heated to 160 °C with protection of argon flow for 30 min to obtain a clear solution and then cooled down to room temperature (RT), followed by the addition of 4.0mmol NH_4F , 2.5mmol NaOH and 2.0 mmol KOH in 8 mL methanol. After stirring for 30 min at RT, the solution was heated to 80 °C with argon flow for 20 min to remove methanol, and then the react system was continually heated to 150 °C for another 30 min to remove water in the solution. Finally, the reaction solution was cooled down to room temperature and labeled as 1mmol $\text{NaYF}_4\text{:Yb,Tm}$ shell precursors for further use. For the longitudinal growth of $\text{NaYF}_4\text{:Yb,Tm}$, 0.2 mmol $\text{NaYF}_4\text{:Yb,Tm}$ core particles in cyclohexane were added to a 50 mL three-neck flask containing 1.3mL OA and 3 mL ODE. The mixture solution was heated to 160 °C under protection of argon flow for 30 min to remove cyclohexane, and then the solution was continually heated to 310 °C. Followed with that, 0.4 mmol of as-prepared $\text{NaYF}_4\text{:Yb,Tm}$ shell precursors were injected into the reaction mixture at the speed of 0.1 mL per 10 min and followed by another 0.5 h reaction time at 310 °C. Finally, the formed solution was gradually cooled down to room temperature and the formed upconversion nanorods (AR=2) were purified according to the procedures employed for the purification of $\text{NaYF}_4\text{:Yb,Tm}$ core particles. For fabrication of UCNRs with other ARs, it can be conducted by controlling the ratio of shell precursors and seed, which is equally to the corresponding ARs value.

PEGylation of as-prepared UCNRs with various ARs First, NOBF_4 in dichloromethane solution was used to transfer each type of original UCNRs with various ARs from hydrophobic to hydrophilic via ligand exchange protocol according to the literatures.^{32, 33} Typically, 5 mL of 5mg/mL UCNPRs in cyclohexane was mixed with 5 mL of 0.01M NOBF_4 in dichloromethane (DCM) solution at room temperature (RT). The mixture solution was shaken overnight to

transfer UCNPs from the upper cyclohexane layer to the bottom DCM layer. Then the formed intermediate of NOBF₄-UCNRs were separated by centrifugation and were further purified by precipitation with toluene and cyclohexane (1:1 by volume). Thereafter, the purified NOBF₄-UCNRs were re-dispersed in DMF at the concentration of 10mg/mL. Then, take 200 μ L of solution (~2mgUCNPs) into a glass bottle, adding 2mL absolute ethanol into the glass bottle. Followed by adding 10 mg PEG dispersed in 1 mL water. The mixture solution will become cloudy. Then add water (~3mL) until solution become clear and keep stirring for 48 h. Finally, the UCNRs-PEG-COOH were washed by water for 3 times.

Size, Zeta Potential and Emission Spectrum Measurements The as-synthesized UCNRs were confirmed with transmission electron microscopy (TEM). 10ul of UCNRs in cyclohexane was added on a formvar-coated copper grids, and was determined with a Philips CM10 TEM with Olympus Sis Megaview G2 Digital Camera after it dried. Furthermore, ImageJ freeware was used for the UCNRs size distribution analysis. Moreover, the zeta-potentials of PEGylated UCNRs were measured using a Zeta sizer Nano ZS (Malvern Instruments, U.K.) at 25°C in MilliQ water (at the concentration of 1mg/mL). The HORIBA Scientific FluoroLog spectrofluorometer with the 980nm laser excitation was employed to measure the emission spectrum of the PEGylated UCNRs with various ARs.

Cell imaging with confocal microscopy PEGylated UCNRs at the concentration of 0, 20, 50, 100, 500 μ g/mL were incubated with endothelial cells, NSC-34 cells and primary neurons at 37 °C for 4 h under 5% CO₂, respectively. After rinsing with PBS for three times, cells were further fixed in 4% paraformaldehyde for 0.5 h at room temperature. Thereafter, the fixed cells were washed with PBS and then were stained with 2 μ M Hoechst 33342 and 1.5X deep red plasma membrane for 10min at 37°C in dark. The stained cells were washed with PBS and mounted with mounting media before the coverslips were sealed with nail polish. The cells without UCNRs-PEG-COOH incubation served as the blank control. Confocal microscopy measurement was conducted to confirm the location and uptake efficiency of the UCNPs using a confocal microscope (ZEISS LSM 880 with

Airyscan) illuminated with a 980-nm laser module. The oil-immersions of 40 \times and 100 \times objectives were employed in this measurement process. The excitation intensity of 980nm laser was set to $9.8 \times 10^7 \text{W/cm}^2$. For each type of cell incubation with PEGylated UCNRs (including various ARs 1, 2, 3 and 4), a minimum of three different cell areas was imaged.

Quantification of uploaded PEGylated UCNRs in cells The cellular uptake of PEGylated UCNRs with various ARs was quantitatively measured with the Imaris analysis software. For each cell-cultured glass slide, a minimum of three different cell regions was imaged. For the image analysis, the label of cell nuclear and membranes were used to distinguish single cell and cell cluster within the excitation spot. The resulting PEGylated UCNRs signals were quantified as a mean signal value per area, which was the measurement of the mean cellular uptake capability of PEGylated UCNRs. The relative intensity of PEGylated UCNRs photoluminescent signal was recorded and normalized with respect to the largest cellular uptake level observed (PEGylated UCNRs with ARs 1:2), which was set to 100%.

Cell Cytotoxicity Assay To detect the cellular cytotoxicity of PEGylated UCNRs in endothelial cells, NSC-34 neuron like cells and primary neurons, 3-[4,5-dimethylthiazol-2-yl]-2,5-diphenyltetrazolium-bromide (MTT) proliferation assay was employed in this study. The MTT assay is based on the approach firstly described by Mossmann (1983).³⁴ The assay was modified for the cell lines used in the experiments. Typically, 200 μL of 1.0×10^4 cells/mL hCMEC/D3 endothelial cells (or NSC-34 cells or primary neurons) were seeded into each well of a 96-well microplate with cell cultured medium and incubated for totally 24h at 37 °C. Thereafter, the cell culture media was replaced with another 200 μL fresh cell culture media containing increasing PEGylated UCNRs concentrations (0, 1, 10, 20, 50 and 100mg/ml). Then the plates were further incubated for another 24 h before 10 μL of 5.0 mg/mL MTT in phosphate buffered saline was added into each well for detection of cell viability. Followed with that, the cells were incubated at 37 °C for 4 h to form the insoluble purple formazan crystals. Thereafter, the supernatant was carefully removed before 150 μL dimethyl sulfoxide was added into each well and incubated for 2h in the dark at

room temperature. Ultimately, the absorbance was recorded using the Biotek Microplate Reader (Biotek, U.S.A.) at a wavelength of 570 nm.^{34, 35} The cell wells without PEGylated UCNRs treatment as control were assumed have 100% viability. Therefore, the PEGylated UCNRs treated viable cells percentage was calculated based on the absorbance of the control cultures.

Luminescent Intensity of Single PEGylated UCNRs To further confirm the optical property of each ARs of PEG-UCNRs for quantification use, the comparison of luminescent intensity of single PEG-UCNPs with various ARs was conducted in this study. 100uL of 0.5mg/mL PEG-UCNPs in water were used to rinse the coverslip, then it was upside down attached on a glass slide and sealed with nail polish after the coverslip was dried. The luminescent intensity of ARs of PEG-UCNRs were confirmed by homemade microscopy with a built-in 980nm laser. The intensity of each ARs of PEG-UCNRs were measured 3 times and the average value was obtained for comparison.

Reference

- (1) Jiang, W.; Kim, B. Y. S.; Rutka, J. T.; Chan, W. C. W. Nanoparticle-Mediated Cellular Response Is Size-Dependent. *Nat. Nanotechnol.* **2008**, *3*, 145–150.
- (2) Alivisatos, A. P.; Gu, W.; Larabell, C. Quantum Dots as Cellular Probes. *Annu. Rev. Biomed. Eng.* **2005**, *7*, 55–76.
- (3) Prabha, S.; Zhou, W. Z.; Panyam, J.; Labhasetwar, V. Size-Dependency of Nanoparticle-Mediated Gene Transfection: Studies with Fractionated Nanoparticles. *Int. J. Pharm.* **2002**, *244*, 105–115.
- (4) Chithrani, B. D.; Chan, W. C. W. Elucidating the Mechanism of Cellular Uptake and Removal of Protein-Coated Gold Nanoparticles of Different Sizes and Shapes. *Nano Lett.* **2007**, *7*, 1542–1550.
- (5) Cho, E. C.; Au, L.; Zhang, Q.; Xia, Y. The Effects of Size, Shape, and Surface Functional Group of Gold Nanostructures on Their Adsorption and Internalization by Cells. *Small* **2010**, *6*, 517–522.
- (6) Zorko, M.; Langel, Ü. Cell-Penetrating Peptides: Mechanism and Kinetics of Cargo Delivery. *Advanced Drug Delivery Reviews*, 2005, *57*, 529–545.
- (7) Verma, A.; Uzun, O.; Hu, Y.; Hu, Y.; Han, H.-S.; Watson, N.; Chen, S.; Irvine, D. J.; Stellacci, F. Surface-Structure-Regulated Cell-Membrane Penetration by Monolayer-Protected Nanoparticles. *Nat. Mater.* **2008**, *7*, 588–595.
- (8) Cho, E. C.; Xie, J.; Wurm, P. A.; Xia, Y. Understanding the Role of Surface Charges in Cellular Adsorption versus Internalization by Selectively Removing Gold Nanoparticles on the Cell Surface with a I 2/KI Etchant. *Nano Lett.* **2009**, *9*, 1080–1084.
- (9) Verma, A.; Stellacci, F. Effect of Surface Properties on Nanoparticle-Cell

- Interactions. *Small*, 2010, 6, 12–21.
- (10) Chithrani, B. D.; Ghazani, A. A.; Chan, W. C. W. Determining the Size and Shape Dependence of Gold Nanoparticle Uptake into Mammalian Cells. *Nano Lett.* **2006**, 6, 662–668.
- (11) Yoo, J. W.; Doshi, N.; Mitragotri, S. Endocytosis and Intracellular Distribution of PLGA Particles in Endothelial Cells: Effect of Particle Geometry. *Macromol. Rapid Commun.* **2010**, 31, 142–148.
- (12) Meng, H.; Yang, S.; Li, Z.; Xia, T.; Chen, J.; Ji, Z.; Zhang, H.; Wang, X.; Lin, S.; Huang, C.; *et al.* Aspect Ratio Determines the Quantity of Mesoporous Silica Nanoparticle Uptake by a Small Gtpase-Dependent Macropinocytosis Mechanism. *ACS Nano* **2011**, 5, 4434–4447.
- (13) Perry, J. L.; Herlihy, K. P.; Napier, M. E.; Desimone, J. M. PRINT: A Novel Platform toward Shape and Size Specific Nanoparticle Theranostics. *Acc. Chem. Res.* **2011**, 44, 990–998.
- (14) Geng, Y.; Dalhaimer, P.; Cai, S.; Tsai, R.; Tewari, M.; Minko, T.; Discher, D. E. Shape Effects of Filaments versus Spherical Particles in Flow and Drug Delivery. *Nat. Nanotechnol.* **2007**, 2, 249–255.
- (15) Chauhan, V. P.; Popović, Z.; Chen, O.; Cui, J.; Fukumura, D.; Bawendi, M. G.; Jain, R. K. Fluorescent Nanorods and Nanospheres for Real-Time in Vivo Probing of Nanoparticle Shape-Dependent Tumor Penetration. *Angew. Chemie - Int. Ed.* **2011**, 50, 11417–11420.
- (16) Shimoni, O.; Yan, Y.; Wang, Y.; Caruso, F. Shape-Dependent Cellular Processing of Polyelectrolyte Capsules. *ACS Nano* **2013**, 7, 522–530.
- (17) Shukla, S.; Eber, F. J.; Nagarajan, A. S.; Difranco, N. A.; Schmidt, N.; Wen, A. M.; Eiben, S.; Twyman, R. M.; Wege, C.; Steinmetz, N. F. The Impact of Aspect Ratio on the Biodistribution and Tumor Homing of Rigid Soft-Matter Nanorods. *Adv. Healthc. Mater.* **2015**, 4, 874–882.
- (18) Link, S.; Mohamed, M. B.; El-Sayed, M. A. Simulation of the Optical Absorption Spectra of Gold Nanorods as a Function of Their Aspect Ratio and the Effect of the Medium Dielectric Constant. *J. Phys. Chem. B* **1999**, 103, 3073–3077.
- (19) Tian, G.; Gu, Z.; Zhou, L.; Yin, W.; Liu, X.; Yan, L.; Jin, S.; Ren, W.; Xing, G.; Li, S.; *et al.* Mn²⁺ Dopant-Controlled Synthesis of NaYF₄:Yb/Er Upconversion Nanoparticles for in Vivo Imaging and Drug Delivery. *Adv. Mater.* **2012**, 24, 1226–1231.
- (20) Lu, Y.; Zhao, J.; Zhang, R.; Liu, Y.; Liu, D.; Goldys, E. M.; Yang, X.; Xi, P.; Sunna, A.; Lu, J.; *et al.* Tunable Lifetime Multiplexing Using Luminescent Nanocrystals. *Nat. Photonics* **2013**, 8, 32–36.
- (21) Liu, D.; Xu, X.; Du, Y.; Qin, X.; Zhang, Y.; Ma, C.; Wen, S.; Ren, W.; Goldys, E. M.; Piper, J. A.; *et al.* Three-Dimensional Controlled Growth of Monodisperse Sub-50 Nm Heterogeneous Nanocrystals. *Nat. Commun.* **2016**, 7, 10254.
- (22) Auzel, F. Upconversion and Anti-Stokes Processes with F and D Ions in Solids. *Chemical Reviews*, 2004, 104, 139–173.
- (23) Wang, F.; Liu, X. Recent Advances in the Chemistry of Lanthanide-Doped Upconversion Nanocrystals. *Chem. Soc. Rev.* **2009**, 38, 976.
- (24) Chatterjee, D. K.; Gnanasammandhan, M. K.; Zhang, Y. Small Upconverting Fluorescent Nanoparticles for Biomedical Applications. *Small* **2010**, 6, 2781–2795.
- (25) Haase, M.; Schäfer, H. Upconverting Nanoparticles. *Angew. Chemie - Int. Ed.*

- 2011**, 50, 5808–5829.
- (26) Wen, S.; Li, D.; Liu, D.; Xu, X.; Du, Y.; Mitchell, D. R. G.; Shi, B.; Shi, X.; Jin, D. Seed Mediated One-Pot Growth of Versatile Heterogeneous Upconversion Nanocrystals for Multimodal Bioimaging. **2016**, 10013, 1001315.
 - (27) Fu, L.; Morsch, M.; Shi, B.; Wang, G.; Lee, A.; Radford, R.; Lu, Y.; Jin, D.; Chung, R. Versatile Upconversion Surface Evaluation Platform for Bio-Nano Surface Selection for Nervous System. *Nanoscale* **2017**.
 - (28) Liu, Y.; Lu, Y.; Yang, X.; Zheng, X.; Wen, S.; Wang, F.; Vidal, X.; Zhao, J.; Liu, D.; Zhou, Z.; *et al.* Amplified Stimulated Emission in Upconversion Nanoparticles for Super-Resolution Nanoscopy. *Nature* **2017**, 543, 229–233.
 - (29) Ma, C.; Xu, X.; Wang, F.; Zhou, Z.; Liu, D.; Zhao, J.; Guan, M.; Lang, C. I.; Jin, D. Optimal Sensitizer Concentration in Single Upconversion Nanocrystals. *Nano Lett.* **2017**, 17, 2858–2864.
 - (30) Liu, D.; Xu, X.; Du, Y.; Qin, X.; Zhang, Y.; Ma, C.; Wen, S.; Ren, W.; Goldys, E. M.; Piper, J. A.; *et al.* Three-Dimensional Controlled Growth of Monodisperse Sub-50 Nm Heterogeneous Nanocrystals. *Nat. Commun.* **2016**, 7, 10254.
 - (31) Zhao, J.; Lu, Z.; Yin, Y.; McRae, C.; Piper, J. A.; Dawes, J. M.; Jin, D.; Goldys, E. M. Upconversion Luminescence with Tunable Lifetime in NaYF₄:Yb,Er Nanocrystals: Role of Nanocrystal Size. *Nanoscale* **2013**, 5, 944–952.
 - (32) Dong, A.; Ye, X.; Chen, J.; Kang, Y.; Gordon, T.; Kikkawa, J. M.; Murray, C. B. A Generalized Ligand-Exchange Strategy Enabling Sequential Surface Functionalization of Colloidal Nanocrystals. **2011**, 998–1006.
 - (33) Shi, Y.; Shi, B.; Dass, A. V. E.; Lu, Y.; Sayyadi, N.; Kautto, L.; Willows, R. D.; Chung, R.; Piper, J.; Nevalainen, H.; *et al.* Stable Upconversion Nanohybrid Particles for Specific Prostate Cancer Cell Immunodetection. *Sci. Rep.* **2016**, 6, 37533.
 - (34) Mosmann, T. Rapid Colorimetric Assay for Cellular Growth and Survival: Application to Proliferation and Cytotoxicity Assays. *J. Immunol. Methods* **1983**, 65, 55–63.
 - (35) Shi, B.; Zhang, H.; Bi, J.; Dai, S. Endosomal pH Responsive Polymers for Efficient Cancer Targeted Gene Therapy. *Colloids Surfaces B Biointerfaces* **2014**, 119, 55–65.

The Effect of Aspect Ratio of PEGylated Upconversion Nanocrystals upon the Cellular Uptake

*Libing Fu,^{a,b,c} Bingyang Shi,^{*a,b,c} Guoying Wang,^b Deming Liu,^d Dayong Jin,^e and Roger Chung^{*b}*

^a International Joint Center for Biomedical Innovation, School of Life Sciences, Henan University, Jin Ming Avenue, Kaifeng, Henan, 457004, China

^b Department of Biomedical Sciences, Faculty of Medicine & Health Sciences, Macquarie University, Sydney, NSW 2109, Australia

^c ARC Centre for Nanoscale Biophotonics, Macquarie University, Sydney, NSW 2109, Australia

^d Department of Chemistry and Biochemistry, Concordia University, 7141 Sherbrooke Street West, Montreal, QC H4B 1R6, Canada

^e Institute for Biomedical Materials and Devices (IBMD), Faculty of Science, University of Technology Sydney, Sydney, NSW2007, Australia

E-mail: bingyang.shi@mq.edu.au; roger, chung@mq.edu.au.

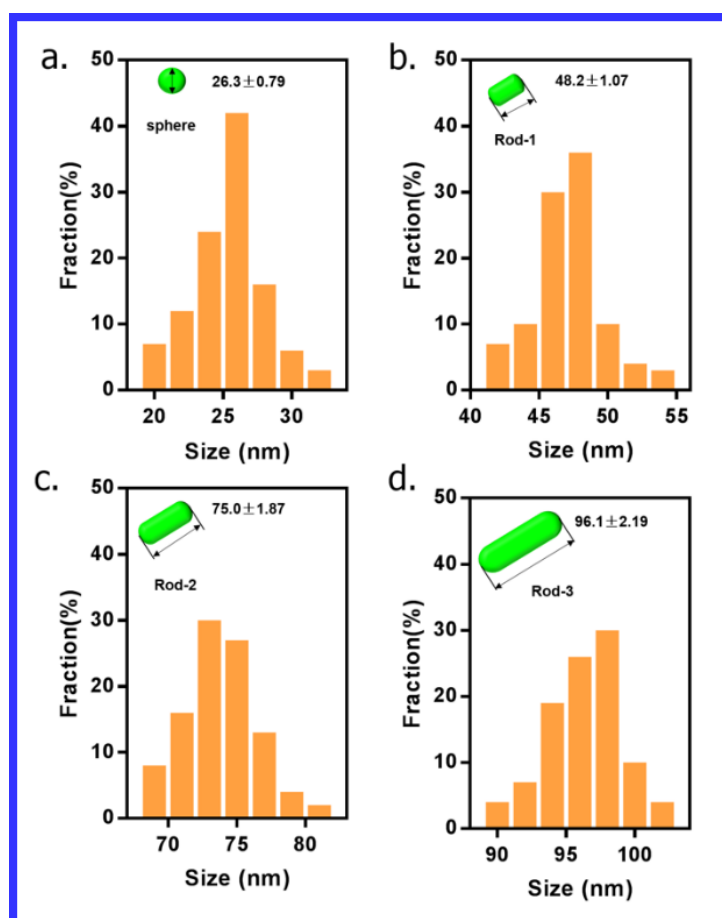


Figure. S1 The size distribution characterization of the unmodified UCNPs with various ARs. a) Sphere, b) AR2, c) AR3, d) AR4.

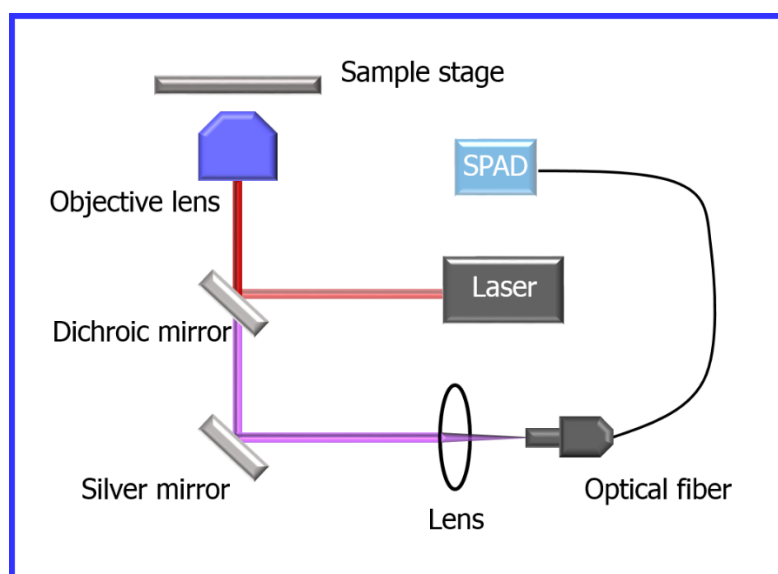


Fig S2. Schematic illustration of the system setup for customized scanning confocal microscope.

5.3 Remarks of Manuscript 3

The key findings of this manuscript: (i) A series of lanthanide ions-doped upconversion nanorods with various ARs (2, 3, and 4) were designed and fabricated via a one-pot hot-injection method that allowed for the precise control of longitudinal growth of core-shell structure from an original spherical UCNPs; (ii) It was found that nanorods with an AR=2 displayed superior cellular uptake by NSC-34 neuron like cells, primary neurons and hCMEC/D3 brain endothelial cells; (iii) A confocal microscopy protocol was developed for single-nanoparticle characterization.

Limitations and future directions: While it was clearly demonstrated that nanorods with an AR=2 displayed the best cell uptake capability in this study, it is recognised that altering AR significantly changes the size and volume of UCNPs. Therefore, it is difficult to separately study the effect of AR and volume/size upon cell uptake. In order to solve this problem, future studies will need to fabricate a variety of nanoparticles with different size but same shape (or same volume with different AR) to compare the influence extent of shape, size and ARs upon cellular uptake capability.

Alternatively, another way to solve this challenge is to use coarse-grained molecular dynamic (CGMD) simulations to mimic the interaction of nanoparticles of various AR, size and shape with the cellular membrane. Such simulation studies can then be correlated with experimental cell culture studies.

This Chapter presents a protocol for single-nanoparticle characterization, which can be used in future for studies that investigate the precise mechanisms that regulate individual UCNPs cellular uptake.

Chapter 6: Summary and Future Scope

6.1 Summary

The mortality rate of Alzheimer's disease, the most common type of the central nervous system(CNS) has increased 68% over last few years ,[1] leading to become the sixth highest cause of death in the United States five years ago.[2] Meanwhile other types of CNS disorders including Parkinson's disease, strokes and brain cancer also desperately need an effective and noninvasive therapy.[3, 4] A key challenge to treat these CNS diseases is the existence of blood-brain barrier, which is supposed to protect the brain from noxious agents, however as a consequence also hinders about 99% of drugs from crossing the BBB to enter the CNS.

Several strategies have been utilized to deliver drugs across this barrier, however some of these methods may damage the structure of the BBB by forcibly opening it to allow the uncontrolled passage of drugs. Therefore a preferable method is to transport drugs across the BBB in a controllable manner that does not damage the barrier. Nanoparticles-based drug delivery strategies provide one approach to achieve this goal, because they have numerous advantages including tunable biophysical properties including surface engineering, size and shape leading to various biological response (like biodistribution, biocompatibility and clearance) in the biological environment.

In recent years, lanthanide-doped upconversion nanoparticles (UCNPs) have received attention due to their unique and outstanding properties, including non-photobleaching, low auto-fluorescence and tunable size and shape. Furthermore, upconversion nanoparticles are photoactivatable in near-infrared (NIR) light to produce emission at multiple visible light wavelengths and even NIR light, leading to exhibit deep tissue penetration capability for tracking and bioimaging in deep tissues. Therefore, this thesis employed the Ln^{3+} -UCNPs as a versatile platform to explore the roles of biophysical characteristics such as nanoparticle surface, shape on BBB penetration in vitro and in vivo for providing a guideline to future construction of multifunctional nano-carrier for

neurodegenerative diseases therapy. The main results of this PhD work can be summarized below:

(I) An upconversion nano–bio surface evaluation platform was established for the first time, based upon the surface modification of a new generation of UCNPs, evaluated *in vitro* with cultured NSC-34 neuron-like cells and *in vivo* with living zebrafish, to systematically determine the optimal biophysical characteristics of UCNPs for future theranostic applications in the central nervous system (CNS)[Chapter 3]. First, I synthesized high lanthanide-doped UCNPs (β -NaYF₄:20%Yb,4% Tm, Ln³⁺-UCNPs) with tissue penetrative emission at wavelength of 800 nm. New methodologies (described in Chapter 2) were developed to modify these Ln³⁺-UCNPs with various surface engineering strategies, leading to form four popular hydrophilic surfaces which are OA-free, DNA, solid silica layer coating with amino group and PEG-COOH for systematic evaluation. Second, I compared the biophysical characteristics of the functionalized UCNPs such as luminescence spectral properties and brightness, size, surface charge, aqueous stability and cytotoxicity with cultured neuron-like cells. Subsequently, I evaluated cellular uptake by the cultured NSC-34 neuron-like cells and bio-distribution of the surface-modified Ln³⁺-UCNPs in living zebrafish by using confocal microscopy and Imaris software. Through this evaluation workflow, it was found that the surface priorities for NSC-34 cells are PEG-COOH > DNA > OA-free > silica-NH₂ in terms of stability, low cytotoxicity and high cell uptake efficiency *in vitro* and *in vivo*. Finally, I confirmed that PEG is a preferable surface among other surface modification approaches for nanoparticle applications in the nervous system via evaluating the dispersion and bioavailability of those modified Ln³⁺-UCNPs in the spinal cord of living zebrafish. This provides significant information towards future design of nanoparticle-based theranostic applications in CNS disorders.

(II) The second major outcome of this PhD study was that numerous types of transferrin-coated upconversion nanoparticles (Tf-UCNPs) with various morphologies, such as sphere, rod, disk and dumbbell with similar size were designed to investigate the effect of nanoparticle shape upon cellular endocytosis and import across the blood-brain barrier and into the brain. I compared the biophysical characteristics of the functionalized UCNPs including particle morphology, surface conjugation, UVvis absorbance and cytotoxicity.

Furthermore, I investigated the cellular uptake and BBB penetration of these Tf-UCNPs with cultured hCMEC/D3 brain endothelial cells and microinjection into the bloodstream of living zebrafish, employing confocal microscopy and Imaris software to quantification analysis. The results revealed that rod-shaped Tf-UCNPs were the superior shape to mediate low cytotoxicity and maximal cellular uptake in comparison to three other shapes of UCNPs namely sphere-, disk- and dumbbell-shapes. In addition, transferrin significantly improved the cellular uptake efficiency of the UCNPs by the brain endothelial cells. Zebrafish were employed to study the BBB penetration ability of nanoparticles in vivo, where it was identified that rod-shaped UCNPs are the most suitable and appropriate morphology for BBB permeation compared to other shapes (such as spherical, disc and dumbbell-like). In conclusion, this provides important information and guideline for structure design of high-efficiency nanoparticle-based vector to delivery drugs across the BBB for neurodegenerative disorder therapy.

(III) The third key outcome is that a series of PEGylated lanthanide-doped unconversion nanorods (Ln^{3+} -UCNRs, $\text{NaYF}_4:20\% \text{Yb}, 4\% \text{Tm}$) with various length/ width aspect ratios ($\text{ARs} = 2, 3$ and 4) was generated with a modified protocol (optimization of this fabrication process is described in Chapter 2) and their cell uptake capability were systematically evaluated in the cultured hCMEC/D3 brain endothelial cells and neurons (NSC-34 neuron-like cells and primary neurons). Typically, nanorods with an $\text{AR} = 2$ displayed superior cellular uptake ability and lower cytotoxicity than nanorods with other ARs or spherical PEGylated Ln^{3+} -UCNPs. In particular, PEG-UCNRs with greater length 75nm ($\text{AR}=3$) to 96nm ($\text{AR}=4$) showed decreased cellular uptake and increased cytotoxicity in all three types of cells. Furthermore, a protocol was developed and optimized to visualize single UCNPs within cultured cells - using this approach it was possible to confirm that while UCNRs with $\text{AR}=2$ do not appear to aggregate, UCNRs with $\text{AR}=3$ or 4 demonstrate significant aggregation. Through this study, I have identified that the ARs of UCNPs provides substantial control over their cellular uptake properties, providing significant information for future optimization of UCNP-based drug carriers for use to treat CNS diseases.

6.2 Future Scope

I believe this work has presented a solid body of knowledge for understanding the effect of biophysical properties such as surface functionalization, shape and aspect ratios of bio-nano hybrids on the BBB permeation properties of Ln^{3+} -UCNPs. To the best of my knowledge, this is the first study that has been undertaken to systematically evaluate how the biophysical properties of high lanthanide-doped UCNPs effects their cellular uptake and BBB penetration. Importantly, the outstanding chemical and physical advantages of UCNPs including photo-stability, absence of auto-fluorescence and their excellent ability to penetrate light in tissue brought a lot of simplicity and convenience during this study. For instance, the optical properties of these UCNPs enables them to be used directly as an imaging probe without further functionalization, and their permanent photo-stability make it possible for long-term 3-D imaging without fear of photo-bleaching, which is quite superior to equivalent imaging probes that rely upon a fluorescent dye that rapidly bleaches. The results of this study provide significant guidance for future construction of UCNP-based nanocomposites for diagnosis and CNS disorders therapy. There are a number of future directions that can expand upon this knowledge. Here, I will provide opinions on future directions of UCNP-based drug delivery based on the outcome of this PhD study and extend to overcome the challenges remained for CNS diseases therapy.

(i) **Imaging Probe.** Due to their unique optical properties, UCNPs have potential to achieve long-term real-time tracking of processes such as cellular endocytosis and BBB model penetration. Such applications require high luminescent intensity for the small-sized Ln^{3+} -UCNPs. However, luminescent intensity generally increases dramatically with the increasing size of nanoparticles, not only because of the surface quench, but also the smaller-sized UCNPs possess fewer photons in each particle. Therefore, it is a great challenge to fabricate high sensitivity but small (so that they are biocompatible) Ln^{3+} -UCNPs with dense photon nanocrystals. This thesis has developed a modified technique that can tightly control the size of nanoparticle through modification of the heating-up speed, making it possible to fabricate small-sized Ln^{3+} -UCNPs with high quality and optical sensitivity for single nanoparticles tracking in the living endothelial cells for unveiling underlying mechanisms of interactions between BBB and nanoparticles.

(ii) **Drug delivery.** The drug loading capability is a crucial factor for the efficacy of various pharmaceutical payload and improve the solubility, stability of the drugs.[5]

Combined with the finding from this study, I can further utilize PEGylated Ln^{3+} -UCNRs with AR=2 (width = 26nm, length = 50 nm) as a vector to load drugs and test their drug delivery capability. In order to increase the drug loading efficiency, there are three methods:

(a) “Hydrophobic pocket” is for loading hydrophobic therapeutic agents, the hydrophobic-hydrophobic interaction between the hydrophobic ligand on the particle surface and the drugs.[6]

(b) Mesoporous silica layers. Drugs are deposited in the pores of mesoporous silica shells coated onto the surface of UCNPs. The mesoporous in the silica shell have a high surface area and large pore volume,[7, 8] enabling it to accommodate large amount of drugs.[9]

(c) Hollow sphere with mesoporous surface. In the third method, drugs are loaded into a hollow UCNP with a mesoporous shell. The hollow structure enables adequate levels of drug loading while maintaining UC PL imaging ability.[10, 11]

Future studies should investigate which method can most effectively improve the drug-carrying capacity of Ln^{3+} -UCNPs.

(iii) **Targeted Functionalization.** Typically, the smaller biocompatible Ln^{3+} -UCNPs (within 50nm) need to be targeted functionalized with “stealth” character and bypass the nonspecific organ uptake and monocyte- macrophage system scavenging for improving blood circulation and targeting efficiency in the body. Meanwhile, the sensitivity of measurement and analysis will profoundly benefit from the increasing targeted efficiency. Therefore, I can go deeper to localize the UCNPs when they passed the BBB and enter into the brain.

(iv) **Nanotoxicity of Lanthanide UCNPs.** Nanotoxicology studies and safety assessment are significant and essential for developing UCNPs for clinical applications. This covers nanoparticle distribution and transformation, clearance and any induced changes of the organs or tissues both at macroscopic and microscopic levels. However, this part of study has not been investigated in this project. Therefore, in future studies, the biodistribution and clearance of Ln^{3+} -UCNPs in zebrafish or rats needs to be investigated. In addition, it was found that aggregation of Ln^{3+} -UCNPs in biological media was common and this

affects cellular uptake capability. This is likely to be related to the interaction of Ln^{3+} -UCNPs with proteins to form a protein corona. Therefore future studies should seek to characterize the protein corona, and understand how it influences UCNP bioactivity.

6.3 Reference

- [1] A. Association, 2013 Alzheimer's disease facts and figures, *Alzheimer's Dement.* 9 (2013) 208–245.
- [2] S. National Center for Health, Table A-3. Cancer among adults aged 18 and over, by selected characteristics: United States, 2014, *Heal. United States*, 2014 With Spec. Featur. Adults Aged 55-64. 6 (2015) 1–9.
- [3] B.T. Hawkins, The Blood-Brain Barrier/Neurovascular Unit in Health and Disease, *Pharmacol. Rev.* 57 (2005) 173–185.
- [4] M. Ricci, P. Blasi, S. Giovagnoli, C. Rossi, Delivering drugs to the central nervous system: a medicinal chemistry or a pharmaceutical technology issue?, *Curr. Med. Chem.* 13 (2006) 1757–1775.
- [5] J. Xie, S. Lee, X. Chen, Nanoparticle-based theranostic agents, *Adv. Drug Deliv. Rev.* 62 (2010) 1064–1079.
- [6] H. Xu, L. Cheng, C. Wang, X. Ma, Y. Li, Z. Liu, Polymer encapsulated upconversion nanoparticle/iron oxide nanocomposites for multimodal imaging and magnetic targeted drug delivery, *Biomaterials*. 32 (2011) 9364–9373.
- [7] C. Argyo, V. Weiss, C. Bräuchle, T. Bein, Multifunctional mesoporous silica nanoparticles as a universal platform for drug delivery, *Chem. Mater.* 26 (2014) 435–451.
- [8] J. Kim, H.S. Kim, N. Lee, T. Kim, H. Kim, T. Yu, I.C. Song, W.K. Moon, T. Hyeon, Multifunctional uniform nanoparticles composed of a magnetite nanocrystal core and a mesoporous silica shell for magnetic resonance and fluorescence imaging and for drug delivery, *Angew. Chemie - Int. Ed.* 47 (2008) 8438–8441.
- [9] X. Zhang, P. Yang, Y. Dai, P. Ma, X. Li, Z. Cheng, Z. Hou, X. Kang, C. Li, J. Lin, Multifunctional up-converting nanocomposites with smart polymer brushes gated mesopores for cell imaging and thermo/pH dual-responsive drug controlled release, *Adv. Funct. Mater.* 23 (2013) 4067–4078.

- [10] L. Dong, D. An, M. Gong, Y. Lu, H.L. Gao, Y.J. Xu, S.H. Yu, PEGylated upconverting luminescent hollow nanospheres for drug delivery and in vivo imaging, *Small*. 9 (2013) 3235–3241.
- [11] Z. Xu, P. Ma, C. Li, Z. Hou, X. Zhai, S. Huang, J. Lin, Monodisperse core-shell structured up-conversion $\text{Yb(OH)CO}_3 @ \text{YbPO}_4 : \text{Er}^{3+}$ hollow spheres as drug carriers., *Biomaterials*. 32 (2011) 4161–73.